



Universidade Estadual de Campinas
Instituto de Química

Leonardo José Duarte

Chemistry of Molecular Vibrations

Química de Vibrações Moleculares

Campinas
2023

Leonardo José Duarte

Chemistry of Molecular Vibrations

Química de Vibrações Moleculares

Doctor's Thesis presented to the Institute of Chemistry of the University of Campinas as part of the requirements to obtain the title of Doctor in Sciences.

Tese de Doutorado apresentada ao Instituto de Química da Universidade Estadual de Campinas como parte dos requisitos exigidos para a obtenção do título de Doutor em Ciências.

Supervisor: Emeritus Prof. Dr. Roy Edward Bruns.

O arquivo digital corresponde à versão final da Tese defendida pelo aluno Leonardo José Duarte e orientada pelo Prof. Emérito Dr. Roy Edward Bruns.

Campinas
2023

Ficha catalográfica
Universidade Estadual de Campinas
Biblioteca do Instituto de Química
Simone Luiz Alves - CRB 8/9094

D85c Duarte, Leonardo José, 1995-
Chemistry of molecular vibrations / Leonardo José Duarte. – Campinas, SP
: [s.n.], 2023.

Orientador: Roy Edward Bruns.
Tese (doutorado) – Universidade Estadual de Campinas, Instituto de
Química.

1. Espectroscopia vibracional. 2. Constantes de força. 3. Reação
nucleofílica. 4. Espectroscopia de infravermelho. 5. QAIM (Teoria Quântica de
Átomos em Moléculas) . I. Bruns, Roy Edward, 1941-. II. Universidade Estadual
de Campinas. Instituto de Química. III. Título.

Informações Complementares

Título em outro idioma: Química de vibrações moleculares

Palavras-chave em inglês:

Vibrational spectroscopy

Force constant

QAIM (Quantum Theory of Atoms in Molecules)

Nucleophilic reactions

Force constant

Infrared spectroscopy

Área de concentração: Físico-Química

Titulação: Doutor em Ciências

Banca examinadora:

Roy Edward Bruns [Orientador]

Adalberto Bono Maurizio Sacchi Bassi

Diego Pereira dos Santos

Mauro Carlos Costa Ribeiro

Roberto Luiz Andrade Haiduke

Data de defesa: 02-02-2023

Programa de Pós-Graduação: Química

Identificação e informações acadêmicas do(a) aluno(a)

- ORCID do autor: <https://orcid.org/0000-0002-1955-6872>

- Currículo Lattes do autor: <http://lattes.cnpq.br/1830078543017489>

Banca Examinadora

Prof. Dr. Roy Edward Bruns (Orientador)

Prof. Dr. Adalberto Bono Maurizio Sacchi Bassi (Universidade Estadual de Campinas)

Prof. Dr. Diego Pereira dos Santos (Universidade Estadual de Campinas)

Prof. Dr. Mauro Carlos Costa Ribeiro (Universidade de São Paulo)

Prof. Dr. Roberto Luiz Andrade Haiduke (Universidade de São Paulo)

A Ata da defesa, assinada pelos membros da Comissão Examinadora, consta no SIGA/Sistema de Fluxo de Dissertação/Tese e na Secretaria do Programa da Unidade.

Este exemplar corresponde à redação final da Tese de Doutorado defendida pelo aluno **Leonardo José Duarte**, aprovada pela Comissão Julgadora em 2 de fevereiro de 2023.

*Dedicado com toda gratidão aos meus pais,
Reinaldo J. Duarte Jr. e Denise N. Savioli
Duarte.*

Acknowledgment

Special thanks to Professor Dr. Roy Edward Bruns for accepting me as student, for being an example of a scientist and teaching me how to progress in the scientific career.

To my friends Arnaldo F. S. Filho and Wagner E. Richter, for the friendship and the opportunities they have given me over the years.

To my colleagues in the department, especially Professor Dr. Pedro Vazquez, Guilherme Morais, Professor Dr. Rogerio Custódio and his students.

To the friends who welcomed me in Manchester, especially Bruna Zucoloto, and to Professor Dr. Paul Popelier for having me in his research group during my internship abroad.

To my family, Denise N. S. Duarte, Reinaldo J. Duarte Júnior.

To my friends, Lucas. G. Vazquez and Rafael L. Soares, their belief in me has kept my motivation high during this process.

To Adriana H. Uehara, for the all the patience and long time companionship.

This study was financed in part by the Coordenação de Aperfeiçoamento de Pessoal de Nível Superior – Brasil (CAPES) – Finance Code 001 and in part by the São Paulo Research Foundation (FAPESP) grants 2017/22741-3 and 2018/24844-7.

A printable version of this document is available at:
github.com/ljduarte/chemistry_of_molecular_vibrations

Molecules react with each other while vibrating about an equilibrium configuration, rotating as a whole around the center of mass, and exchanging energies in all degrees of freedom.

“Kenichi Fukui”

Resumo

O modelo de carga-transferência de carga-polarização dipolar, baseado na Teoria Quântica de Átomos em Moléculas, consegue estimar valores teóricos das derivadas do momento de dipolo elétrico molecular e intensidades no infravermelho com pequeno erro numérico. Valores calculados com métodos teóricos sofisticados tendem a concordar com os valores experimentais dentro de uma pequena margem de erro.

Para os modos normais fora-do-plano, incluir os momentos de dipolo atômico e, conseqüentemente, o termo de polarização dipolar, é mandatório para obter uma descrição acurada das mudanças na densidade eletrônica durante pequenas amplitudes vibracionais. A inclusão do termo de polarização dipolar também é importante para descrever corretamente a densidade eletrônica para distorções de maior amplitude. No caso do modo normal fora-do-plano, a tendência dos átomos sp^2 em adotar uma geometria sp^3 cresce com a amplitude da distorção angular partindo da geometria de equilíbrio. Os termos de polarização também são importantes para reproduzir as intensidades no infravermelho, dado que modelos contendo apenas cargas atômicas irão subestimar a transferência de carga por ignorar os efeitos de relaxação de contrapolarização.

Considerando os modos normais de estados de transição S_N2 , a principal contribuição para a intensidade tem origem nos termos de transferência de carga entre o nucleófilo e o grupo de saída, passando pelo carbono eletrofílico. Quando os átomos vibram dentro do modo normal imaginário, as mudanças na densidade eletrônica do sistema são consistentes com o mecanismo de reação. Particularmente, a direção dos termos de transferência de carga corresponde à direção do movimento dos elétrons representado pelo uso das clássicas setas curvas. A diferença entre os termos de transferência de carga do nucleófilo e do grupo de saída reflete a tendência do átomo de carbono em receber elétrons. Contribuições de polarização dipolar resultam da inversão da geometria molecular e da substituição do grupo de saída por um nucleófilo com diferente eletronegatividade. Esses resultados mostram que o modelo de carga-transferência de carga-polarização dipolar pode, portanto, ser empregado no estudo de reações químicas.

Vibrações moleculares são determinadas por constantes de força provenientes das derivadas de segunda ordem da energia do sistema. Como a energia total resulta de uma soma de contribuições atômicas, a constante de força também pode ser dividida em termos atômicos. Para calcular esses termos, modifica-se o método das matrizes **FG** de Wilson adicionando uma terceira dimensão à matriz Hessiana, contendo as derivadas de segunda ordem dos termos IQA. O método é capaz de reproduzir valores experimentais e teóricos.

A magnitude das constantes de força recebe maior contribuição da componente de Coulomb a de potenciais intra-atômicos. Contribuições de troca e correlação são mais importantes para as constantes de força de estiramento de moléculas diatômicas homonucleares. O aumento da ordem de ligação é associado com um aumento da componente de Coulomb da constante de força. O refinamento da metodologia deve levar a um melhor entendimento da superfície de energia potencial, tornando-se uma ferramenta auxiliar na construção de campos de força.

Abstract

A charge-charge transfer-dipolar polarization model, based on the Quantum Theory of Atoms in Molecules, successfully estimates theoretical dipole moment derivatives and infrared intensities determined directly from wavefunction calculations within numerical errors. High quality quantum level calculations usually agree with experimental measurements within a few percent.

For out-of-plane vibrations, the inclusion of atomic dipole moments, i.e. dipolar polarization effects, is very important to obtain accurate electronic density descriptions for small amplitude vibrations. They can be expected to be just as important for large molecular distortions. For out-of-plane bendings, the sp^2 to sp^3 tendency will be increased for larger angular movements from equilibrium. These polarizations have been found to be important for predicting accurate intensities for most molecules. Models containing only atomic charges will tend to underestimate charge transfer owing to the charge transfer – dipolar polarization vibrational relaxation effect.

Considering the imaginary normal mode of S_N2 transition states, the principal contributions are the charge transfers that occur between the nucleophile and leaving group through the carbon atom. As the atoms vibrate, the changes in the molecular electronic density are consistent with the mechanism of the reaction itself and the direction of CT vectors corresponds to the movement of electrons as described by the classical curved arrows representation of the reaction mechanism. The difference between the charge transfer of the nucleophile and the leaving group indicates the tendency of carbon to receive charge along the reaction coordinate. Dipolar polarizations contributions results from the inversion of the molecular geometry and from the substitution of LG by Nu with different electronegativities. These results show that the charge-charge transfer-dipolar polarization QTAIM formulation provides a much more accurate and detailed description of electronic density changes for small amplitude vibrations than other available models. It can readily be applied to larger molecular distortions as well and may be useful to study chemical reactivity.

Molecular vibrations are determined by force constants, which arise from the potential energy second derivatives. Since the energy of a molecular system results from a sum of atomic terms, the force constant can also be divided into atomic contributions. In order to calculate such contributions, a modification of Wilson's **FG** method was made, in which a new dimension is added to the Hessian matrix. The new dimension contains second derivatives of IQA contributions to the total energy of the system. The method is able to reproduce experimental and theoretical data obtained with analytic methods.

The magnitude of the force constants receive major contributions from the Coulomb and intra-atomic potentials. Exchange-correlation contributions, however, appear as determining factors only for the homonuclear diatomic molecules. The increase in bond order is accompanied by the increase in the Coulomb contribution, while exchange-correlation and intra-atomic terms remain almost unchanged. Although the results herein are incipient, the refinement of the methodology can lead to a better understanding of the potential energy surface and can act as an auxiliary tool in designing force fields for molecular mechanics.

List of Figures

| | | |
|-----|--|----|
| 1.1 | Contour plots of the electron density (ρ), gradient vector field and, Laplacian of ρ , of the water molecule | 16 |
| 1.2 | Experimental dipole moment of CO. | 19 |
| 1.3 | Laplacian of ρ of CO | 20 |
| 2.1 | Schematics of dispersive and FTIR spectrometers | 25 |
| 2.2 | FTIR spectrum of F ₂ CO. | 25 |
| 2.3 | Energy levels of a harmonic oscillator | 26 |
| 2.4 | Difference between FTIR and dispersive IR intensities of halomethanes | 29 |
| 2.5 | Total intensity obtained with the electronegativity model using both experimental and theoretical data. | 32 |
| 2.6 | Plot of the square root of the dynamic carbon contribution against the average electronegativity of the terminal atoms. | 33 |
| 2.7 | Plot of experimental carbon 1s ionization energies corrected for the nearest neighbor potentials against the square root of the dynamic carbon contributions from the electronegativity model. | 34 |
| 2.8 | Normal plot of the difference between the PNNL and the low resolutions intensities. | 36 |
| 2.9 | Comparative graph between FTIR, dispersive and theoretical IR intensities of hydrocarbon. | 37 |
| 3.1 | Flowchart of the theoretical procedure applied to calculate the APT derivatives from single point SCF calculations. | 40 |
| 3.2 | Charge-Transfer and Dipolar Polarization contribution of CH stretch | 46 |
| 3.3 | Counterpolarization effect on a CH bond. | 47 |
| 3.4 | Charge-Transfer and Dipolar Polarization contribution of CH bendings | 47 |
| 3.5 | Counterpolarization effect during the stretching of a chemical bond | 52 |
| 4.1 | Positioning system for planar molecules and normal coordinates for out-of-plane bending vibrations. | 56 |
| 4.2 | Hydrogen atomic charges and their derivatives with respect to displacements perpendicular to the molecular plane. | 58 |
| 4.3 | Schematic representation of a CH Bond in a planar molecule during an out-of-plane angular bending vibrational movement | 58 |
| 4.4 | Atomic dipole and its derivative with respect to displacements perpendicular to the molecular plane. | 59 |
| 4.5 | Experimental NIST/PNNL intensities versus calculated B3LYP/6-311++G(d,p) intensities of substituted benzenes. | 61 |

| | | |
|------|--|-----|
| 4.6 | Static charge \mathcal{A}_{C^2} , dipolar polarization \mathcal{A}_{DP^2} , and interaction \mathcal{A}_{2CDP} contributions for out-of-plane CH bendings of substituted benzenes. | 63 |
| 4.7 | Schematic representation of the 23 out-of-plane vibrations investigated for substituted benzenes. | 64 |
| 4.8 | Linear dependence of square root of experimental intensities and the sum of the hydrogen out-of-plane displacements. | 65 |
| 4.9 | Test set for the linear dependence of square root of experimental intensities and the sum of the hydrogen out-of-plane displacements | 66 |
| 4.10 | Estimate of the rehybridization moment from AIM parameters. | 69 |
| 4.11 | Components of the rehybridization moment. | 69 |
| 4.12 | Relative displacements of the hydrogen and fluorine atoms with their accompanying carbon atom polarizations for normal coordinates of out-of-plane bendings of ethylene and fluoroethylene. | 72 |
| 4.13 | Out-of-plane normal coordinates of boron trihalides and borane. | 78 |
| 4.14 | Stacked bar chart for charge, polarization, and their interaction contributions to the total intensities obtained at the QCISD/aug-cc-pVTZ level. | 80 |
| 4.15 | Schematic representation of dipole moment derivatives vectors for the out-of-plane normal modes of BH_3 and BF_3 | 82 |
| 4.16 | Graph of estimated atomic charges of boron halides obtained from the optimized decision trees against QTAIM charges calculated at the QCISD/aug-cc-pVTZ level. | 84 |
| 4.17 | Graph of estimated atomic dipole derivatives of boron halides obtained from the optimized decision trees against QTAIM derivatives calculated at the QCISD/aug-cc-pVTZ level. | 85 |
| 5.1 | Schematic representation of the hydrogen-bond complexes. | 88 |
| 5.2 | Negatives of hydrogen bond formation enthalpies plotted against the differences of the square roots of complex and monomer intensification of the hydrogen contributions for the AH stretching vibrations. | 92 |
| 5.3 | Theoretical formation enthalpy values graphed against complex-monomer differences in the sum of the charge transfer and dipolar polarization hydrogen contributions to the dipole moment derivatives. | 95 |
| 5.4 | Charge, charge transfer and dipolar polarization contributions for the HF monomer and dimer that explain the intensity enhancement of the hydrogen stretch on complexation. | 96 |
| 5.5 | Charge, charge transfer, and dipolar polarization contributions to the dipole moment derivatives of the HF complexes with HF, H_2O , and NH_3 bases. | 98 |
| 5.6 | Plots of the hydrogen bond enthalpy of formations versus the charge transferred and the sum of the hydrogen and halogen atomic dipole moments along the z axis during the formation of the H-bond | 99 |
| 6.1 | Reaction path for a generic S_N2 reaction. | 101 |
| 6.2 | Structure of S_N2 transition states. | 104 |
| 6.3 | Positioning system and normal coordinate displacements (red arrows) utilized in all transition states. | 105 |
| 6.4 | Structure of the z component of the atomic polar tensor of D, F and Cl atoms aligned with the Cartesian z direction. | 107 |
| 6.5 | S_N2 mechanism represented by red curved arrows. Grey arrows correspond to the weighted charge transfer vectors that points to the positive end. | 111 |

| | | |
|-----|--|-----|
| 6.6 | Charge, charge transfer and dipolar polarization contributions for the molecular dipole moment derivative for transitions states and reagents. | 112 |
| 6.7 | Comparison between the intensities calculated with all atomic terms in all three Cartesian directions and the intensities calculated using only atomic contributions in z direction, using only contributions from the Nu, C and LG in z directions and using only contributions from the Nu, C and LG in all directions | 113 |
| 6.8 | Atomic AIM charges along the IRC path of nine S_N2 transition states. . . | 115 |
| 6.9 | Variation of carbon charge after and before the reaction against the difference between charge transfer of the nucleophile and leaving group. | 116 |
| 7.1 | Structure of $\mathbf{\Lambda}_k^{\text{IQA}}$ matrices. Moving along the k -axis, each λ_{ijk} corresponds to the contribution of energy component k to the eigenvalue of normal mode j . | 121 |
| 7.2 | Infrared spectra of H_2O obtained by three different methods: Analytically calculated by Gaussian16 (dotted black line), numerically calculated with AIM parameters (red line) and, experimentally obtained from PNNL database. | 123 |
| 7.3 | Comparison of force constants calculated with the IQA components with experimental results. | 124 |
| 7.4 | Bond dissociation energy D_o , in $\text{kJ} \cdot \text{mol}^{-1}$ versus bond stretching force constant, in $\text{mdyne} \cdot \text{\AA}^{-1}$ | 124 |
| 7.5 | IQA partitioning of dissociation energy and force constants in diatomic molecules. | 125 |
| 7.6 | Internal coordinates for linear YCX , $X, Y = \text{O}, \text{S}$ | 127 |
| 7.7 | Contributions from second derivatives of IQA terms to the bond stretch, f_{CX} , and angular bend, f_{YCX} , force constants, where $X, Y \in \{\text{O}, \text{S}\}$ | 129 |
| 7.8 | Trend in IQA force constant contributions for F_2CO , Cl_2CO , Br_2CO and H_2CO | 130 |
| A.1 | Diagram for deriving the Beer-Lambert-Bouquer Law. | 133 |
| A.2 | Infrared spectrum of Phosgene | 135 |
| B.1 | Energy diagram for a system transitioning to a higher energy state. | 140 |
| B.2 | Amplitude of the x component of an electric field | 141 |
| D.1 | Cartesian coordinates for ethylene. | 147 |
| D.2 | Bond internal coordinate of the $\text{C}=\text{C}$ bond in ethylene. | 148 |
| D.3 | Angle internal coordinate of the $\text{H}-\text{C}=\text{C}$ bond in ethylene. | 149 |
| D.4 | Torsion internal coordinate in ethylene. | 150 |
| D.5 | Ethylene out-of-plane internal coordinate. | 151 |
| E.1 | Theovib python library. | 153 |
| E.2 | Displacements needed to compute the numerical second derivatives of IQA energies | 155 |
| E.3 | Dependency of model's accuracy on the parameter $\Delta\sigma$ | 155 |
| E.4 | Directory structure of theovib generated files. | 157 |

List of Tables

| | | |
|-----|---|----|
| 2.1 | Experimental and calculated intensities for fluorochloromethanes. | 28 |
| 2.2 | FTIR, dispersive, QCISD/aug-cc-pVTZ, QCISD/cc-pVTZ and MP2/aug-cc-pVTZ total intensity of fluorochloromethanes | 30 |
| 2.3 | Atomic contributions to the total intensity of fluorochloromethanes | 31 |
| 2.4 | Experimental and calculated intensities for hydrocarbons. | 35 |
| 3.1 | CCTDP contributions for CH stretching mode. | 45 |
| 3.2 | CCTDP contributions for CH bending mode. | 48 |
| 3.3 | CCTDP contributions for CF stretching mode. | 49 |
| 3.4 | CCTDP contributions for CCl stretching mode. | 50 |
| 3.5 | CCTDP contributions for CF and Cl bending modes. | 51 |
| 3.6 | Variation of the charge transfer and dipolar polarization sums with the level of theory. | 53 |
| 3.7 | Average variation of the charge and charge transfer-dipolar polarization with the level of theory. | 54 |
| 4.1 | CCTDP contributions and their sums for the CH out-of-Plane bending intensities. | 62 |
| 4.2 | Equilibrium charge of hydrogen atoms and atomic polarization dipole moment derivatives with respect to hydrogen atom out-of-plane displacements | 67 |
| 4.3 | Total charge and dipolar polarization contributions to the dipole moment derivative and IR intensities ($\text{km}\cdot\text{mol}^{-1}$) of out-of-plane bending vibrations of ethylene, tetrafluoroethylene and difluoro- and dichloroethylenes as well their isotopologues. | 72 |
| 4.4 | IR wavenumbers and intensities from Gaussian and from various charge models. | 77 |
| 4.5 | CCTDP, approximate and decision tree transferred intensities of boron halides and borane. | 79 |
| 4.6 | Atomic contributions to the out-of-plane intensity of boron halides. | 81 |
| 5.1 | Hydrogen-bond formation enthalpy, and differences in square roots of the complex and monomer intensities of the AH stretching mode. | 91 |
| 5.2 | AH stretching CCTDP intensity contributions for the HF and HCl proton donors and monomers. | 93 |
| 5.3 | Charge-charge transfer-dipolar polarization hydrogen contributions to the dipole moment derivatives for HF and HCl hydrogen bond complexes. | 94 |
| 5.4 | Individual charge, charge transfer and dipolar polarization contributions (in e) to the dipole moment derivative of AH stretching. | 97 |

| | | |
|-----|---|-----|
| 5.5 | Charge transferred from the base to the acid (e) and base-induced polarization ($e \cdot Bohr$) in the acid for the HF and HCl complexes. | 100 |
| 6.1 | CCTDP parameters for CH ₄ (or CH ₃ D), CH ₃ F and CH ₃ Cl. | 106 |
| 6.2 | CCTDP contributions to the intensities of the imaginary normal mode . . | 109 |
| 6.3 | Atomic contributions and bond contributions for the imaginary normal mode of transition states. | 110 |
| 6.4 | Infrared intensities of S_N2 imaginary normal modes. | 112 |
| 7.1 | Second derivatives of IQA contributions to the forces constants of CO ₂ , SCO, CS ₂ and CO. | 128 |
| 7.2 | Bond force constant for the series: ethane, ethylene, benzene and O ₂ , O ₃ , H ₂ O ₂ | 131 |
| A.1 | Conversion constants for infrared intensity units. | 135 |
| D.1 | Cartesian coordinates of ethylene equilibrium structure at the B3LYP/aug-cc-pVTZ level. | 147 |
| D.2 | B matrix of ethylene. | 152 |
| E.1 | Cartesian coordinates of water equilibrium structure at the B3LYP/aug-cc-pVTZ level. | 154 |

List of Acronyms

| | | |
|--------|-------|--|
| QTAIM | | Quantum Theory of Atoms In Molecules |
| AIM | | Atoms In Molecules |
| QCISD | | Quadratic Configuration Interaction with Singles and Doubles |
| IQA | | Interacting Quantum Atoms |
| EDS | | Energy Decomposition Scheme |
| FTIR | | Fourier Transform Infrared Spectroscopy |
| PNNL | | Pacific Northwest National Laboratory |
| CCTDP | | Charge-Charge Transfer-Dipolar Polarization |
| APT | | Atomic Polar Tensor |
| RMSE | | Root Mean Square Error |
| RMSD | | Root Mean Square Difference |
| MAE | | Mean Absolute Error |
| ESCA | | Electron Spectroscopy for Chemical Analysis |
| VSEPR | | Valence Shell Electron Pair Repulsion |
| CCCBDB | | Computational Chemistry Comparison and Benchmark Database |
| SCF | | Self-Consistent Field |
| PES | | Potential Energy Surface |
| RHS | | Right Hand Side |
| LHS | | Left Hand Side |
| TS | | Transition State |
| C | | Charge |
| CT | | Charge Transfer |
| DP | | Dipolar Polarization |
| LG | | Leaving Group |
| Nu | | Nucleophile |
| IR | | Infrared |

Contents

| | | |
|----------|--|------------|
| 1 | Atoms in Molecules | 14 |
| 1.1 | Quantum Theory of Atoms in Molecules | 15 |
| 1.2 | QTAIM Charges and Dipoles | 18 |
| 1.3 | The Interacting Quantum Atoms | 19 |
| 2 | Experimental Infrared Intensities | 24 |
| 2.1 | FTIR and Dispersive Gas-Phase Fundamental Infrared Intensities of halo- methanes | 26 |
| 2.2 | FTIR and Dispersive Gas-Phase Absolute IR Intensities of Hydrocarbons Fundamental Bands | 33 |
| 2.3 | Concluding Remarks | 37 |
| 3 | Decomposition of Infrared Intensities | 39 |
| 3.1 | The CCTDP Model for Infrared Intensities | 40 |
| 3.2 | CCTDP Classification of IR Intensities | 43 |
| 3.3 | Probing the Robustness of the CCTDP model | 52 |
| 3.4 | Concluding Remarks | 55 |
| 4 | Out-of-Plane vibrations | 56 |
| 4.1 | The Charge Transfer Equals Zero | 57 |
| 4.2 | CH Out-of-Plane Bending Intensities of Benzene Molecules | 59 |
| 4.3 | IR Intensities of Fundamental Bands for Out-of-Plane bending in Ethylene and Dichloro and Difluoroethylenes | 71 |
| 4.4 | The Unavoidable Failure of Point Charges | 73 |
| 4.5 | The Rehybridization Moment in Boron Trihalides | 78 |
| 4.6 | Concluding Remarks | 86 |
| 5 | Infrared Intensification and Hydrogen Bond Stabilization | 87 |
| 5.1 | The CCTDP Model for Infrared Intensification | 88 |
| 5.2 | Charge Transfer and Dipolar Polarization Mechanism for Hydrogen Bond- ing Intensity Enhancement | 95 |
| 5.3 | Complex Formation | 98 |
| 5.4 | Concluding Remarks | 99 |
| 6 | Infrared Intensities of Imaginary Frequencies | 101 |
| 6.1 | The Intrinsic Reaction Coordinate | 103 |
| 6.2 | Translational Invariability of the Dipole Moment Derivative for Charged Systems | 104 |
| 6.3 | Imaginary Normal Mode | 105 |

| | | |
|----------|--|------------|
| 6.4 | CCTDP analysis of CH ₄ , CH ₃ F and CH ₃ Cl | 106 |
| 6.5 | CCTDP Partitioning of Transition States | 108 |
| 6.6 | Charges Along the Reaction Coordinate | 113 |
| 6.7 | Concluding Remarks | 116 |
| 7 | Energetic Origins of Force Constants | 118 |
| 7.1 | The 3D Hessian Matrix | 119 |
| 7.2 | Force Constants in Internal Coordinates | 120 |
| 7.3 | Calculating the IQA Hessian | 122 |
| 7.4 | QTAIM IR Spectra | 122 |
| 7.5 | Force Constants and Bond Dissociation Energies | 122 |
| 7.6 | Force Constants of CO, CO ₂ , SCO and CS ₂ | 127 |
| 7.7 | Bond order: the C–C Bond in Ethane, Ethylene and Benzene and the O–O, Bond in O ₂ , O ₃ and H ₂ O ₂ | 130 |
| 7.8 | Concluding Remarks | 130 |
| A | Dimensions and Units of Infrared Intensities | 132 |
| A.1 | The Beer–Lambert–Bouguer law | 132 |
| A.2 | Experimental intensities | 134 |
| A.3 | Calculated Intensities | 136 |
| B | Absorption of Radiation and Infrared Intensity | 138 |
| B.1 | Time–Dependent Schrödinger Equation | 138 |
| B.2 | Einstein Coefficients and Absorption of Radiation | 139 |
| B.3 | Infrared Intensity of a Normal Mode of Vibration[15] | 142 |
| C | Matrix Treatment for the CCTDP Model | 145 |
| C.1 | Obtaining the CCTDP Contributions | 146 |
| D | Definition of Internal Coordinates | 147 |
| D.1 | Bond stretching | 148 |
| D.2 | Angular bending | 148 |
| D.3 | Dihedral torsion | 150 |
| D.4 | Out–of–plane bending | 151 |
| E | The Theovib library | 153 |
| E.1 | Installation | 153 |
| E.2 | Usage | 154 |

Chapter 1

Atoms in Molecules

The concept of “atom” was first introduced by early Greek philosophers. Thales of Miletus proposed water to be the primordial matter of all things. Anaximenes adopted a similar idea, defining air as primordial matter. Heraclitus, in turn, attributed this same property to fire. The first definition of an atomistic philosophy, however, came from Democritus (470-380 BCE). Although we cannot treat Democritus’ atom as a real scientific model, the similarities between his hypothesis and the modern concept of atom are startling. The properties of his atoms are as follows:

- The number of atoms is infinite, they are identical in nature, but differ in size and shape. The observed characteristic of things arises not only from their different shapes, but also from their relative positions;
- Atoms are always in ceaseless motion, that can be changed through pressure.

These properties were sufficient to describe the different states of aggregation of matter (solid, liquid, and gas) and lead to an exact definition of “density”[1].

Later, Empedocles, Aristotle and other philosophers also contributed to the atomistic philosophy. Democritus’ ideas, however, were never forgotten and the first scientific model of the atom would see the light two thousand years later, formulated by John Dalton (1766-1844). Dalton was himself highly influenced by Newton’s (1642-1727) corpuscular theory that was based in Boyle’s (1626-1691) theory of the behavior of gases. Dalton’s observations on pressure and solubility of gases in water lead him to assume that atoms are indivisible solid particles that can combine to form “compound atoms”. This assumption allowed the determination of relative atomic weights and chemical formulas [2].

The next great advance in the atomic theory was the discovery of the electron by J. J. Thomson (1856-1940). Since atoms are neutral in charge, the existence of electrons led Thomson to state that an atom was not just a small solid particle, but a sphere of positive charges that has electrons attached to it. A couple of years later, Ernest Rutherford (1871-1937) was analyzing the scattering pattern of alpha particles through a very thin gold foil. He discovered that the atom was not a massive sphere, but it was composed of one small and positively charged nucleus surrounded by electrons[3].

However, the model of Rutherford faced a problem, it could not properly explain the spectra of hydrogen, and there was no explanation of why the electrons does not collapse into the nucleus, as predicted by the Coulomb law. The explanation came through

the works of Niels Bohr (1885-1962). Influenced by the photoelectric effect described by Einstein, Bohr proposed the following postulates:

- An atom can only exist in stationary states, which corresponds to a well-defined value for the total energy of the system;
- If any frequency of radiation is emitted by the atom, then the radiation energy equals the difference between two stationary state energies.

Bohr determined the quantized energy level of the hydrogen by restricting the momentum of electron orbits to integer multiples of the reduced Planck constant. The full understanding of the energy quantization came with the introduction of the Schrödinger (1887-1961) wave-equation:

$$\hat{H}\Psi = E\Psi \quad (1.1)$$

where \hat{H} is the Hamiltonian operator, Ψ is the wavefunction and E is the energy eigenvalue. When solving equation 1.1 the quantization of the energy eigenvalues emerges naturally, since the equation can only be solved for certain values of E . For most applications in chemistry, although analytic solutions are only available for hydrogen and hydrogen-like atoms, *ab initio* methods can solve equation 1.1 for a molecular system with great accuracy, being the state of art¹ in the theoretical framework.

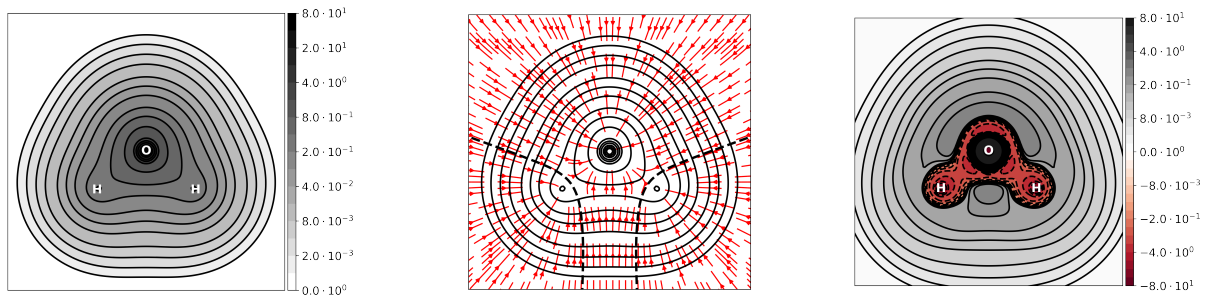
According to the School of Copenhagen interpretation, the squared wavefunction is a probability distribution from which the molecular electronic density function, ρ , and the corresponding energy can be obtained. Every observable property of a molecule can be obtained directly from ρ (which is, itself, observable) through some mathematical operation. Properties of atoms and any information about their existence in a molecule are provided by the Quantum Theory of Atoms in Molecules (QTAIM) formulated by Richard Bader[4]. The brilliancy of Bader’s theory relies on the fact that it does not try to define atoms to build molecules, but it starts from a well-defined molecule and extract the atoms from its electronic density.

1.1 Quantum Theory of Atoms in Molecules

The QTAIM can be summarized to a set of topological elements that identify the atoms and their corresponding atomic basins in the molecular electron density. Once the atomic basins are found, atomic properties are obtained via the integration of ρ within the limits of each atomic basin. Consider a molecular system of N electrons into the nuclear arrangement whose coordinates are simply denoted by \vec{X} and the coordinates, both spatial and spin, of the electrons are denoted by \vec{x} . The wavefunction of this system is $\Psi(\vec{x}; \vec{X})$. After solving equation 1.1 the probability density of finding electron 1 in the infinitesimal space $d\tau_1$ is equal to:

$$\sum_{\text{spins}} \left[\int d\vec{\tau}_2 \int d\vec{\tau}_3 \cdots \int d\vec{\tau}_N \Psi(\vec{x}; \vec{X})^* \Psi(\vec{x}; \vec{X}) \right] d\vec{\tau}_1 \quad (1.2)$$

¹Dirac equation accounts for relativistic effects, however, the Schrödinger equation remains the base of theoretical and quantum chemistry.



(a) electron density, ρ , of H_2O . The lateral bar indicates the magnitude of the electron density in units of $e \cdot \text{bohr}^{-3}$.

(b) Gradient vector field, $\nabla\rho$, of H_2O . Dotted lines corresponds to the interatomic (zero-flux) surfaces.

(c) Laplacian of the electron density, $\nabla^2\rho$, of H_2O . The lateral bar indicates the magnitude of the electron density in units of $e \cdot \text{bohr}^{-5}$.

Figure 1.1: Contour plots of ρ , $\nabla\rho$, and $\nabla^2\rho$ of the water molecule in the σ_v plane of symmetry, calculated at the MP2/cc-pVTZ level of theory.

Therefore, the electron density is given by multiplying this probability by the total number of electrons in the system:

$$\rho(\vec{x}; \vec{X}) = N \sum_{\text{spins}} \left[\int d\vec{\tau}_2 \int d\vec{\tau}_3 \cdots \int d\vec{\tau}_N \Psi(\vec{x}; \vec{X})^* \Psi(\vec{x}; \vec{X}) \right] d\vec{\tau}_1 \quad (1.3)$$

note that the electron density is also the probability density of finding electrons in $d\vec{\tau}$.

The contour plot of ρ for the water molecule is shown in Figure 1.1a. Near the nuclei, the electron density increases, forming a cusp as consequence of the electron concentration in the core shell of atoms. At the infinity, the electron density becomes null. The black lines indicate isodensity surfaces, which means that every point on the line have the same value of ρ . Starting from the the most external line, the value of ρ in each isodensity surface is: 0.001, 0.002, 0.004, 0.008, 0.02, 0.04, 0.08, 0.2, 0.4, 0.8, 2.0, 4.0, 8.0, 20.0, 40.0 and $80.0 e \cdot \text{bohr}^{-3}$.

The gradient of the electron density, in Figure 1.1b, is a set of vectors that are always perpendicular to the isodensity surfaces and point towards the direction of increasing electron density. The vectors start at infinity, where the electron density is null, and end at a maximum point near a nucleus critical point. Following the vectors, one will notice the existence of a particular surface that does not contain any gradient path, *i.e.* at every point of this surface the gradient vector field flux is zero, that is:

$$\vec{n} \cdot \vec{\nabla}\rho = 0 \quad (1.4)$$

with \vec{n} being the normal vector to the surface. This surface is called interatomic, or zero-flux, surface and defines the boundaries of atoms in a molecular system. With the definition of the intratomic surface, the atomic properties can be obtained by integrating

over the atomic basin.² The volume, $v(\Omega_A)$, of atom A, for example, is given by:

$$v(\Omega_A) = \int_{\Omega_A} d\vec{\tau} \quad (1.5)$$

Plenty of information about the electronic structure can be accessed using a function that is also defined by ρ , such a function is the Laplacian of the electron density, $\nabla^2\rho$, as shown in 1.1c. The Laplacian measures the curvature of ρ . In regions where the curvature is negative, one finds a concentration³ of electron density, while regions where the curvature is positive will present a depletion of electron density. That means:

$$\nabla^2\rho \begin{cases} < 0 & \text{if } \rho \text{ is locally concentrated} \\ > 0 & \text{if } \rho \text{ is locally depleted} \end{cases} \quad (1.6)$$

The structure of $\nabla^2\rho$ correlates with the valence shell electron pair repulsion (VSEPR) and redefines classical chemical concepts while using only the electron density as reference[5].

1.1.1 Atomic Properties

To extracted atomic properties from the molecular electron density we make use of operators. The expectation value of an observable \hat{O} is defined as:

$$\langle \hat{O} \rangle = \int d\vec{\tau} \int \frac{N}{2} [\Psi^* \hat{O} \Psi + (\hat{O} \Psi) \Psi^*] d\vec{\tau}' \quad (1.7)$$

with $\vec{\tau}'$ being the spin coordinate. If the operator \hat{O} is Hermitian⁴, the equation becomes:

$$\langle \hat{O} \rangle = \int d\vec{\tau} N \int \Psi^* \hat{O} \Psi d\vec{\tau}' \quad (1.8)$$

The second integral in equation 1.8 is a density function of the operator \hat{O} . In this way, it is convenient to introduce a property density function, ρ_O , which is:

$$\rho_O = N \int \Psi^* \hat{O} \Psi d\vec{\tau}' \quad (1.9)$$

and the observable value is simply:

$$\langle \hat{O} \rangle = \int \rho_O d\vec{\tau} \quad (1.10)$$

²According to Bader, an atom is the union of the nuclear attractor and its associated basin.

³The electronic density always decreases in the direction away from nuclei, however, in regions where the electronic density is concentrating the decrease in electronic density occurs slower than in regions of electronic depletion.

⁴The expectation value of an Hermitian operator is real and $\langle \Psi | \hat{O} | \Psi \rangle = \langle \hat{O} \Psi | \Psi \rangle$.

Once the interatomic surfaces are found and the atomic basins are defined, the expectation value of \hat{O} for atom A can be calculated by setting up the integration limits:

$$\langle \hat{O}_{\Omega_A} \rangle = \int_{\Omega_A} \rho_O d\vec{\tau} \quad (1.11)$$

1.2 QTAIM Charges and Dipoles

Considering the operator \hat{O} in Equation 1.11 to be equal to 1, the resulting integral will represent the electronic population, $N(\Omega)$, of atom A, that is:

$$N(\Omega_A) = \int_{\Omega_A} \rho d\vec{\tau} \quad (1.12)$$

which is the number of electrons inside the limits of the atomic basin. The atomic charge of atom A, q_{Ω_A} , is simply the difference between the population and the atomic number of A:

$$q_{\Omega_A} = Z_{\Omega_A} - N_{\Omega_A} = Z_{\Omega_A} - \int_{\Omega_A} \rho d\vec{\tau} \quad (1.13)$$

The resulting charge from the equation above is called AIM-charge⁵ and, due to the probabilistic nature of electrons, it isn't restricted to integer numbers.

Determining the atomic charge, however, is often insufficient to describe some molecular properties. For example, if one tries to reproduce the dipole moment of the CO molecule using only AIM charges, the result does not agree the experimental data. Aligning the molecule with the Cartesian z -axis and positioning the C atom at the left-hand side, the magnitude of the experimental dipole moment, obtained with microwave spectroscopy, is 0.112 ± 0.005 D pointing toward the O atom.

Considering that the dipole moment vector always points to the positive end, we found a contradiction: considering only point charges, the oxygen must have a small and positive charge, which isn't supported by the difference in electronegativity of C and O. The problem with this analysis is that it does not account for the anisotropy of the electron density distribution inside the atomic basins. For example, using only atomic charges, the molecular dipole moment is equal to:

$$\vec{p} = \sum_{A=1}^N q_{\Omega_A} \vec{r}_{\Omega_A} \quad (1.14)$$

where N is the number of atoms in the molecule and \vec{r} is the position vector.

The AIM charges for carbon and oxygen in CO at the QCISD/aug-cc-pVTZ level of theory are $+1.224e$ and $-1.224e$, respectively. If the dipole moment is calculated using only the atomic charges its magnitude is equal to $6.646D$. Not only the value of the dipole moment is bigger than the experimental data, but its direction points to the carbon atom. The explanation behind the disagreement between AIM and experimental data relies on the fact that atoms in molecules cannot be taken as spherical and isotropic

⁵AIM-charges are also called "zero-flux" charges as a reference to the interatomic surfaces.

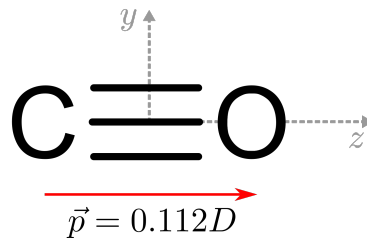


Figure 1.2: The experimental dipole moment for carbon monoxide is $0.112D$. The electric dipole moment vector always points to the positive end, or oxygen atom.

entities. In order to properly calculate the molecular dipole moment, one needs to include the atomic dipole moments, m_{Ω_A} . In this way we can write:

$$\vec{p} = \sum_{A=1}^N [q_{\Omega_A} \vec{r}_{\Omega_A} + \vec{m}_{\Omega_A}] \quad (1.15)$$

where the Cartesian components of the AIM atomic dipole moment of atom A are given by[4]:

$$m_{\Omega,x} = - \int_{\Omega_A} x_{\Omega_A} \rho(\vec{\tau}) d\vec{\tau} \quad (1.16)$$

$$m_{\Omega,y} = - \int_{\Omega_A} y_{\Omega_A} \rho(\vec{\tau}) d\vec{\tau} \quad (1.17)$$

$$m_{\Omega,z} = - \int_{\Omega_A} z_{\Omega_A} \rho(\vec{\tau}) d\vec{\tau} \quad (1.18)$$

where x_{Ω_A} , y_{Ω_A} , z_{Ω_A} means that the vector components are centred on the nucleus. Using the Laplacian function, the anisotropy of the electron density in each atomic basin is evidenced. The $\nabla^2 \rho(\vec{\tau})$ of the CO molecule is presented in Figure 1.3.

The red color indicates regions where there is a concentration of electron density. For the carbon atom we see a concentration of electrons on the left-hand side, so the atomic dipole moment points to the right. For the oxygen atom we see a concentration of charge near the interatomic surface, resulting in a atomic dipole moment that also points to the right-hand side. Calculated atomic dipoles moments of C and O are, respectively, $4.204D$ and $2.478D$ pointing to the positive direction of z . The sum of the atomic dipoles with the charge contribution reproduces the experimental dipole moment without contradicting the chemical knowledge.

1.3 The Interacting Quantum Atoms

The Interacting Quantum Atoms (IQA) [6] is an increasingly popular Energy Decomposition Scheme (EDS) [7] based on QTAIM. The IQA approach was proposed in

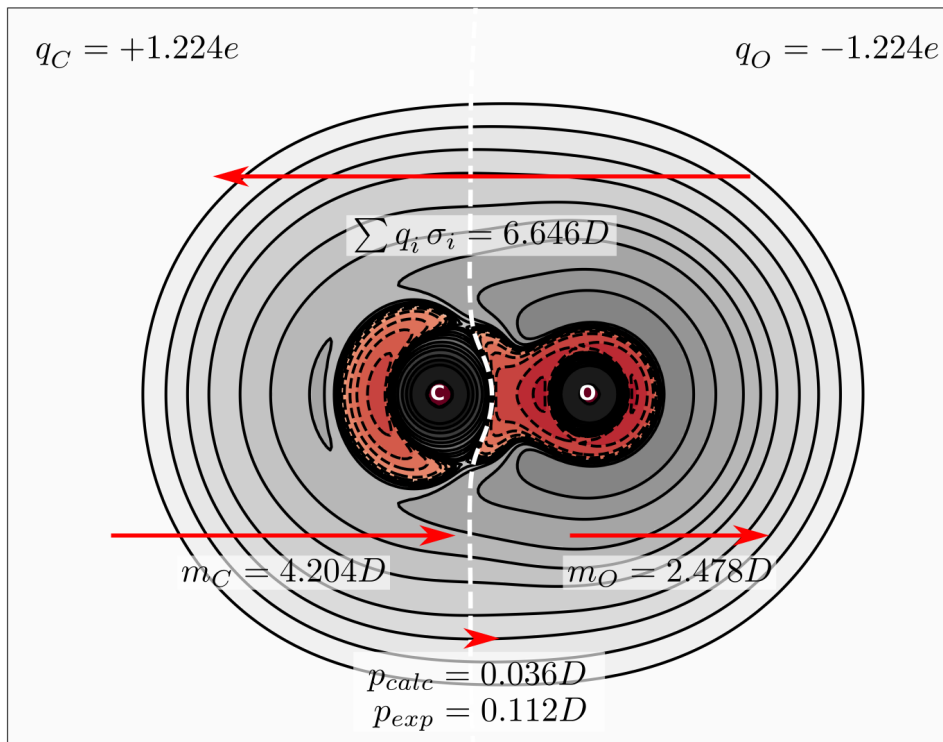


Figure 1.3: Laplacian of the electron density of carbon monoxide. The white dotted line indicates the intratomic surface. According to the AIM population analysis, the carbon is the positive atom as expected by the electronegativity series. The atomic dipole moments, however, point to the oxygen atom. The summation of these vectors results in a dipole moment vector pointing towards the oxygen atom, reproducing the experimental dipole moment.

2005 and was inspired by earlier works[8, 9] that invoked six-dimensional integration to obtain atomic contributions to potential energies. The IQA approach consists of dividing the molecule's total energy, E_{IQA}^{Total} , into a sum of intratomic and interatomic energy components. The total molecular energy is then recovered by summing each individual atomic energy contribution, E_{IQA}^A , according to

$$E_{IQA}^{Total} = \sum_{A=1}^N E_{IQA}^A \quad (1.19)$$

where N is the total number of atoms in the system and A labels the atoms. Each atomic term can be expanded as a sum of intra- and interatomic contributions such that equation 1.19 becomes

$$E_{IQA}^{Total} = \sum_{A=1}^N E_{Intra}^A + \sum_{A=1}^{N-1} \sum_{B>A}^N V_{Inter}^{AB} \quad (1.20)$$

where V_{Inter}^{AB} corresponds to the potential energy between atoms A and B . The intratomic terms encompasses the kinetic, T , as well as the electron-electron, V_{ee} , and electron-

nucleus potential energies V_{en}

$$E_{Intra}^A = T^A + V_{ee}^{AA} + V_{en}^{AA} \quad (1.21)$$

E_{Intra}^A can be seen as a measure of the intrinsic stability of an atom in the molecule and turns out [10, 11] to behave like classic steric repulsion in van der Waals complexes, as proven by successful fits to the Buckingham potential. The interatomic contribution can also be split into several terms, that is:

$$V_{Inter}^{AB} = V_{nn}^{AB} + V_{en}^{AB} + V_{ne}^{AB} + V_{ee}^{AB} \quad (1.22)$$

The subscripts “e” and “n” stand for electron and nucleus, respectively. The term V_{en}^{AB} refers to the potential energy between the electrons from atom A and the nucleus of atom B , whereas V_{ne}^{AB} is the potential energy between the nucleus of atom A and electrons from atom B .

The electron correlation term [12] is hidden inside both intratomic and interatomic electron-electron potential, as stated by the following equations, 1.23 and 1.24:

$$V_{ee}^{AA} = V_{coul}^{AA} + V_{xc}^{AA} \quad (1.23)$$

$$V_{ee}^{AB} = V_{coul}^{AB} + V_{xc}^{AB} \quad (1.24)$$

Note that V_{xc}^{AB} and V_{xc}^{AA} both combine the exchange and electron correlation energy. All interatomic terms are obtained directly from the integration of the electron density over the volumes of both topological atoms A and B.

1.3.1 IQA terms from density matrices [6, 12]

Once the desired multi-electron wavefunction is found, the first- and second-order density matrices can be respectively obtained as follows:

$$\rho_1(\vec{\tau}_1, \vec{\tau}'_1) = N_e \int \Psi(\vec{\tau}_1, \dots, \vec{\tau}_{N_e}) \Psi(\vec{\tau}'_1, \dots, \vec{\tau}_{N_e})^* d\vec{\tau}_2 \cdots d\vec{\tau}_{N_e} \quad (1.25)$$

and

$$\rho_2(\vec{\tau}_1, \vec{\tau}_2) = \frac{N_e(N_e - 1)}{2} \int \Psi(\vec{\tau}_1, \dots, \vec{\tau}_{N_e}) \Psi(\vec{\tau}_1, \dots, \vec{\tau}_{N_e}) d\vec{\tau}_3 \cdots d\vec{\tau}_{N_e} \quad (1.26)$$

where $\vec{\tau}_n$ is the vector encompassing both the spatial coordinates and the spin coordinates for electron n while N_e is the total number of electrons.

According to the Born-Oppenheimer approximation, the multi-electron Hamiltonian is given by (in atomic units):

$$H_{N_e} = \hat{T} + \hat{V}_{en} + \hat{V}_{ee} = - \sum_{n=1}^{N_e} \frac{1}{2} \nabla_n^2 - \sum_{n=1}^{N_e} \sum_{A=1}^N \frac{Z_A}{r_{nA}} - \sum_{n=1}^{N_e-1} \sum_{l>n}^{N_e} \frac{1}{r_{nl}} \quad (1.27)$$

where \hat{T} is the one-electron kinetic energy operator, while \hat{V}_{en} and \hat{V}_{ee} correspond respectively to the attractive electron-nucleus potential and electron-electron repulsive potential. The quantities r_{nA} and r_{nl} respectively refer to the distance between electron n and nucleus A , and that between electron n and electron l while Z_A is the nuclear charge associated with atom A . The total energy is given by

$$E^{Total} = E^{Electronic} + V_{nn} \quad (1.28)$$

with the potential energy between two nuclei simply defined as

$$V_{nn} = \sum_{A=1}^{N-1} \sum_{B>A}^N V_{nn}^{AB} = \sum_{A=1}^{N-1} \sum_{B>A}^N \frac{Z_A Z_B}{r_{AB}} \quad (1.29)$$

The electronic energy is obtained by solving the Schrödinger equation

$$\hat{H}_{N_e} \Psi(\vec{\tau}_1, \dots, \vec{\tau}_{N_e}) = E^{Electronic} \Psi(\vec{\tau}_1, \dots, \vec{\tau}_{N_e}) \quad (1.30)$$

which results in

$$E^{Electronic} = \int_{-\infty}^{\infty} \hat{T} \rho_1(\vec{\tau}_1, \vec{\tau}'_1) d\vec{\tau}_1 + \int_{-\infty}^{\infty} \hat{V}_{en} \rho_1(\vec{\tau}_1, \vec{\tau}'_1) d\vec{\tau}_1 + \int_{-\infty}^{\infty} \int_{-\infty}^{\infty} \hat{V}_{ee} \rho_2(\vec{\tau}_1, \vec{\tau}_2) d\vec{\tau}_1 d\vec{\tau}_2 \quad (1.31)$$

In order to compute individual terms for each atom, the topological partitioning method is invoked. For example, the kinetic energy contribution for atom A can be written as:

$$T^A = \int_{\Omega_A} \hat{T} \rho_1(\vec{\tau}_1) d\vec{\tau}_1 \quad (1.32)$$

The monoelectronic interatomic terms are obtained as follows:

$$V_{en}^{AB} = \int_{\Omega_A} \hat{V}_{en}^B \rho_1(\vec{\tau}_1, \vec{\tau}'_1) d\vec{\tau}_1 = - \int_{\Omega_A} \frac{\rho_1(\vec{\tau}_1) Z_B}{r_{1B}} d\vec{\tau}_1 \quad (1.33)$$

The two-electron terms are obtained from the second-order density matrix, which describes how electrons interact with each other

$$V_{ee}^{AB} = \int_{\Omega_A} \int_{\Omega_B} \rho_2(\vec{\tau}_1, \vec{\tau}_2) r_{12}^{-1} d\vec{\tau}_1 d\vec{\tau}_2 \quad (1.34)$$

if $A = B$, then:

$$V_{ee}^{AA} = \frac{1}{2} \int_{\Omega_A} \int_{\Omega_A} \rho_2(\vec{\tau}_1, \vec{\tau}_2) r_{12}^{-1} d\vec{\tau}_1 d\vec{\tau}_2 \quad (1.35)$$

Equation 1.35 contains the Coulomb, V_{Coul}^{AB} , exchange, V_x^{AB} , and correlation,

V_{corr}^{AB} , energy terms, which are made visible by rearranging:

$$\begin{aligned}
 V_{ee}^{AB} &= \int_{\Omega_A} \int_{\Omega_B} \rho_2(\vec{\tau}_1, \vec{\tau}_2) r_{12}^{-1} d\vec{\tau}_1 d\vec{\tau}_2 = \int_{\Omega_A} \int_{\Omega_B} \rho(\vec{\tau}_1) \rho(\vec{\tau}_2) r_{12}^{-1} d\vec{\tau}_1 d\vec{\tau}_2 \\
 &\quad - \int_{\Omega_A} \int_{\Omega_B} \rho_1(\vec{\tau}_1, \vec{\tau}_2) \rho_1(\vec{\tau}_2, \vec{\tau}_1) r_{12}^{-1} d\vec{\tau}_1 d\vec{\tau}_2 + \int_{\Omega_A} \int_{\Omega_B} \rho_2^{corr} r_{12}^{-1} d\vec{\tau}_1 d\vec{\tau}_2 \\
 &= V_{Coul}^{AB} + V_x^{AB} + V_{corr}^{AB} \quad (1.36)
 \end{aligned}$$

Exchange and correlation terms are typically lumped together in the exchange-correlation term $V_{xc}^{AB} = V_x^{AB} + V_{corr}^{AB}$. Note that V_x^{AB} is related to the covalency degree between atoms A and B , as well the bond order[13]. The classical electrostatic term, V_{coul}^{AB} , on the other hand is related to the bond polarity and the degree of ionicity. The final term, V_{corr}^{AB} is responsible to increase the magnitude of the nucleus-electron potential energy and decrease the electron-electron repulsion. All these terms constitute the so-called fine structure[14] of ρ_2 .

This chapter contains excerpts from texts previously published by the author. The following material was reprinted with permission:

Silva, A. F., **Duarte, L. J.**, Popelier, P. L., *Contributions of IQA electron correlation in understanding the chemical bond and non-covalent interactions*. Structural Chemistry, 31(2), 507-519, 2020, Springer Nature.

Chapter 2

Experimental Infrared Intensities

Gas-phase vibrational intensities provide quantitative measures of dipole moment changes for small molecular distortions. These changes can be interpreted in terms of changes in electronic density owing to molecular bond extensions and angle deformations. As such, they are important for testing quantum chemical and force field models aimed at explaining chemical reactivity. As intensities are very sensitive measures of electronic density changes, they are also significant for assessing the quality of molecular wave functions.

Many gas phase infrared intensities of fundamental bands were measured, from the 1950s through the 1970s with dispersive infrared spectrometers having a wavelength selector which encompasses a narrow slit and a segregating device, earlier a prism but later on a diffraction grating (see Figure 2.1a). Owing to finite slit width problems, these instruments had resolutions of a few wavenumbers[15, 16]. To accurately measure integrated band intensities, the sample gas was usually subjected to high pressures through the addition of an inert transparent gas in the sample cell. In this way, the rotational lines were pressure broadened to a width comparable to the instrument resolution[17, 18].

Besides being work-intensive, errors could occur owing to incomplete pressure broadening or even from pressure induced absorptions. Unlike the conventional dispersive instruments, Fourier Transform Infrared spectrometers (FTIR), schematized in 2.1b, performs a continuous spectral scan of a sample resulting in an interference pattern, called an interferogram. The interferometer is coupled to a microcomputer that controls data acquisition and processing.

Sharpe et al. at the Pacific Northwest National Laboratory (PNNL)[19–21] made an impressive experimental advance. Through modifications in the traditional FTIR apparatus, they were able to correct artifacts related to the source of IR light and interference of black-body radiation. The spectra obtained with the modified equipment is made available to the public at the National Institute of Standards and Technology (NIST) Chemistry WebBook (webbook.nist.gov/chemistry). In their database, it is possible to find hundreds of spectra obtained with spectrometers having much better resolutions, about 0.1 cm^{-1} , than those used for the earlier measurements. This is comparable to the line widths of most rotational-vibrational transition bands at atmospheric pressure, so little pressure broadening is necessary to obtain more accurate intensity values than those determined with the low-resolution instruments. Moreover, uncertainties in absorbance values were minimized by measuring multiple (usually 9 or 10) path length-concentration

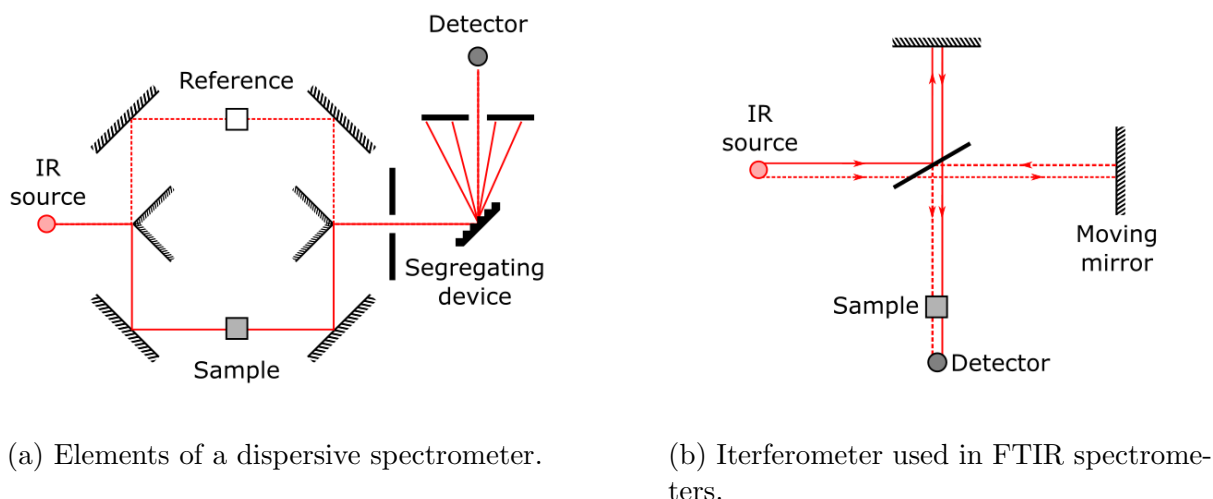


Figure 2.1: A comparative drawing between dispersive and FTIR spectrometers.

burdens and fitting a weighted Beer's law plot for each wavenumber channel.

An example of a PNNL spectra is given in Figure 2.2, a zoom is applied on the region between 740 and 810 cm^{-1} . Notice that it is possible to identify the fine lines of the P and R branch. Given the high resolution and quantitative nature of their experimental spectra, the PNNL intensities will be used as validation of the results presented in this thesis. We start by comparing the new experimental data with the dispersive data and *ab initio* calculations.

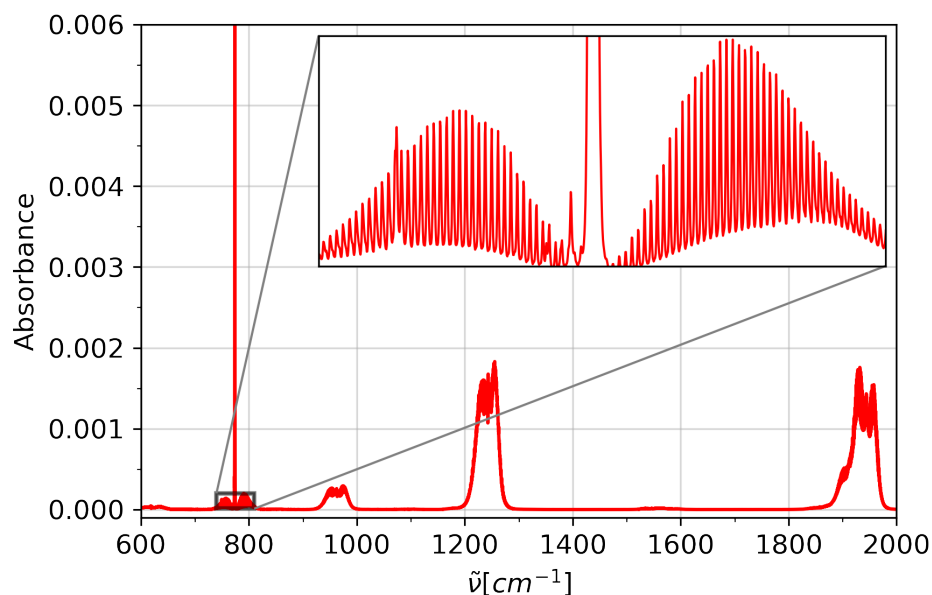


Figure 2.2: FTIR spectrum of F_2CO from the NIST/PNNL. A zoom-in of the 740 - 810 cm^{-1} region reveals the ro-vibrational transitions[19].

The intensity, \mathcal{A} , in $\text{km} \cdot \text{mol}^{-1}$ of a normal mode is obtained by integrating

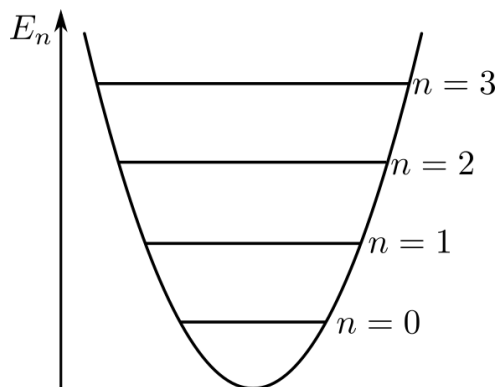


Figure 2.3: Energy levels of a harmonic oscillator. The eigenvalue of Ψ_n is E_n .

the spectrum over the respective band, that is:

$$\mathcal{A} = \frac{1}{\gamma l} \int_{\tilde{\nu}_i}^{\tilde{\nu}_f} \ln \left(\frac{P_o}{P_f(\tilde{\nu})} \right) d\tilde{\nu} \quad (2.1)$$

where $\tilde{\nu}_i$ and $\tilde{\nu}_f$ are the band limits, γ is the concentration and l is the optical path. Theoretical intensities, on the other hand, can be analytically obtained through the transition dipole moment or numerically obtained by using elements of the Atomic Polar Tensor (APT). If the first option is chosen and considering a harmonic model, the IR intensity is given by:

$$\mathcal{A} = \tilde{\nu}_{m \rightarrow n} \frac{8N_A \pi^3}{3ch} \langle \psi_n^o | \hat{p} | \psi_m^o \rangle \quad (2.2)$$

where $\tilde{\nu}_{m \rightarrow n}$ is the vibrational frequency of the normal mode, \hat{p} is the dipole moment operator and ψ_n^o and ψ_m^o are the wavefunctions of state n and m . The energy levels associated with Ψ_n are schematized in Figure 2.3 Note that in order to be active in the IR spectra a normal mode must obey the selection rules:

- The derivative of the molecular dipole moment with respect to the normal mode coordinate is not null;
- m and n must differ by one unit, *i.e.* $n - m = \pm 1$.

2.1 FTIR and Dispersive Gas–Phase Fundamental Infrared Intensities of halomethanes

For this initial study, the halomethane molecules were chosen to compare the early low resolution results with intensities integrated from the NIST/PNNL data base for two major reasons: first, these molecules contain some very weak bands, of a few $\text{km} \cdot \text{mol}^{-1}$, as well as some very intense ones, of more than a $1000 \text{ km} \cdot \text{mol}^{-1}$; second, there is a simple electronegativity model [22] permitting estimations of intensity sums for substituted methane molecules. Carbon atom intensity contributions depend on the average electronegativities of the terminal hydrogen and halogen atoms for this family of molecules whereas the terminal atom contributions are constant values, dependent on

their own electronegativities[22, 23]. Interestingly the square root of the carbon atom intensity contribution is linearly related to the carbon 1s electron ionization energy that is associated with the atomic charge on carbon[24].

The band intensities of the experimental PNNL spectra were integrated with a homemade program, while low resolution intensity values were obtained from earlier experimental work elsewhere in the literature that obeyed the following criteria for most bands:

1. intensities must have been measured for all the fundamental ro-vibrational bands.
2. dispersions of Beer’s law plots must have been reported to obtain error estimates.
3. if the investigated molecule contained hydrogen atoms, error estimates must have been reported for at least two isotopomers.

In order to obtain theoretical data, methane, fluoromethane and chloromethane molecules had their geometries optimized and infrared intensities calculated at QCISD level with aug-cc-pVTZ basis set with the Gaussian09 program[25]. Taking the computational cost into account, the fluorochloromethane geometry optimization and intensities were calculated at QCISD level of theory with the cc-pVTZ basis set. For the bromomethanes MP2/cc-pVTZ was used. For iodomethane, a pseudopotential basis-set (cc-pVTZ-PP) was used also at MP2 level.

Table 2.1 contains integrated intensity values calculated from the PNNL library spectra, low resolution intensity values from work published in the last half of the 20th century and the theoretical values calculated in this work. The frequency values to label the fundamental bands were obtained by inspection of maximum absorbance values in the PNNL spectra.

The low-resolution values are averages and standard deviations of data taken from the cited references when more than one is given[26–56]. In a few cases no error estimate could be made. Of the 60 bands listed in Table 2.1, 30 PNNL and low-resolution intensity differences are within one standard deviation of the error estimate for the low resolution values, five have residuals between one and two standard deviations and two pairs have discrepancies between 2 and 3 standard deviations and three low resolution intensity values are more than three standard deviations from their PNNL value. Of the 45 possible comparisons between the PNNL and low-resolution intensities, in Table 2.1, a Root Mean Square Error (RMSE) of $23.5 \text{ km} \cdot \text{mol}^{-1}$ is calculated. This difference is greatly inflated by three bands, $\tilde{\nu} = 795 \text{ cm}^{-1}$ of CCl_4 and $\tilde{\nu} = 846 \text{ cm}^{-1}$ of CFCl_3 that have PNNL intensity values that are 66.7 and 57.4 $\text{km} \cdot \text{mol}^{-1}$ above their low resolution values and the overlapped bands, $\tilde{\nu} = 1109 \text{ cm}^{-1}, 1210 \text{ cm}^{-1}$, for CF_3Cl that has a low resolution intensity $102.5 \text{ km} \cdot \text{mol}^{-1}$ superior to the PNNL value. Removing these intensities from the calculation the RMSE is almost halved to $12.4 \text{ km} \cdot \text{mol}^{-1}$.

The rest of the possible comparisons in Table 2.1 have frequencies below 600 cm^{-1} and are not measurable with the PNNL spectrometers, so the low-resolution intensities are remarkably good considering all the difficulties inherent in their measurement.

For most bands the PNNL values are larger than the low-resolution values. This can be seen in the plot given in Figure 2.4, where the differences between the PNNL and the low-resolution intensities are shown for each molecule. There is only one significant negative difference owing to the $\tilde{\nu} = 1109 \text{ cm}^{-1}, 1210 \text{ cm}^{-1}$ overlapped bands of CF_3Cl with the high intensity estimate for the low resolution measurement as mentioned above. Of course, incomplete pressure broadening has long been known to be one of the

Table 2.1: Frequencies, ν in (cm^{-1}), and intensity values, ($km \cdot mol^{-1}$), from PNNL, \mathcal{A}_{PNNL} , earlier work $\mathcal{A}_{low\ res.}$, and ab initio calculations, \mathcal{A}_{calc} , at four quantum levels: Fluoro- and chloromethanes at QCISD/aug-cc-pVTZ, fluorochloromethanes at QCISD/cc-pVTZ, CH_3Br at MP2/cc-pVTZ and CH_3I at MP2/cc-pVTZ(C,H) + cc-pVTZ-PP(I) level.

| Molecule | ν | $\sum \mathcal{A}_{PNNL}$ | $\sum \mathcal{A}_{low\ res.}$ | $\sum \mathcal{A}_{calc}$ |
|------------|------------------|---------------------------|--------------------------------|---------------------------|
| CH_4 | 3157 | 67.6 | 68.4 ± 3.2 [26, 37, 48] | 67.8 |
| | 1358 | 33.1 | 33.9 ± 1.9 | 28.3 |
| CH_3F | 2980, 3006 | 90.0 | 80.3 ± 6.6 [51, 52] | 85.3 |
| | 1464, 1467 | 9.7 | 9.5 ± 0.6 | 10.4 |
| | 1048, 1182 | 108.9 | 103.8 ± 9.5 | 102.6 |
| CH_3Cl | 2966, 3042 | 35.4 | 28.9 ± 2.1 [51, 53–55] | 31.6 |
| | 1355, 1455 | 20.9 | 19.3 | 23.2 |
| | 732 | 25.0 | 23.7 | 24.8 |
| | 1015 | 4.0 | 3.5 ± 0.7 | 3.1 |
| CH_3Br | 2972, 3056 | 23.8 | 22.3 ± 1.5 | 22.9 |
| | 1305, 1445 | 26.6 | 27.0 ± 1.5 | 31.7 |
| | 611 | 10.6 | 9.9 ± 1.8 | 10.2 |
| CH_3I | 952 | 7.1 | 7.2 ± 0.1 | 7.7 |
| | 2970 | 11.53 | 12.7 ± 0.9 [56] | 12.4 |
| | 1251 | 21.56 | 20.7 ± 0.5 | 24.7 |
| | 533 | 1.87 | 1.9 ± 0.0 | 0.4 |
| | 3061 | 2.38 | 2.2 ± 0.1 | 1.6 |
| | 1440 | 10.25 | 10.6 ± 0.2 | 9.5 |
| | 880 | 9.19 | 8.9 ± 0.1 | 15.9 |
| CH_2F_2 | 2948, 3014 | 69.9 | 64.6 ± 12.0 [27–29] | 65.6 |
| | 1508, 1435 | 10.7 | 10.3 ± 0.6 | 16.6 |
| | 1111, 1178, 1090 | 364.82 | 333.9 ± 41.6 | 363.2 |
| | 529 | N.A. ⁱ | 4.8 ± 0.3 | 5.4 |
| CHF_3 | 3035 | 24.3 | 24.3 ± 0.7 [30–32, 48] | 24.0 |
| | 1141, 1157 | 658.4 | 629.0 ± 65.6 | 654.3 |
| | 700 | 13.2 | 13.3 ± 1.0 | 14.2 |
| | 1378 | 88.0 | 86.1 ± 2.7 | 108.5 |
| | 508 | N.A. | 4.6 ± 0.3 | 5.7 |
| CF_4 | 1298 | 1172.7 | 1123.5 ± 145.3 | 1198.8 |
| | 632 | 12.9 | 12.3 ± 1.6 | 16.2 |
| CH_2Cl_2 | 2997 | 6.9 | 7.1 ± 0.3 [29–33] | 5.7 |
| | 1430 | 0.8 | 1.5 ± 1.2 | 0.0 |
| | 714, 757 | 131.4 | 107.2 ± 17.3 | 127.6 |
| | 896 | 1.1 | 2.6 ± 2.0 | 0.9 |
| | 1268 | 31.5 | 29.7 | 41.0 |
| $CHCl_3$ | 3034 | 0.2 | 0.4 ± 0.1 [34–36] | 1.0 |
| | 678, 773 | 262.1 | 242.5 | 253.4 |
| | 366 | N.A. | 0.5 | 0.3 |
| | 1219 | 35.3 | 34.5 ± 6.4 | 45.0 |
| | 262 | N.A. | 0.1 ± 0.1 | 0.1 |
| | | | 1087.4 ± 112.5 | |
| CF_3Cl | 1109, 1212 | 984.9 | $[38, 40, 41, 47]$ | 1061.0 |
| | 785 | 28.8 | 31.5 ± 5.1 | 34.3 |
| | 476 | N.A. | 0.0 | 0.0 |
| | 562 | N.A. | 3.3 ± 0.3 | 5.0 |
| | 348 | N.A. | 0.0 | 0.1 |
| CF_2Cl_2 | 1095, 1152 | 467.49 | 467.6 ± 11.9 [29, 40, 41] | 504.9 |
| | 442 | N.A. | 0.2 | 0.0 |
| | 665 | 10.21 | 12.3 | 11.5 |
| | 261 | N.A. | 2.6 | 0.0 |
| | 475 | N.A. | 0.1 | 0.0 |
| | 915 | 358.4 | 324.8 ± 20.9 | 375.2 |
| | 432 | N.A. | 0.1 | 0.5 |
| | | | 158.0 ± 12.5 | |
| $CFCl_3$ | 1085 | 161.76 | $[40, 42, 43, 47]$ | 179.3 |
| | 539 | 0.11 | 1.1 | 1.5 |
| | 147 | N.A. | 0.3 | 0.0 |
| | 846 | 445.73 | 388.3 ± 21.4 | 468.7 |
| | 394 | N.A. | 0.1 | 0.0 |
| | 243 | N.A. | 0.0 | 0.0 |
| CCl_4 | 795 | 388.68 | 322 ± 60 [34] | 372.4 |
| | 310 | N.A. | 0.20 ± 0.05 | 0.0 |

ⁱ Not Available

most important sources of error in intensity measurements. At sufficiently high pressures the rotational fine structure becomes completely smeared out to give bands smoother contours. In these situations, the apparent intensity approaches the intensity that would be measured if the slit width error were negligible. Insufficient pressure broadening is expected to result in underestimates of the integrated intensity. This has been shown on comparing the Wilson–Wells method with curve of growth measurements[15].

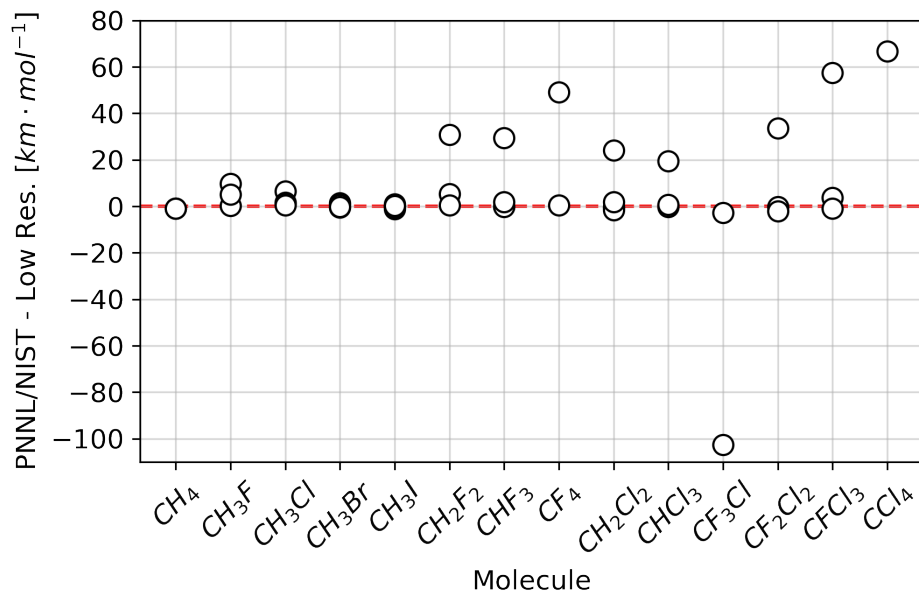


Figure 2.4: Graph of the differences between the PNNL and the earlier low resolution infrared intensities reported in the literature.

In order to see the effect of basis set and electron correlation treatment level on the theoretical values, it is convenient to examine their intensity sums for the fluorochloromethanes for comparison with the experimental values. Table 2.2 contains the QCISD/aug-cc-pVTZ, QCISD/cc-pVTZ and MP2/aug-cc-pVTZ calculated intensity sums as well as the PNNL and low-resolution intensity sums.

Table 2.2: Experimental and theoretical infrared intensity sums for the fluorochloromethanes ($km \cdot mol^{-1}$).

| Molecule | PNNL | Low resolution | QCISD/aug- cc-pVTZ | QCISD/cc- pVTZ | MP2/aug-cc- pVTZ |
|---------------------------------|--------|----------------|-----------------------|-------------------|---------------------|
| CH ₄ | 100.7 | 102.2 | 96.0 | 100.1 | 81.5 |
| CH ₃ F | 208.6 | 193.6 | 203.4 | 213.0 | 195.7 |
| CH ₂ F ₂ | 445.4 | 408.8 | 445.5 | 459.6 | 446.7 |
| CHF ₃ | 810.8 | 752.7 | 801.1 | 814.0 | 813.2 |
| CF ₄ | 1185.6 | 1135.8 | 1214.7 | 1287.5 | – |
| CH ₃ Cl | 85.3 | 75.4 | 82.6 | 87.2 | 76.8 |
| CH ₂ Cl ₂ | 171.7 | 148.1 | 175.2 | 181.8 | 173.9 |
| CHCl ₃ | 297.6 | 277.4 | 299.3 | 316.4 | 316.1 |
| CCl ₄ | 388.7 | 322.0 | 372.4 | 412.5 | 407.6 |
| CClF ₃ | 1013.7 | 1122.2 | – | 1100.4 | 1068.2 |
| CCl ₂ F ₂ | 836.1 | 807.7 | 828.3 | 892.1 | 857.7 |
| CCl ₃ F | 607.6 | 547.8 | – | 649.5 | 627.2 |

The agreement between the PNNL and QCISD/aug-cc-pVTZ values is quite good with an RMSE of only $8.4 \text{ km} \cdot \text{mol}^{-1}$. As the average of these PNNL intensities is $135.8 \text{ km} \cdot \text{mol}^{-1}$ this corresponds to a 6.2% difference. The RMSE between the low-resolution values and these theoretical ones is almost three times as much, $20.2 \text{ km} \cdot \text{mol}^{-1}$, owing to the lower precision of the earlier measurements as mentioned earlier.

One of the largest differences between the PNNL and the theoretical QCISD/aug-cc-pVTZ values occurs for $\tilde{\nu} = 1378 \text{ cm}^{-1}$ of CHF_3 of $20.5 \text{ km} \cdot \text{mol}^{-1}$, which has a $88.0 \text{ km} \cdot \text{mol}^{-1}$ experimental value for a 23% difference. The $1198.2 \text{ km} \cdot \text{mol}^{-1}$ calculated value for $\tilde{\nu} = 1298 \text{ cm}^{-1}$ of CF_4 overestimates the $1172.7 \text{ km} \cdot \text{mol}^{-1}$ experimental value by $25.5 \text{ km} \cdot \text{mol}^{-1}$ but this corresponds to only 2.2% of the band intensity. The next largest deviation occurs for the experimental asymmetric stretching intensity of CCl_4 , that is $16.3 \text{ km} \cdot \text{mol}^{-1}$ larger than the calculated value. All other deviations are less than $10 \text{ km} \cdot \text{mol}^{-1}$.

The use of an augmented basis set is warranted to obtain good accuracy. The use of QCISD/cc-pVTZ basis sets for these same molecules results in an RMSE that is twice as big as the one for the augmented basis set, $16.2 \text{ km} \cdot \text{mol}^{-1}$. The agreement between the total PNNL intensities of fluorochloromethanes and the QCISD/cc-pVTZ values is $32 \text{ km} \cdot \text{mol}^{-1}$, whereas this difference is only a little higher for the low-resolution values, $38 \text{ km} \cdot \text{mol}^{-1}$. These values seem high as the fluorochloromethanes have some very intense bands. Their average PNNL intensity is $307.2 \text{ km} \cdot \text{mol}^{-1}$, so these differences correspond to 10.4% and 12.4% of the RMSE value. Based on these results, the use of more accurate experimental intensity values becomes increasingly more important as highly sophisticated basis set and electron correlation treatment alternatives are compared to determine best agreements between theory and experiment.

2.1.1 Atomic contributions and the Electronegativity Model

The electronegativity model for intensities has been developed using low resolution intensities that were available at the time[22, 23]. This model assumes that the mean dipole moment derivatives of the carbon atoms depend only on the average electronegativities of their halogen substituents. Furthermore the halogen mean dipole moment derivatives depend only on their own electronegativities. The model expresses the total molecular intensity as a sum of individual atomic contributions, \mathcal{A}^A :

$$\sum_{k=1}^{3N-6} \mathcal{A}_k = \sum_{A=1}^{3N} \mathcal{A}^A \quad (2.3)$$

where the sum on the left contains all the fundamental infrared intensities and the one on the right sums over all the atoms in the molecule. As the squares of dipole moment derivatives are proportional to the intensities these derivative can be used to calculate the atomic contributions to the intensities. A training set consisting of CH_4 , CH_3I , CH_3Br , CH_3F , CHCl_3 , CHF_3 and CF_4 was used to determine the dynamic atomic contributions for the halomethane family. This set of molecules, except for CH_3Br and CH_3I , is identical to the one used in earlier study[23] with low resolution intensities. Training set atomic contributions can then be used to calculate the total intensities of the other halomethanes.

Table 2.3 contains the atomic contributions obtained using the intensities of both the high and low-resolution spectra. As can be seen, the agreement is very good

with the largest difference of $27.8 \text{ km} \cdot \text{mol}^{-1}$ occurring for the carbon contribution for CF_4 . This is less than 3% of its high-resolution estimate. Included in this table are theoretical values of these contributions calculated from QCISD/cc-pVTZ wave functions[57]. These dynamic intensity contributions correspond to the portion of the total intensity obtained by displacing just the carbon, hydrogen, fluorine or chlorine atom according to the molecule’s normal coordinates and summing over all the $3N - 6$ vibrations. Figure

Table 2.3: Atomic contributions obtained using the intensities of both the PNNL, $\mathcal{A}_{\text{PNNL}}^{\text{C}}$, and low-resolution spectra, $\mathcal{A}_{\text{low res}}^{\text{C}}$, and those calculated, $\mathcal{A}_{\text{calc}}^{\text{C}}$, at the QCISD/cc-pVTZ level and cited in reference[58] (in $\text{km} \cdot \text{mol}^{-1}$).

| Molecule | $\mathcal{A}_{\text{PNNL}}^{\text{C}}$ | $\mathcal{A}_{\text{low res}}^{\text{C}}$ | $\mathcal{A}_{\text{calc}}^{\text{C}}$ |
|---|--|---|--|
| CH_4^{i} | 5.1 | 5.1 | 0.3 |
| $\text{CH}_3\text{F}^{\text{i}}$ | 95.7 | 97.9 | 86.3 |
| CH_2F_2 | 299.4 | 307.1 | 303.8 |
| CHF_3^{i} | 616.2 | 632.8 | 638.3 |
| CF_4^{i} | 1046.0 | 1073.8 | 1029.7 |
| $\text{CH}_3\text{Cl}^{\text{i}}$ | 31.2 | 31.6 | 33.7 |
| CH_2Cl_2 | 79.2 | 81.1 | 140.3 |
| CHCl_3^{i} | 149.2 | 153.1 | 265.7 |
| CCl_4 | 241.3 | 246.4 | 354 |
| CFCl_3 | 389.5 | 398.3 | 542.9 |
| CF_2Cl_2 | 573 | 586.5 | 735.9 |
| CF_3Cl | 791.8 | 811 | 905.3 |
| Terminal Atom Intensity Contribution | | | |
| \mathcal{A}^{H} | 10.3 | 18.1 | 17.3 ± 8.1 |
| \mathcal{A}^{F} | 50.7 | 56.4 | 56.5 ± 7.4 |
| \mathcal{A}^{Cl} | 6.4 | 8.0 | 12.0 ± 3.0 |

ⁱ Calibration set molecules used in reference [23]

2.5 contains a graph of the carbon and halogen atomic contributions obtained using the electronegativity model and the high-resolution intensities against the QCISD/cc-pVTZ values. As can be seen the fluoromethane results for carbon are very accurate as all their points fall on the line representing exact agreement. On the other hand, the chloro- and fluorochloromethane points deviate from this line by as much as $163 \text{ km} \cdot \text{mol}^{-1}$. The higher the number of chlorines in the molecule the larger the deviations become. Only the fluoromethane molecules appear to strictly follow the electronegativity model whereas the molecules containing the more polarizable chlorine atoms deviate from it.

Figure 2.6 presents a plot of the square root of the dynamic carbon contribution against the average electronegativity of the terminal atoms. The Mulliken-Jaffe values in previous study were also used here: H, 7.17; F 12.18 and Cl, 9.38. As can be seen there, all the dynamic contributions obtained from the PNNL spectra and the electronegativity model show excellent agreement as expected. The QCISD/cc-pVTZ values for the fluoromethanes are in good agreement with the electronegativity model values whereas deviations with a pattern similar to those in Figure 2.5 are observed for molecules containing chlorine.

These new atomic contributions, calculated with PNNL data, were used to predict intensity values for a test set of halomethanes similar to a previous study[22]. The only fluoromethane not included in the data set, CH_2F_2 , has an electronegativity estimate of $421.4 \text{ km} \cdot \text{mol}^{-1}$ within $24.0 \text{ km} \cdot \text{mol}^{-1}$ of the experimental intensity sum of $445.4 \text{ km} \cdot \text{mol}^{-1}$. On the other hand, the CH_2Cl_2 has a model estimate $58.3 \text{ km} \cdot \text{mol}^{-1}$

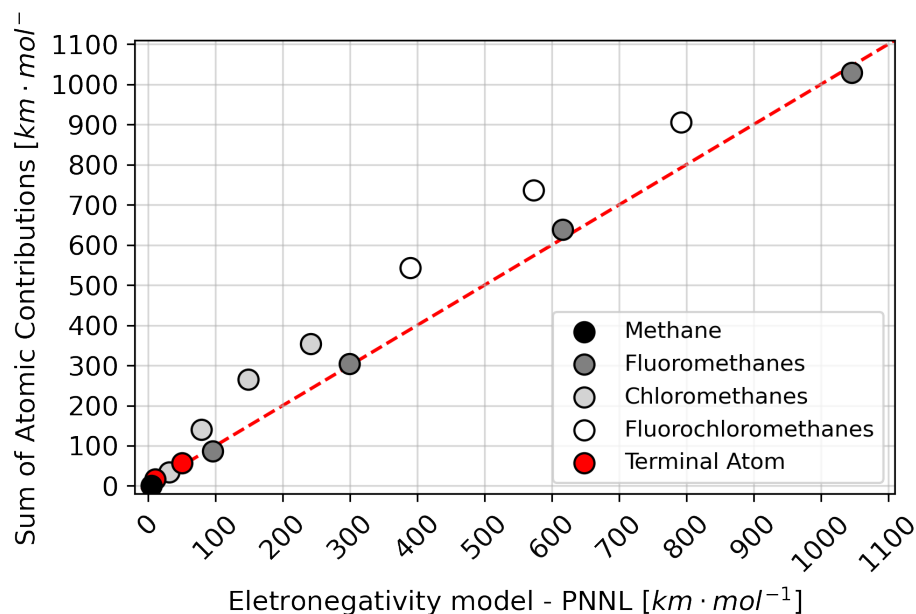


Figure 2.5: Graph of the carbon, hydrogen and halogen atomic contributions obtained using the electronegativity model and the high-resolution intensities against the QCISD/cc-pVTZ values. The red dotted line represents the perfect agreement between the two quantities.

below the experimental sum of $171.7 \text{ km} \cdot \text{mol}^{-1}$. The electronegativity model value calculated from the atomic contributions for CCl_4 has an error twice as large, $-120.4 \text{ km} \cdot \text{mol}^{-1}$. As the number of chlorine atoms in the molecule increases, so does the differences in the electronegativity estimates.

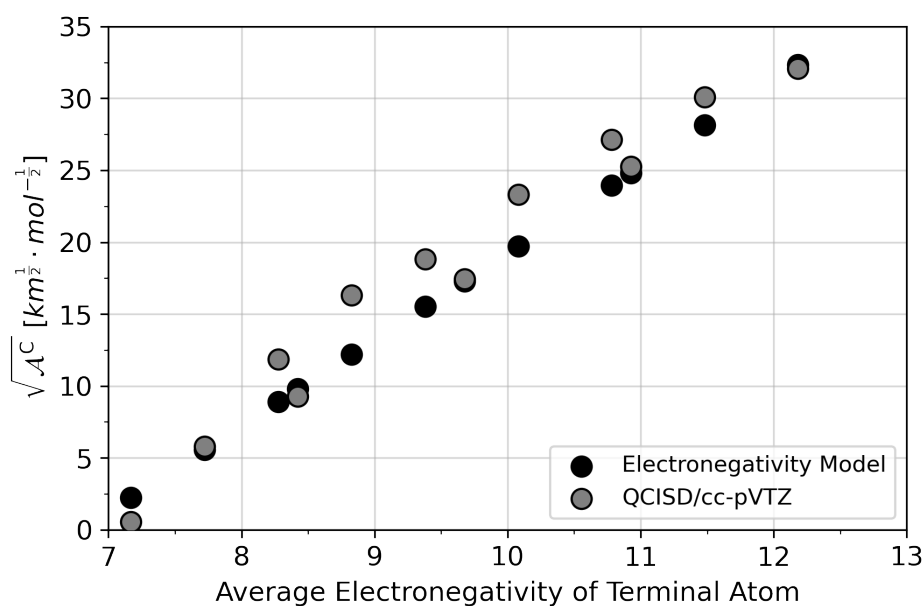


Figure 2.6: Plot of the square root of the dynamic carbon contribution [$km^{1/2} \cdot mol^{-1/2}$] against the average electronegativity of the terminal atoms.

In his pioneering work on Electron Spectroscopy for Chemical Analysis (ESCA), Siegbahn [59] showed that the carbon 1s electron ionization energies corrected for their nearest neighbor atom potentials are linearly related to the theoretical atomic charge of carbon for a large number of molecules. Later our group showed that this corrected ionization energy was linearly related to the mean dipole moment derivative of carbon, an invariant of the atomic polar tensor determined from all the fundamental intensities of a molecule[22]. This invariant is closely related to another tensor invariant, the effective charge. The square of the effective charge weighted by the inverse atomic mass is an atomic partition term of the molecular intensity sum[60]. One can expect that a simple relation exists between these core electron ionization energies and the square root of the dynamic carbon contribution.

This is indeed true as can be seen in Figure 2.7 where the experimental carbon 1s ionization energies are plotted against the square root of the dynamic carbon contributions determined from the electronegativity model and the intensities obtained from the PNNL fluorochloromethane spectra.

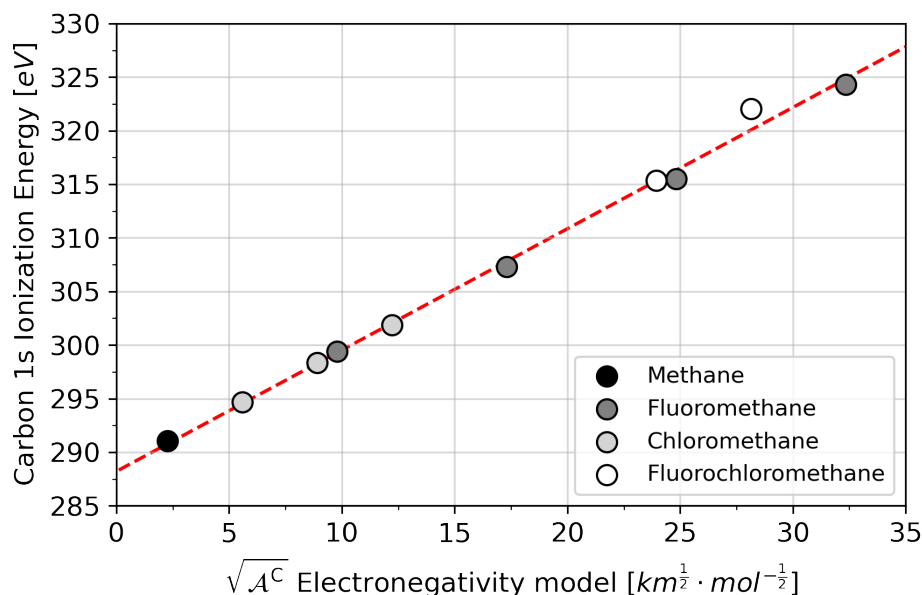


Figure 2.7: Plot of experimental carbon 1s ionization energies corrected for the nearest neighbor potentials [eV] against the square root of the dynamic carbon contributions from the electronegativity model with PNNL intensities [$km^{\frac{1}{2}} \cdot mol^{-\frac{1}{2}}$]. The square Pearson coefficient between the quantities is equal to 0.995.

As shown there, an excellent linear relationship is found. This certainly could be expected for molecules that have electronic structure changes consistent with the electronegativity model expectations. Electronic structure changes for their vibrations depend mostly on movement of the equilibrium atomic charges of the molecule. As the dynamic carbon contributions are determined by the displacement of only the carbon atom it is not surprising that the square root of its intensity contribution is simply related to the carbon 1s electron ionization energy.

2.2 FTIR and Dispersive Gas–Phase Absolute IR Intensities of Hydrocarbons Fundamental Bands

The hydrocarbon low resolution intensities used as reference in this section follow the same three criteria as the intensities of halomethanes. The experimental data for methane were obtained from four different references[26, 37, 48, 51], acetylene intensities from three sources[61–63], ethylene[64, 65] and propyne[66, 67] from two, and ethane [68], allene [69] and cyclopropane[70] each from a different laboratory. Molecular geometries were optimized and theoretical intensities were obtained at the QCISD/6-311++G(3d,3p) level of theory. QCISD/aug-cc-pVTZ intensities and frequencies were taken from the Computational Chemistry Comparison and Benchmark DataBase (CCCBDB), except for allene and propyne for which calculations were performed by our group. MP2/cc-pVTZ results were obtained from reference[71].

Table 2.4 contains the intensity values of the fundamental vibrations of the hydrocarbons determined from the PNNL spectral library. Overlapped bands were not separated so their intensity sums are given. Low resolution values are given in the adjacent column with their error estimates. In cases of multiple determinations, inter-laboratory standard errors were determined. Ethane, allene and cyclopropane have absolute integrated intensity determinations from only one laboratory. As such, regression dispersion errors from Beer’s law plots reported for the measurements are given in the above mentioned table.

Figure 2.8 shows a normal distribution plot for the differences between the PNNL and the low resolution intensities. Points near the red line follow the normal distribution behaviour expected for random measurement errors. Only three points in the upper right corner have serious deviations from the line. The point for the 2840–3220 cm^{-1} overlapped bands of C_3H_6 has a residual of $8.7 \text{ km} \cdot \text{mol}^{-1}$, whereas the Beer’s law dispersion estimate of the standard deviation of the low resolution value is only $3.5 \text{ km} \cdot \text{mol}^{-1}$ [50]. The 650–850 cm^{-1} C_2H_2 value has a residual of $8.4 \text{ km} \cdot \text{mol}^{-1}$, much less than the experimental error estimate of $21.0 \text{ km} \cdot \text{mol}^{-1}$. The point for the sum of the intensities of the overlapped 825–1125 cm^{-1} bands of ethylene also falls far from this line with a PNNL value $6.2 \text{ km} \cdot \text{mol}^{-1}$ larger than the low resolution average. In spite of the above complications the RMSE between the PNNL intensities and the low resolution averages is only about two and a half times larger than the estimated error of the low resolution values of $\pm 2.5 \text{ km} \cdot \text{mol}^{-1}$. As can be seen in Figure 2.8 only six of the low resolution intensities have higher values than their PNNL counterparts.

Table 2.4 also contains QCISD level results for the hydrocarbons calculated with the cc-pVTZ and 6-311G+(3d,3p) basis sets. The QCISD/6-311G++(3d,3p) values have an RMSE of $4.4 \text{ km} \cdot \text{mol}^{-1}$ compared with the PNNL values. Points for these theoretical values have been included in Figure 2.9. QCISD/6-311G++(3d,3p) values above $40 \text{ km} \cdot \text{mol}^{-1}$ tend to be positioned a little higher than the line representing exact agreement. The QCISD/cc-pVTZ results have an RMSE with the PNNL intensities about the same as the one for QCISD/6-311G++(3d,3p), $4.9 \text{ km} \cdot \text{mol}^{-1}$.

Figure 2.9 shows a graph of both the low resolution and theoretical QCISD/6-311++G(3d,3p) intensity values against those determined from the PNNL spectral library for this report. The agreement is excellent between the low resolution and PNNL values, with an RMSE of only $3.1 \text{ km} \cdot \text{mol}^{-1}$. Half of the PNNL values agree with the low resolution averages within one standard deviation, seven differ by two standard deviations

Table 2.4: Experimental ranges for frequencies (in cm^{-1}) and experimental intensities for both PNNL and low resolution measurements and calculated intensities for three basis sets at the QCISD level (in $km \cdot mol^{-1}$).

| Molecule | Frequency range | $\mathcal{A}_{\text{PNNL}}$ | $\mathcal{A}_{\text{low res.}}$ | $\mathcal{A}_{\text{6-311++G (3d,3p)}}$ | $\mathcal{A}_{\text{cc-pVTZ}}$ | $\mathcal{A}_{\text{aug-cc-pvtz}}$ |
|--|-----------------|-----------------------------|---------------------------------|---|--------------------------------|------------------------------------|
| CH ₄ | 2830-3200 | 66.7 | 67.5±1.5 | 72.9 | 69.3 | 67.8 |
| | 1200-1400 | 32.9 | 33.5±0.8 | 29.3 | 30 | 28.2 |
| C ₂ H ₂ | 3175-3380 | 72.5 | 70.2±4.3 | 78.7 | 84.7 | 84.3 |
| | 650-850 | 185.4 | 177±21.0 | 183.6 | 181.6 | 182.5 |
| C ₂ H ₄ | 825-1125 | 88.6 | 82.4±2.5 | 93.3 | 89.1 | 91.4 |
| | 2900-3300 | 41.4 | 39.4±2.2 | 36.8 | 34.1 | 31.9 |
| | 1360-1521 | 10.5 | 10.1±0.2 | 7.5 | 8.6 | 8.5 |
| C ₂ H ₆ | 2830-3092 | 175.3 | 171±1.5 | 186.3 | 177.7 | 174.2 |
| | 1310-1627 | 17.4 | 17.4±0.4 | 16.2 | 15.5 | 15 |
| | 760-900 | 6.1 | 6.1±0.1 | 4.6 | 5.3 | 5.1 |
| C ₃ H ₄ (propyne) | 3250-3380 | 45.0 | 44.2±2.4 | 49.4 | 53.2 | 53.3 |
| | 2800-3150 | 31.3 | 33.8±3.1 | 32.4 | 30.6 | 28.4 |
| | 2090-2180 | 5.0 | 5.3±0.3 | 3.7 | 2.9 | 4.2 |
| | 1350-1650 | 17.4 | 19.4±1.3 | 15.1 | 14.5 | 15.7 |
| | 750-1125 | 1.5 | 1.1±0.4 | 1.1 | 1.1 | 0.9 |
| | 559-720 | 90.1 | 87.9±5.0 | 90.7 | 89.4 | 90 |
| C ₃ H ₆ | 2840-3220 | 77.4 | 68.7±3.5 | 74.8 | 69.2 | 65.5 |
| | 750-980 | 33.9 | 31.6±0.6 | 39.3 | 39.7 | 40.5 |
| | 1380-1500 | 3.1 | 1.8±0.1 | 0.8 | 1.4 | 1.2 |
| C ₃ H ₄ (allene) | 960-1100 | 21.3 | 20.3±0.3 | 13.3 | 15.3 | 14.1 |
| | 2930-3040 | 7.1 | 5.5±0.8 | 2.5 | 2.3 | 1.5 |
| | 1890-2000 | 50.3 | 47.8±1.2 | 54.7 | 51.4 | 59.6 |
| | 1346-1450 | 17.3 | 6.1±1.3 | 1.7 | 2.5 | 2.5 |
| | 3040-3190 | 3.5 | 3.5±0.6 | 2.4 | 1.6 | 1.4 |
| | 950-1150 | 8.7 | 8.6±1.8 | 6.1 | 3.9 | 5.8 |
| | 700-950 | 94.7 | 91.6±2.0 | 99 | 103.5 | 99.9 |

and three values within three deviations. Even then these deviations are very small, 2.3 and 1.3 $km \cdot mol^{-1}$. The low resolution points tend to fall slightly below the line representing exact agreement between the intensity estimates in Figure 2.9. This is why the linear behaviour of the points in Figure 2.8 passes a little to the right of the graph origin.

QCISD/aug-cc-pVTZ calculations were undertaken to obtain still more accurate intensity estimates with the aim of obtaining better agreement with the PNNL intensity values. However an RMSE of 5.41 $km \cdot mol^{-1}$ was obtained, which is a bit higher than the differences found for more modest basis sets. RMSE calculated between these theoretical values and the low resolution intensities were slightly higher than those for the PNNL values, 5.9 $km \cdot mol^{-1}$.

Comparing PNNL intensity values with low resolution results for the fluorochloromethanes, an RMSE of 26.6 $km \cdot mol^{-1}$ was found corresponding to an intensity range from close to zero to 1073.8 $km \cdot mol^{-1}$. The intensity range for the hydrocarbons treated here is much smaller, 1.5 to 185.4 $km \cdot mol^{-1}$ as are their RMSE of 3.1 $km \cdot mol^{-1}$. Both of these differences are about 2% of their intensity ranges.

Galabov *et al.*[57] performed infrared intensity calculations at about 75 different quantum levels for methane and acetylene among other small molecules. Best

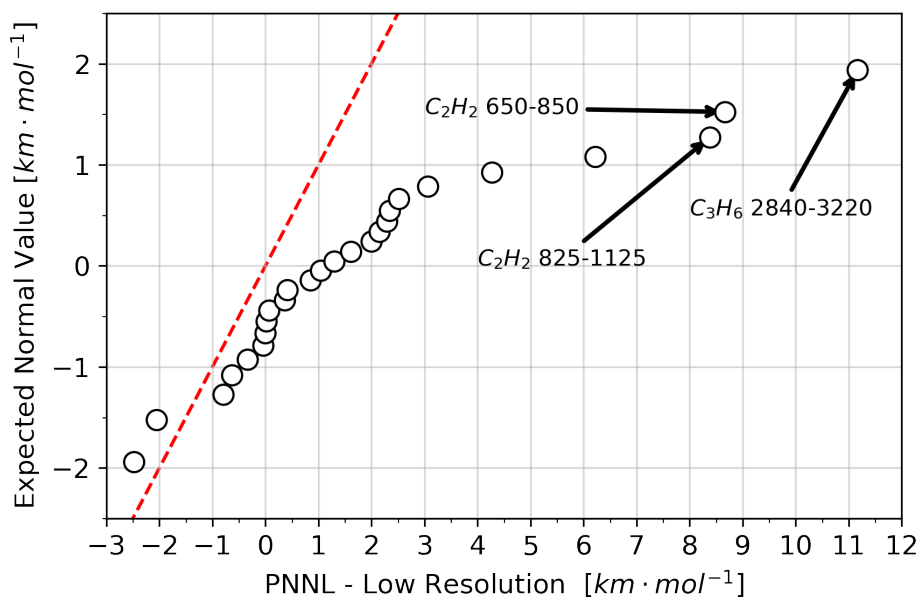


Figure 2.8: Normal plot of the difference between the PNNL and the low resolutions intensities. Points falling close to the red line follow the normal distribution expected behavior for random measurement error.

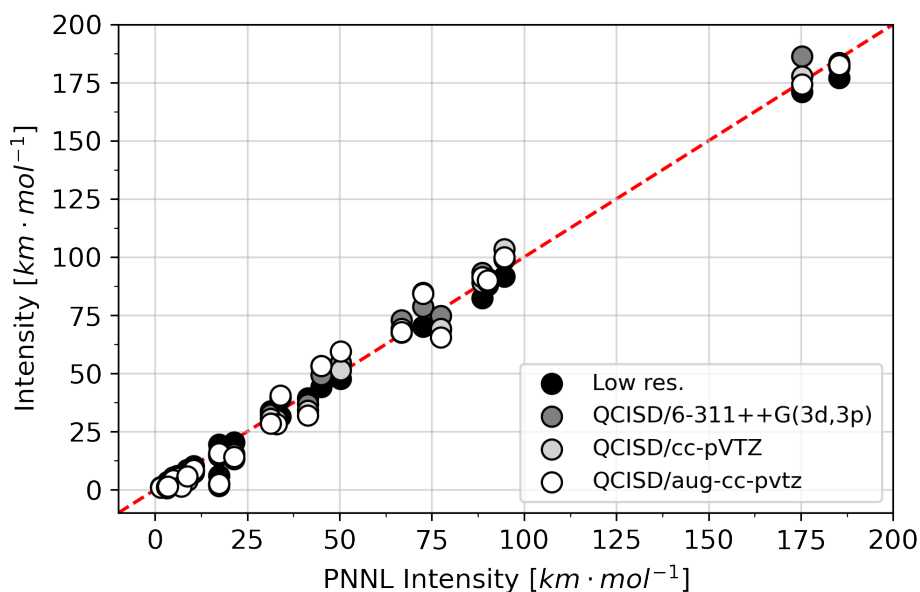


Figure 2.9: Comparative graph of the low-resolution experimental and the QCISD theoretical intensities against the experimental values determined from the PNNL spectral library ($km \cdot mol^{-1}$).

overall agreement was obtained with highly correlated wavefunctions, QCISD, CCSD and CCSD(T), combined with Dunning's correlation consistent aug-cc-pVXZ ($X = 3 - 5$) basis sets. These level of theory leads to best agreement with both the PNNL and low resolution averages for methane in Table 2.4, specially the TZ2P(f,d) and cc-pVTZ basis sets at the CCSD(T) level.

The most notable disagreement between experimental and theoretical intensities in Table 2.4 occurs for the CH stretching mode of acetylene. The PNNL and average low resolution values of 72.5 and 70.2 $\text{km} \cdot \text{mol}^{-1}$ are substantially lower than our theoretical results that range from 78.7 to 84.7 $\text{km} \cdot \text{mol}^{-1}$. Of the 75 quantum levels given in reference[57], the lowest is 74.7 $\text{km} \cdot \text{mol}^{-1}$, still higher than both experimental values. This value was obtained with the relatively poor DZP basis set at the CCSD(T) level. The use of more extensive basis sets led to higher values, most falling within the range of our theoretical values in Table 2.4. Their CCSD(T) level calculation with an aug-cc-pVTZ basis produces an 81.8 $\text{km} \cdot \text{mol}^{-1}$ value compared with our QCISD value of 84.3 $\text{km} \cdot \text{mol}^{-1}$.

The theoretical data are in good agreement with the experimental intensities from NIST/PNNL, especially when high level of theory and augmented base are utilized. However, even when smaller basis sets are applied, there is no significant increase in the RMSE. As such, the NIST/PNNL intensities will be used as reference, in this thesis, to the development of new theoretical methods and models that can interpret the physical phenomena behind the IR absorption phenomena.

2.3 Concluding Remarks

The high-resolution infrared spectra obtained by NIST/PNNL research groups are impressive and can be used to validate the theoretical data, either obtained from *ab initio* calculations or empirical models developed using low-resolution intensities from dispersive instruments. One of these models is the electronegativity model for partitioning of IR bands of halomethanes, allowing physical interpretations of atomic contributions to the electron density changes that occur with the vibrational movement.

In the next chapter, *ab initio* method will be invoked to construct the Charge – Charge Transfer – Dipolar Polarization (CCTDP) model, which calculates atomic contributions directly from the electron density using the principles of the Quantum Theory of Atoms in Molecules.

This chapter contains excerpts from texts previously published by the author. The following materials were reprinted with permission:

Duarte, L. J., Silva, A. F., Richter, W. E., Bruns, R. E., *FTIR and dispersive gas phase fundamental infrared intensities of the fluorochloromethanes: Comparison with QCISD/cc-pVTZ results*. Spectrochimica Acta Part A: Molecular and Biomolecular Spectroscopy, 205, 269-275, 2018, Elsevier.

Duarte, L. J., Bruns, R. E., *FTIR and dispersive gas phase absolute infrared intensities of hydrocarbon fundamental bands*. Spectrochimica Acta Part A: Molecular and Biomolecular Spectroscopy, 214, 1-6, 2019, Elsevier.

Chapter 3

Decomposition of Infrared Intensities

Chemical properties of atoms and molecules arise from their electronic structures. Electrons are distributed around nuclei following a probability density that is determined by the solution of the Schrödinger equation. Considering the Born-Oppenheimer approximation, the wavefunction is parameterized by the positions of nuclei, which are considered stationary. Molecules, however, present a dynamic behavior, vibrating and rotating all the time around their equilibrium positions. When an atom moves within a normal coordinate of vibration, it perturbs the electronic density of the entire molecule. The magnitude, direction and sense of the perturbation is expressed by the APT[72–74]. Each element of the APT is the derivative of one component of the molecular dipole moment with respect to an atomic displacements.

When analysing a band in the IR spectrum, the APT can be obtained experimentally through matrix manipulation if band intensities, normal coordinates, equilibrium geometries and permanent molecular dipole moments are previously known [15, 75, 76]. Even with the lower resolution dispersive spectrometers available in the 60-70's, the determination of APTs was accurate and the results compatible with the chemical knowledge[77]. As computing resources became more accessible, SCF calculations allowed the computation of the APT directly from theory through simple numerical calculations. Its theoretical determination consists of optimizing the molecular structure and finding its equilibrium geometry, from which $6N$ non-equilibrium geometries are generated, with N being the number of atoms in the molecule. Each one of the non-equilibrium geometrical configurations is obtained by displacing an atom in either the positive or negative direction of one of the Cartesian axes (x , y , z). A summary of this procedure is presented in Figure 3.1.

AIM atomic charges and dipoles are obtained for each one of the non-equilibrium geometries and utilized to compute molecular dipole moments. At this point, the inclusion of atomic polarizations is crucial to properly describe the APT without corrupting its physical meaning[78]. When using charge models that do not provide explicit determination of atomic polarizations, one may find that the APT values are often correctly obtained; however, on careful examination, the absence of explicit atomic polarization terms can lead to chemically inconsistent results. The importance of including atomic polarizations becomes more evident when studying planar molecules, for which the atomic out-of-plane motions[79] prevent any charge transfer to occur and the interplay between charges and dipoles is essential to represent the dynamic nature of the molecular struc-

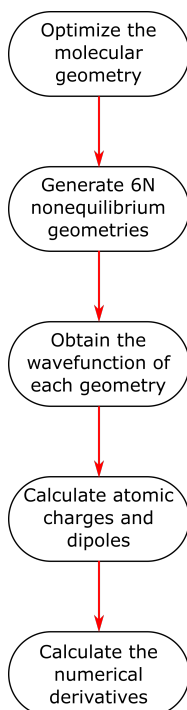


Figure 3.1: Flowchart of the theoretical procedure applied to calculate the APT derivatives from single point SCF calculations.

ture[78]. This will be explained in detail later.

Once the molecular dipole moment of each nonequilibrium geometry is determined, the APT elements are calculated by numerically differentiating the dipole moment with respect to the atomic displacements that generated them. If the normal coordinates of the vibrational modes are previously known, the juxtaposition of the N APTs allows the computation of infrared intensities.

As the total intensity of a band is proportional to the square of the molecular dipole moment derivative with respect to the normal coordinate, the evaluation of infrared intensities by means of APT elements contains insightful information about the dynamic nature of chemical systems. The development of the Charge - Charge Transfer - Dipolar Polarization (CCTDP) model [80] over the past 15 years allows the interpretation of infrared intensities and has been fruitful in solving key problems in chemistry, e.g. identifying characteristic electronic density changes for functional groups [81] and amino acids [82], describing out-of-plane displacements in planar molecules[83–85] and explaining the infrared band intensifications owing to hydrogen bond formations[86–88].

3.1 The CCTDP Model for Infrared Intensities

Since the dipole moment is a vector that measures the charge separation in a system, indicating its polarity, the molecular dipole moment derivative can be decomposed into atomic charge and atomic dipole contributions. We start by rewriting equation 1.15 in terms of the σ Cartesian component of the dipole moment of an N atom molecule, that

is:

$$p_\sigma = \sum_{A=1}^N [q_A \sigma_A + m_{A,\sigma}] \quad (3.1)$$

where $\sigma = 1, 2, 3$ are the axes x, y, z , respectively. q_A and σ_A are the charge of the atom A and its Cartesian position on the σ axis. $m_{A,\sigma}$ is the σ component of the A^{th} atomic dipole. The derivative of the component σ of the dipole moment with respect to the B^{th} atomic Cartesian coordinate, θ_B , evaluated at equilibrium geometry is given by:

$$\frac{\partial p_\sigma}{\partial \theta_B} = \begin{cases} q_B + \sum_{A=1}^N \sigma_A \frac{\partial q_A}{\partial \theta_B} + \sum_{A=1}^N \frac{\partial m_{A,\sigma}}{\partial \theta_B} & \text{if } \sigma = \theta \\ \sum_{A=1}^N \sigma_A \frac{\partial q_A}{\partial \theta_B} + \sum_{A=1}^N \frac{\partial m_{A,\sigma}}{\partial \theta_B} & \text{if } \sigma \neq \theta \end{cases} \quad (3.2)$$

with $\sigma, \theta = 1, 2, 3$ and $A, B = 1, 2, \dots, N$. The atomic charge derivatives in both cases of Equation 3.2 correspond to atomic charge rearrangements occurring for atomic displacements of the B^{th} atom resulting in Cartesian position-weighted charge transfer terms. The last terms in these equations represent changes in the atomic dipole components for Cartesian atomic displacements and are called dipolar polarizations.

For each atom, equation 3.2 generates nine derivatives that arise from the combination of the dipole moment directions in rectangular Cartesian space with the spatial coordinates. The derivatives are APT elements of $\mathbf{P}_\mathbf{x}$. The APT of the B^{th} atom is given by:

$$\mathbf{P}_\mathbf{x}^{(\mathbf{B})} = \begin{bmatrix} \frac{\partial p_x}{\partial x_B} & \frac{\partial p_x}{\partial y_B} & \frac{\partial p_x}{\partial z_B} \\ \frac{\partial p_y}{\partial x_B} & \frac{\partial p_y}{\partial y_B} & \frac{\partial p_y}{\partial z_B} \\ \frac{\partial p_z}{\partial x_B} & \frac{\partial p_z}{\partial y_B} & \frac{\partial p_z}{\partial z_B} \end{bmatrix} \quad (3.3)$$

where the diagonal elements correspond to the first case of Equation 3.2 and off-diagonal elements correspond to the second case. The tensor describes how the electronic density will change as any atom is displaced from its original position.

Within the harmonic oscillator-linear dipole moment approximation, the infrared intensity is proportional to the square of the molecular dipole moment derivative with respect to the vibrational normal coordinate. The conversion of the Cartesian APT ($\mathbf{P}_\mathbf{x}$)^(B) into the vector of derivatives with respect to the normal coordinate Q is done with the help of the $\mathbf{L}^{(\mathbf{B})}$ matrix that is:

$$(\mathbf{P}_\mathbf{x})^{(\mathbf{B})}_{3 \times 3} \cdot \mathbf{L}^{(\mathbf{B})}_{3 \times 1} = (\mathbf{P}_\mathbf{Q})^{(\mathbf{B})}_{3 \times 1} \quad (3.4)$$

where each element of $\mathbf{L}^{\mathbf{B}}$ is a derivative of the σ_B component with respect to Q .

Since the square of a vector is equal to the sum of squares of its Cartesian components, the IR intensity, \mathcal{A} , of the Q_k normal mode is ¹:

$$\mathcal{A}_k = \frac{N_A \pi}{3c^2} \left[\left(\frac{\partial p_x}{\partial Q_k} \right)^2 + \left(\frac{\partial p_y}{\partial Q_k} \right)^2 + \left(\frac{\partial p_z}{\partial Q_k} \right)^2 \right] \quad (3.5)$$

where $k = 1, 2, \dots, 3N - 6$ for an N atom non-linear molecule or $k = 1, 2, \dots, 3N - 5$ for linear molecules. N_A is the Avogadro's constant and c is the speed of light.

¹See Appendix B.

Dipole moment derivatives with respect to normal coordinates involve simultaneous displacements of all atoms in the molecule. As such, each Cartesian component of the dipole moment derivative with respect to the normal coordinate must consider contributions from atomic displacements in all directions:

$$\frac{\partial p_\sigma}{\partial Q_k} = \sum_{B=1}^N \left(\sum_{A=1}^N \sum_{\theta=1}^3 \frac{\partial p_{\sigma_A}}{\partial \theta_B} \frac{\partial \theta_B}{\partial Q_k} \right) = \sum_{B=1}^N \left(\frac{\partial p_\sigma}{\partial Q_k} \right)^{(B)} \quad (3.6)$$

and substituting equation 3.2 in equation 3.6

$$\left(\frac{\partial p_\sigma}{\partial Q_k} \right)^{(B)} = q_B \frac{\partial \sigma_B}{\partial Q_k} + \sum_{A=1}^N \sum_{\sigma=1}^3 \left(\sigma_A \frac{\partial q_A}{\partial \theta_B} + \frac{\partial m_{A,\sigma}}{\partial \theta_B} \right) \frac{\partial \theta_B}{\partial Q_k} \quad (3.7)$$

leading to:

$$\left(\frac{\partial p_\sigma}{\partial Q_k} \right)^{(B)} = q_B \frac{\partial \sigma_B}{\partial Q_k} + \sum_{A=1}^N \left[\sigma_A \left(\frac{\partial q_A}{\partial Q_k} \right)^{(B)} + \left(\frac{\partial m_{A,\sigma}}{\partial Q_k} \right)^{(B)} \right] \quad (3.8)$$

noticing that $\left(\frac{\partial p_\sigma}{\partial Q_k} \right)^{(B)}$ is an element of $(\mathbf{P}_Q)^{(B)}$.

Each one of the terms in the right side of equation 3.8 corresponds to an atomic parcel of the Charge–Charge Transfer–Dipolar Polarization model. The first term is the atomic charge of the B^{th} atom weighted by its displacement within the normal coordinate Q_k , i.e. the Charge (C) contribution.

The first term in the summation corresponds to weighted changes in atomic charges as the molecule vibrates. Since the overall molecular charge must be conserved, any fraction of electronic density lost by one atom will be gained by the other(s). For this reason, the term is named the Charge Transfer (CT) contribution of the CCTDP model.

The last term corresponds to rearrangements that occur for electronic densities of individual atoms. They arise from electronic density asymmetries in the domains of each atom. These polarizations are atomic dipole derivatives and correspond to Dipolar Polarization (DP) contributions to the CCTDP model. In simplified notation, equation 3.6 becomes:

$$\frac{\partial p_\sigma}{\partial Q_k} = \sum_{B=1}^N \left[\left(\frac{\partial p_\sigma}{\partial Q_k} \right)_{(C)}^{(B)} + \left(\frac{\partial p_\sigma}{\partial Q_k} \right)_{(CT)}^{(B)} + \left(\frac{\partial p_\sigma}{\partial Q_k} \right)_{(DP)}^{(B)} \right] \quad (3.9)$$

and the labels of the CCTDP contributions are always written inside parenthesis.

At this point, it is important to stress that the contributions have a mechanical weight that are proportional to the inverses of the square roots of atomic masses. Therefore, lighter atoms tend to have greater charge contributions than heavier atoms, even if their atomic charges are smaller in absolute values.

3.2 CCTDP Classification of IR Intensities

In this section, the CCTDP model is applied to a group of 29 molecules including hydrocarbons, halomethanes and the X_2CY ($X = F, Cl$; $Y = O, S$) molecules whose theoretical intensities have already been reported in the literature[89]. Intensities of all the active normal modes of these molecules have been measured and, when possible, their accuracy and precision have been estimated using measurements on isotopomers containing deuterium atoms instead of hydrogen.

We start by substituting equation 3.9 into equation 3.5 and summing over all atoms. In this way, the IR intensity of normal mode k becomes:

$$\mathcal{A}_k = \frac{N_A\pi}{3c^2} \sum_{\sigma=1}^3 \left[\left(\frac{\partial p_\sigma}{\partial Q_k} \right)_{(C)}^2 + \left(\frac{\partial p_\sigma}{\partial Q_k} \right)_{(CT)}^2 + \left(\frac{\partial p_\sigma}{\partial Q_k} \right)_{(DP)}^2 + \right. \\ \left. 2 \left(\frac{\partial p_\sigma}{\partial Q_k} \right)_{(C)} \left(\frac{\partial p_\sigma}{\partial Q_k} \right)_{(CT)} + 2 \left(\frac{\partial p_\sigma}{\partial Q_k} \right)_{(C)} \left(\frac{\partial p_\sigma}{\partial Q_k} \right)_{(DP)} + \right. \\ \left. 2 \left(\frac{\partial p_\sigma}{\partial Q_k} \right)_{(CT)} \left(\frac{\partial p_\sigma}{\partial Q_k} \right)_{(DP)} \right] \quad (3.10)$$

the first three terms are charge, charge transfer, and dipolar polarization contributions to the intensities, whereas the last three terms correspond to interactions between these dipole moment derivative contributions. In order to simplify the expression, the $(CT)^2$, $(DP)^2$ and $2(CTDP)$ are combined into a single contribution:

$$\mathcal{A}_{k(CTDP)} = \frac{N_A\pi}{3c^2} \sum_{\sigma=1}^3 \left[\left(\frac{\partial p_\sigma}{\partial Q_k} \right)_{(CT)}^2 + \left(\frac{\partial p_\sigma}{\partial Q_k} \right)_{(DP)}^2 + 2 \left(\frac{\partial p_\sigma}{\partial Q_k} \right)_{(CT)} \left(\frac{\partial p_\sigma}{\partial Q_k} \right)_{(DP)} \right] \quad (3.11)$$

Each of the first two terms have large positive values, and often, their sum is almost completely cancelled by the large negative values of the charge transfer—dipolar polarization interaction. Often these much smaller net values are seen to be the result of atomic charge transfer within the molecule that is accompanied by dipolar polarizations in opposite directions to one another. This is called the counter-polarization effect.

The two interaction terms involving the equilibrium charge factor can be given as:

$$\mathcal{A}_{k(CCT,CDP)} = \frac{N_A\pi}{3c^2} \sum_{\sigma=1}^3 \left[2 \left(\frac{\partial p_\sigma}{\partial Q_k} \right)_{(C)} \left(\frac{\partial p_\sigma}{\partial Q_k} \right)_{(CT)} + 2 \left(\frac{\partial p_\sigma}{\partial Q_k} \right)_{(C)} \left(\frac{\partial p_\sigma}{\partial Q_k} \right)_{(DP)} \right] \quad (3.12)$$

and interpreted as an interaction between equilibrium atomic charge movements and the sum of differential changes to the electronic densities of these atoms. The IR intensity becomes:

$$\mathcal{A}_k = \mathcal{A}_{k(C)} + \mathcal{A}_{k(CTDP)} + \mathcal{A}_{k(CCT,CDP)} \quad (3.13)$$

where $\mathcal{A}_{k(C)}$, $\mathcal{A}_{k(CTDP)}$, and $\mathcal{A}_{k(CCT,CDP)}$ are the charge, charge transfer–dipolar polarization, and the interaction contribution to the IR intensity of normal mode k . Almost all of the CCTDP parameters reported here were obtained from works that can be found in the literature[71, 80, 89, 90]. The QCISD electron correlation treatment level and the cc-pVTZ, 6–31G(2d,2p), and 6–31G(3d,3p) basis sets were used for almost all molecules. All the theoretical intensities reproduce the experimental intensities within $11.4 \text{ km} \cdot \text{mol}^{-1}$. This error can be compared with experimental values ranging from zero to $493 \text{ km} \cdot \text{mol}^{-1}$ and having an average of $59.5 \text{ km} \cdot \text{mol}^{-1}$. Furthermore, an RMSE of only $5.0 \text{ km} \cdot \text{mol}^{-1}$ is found between the intensities calculated directly from the molecular wave function and the values obtained by the CCTDP model. Such error arises mostly from the AIM properties derivatives that are numerically calculated. The objective of this section is to differentiate the electronic structure changes that accompany vibrations using the CCTDP model applied to the characteristic group intensities of the CH, CF, and CCl stretching and bending vibrations.

3.2.1 CH Stretching Modes

Table 3.1 contains the $\mathcal{A}_{(C)}$, $\mathcal{A}_{(CTDP)}$, and $\mathcal{A}_{(CCT,CDP)}$ contributions along with the total calculated intensity values of the CH stretching vibrations. The charge contribution, with an average value of $2.5 \text{ km} \cdot \text{mol}^{-1}$, are usually substantially smaller than the $\mathcal{A}_{(CTDP)}$ contributions, that have an average of $16.8 \text{ km} \cdot \text{mol}^{-1}$. As such, the sum of $\mathcal{A}_{(CTDP)}$, and $\mathcal{A}_{(CCT,CDP)}$ can recover much of the total intensity values.

In Figure 3.2 there are only a few small deviations from the red line representing exact agreement between the $\mathcal{A}_{(CTDP)} + \mathcal{A}_{(CCT,CDP)}$ total calculated intensities for the CH stretching modes. The charge contributions are less than $2 \text{ km} \cdot \text{mol}^{-1}$ for all of these molecules, except for C_2H_2 , which has a $25.2 \text{ km} \cdot \text{mol}^{-1}$ charge contribution and contributions ranging between 2.2 and $9.5 \text{ km} \cdot \text{mol}^{-1}$ for the CH stretches of propyne, CH_2F_2 , CHF_3 , CH_2Cl_2 , and CHCl_3 .

Acetylene and propyne have acidic hydrogens as they are bonded to *sp* hybridized carbon atoms, and one would also expect higher charge contributions for the hydrogen and carbon atoms in halomethane molecules with multiple fluorine and chlorine substituents. All the CH stretching modes for the difluoro- and dichloroethylenes have very small charge contributions of less than $2.4 \text{ km} \cdot \text{mol}^{-1}$.

In summary, deviations from the line indicate a greater contribution of the equilibrium charge on the hydrogen atom, either by the inductive effect of electronegative substituents, such as F, or by the greater *s* character of the carbon atom. Removing from consideration the CH stretching vibrations of the *sp* CH bonds, the $\mathcal{A}_{(CTDP)}$ and the $\mathcal{A}_{(CCT,CDP)}$ sum estimate the CH stretching intensities for the other molecules studied here with only a $2.5 \text{ km} \cdot \text{mol}^{-1}$ RMSE. These calculated intensities range from zero to $62 \text{ km} \cdot \text{mol}^{-1}$ with an average value of $18.4 \text{ km} \cdot \text{mol}^{-1}$. It should be mentioned that all the CH stretching vibrations have individual charge transfer and dipolar polarization contributions of opposite sign; i.e., they follow a charge transfer—counterpolarization model[71].

The counterpolarization effect occurs when the charge–transfer and the dipolar–polarization contributions have opposite signs. In Figure 3.3a the red arrow indicates the direction of displacement of one hydrogen atom in methane. When the hydrogen moves, its atomic charges increase, i.e. electronic density is transferred from H to the C atom. As a response to the charge transfer, the electron density in each atomic basin polarizes

Table 3.1: Charge, charge transfer – dipolar polarization contributions to the CH stretching intensities of the difluoro- and dichloroethylenes, fluorochloromethanes and hydrocarbons. Values in $km \cdot mol^{-1}$.

| Molecule | $\mathcal{A}_{k(C)}$ | $\mathcal{A}_{k(CTDP)}$ | $\mathcal{A}_{k(CCT,CDP)}$ | $\mathcal{A}_{k(CTDP)} + \mathcal{A}_{k(CCT,CDP)}$ | \mathcal{A}_k |
|---|----------------------|-------------------------|----------------------------|--|-----------------|
| cis-C ₂ H ₂ F ₂ | 0.7 | 6.1 | 4.0 | 10.1 | 10.8 |
| | 0.3 | 2.3 | -1.7 | 0.6 | 0.9 |
| trans-C ₂ H ₂ F ₂ | 0.1 | 2.1 | 1.0 | 3.1 | 3.2 |
| 1,1-C ₂ H ₂ F ₂ | 0.4 | 5.4 | 2.9 | 8.3 | 8.7 |
| cis-C ₂ H ₂ Cl ₂ | 0.2 | 0.0 | 0.2 | 0.2 | 0.4 |
| | 1.0 | 7.7 | -5.7 | 2.0 | 3.0 |
| trans-C ₂ H ₂ Cl ₂ | 0.4 | 4.3 | 2.6 | 6.9 | 7.3 |
| | 2.4 | 3.8 | 6.0 | 9.8 | 12.2 |
| CH ₄ | 0.0 | 21.7 | 1.4 | 23.1 | 23.1 |
| CH ₃ F | 0.3 | 23.7 | 5.3 | 29.0 | 29.3 |
| CH ₂ F ₂ | 1.7 | 19.8 | 11.6 | 31.4 | 33.1 |
| | 2.2 | 26.5 | 15.1 | 41.6 | 43.8 |
| CHF ₃ | 5.4 | 16.5 | 18.9 | 35.4 | 40.8 |
| | 6.6 | 11.2 | 17.2 | 28.4 | 35.0 |
| CH ₃ Cl | 0.2 | 28.3 | -5.2 | 23.1 | 23.3 |
| CH ₂ Cl ₂ | 1.1 | 12.3 | -7.5 | 4.8 | 5.9 |
| | 2.2 | 19.0 | -13.0 | 6.0 | 8.2 |
| CHCl ₃ | 5.0 | 6.3 | -11.2 | -4.9 | 0.1 |
| | 7.7 | 6.6 | -14.2 | -7.6 | 0.1 |
| C ₂ H ₂ | 25.2 | 20.8 | 44.7 | 65.5 | 90.7 |
| C ₂ H ₄ | 1.5 | 34.5 | -14.4 | 20.1 | 21.6 |
| C ₂ H ₆ | 0.6 | 17.8 | -6.4 | 11.4 | 12.0 |
| | 0.3 | 47.9 | 7.7 | 55.6 | 55.9 |
| C ₃ H ₆ | 1.1 | 46.5 | 14.0 | 60.5 | 61.6 |
| | 1.1 | 42.2 | -13.2 | 29.0 | 30.1 |
| C ₃ H ₄ (allene) | 0.2 | 25.5 | -4.6 | 20.9 | 21.1 |
| | 0.5 | 4.7 | -1.8 | 2.9 | 3.4 |
| C ₃ H ₄ (prop. sp) | 1.5 | 7.1 | -6.4 | 0.7 | 2.2 |
| | 9.5 | 19 | 26.8 | 45.8 | 55.3 |
| C ₃ H ₄ (propyne) | 0.1 | 14.3 | 1.7 | 16.0 | 16.1 |
| C ₆ H ₆ | 0.4 | 8.8 | 3.4 | 12.2 | 12.6 |
| | 0.0 | 24.8 | 0.0 | 24.8 | 24.8 |

in the opposite direction. This counterpolarization effect is represented by the grey vectors. The contour plots in Figures 3.3b and 3.3c show the Laplacian of the electronic density along a CH bond at the equilibrium position and after the stretching of the bond. Regions of concentrated electronic density are represented by the red colour. Notice that the negative region elongates towards the carbon as the bond stretches.

3.2.2 CH Bending Modes

The CCTDP contributions for bending normal modes are listed in Table 3.2. The in-plane sp^3 CH bending vibrations also tend to have larger $\mathcal{A}_{k(CTDP)}$ contributions (average of $7.9 km \cdot mol^{-1}$) compared with $\mathcal{A}_{k(C)}$ charges (average of $4.6 km \cdot mol^{-1}$), that is a consequence of the small hydrogen charge. Figure 3.4 contains the sum of the $\mathcal{A}_{k(CTDP)}$ and $\mathcal{A}_{k(CCT,CDP)}$ interaction contributions for the CH bending modes against their total intensities. In-plane bendings are represented by squares (\square), while out-of-plane vibrations are represented by the diamond shapes (\diamond). This sum shows excellent

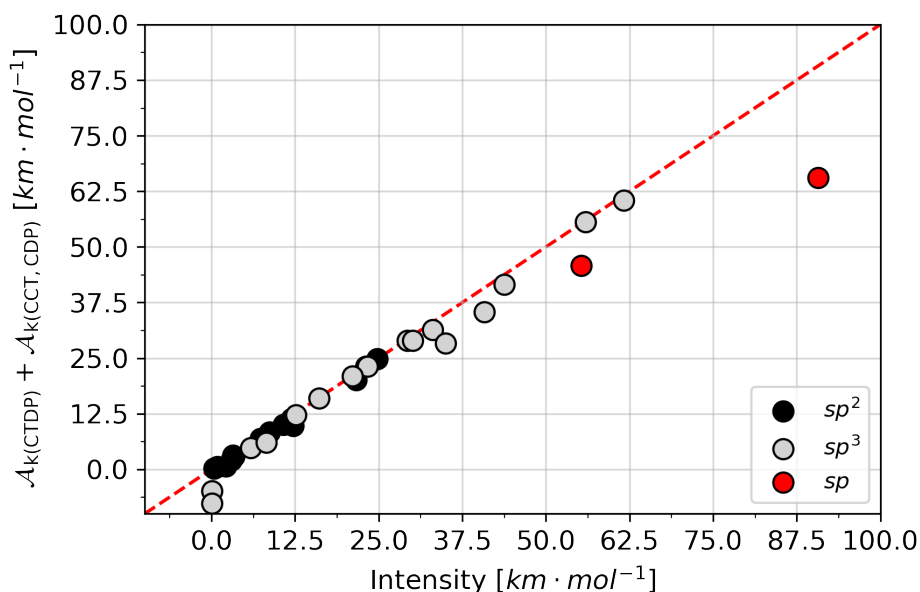


Figure 3.2: Sum of the $\mathcal{A}_{k(\text{CTDP})}$ and $\mathcal{A}_{k(\text{CCT,CDP})}$ against the total calculated intensity for CH stretches.

agreement with the total intensities for all the sp^3 CH bending vibrations except for the asymmetric CH bend of CH_2F_2 and CH bendings of CH_2Cl_2 . The $\mathcal{A}_{k(\text{CTDP})}$ and $\mathcal{A}_{k(\text{CCT,CDP})}$ sum estimates the sp^3 CH bendings with an RMSE of $3.8 \text{ km} \cdot \text{mol}^{-1}$ whereas this error is $9.2 \text{ km} \cdot \text{mol}^{-1}$ for the sp^2 CH bendings. The largest discrepancy occurs for the sp CH bend of propyne. These values can be compared with the total calculated intensities that range from zero to $106 \text{ km} \cdot \text{mol}^{-1}$, besides the larger discrepancies for the sp acetylene and propyne CH bendings.

The CH out-of-plane bending vibrations are, in general, more intense than the in-plane modes. The explanation behind this phenomena is the fact that out-of-plane vibrations have zero charge transfer² contributions[91–93]. As such, there are only dipolar polarization contributions to the total intensity and no counterpolarization effect occurs, i.e., their $\mathcal{A}_{k(\text{CTDP})}$ and $\mathcal{A}_{k(\text{CCT,CDP})}$ terms contains only dipolar polarization contributions. The $\mathcal{A}_{k(\text{CTDP})}$ average for the out-of-plane bendings is much larger than the average of it in-plane counterpart, which is equal to $7.9 \text{ km} \cdot \text{mol}^{-1}$.

These results are strongly supported by experimental evidence. For the bending vibrations, the experimental CH bending intensity average for the out-of-plane modes is $65.7 \pm 20.0 \text{ km} \cdot \text{mol}^{-1}$, more than 5 times the in-plane value of $12.6 \pm 10.4 \text{ km} \cdot \text{mol}^{-1}$. As an example, the larger out-of-plane bending experimental intensity for ethylene, $82.1 \pm 2.5 \text{ km} \cdot \text{mol}^{-1}$, compared to its in-plane bendings, 0.3 ± 0.0 and $10.1 \pm 0.2 \text{ km} \cdot \text{mol}^{-1}$, has long been a subject of discussion in the spectroscopic community[64, 94, 95]. Similar situation holds for benzene for which the measured out-of-plane bending intensity is more than 10 times larger than the in-plane one, 86.4 and $3.6 \text{ km} \cdot \text{mol}^{-1}$, respectively[96–98].

²The null charge transfer in out-of-plane bending is detailed in Chapter 4

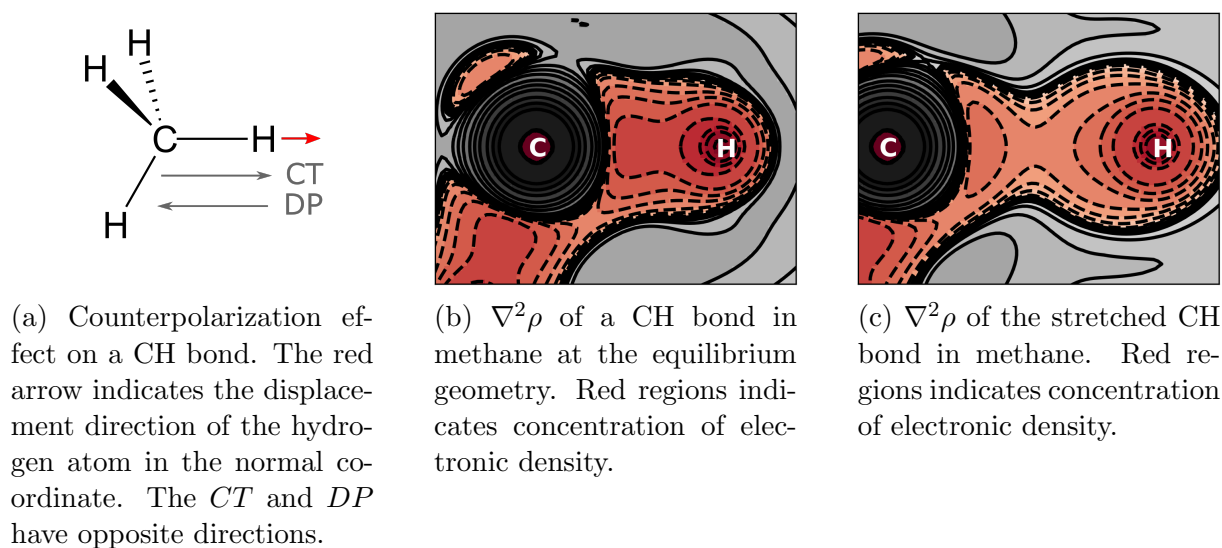


Figure 3.3: Counterpolarization effect on a CH bond. When the *CH* bond stretches, electronic density is transferred from the H to the C atom. In response to the charge-transfer, the atomic electronic densities polarize in the opposite direction. Vectors always point to the positive end.

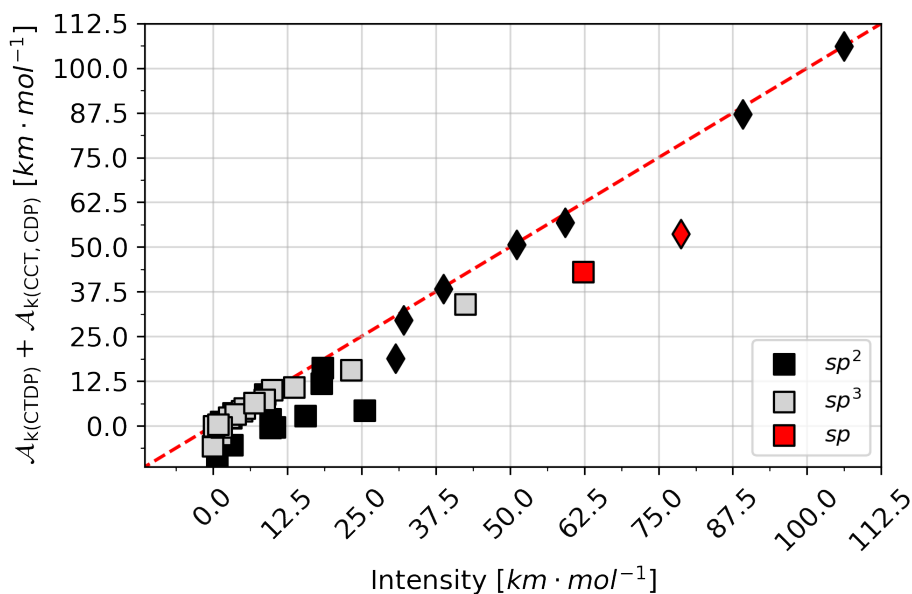


Figure 3.4: Sum of the $\mathcal{A}_{\text{(CTDP)}}$ and $\mathcal{A}_{\text{(CCT,CDP)}}$ against the total calculated intensity for CH bendings. In-plane bending normal modes are represented by square(\square) and out-of-plane bendings are represented by diamonds(\diamond). Notice that out-of-plane vibrations are, in average, more intense than in-plane vibrations.

3.2.3 CF and CCl Stretching Modes

As might be expected considering the electronegativity scale, the CF stretching mode intensities are dominated by the $\mathcal{A}_{\text{(C)}}$ term resulting from larger atomic charges. Their average value of $200.0 \text{ km} \cdot \text{mol}^{-1}$ in Table 3.3 is more than 10 times larger than the average value of the $\mathcal{A}_{\text{(CTDP)}}$ values, $14.9 \text{ km} \cdot \text{mol}^{-1}$.

Table 3.2: Charge, charge transfer – dipolar polarization contributions to the CH bending intensities of the difluoro- and dichloroethylenes, fluorochloromethanes and hydrocarbons. Values in $km \cdot mol^{-1}$.

| Molecule | $\mathcal{A}_{k(C)}$ | $\mathcal{A}_{k(CTDP)}$ | $\mathcal{A}_{k(CCT,CDP)}$ | $\mathcal{A}_{k(CTDP)} + \mathcal{A}_{k(CCT,CDP)}$ | \mathcal{A}_k |
|---|----------------------|-------------------------|----------------------------|--|-----------------|
| cis-C ₂ H ₂ F ₂ | 21.4 | 0.2 | 4.0 | 4.2 | 25.6 |
| | 6.5 | 3.0 | 8.8 | 11.8 | 18.3 |
| trans-C ₂ H ₂ F ₂ | 10.9 | 0.0 | -0.5 | -0.5 | 10.4 |
| 1,1-C ₂ H ₂ F ₂ | 11.4 | 6.6 | -17.3 | -10.7 | 0.7 |
| | 12.9 | 0.1 | 2.6 | 2.7 | 15.6 |
| cis-C ₂ H ₂ Cl ₂ | 1.3 | 3.2 | -4.0 | -0.8 | 0.5 |
| | 0.8 | 12.7 | -6.3 | 6.4 | 7.2 |
| trans-C ₂ H ₂ Cl ₂ | 2.4 | 7.5 | 8.6 | 16.1 | 18.5 |
| CH ₄ | 0.0 | 11.3 | -1.3 | 10.0 | 10.0 |
| CH ₃ F | 1.0 | 0.6 | 1.5 | 2.1 | 3.1 |
| | 0.4 | 5.0 | -2.7 | 2.3 | 2.7 |
| CH ₂ F ₂ | 3.9 | 0.6 | -3.1 | -2.5 | 1.4 |
| | 7.8 | 4.1 | 11.4 | 15.5 | 23.3 |
| CH ₃ Cl | 3.0 | 29.3 | -18.6 | 10.7 | 13.7 |
| | 0.8 | 1.7 | 2.4 | 4.1 | 4.9 |
| CH ₂ Cl ₂ | 5.8 | 6.0 | -11.8 | -5.8 | 0.0 |
| | 8.5 | 89.0 | -55.0 | 34.0 | 42.5 |
| C ₂ H ₄ | 1.4 | 3.1 | 4.2 | 7.3 | 8.7 |
| | 0.5 | 1.4 | -1.7 | -0.3 | 0.2 |
| C ₂ H ₆ | 0.6 | 9.4 | -4.6 | 4.8 | 5.4 |
| | 0.6 | 7.5 | -4.3 | 3.2 | 3.8 |
| | 1.9 | 6.8 | -7.2 | -0.4 | 1.5 |
| C ₃ H ₆ | 0.4 | 0.3 | -0.5 | -0.2 | 0.2 |
| | 0.6 | 0.1 | 0.2 | 0.3 | 0.9 |
| | 0.6 | 3.5 | 2.9 | 6.4 | 7.0 |
| C ₃ H ₄ (allene) | 10.3 | 1.7 | -2.3 | -0.6 | 9.7 |
| | 8.7 | 1.4 | -6.8 | -5.4 | 3.3 |
| C ₃ H ₄ (propyne) | 0.3 | 0.5 | 0.6 | 1.1 | 1.4 |
| | 0.0 | 9.6 | -0.8 | 8.8 | 8.8 |
| | 3.4 | 10.0 | -11.6 | 1.8 | 9.7 |
| C ₃ H ₄ (prop. sp) | 19.0 | 12.6 | 30.8 | 43.0 | 62.4 |
| C ₆ H ₆ | 0.0 | 3.5 | 0.0 | 3.5 | 3.5 |
| Out-of-Plane modes | | | | | |
| cis-C ₂ H ₂ F ₂ | 11.9 | 80.7 | -61.9 | 18.8 | 30.7 |
| trans-C ₂ H ₂ F ₂ | 0.4 | 60.0 | -9.3 | 50.7 | 51.1 |
| 1,1-C ₂ H ₂ F ₂ | 2.5 | 37.6 | 19.2 | 56.8 | 59.3 |
| cis-C ₂ H ₂ Cl ₂ | 0.5 | 30.7 | 7.6 | 38.3 | 38.8 |
| trans-C ₂ H ₂ Cl ₂ | 2.5 | 16.7 | 12.9 | 29.6 | 32.1 |
| C ₂ H ₂ | 25.2 | 14.9 | 38.7 | 53.6 | 78.8 |
| C ₂ H ₄ | 2.0 | 64.5 | 22.7 | 87.2 | 89.2 |
| C ₆ H ₆ | 0.0 | 106.2 | 0.0 | 106.2 | 106.2 |

Excellent agreement between these values can be seen with few exceptions. The discrepancy for the one mode of CHF₃ is owed to a $55.6 \text{ km} \cdot \text{mol}^{-1}$ $\mathcal{A}_{k(CTDP)}$ contribution, although $\mathcal{A}_{k(C)}$ is dominant, $311.3 \text{ km} \cdot \text{mol}^{-1}$. However, one normal mode of the F₂CS and one of cis-C₂H₂F₂ have $\mathcal{A}_{k(CTDP)}$ values of 59.7 and $47.6 \text{ km} \cdot \text{mol}^{-1}$, which are larger than their charge contributions. For all these CF modes, the charge and interaction sum estimates the total CF stretching intensities with an RMSE error of $23.3 \text{ km} \cdot \text{mol}^{-1}$ for intensities ranging from 3.7 to $470.9 \text{ km} \cdot \text{mol}^{-1}$ and averaging $201.7 \text{ km} \cdot \text{mol}^{-1}$.

The CCTDP contributions of Cl stretching intensities are presented in Table

Table 3.3: Charge, charge transfer – dipolar polarization contributions to the CF stretching intensities of the difluoroethylenes, fluorochloromethanes, hexafluorobenzene, F₂CO and F₂CS. Values in km · mol⁻¹.

| Molecule | $\mathcal{A}_{k(C)}$ | $\mathcal{A}_{k(CTDP)}$ | $\mathcal{A}_{k(CCT,CDP)}$ | $\mathcal{A}_{k(C)} + \mathcal{A}_{k(CCT,CDP)}$ | \mathcal{A}_k |
|--|----------------------|-------------------------|----------------------------|---|-----------------|
| cis-C ₂ H ₂ F ₂ | 62.9 | 0.1 | -4.5 | 58.4 | 58.5 |
| | 9.6 | 47.6 | 42.7 | 52.3 | 99.9 |
| trans-C ₂ H ₂ F ₂ | 106.4 | 18.7 | 89.2 | 195.6 | 214.3 |
| 1,1-C ₂ H ₂ F ₂ | 34 | 12.3 | 40.9 | 74.9 | 87.2 |
| | 123.5 | 21.7 | 103.6 | 227.1 | 248.8 |
| F ₂ CO | 21.4 | 5.5 | 21.7 | 43.1 | 48.6 |
| | 515.3 | 13.5 | -166.7 | 348.6 | 362.1 |
| F ₂ CS | 2.9 | 0.1 | 0.7 | 3.6 | 3.7 |
| | 44.3 | 59.7 | 102.8 | 147.1 | 206.8 |
| CH ₃ F | 58.9 | 5.3 | 35.1 | 94 | 99.3 |
| CH ₂ F ₂ | 150 | 4.8 | -53.8 | 96.2 | 101 |
| | 162.7 | 5.5 | 59.6 | 222.3 | 227.8 |
| CHF ₃ | 311.3 | 55.6 | -263.2 | 48.1 | 103.7 |
| | 308.8 | 1.7 | -45.8 | 263 | 264.7 |
| CF ₄ | 660.8 | 30.7 | -285 | 375.8 | 406.5 |
| CClF ₃ | 390.1 | 3.8 | 77 | 467.1 | 470.9 |
| | 422 | 11.6 | -140 | 282 | 293.6 |
| CCl ₂ F ₂ | 226.3 | 4.3 | 62.5 | 288.8 | 293.1 |
| | 242.9 | 1.1 | -32.5 | 210.4 | 211.5 |
| CCl ₃ F | 111.8 | 7.9 | 59.5 | 171.3 | 179.2 |
| C ₆ F ₆ | 233.9 | 0.4 | 19.3 | 253.2 | 253.6 |

3.4. For this type of vibrational mode, the intensity average value is 104.7 km · mol⁻¹, about half the average of the CF stretching normal mode, but still five times greater than the average intensity of the CH stretching. The average $\mathcal{A}_{k(C)}$ contribution of CCl stretch is 33.6 km · mol⁻¹, compared with an average value of 2.5 km · mol⁻¹ for CH stretching and 200.0 km · mol⁻¹ for CF stretching.

The averages of the $\mathcal{A}_{k(C)}$ and $\mathcal{A}_{k(CTDP)}$ contributions are very similar, 33.6 and 40.7 km · mol⁻¹. However, these CCl stretching modes follow different CCTDP patterns. Intensities of mode of cis-C₂H₂Cl₂, CH₂Cl₂, CHCl₃, CClF₃, CCl₂F₂, and two modes of CCl₃F have much larger charge contributions compared to their $\mathcal{A}_{k(CTDP)}$ ones and are estimated quite well by the $\mathcal{A}_{k(C)} + \mathcal{A}_{k(CCT,CDP)}$ sum with only a RMSE of 12.6 km · mol⁻¹ compared to an average calculated intensity of 97.2 km · mol⁻¹. The other modes present a $\mathcal{A}_{k(CTDP)}$ contributions much larger than their charge contributions and are estimated by $\mathcal{A}_{k(CTDP)} + \mathcal{A}_{k(CCT,CDP)}$ with a 10.3 km · mol⁻¹ error for an average intensity of 96.7 km · mol⁻¹.

3.2.4 CF and CCl Bending Modes

Charge and charge transfer–dipolar polarization intensity contributions for the CF and Cl bending modes are given in Table 3.5. Besides the $\mathcal{A}_{k(CCT,CDP)}$ interaction term, the sums of $\mathcal{A}_{k(C)}$ and $\mathcal{A}_{k(CTDP)}$ contributions are also given. The CF bending modes have much smaller intensities than the CF stretchings, with values ranging from about zero to only 65 km · mol⁻¹. Their average value is 10.3 km · mol⁻¹, about 20 times smaller than that of the CF stretching intensities. This can be understood examining the $\mathcal{A}_{k(C)}$, $\mathcal{A}_{k(CTDP)}$, and $\mathcal{A}_{k(CCT,CDP)}$ contributions. The $\mathcal{A}_{k(C)}$ and $\mathcal{A}_{k(CTDP)}$ have about the

Table 3.4: Charge, charge transfer – dipolar polarization contributions to the CCl stretching intensities of the chloroethylenes, chloromethanes, Cl₂CO and Cl₂CS. Values in km · mol⁻¹.

| Molecule | $\mathcal{A}_{k(C)}$ | $\mathcal{A}_{k(CTDP)}$ | $\mathcal{A}_{k(CCT, CDP)}$ | $\mathcal{A}_{k(C)} + \mathcal{A}_{k(CCT, CDP)}$ | $\mathcal{A}_{k(CTDP)} + \mathcal{A}_{k(CCT, CDP)}$ | \mathcal{A}_k |
|---|----------------------|-------------------------|-----------------------------|--|---|-----------------|
| cis-C ₂ H ₂ Cl ₂ | 5.5 | 3.6 | 8.9 | 14.4 | 12.5 | 18.0 |
| | 0.8 | 50.9 | 12.9 | 13.7 | 63.8 | 64.6 |
| trans-C ₂ H ₂ Cl ₂ | 7.3 | 49.8 | 38.2 | 45.5 | 88.0 | 95.3 |
| Cl ₂ CS | 0.8 | 9.8 | 5.7 | 6.5 | 15.5 | 16.3 |
| | 4.3 | 253.9 | -66.0 | -61.7 | 187.9 | 192.2 |
| Cl ₂ CO | 0.2 | 14.4 | 3.5 | 3.7 | 17.9 | 18.1 |
| | 85.3 | 119.1 | 201.7 | 287.0 | 320.8 | 406.1 |
| CH ₃ Cl | 6.0 | 6.1 | 12.1 | 18.1 | 18.2 | 24.2 |
| CH ₂ Cl ₂ | 12.0 | 0.0 | 0.5 | 12.5 | 0.5 | 12.5 |
| | 12.2 | 53.9 | 51.4 | 63.6 | 105.3 | 117.5 |
| CHCl ₃ | 16.6 | 3.2 | -14.5 | 2.1 | -11.3 | 5.3 |
| | 17.2 | 53.9 | 60.9 | 78.1 | 114.8 | 132.0 |
| CCl ₄ | 18.1 | 55.8 | 63.5 | 81.6 | 119.3 | 137.4 |
| CClF ₃ | 66.8 | 5.4 | -37.9 | 28.9 | -32.5 | 34.3 |
| CCl ₂ F ₂ | 9.0 | 9.9 | -18.9 | -9.9 | -9.0 | 0.0 |
| | 242.8 | 14.3 | 117.8 | 360.6 | 132.1 | 374.9 |
| CCl ₃ F | 1.4 | 0.0 | 0.1 | 1.5 | 0.1 | 1.5 |
| | 98.0 | 29.2 | 107.0 | 205.0 | 136.2 | 234.2 |

same sizes but opposite signs compared with their interaction values. Even though these sums and interactions have relatively large magnitudes, they cancel each other resulting in small net intensities.

As for the CH out-of-plane bendings, the charge transfer contribution is zero for the out-of-plane CF bendings, and the charge transfer-counterpolarization effect does not occur. The average $\mathcal{A}_{k(CTDP)}$ contribution for the out-of-plane bendings is 147.7 km · mol⁻¹ that is much larger than the values for the in-plane bendings, 18.2 km · mol⁻¹. In contrast to the CH bendings, the dipolar polarization contribution to the dipole moment derivative has an opposite sign to the charge contribution for the CF bendings. Since the negatively charged fluorine atoms are displaced in an opposite direction to the accumulation of electron density owing to polarization for the out-of-plane bend, there is a canceling effect. In terms of the intensity contributions, the negative $\mathcal{A}_{k(CCT, CDP)}$ terms cancel the sums of $\mathcal{A}_{k(C)}$ and $\mathcal{A}_{k(CTDP)}$ to a large extent resulting in small out-of-plane intensity values that are of comparable size to the in-plane ones.

The CCl bending modes also have very small intensities with a calculated average of 2.4 km · mol⁻¹ compared to the CCl stretching mode average of 104.7 km · mol⁻¹. Again, $\mathcal{A}_{k(C)}$ and $\mathcal{A}_{k(CTDP)}$ sums and the $\mathcal{A}_{k(CCT, CDP)}$ contributions tend to cancel one another. The largest calculated intensity occurs for CCl₂F₂, 11.5 km · mol⁻¹ followed by 8.0 and 5.8 km · mol⁻¹ for trans-C₂H₂Cl₂ and cis-C₂H₂Cl₂. All of the other CCl calculated intensities for the bending modes are less than 1 km · mol⁻¹. As found for the CH and CF bending vibrations, the average $\mathcal{A}_{k(CCT, CDP)}$ contribution for the out-of-plane bendings, 15.2 km · mol⁻¹, is also larger than the $\mathcal{A}_{k(CCT, CDP)}$ average of 2.8 km · mol⁻¹, for the in-plane CCl bending modes.

The experimental out-of-plane F₂CO value[99] of 30.6 km · mol⁻¹ is in good agreement with the QCISD/cc-vPTZ value of 35.8 km · mol⁻¹ and it is 3 times larger

Table 3.5: Charge, charge transfer and dipolar polarization contributions to the CF and Cl bending intensities of the difluoro- and dichloroethylenes, fluorochloromethanes, X_2CY ($X = F, Cl$; $Y = O, S$) and hexafluorobenzene in $km \cdot mol^{-1}$.

| Molecule | $\mathcal{A}_{k(C)}$ | $\mathcal{A}_{k(CTDP)}$ | $\mathcal{A}_{k(CCT,CDP)}$ | $\mathcal{A}_{k(CTDP)} + \mathcal{A}_{k(CCT,CDP)}$ | \mathcal{A}_k |
|---------------------|----------------------|-------------------------|----------------------------|--|-----------------|
| cis- $C_2H_2F_2$ | 13.3 | 4.5 | -15.5 | 17.8 | 2.3 |
| | 65.7 | 7.4 | -44.2 | 73.1 | 28.9 |
| trans- $C_2H_2F_2$ | 104 | 28.4 | -108.6 | 132.4 | 24.0 |
| 1,1- $C_2H_2F_2$ | 35.6 | 31.8 | -67.3 | 67.4 | 0.1 |
| | 2.5 | 2.8 | 2.8 | 5.2 | 10.5 |
| F_2CO | 29.2 | 10.1 | -34.5 | 39.3 | 4.8 |
| | 95.5 | 48.2 | -135.6 | 143.7 | 8.1 |
| F_2CS | 20.1 | 2.7 | -14.9 | 22.8 | 7.9 |
| | 0.1 | 1.9 | 0.7 | 2.0 | 2.7 |
| CH_2F_2 | 38.7 | 15.4 | -48.8 | 54.1 | 5.3 |
| CHF_3 | 97.7 | 36.6 | -119.6 | 134.3 | 14.7 |
| | 48.1 | 1.3 | 15.9 | 49.4 | 65.3 |
| | 35.4 | 17.8 | -50.3 | 53.2 | 2.9 |
| CF_4 | 68.7 | 34.7 | -97.6 | 103.4 | 5.8 |
| $CClF_3$ | 14.1 | 14.4 | -28.5 | 28.5 | 0.0 |
| | 43.3 | 24.9 | -65.7 | 68.2 | 2.5 |
| | 1.5 | 2.0 | -3.4 | 3.5 | 0.1 |
| CCl_2F_2 | 0.2 | 0.1 | -0.3 | 0.3 | 0.0 |
| | 20.9 | 18.1 | -38.9 | 39 | 0.1 |
| | 18.4 | 12.9 | -30.8 | 31.3 | 0.5 |
| C_6F_6 | 31.3 | 4.9 | -24.6 | 36.2 | 11.6 |
| | 47.2 | 31.6 | -77.2 | 78.8 | 1.6 |
| | 0.6 | 0.3 | -0.9 | 0.9 | 0.0 |
| cis- $C_2H_2Cl_2$ | 5.0 | 0.0 | 0.8 | 5.0 | 5.8 |
| | 8.1 | 0.0 | -0.1 | 8.1 | 8.0 |
| trans- $C_2H_2Cl_2$ | 0.3 | 0.1 | 0.2 | 0.4 | 0.6 |
| | 3.3 | 2.1 | -5.3 | 5.4 | 0.1 |
| Cl_2CO | 0.1 | 0.0 | 0.1 | 0.1 | 0.2 |
| | 16.4 | 26.4 | -41.6 | 42.8 | 1.2 |
| CH_2Cl_2 | 2.4 | 0.7 | -2.5 | 3.1 | 0.6 |
| $CHCl_3$ | 3.6 | 1.7 | -4.9 | 5.3 | 0.4 |
| CCl_4 | 1.1 | 1.2 | -2.3 | 2.3 | 0.0 |
| Out-of-Plane | | | | | |
| trans- $C_2H_2F_2$ | 110.4 | 68.3 | -173.6 | 178.7 | 5.1 |
| 1,1- $C_2H_2F_2$ | 123 | 84.5 | -203.9 | 207.5 | 3.6 |
| C_6F_6 | 305.7 | 224.6 | -524.1 | 530.3 | 6.2 |
| F_2CO | 608.7 | 349.4 | -922.3 | 958.1 | 35.8 |
| F_2CS | 39.4 | 11.8 | -43.1 | 51.2 | 8.1 |
| trans- $C_2H_2Cl_2$ | 7.1 | 5.2 | -12.6 | 12.3 | -0.3 |
| Cl_2CO | 94.3 | 38.7 | -120.9 | 133 | 12.1 |
| Cl_2CS | 6.0 | 1.8 | -6.6 | 7.8 | 1.2 |

than the experimental value [100] for H_2CO , $9.9 km \cdot mol^{-1}$. The small H_2CO intensity occurs because the negatively charged oxygen atom is displaced in the opposite direction to the dipolar polarization. The F_2CO value is higher owing to an exceptionally high charge contribution of $608 km \cdot mol^{-1}$. Displacements of three very negatively charged atoms give rise to this exceptionally high charge contribution.

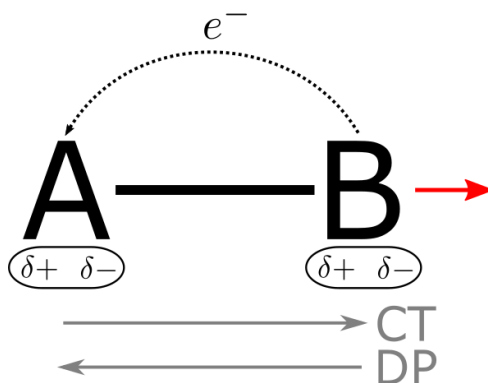


Figure 3.5: Counterpolarization effect during the stretching of a chemical bond. The red arrow indicates the displacement direction. The curved line shows the electron flux going from B to A. The ellipses below the atoms represent the atomic basin polarizations. Total charge-transfer and dipolar polarization vectors are represented by the grey arrows.

3.3 Probing the Robustness of the CCTDP model

From the previous section, it is clear that the intensity of CH, CF, and CCl stretchings are dependent on the counterpolarization effect. Similar behaviour was already reported for normal modes of carbonyl group[101]. As a general rule, if, during a atomic displacement, the atomic charges become more negative along one direction of the molecule the atomic dipoles change, so that their poles in the opposite direction become more negative as illustrated in Figure 3.5.

As the charge transfer and dipolar polarization contributions to the changes in dipole moment on molecular distortion have opposite signs their sums are very small. Furthermore they result in very large positive and negative contributions to the infrared intensity. The CH stretching mode of methane presents a good example of this cancellation. A positive intensity contribution of $2373.6 \text{ km} \cdot \text{mol}^{-1}$ calculated at the QCISD/cc-pVTZ level almost exactly cancels the negative contribution of $-2304.6 \text{ km} \cdot \text{mol}^{-1}$. So the QCISD/cc-pVTZ estimate of the methane CH stretching contribution is only $69.0 \text{ km} \cdot \text{mol}^{-1}$ in excellent agreement with the experimental value of $67.5 \text{ km} \cdot \text{mol}^{-1}$. However one might expect the charge transfer and dipolar polarization contributions to be very sensitive to different quantum level estimations as it is usually a small difference of two large estimated quantities.

We now examine the QTAIM/CCTDP model results for the CH, CF, and CCl stretching and bending distortions of the fluoro- and chloromethanes to determine to what extent the charge transfer and dipolar polarization cancellations affect the calculated intensities. The robustness of the QTAIM/CCTDP parameters are determined examining results calculated at three quantum levels, MP2/6-311G++(3d,3p), QCISD/cc-pVTZ, and QCISD/aug-cc-pVTZ. Model robustness is necessary for a proper description of the electronic density changes occurring for small molecular distortions. As such this information is relevant for investigations involving larger distortions and even chemical reactivity.

Table 3.6 contains the contributions $\mathcal{A}_{k(\text{CCTDP})}$ for the three quantum levels. Inspection shows that the inclusion of the augmented (s, p, d, and f) functions in the basis set produced only minor changes in its magnitude. The agreement between the QCISD/cc-pVTZ and QCISD/aug-cc-pVTZ levels is excellent with a correlation coefficient

Table 3.6: Charge transfer and dipolar polarization contributions sum to IR intensities of the fluoro- and chloromethanes at the MP2/6-311G++(3d,3p), QCISD/cc-pVTZ, and QCISD/aug-cc-pVTZ quantum levels. Values presented in $\text{km} \cdot \text{mol}^{-1}$.

| Molecule | Normal mode | MP2-6-311++(3d,3p) | QCISD/cc-pVTZ | QCISD/aug-cc-pVTZ |
|---------------------------------|-------------|--------------------|---------------|-------------------|
| CH ₄ | CH str. | 10.98 | 22.21 | 21.71 |
| | CH bend | 19.66 | 9.51 | 11.26 |
| CH ₃ F | CH str. | 23.74 | 27.73 | 23.70 |
| | CH bend | 0.08 | 0.63 | 0.63 |
| | CF str. | 8.89 | 7.22 | 5.24 |
| | CH str. | 7.56 | 18.00 | 19.59 |
| | CH bend | 9.80 | 5.37 | 5.04 |
| | mixed | 4.47 | 2.75 | 3.71 |
| | CH Str. | 20.55 | 25.61 | 26.46 |
| CH ₂ F ₂ | CH bend | 1.96 | 0.52 | 0.60 |
| | CF str. | 2.26 | 3.28 | 4.76 |
| | CF bend | 10.14 | 11.32 | 9.73 |
| | CF str. | 16.26 | 7.57 | 5.46 |
| | CH bend | 11.39 | 15.86 | 15.37 |
| | CH bend | 5.25 | 25.61 | 16.50 |
| | CF str. | 1.54 | 11.77 | 4.14 |
| | CH str. | 4.57 | 7.33 | 11.21 |
| | CF str. | 0.41 | 2.13 | 1.70 |
| | CF bend | 42.51 | 68.21 | 55.63 |
| CHF ₃ | CH bend | 27.45 | 39.95 | 36.64 |
| | CF str. | 1.59 | 1.60 | 1.31 |
| | CF bend | 14.69 | 18.75 | 17.81 |
| | CF str. | 9.93 | 34.90 | 30.75 |
| | CF bend | 28.24 | 39.14 | 34.68 |
| CF ₄ | CF str. | 9.93 | 34.90 | 30.75 |
| | CF bend | 28.24 | 39.14 | 34.68 |
| CH ₃ Cl | CH str. | 23.02 | 29.11 | 28.32 |
| | CH bend | 16.07 | 30.74 | 29.34 |
| | C-Cl str. | 6.05 | 6.20 | 6.16 |
| | CH str. | 3.25 | 10.27 | 12.27 |
| | CH bend | 4.10 | 1.70 | 1.68 |
| | CH bend | 3.70 | 1.89 | 1.71 |
| CH ₂ Cl ₂ | CH str. | 9.48 | 16.96 | 18.95 |
| | CH bend | 1.95 | 6.77 | 5.97 |
| | C-Cl str. | 0.00 | 0.02 | 0.00 |
| | C-Cl bend | 0.00 | 0.01 | 0.00 |
| | CH str. | 0.31 | 3.99 | 6.29 |
| | mixed | 3.17 | 1.82 | 1.33 |
| | CH Bend | 67.99 | 88.37 | 88.96 |
| | C-Cl str. | 61.77 | 51.06 | 53.91 |
| CHCl ₃ | CH str. | 0.53 | 4.00 | 6.56 |
| | C-Cl str. | 3.62 | 4.46 | 3.15 |
| | C-Cl bend | 1.55 | 1.72 | 1.68 |
| | CH bend | 47.28 | 61.53 | 59.77 |
| | C-Cl str. | 63.79 | 55.38 | 53.87 |
| | mixed | 0.47 | 1.04 | 0.71 |
| CCl ₄ | C-Cl str. | 64.58 | 47.18 | 55.80 |
| | C-Cl bend | 1.62 | 1.38 | 1.15 |

of 0.988. The RMSE of $3.3 \text{ km} \cdot \text{mol}^{-1}$ is much smaller than the range of the QCISD/aug-cc-pVTZ values from 0.0 to $89.0 \text{ km} \cdot \text{mol}^{-1}$. The variations in the contribution values on changing the electron correlation level from MP2 to QCISD and the basis set from 6-311G++(3d,3p) to aug-cc-pVTZ are much larger as would be expected. The correlation

coefficient between these levels of theory is noticeably smaller, 0.934, with a RMSE of $7.8 \text{ km} \cdot \text{mol}^{-1}$, more than twice the analogous value previously cited.

Table 3.7: Charge transfer–dipolar polarization contribution for CH, CF, and CCl stretchings and bendings ($\text{km} \cdot \text{mol}^{-1}$) for the MP2/6–311G++(3d,3p), QCISD/cc–pVTZ, and QCISD/aug–cc–pVTZ quantum levels.

| c | Normal 2* Mode | MP2 6–311G++(3d,3p) | | QCISD cc–pVTZ | | QCISD aug–cc–pVTZ | |
|---|-------------------|------------------------|-------------------------|----------------------|-------------------------|----------------------|-------------------------|
| | | $\mathcal{A}_{k(C)}$ | $\mathcal{A}_{k(CTDP)}$ | $\mathcal{A}_{k(C)}$ | $\mathcal{A}_{k(CTDP)}$ | $\mathcal{A}_{k(C)}$ | $\mathcal{A}_{k(CTDP)}$ |
| | CH stretch | 2.7 | 11.3 | 3.4 | 15.5 | 2.6 | 16.1 |
| | CH bend | 7.0 | 16.0 | 9.9 | 21.9 | 9.0 | 20.9 |
| | CF stretch | 233.4 | 2.9 | 275.4 | 5.2 | 283.3 | 3.4 |
| | CF bend | 46.5 | 23.9 | 60.1 | 34.4 | 62.0 | 29.5 |
| | CCl stretch | 11.1 | 33.3 | 13.7 | 27.4 | 14.1 | 28.8 |
| | CCl bend | 1.5 | 0.8 | 2.0 | 0.9 | 2.0 | 0.8 |

The average $\mathcal{A}_{k(C)}$ and $\mathcal{A}_{k(CTDP)}$ values at the three quantum levels are given for the CH, CF, and CCl stretching and bending vibrational modes in Table 3.7. These parameters at the QCISD level are very similar for both basis sets. The charge contribution changes are within $1 \text{ km} \cdot \text{mol}^{-1}$ except for the charge contribution of the CF stretch. It is $7.9 \text{ km} \cdot \text{mol}^{-1}$ larger when calculated with the augmented basis set compared with the cc–pVTZ basis at the QCISD level. However, this contribution is very large with a QCISD/aug–cc–pVTZ estimate of $283.3 \text{ km} \cdot \text{mol}^{-1}$. This difference corresponds only to 2.8% of this charge contribution. The CTDP contributions are also in excellent agreement with the largest difference of $4.9 \text{ km} \cdot \text{mol}^{-1}$ occurring for the CF bend on augmenting the basis set at the QCISD level.

The differences are larger comparing the values obtained at the QCISD level with the MP2/6–311G++(3d,3p) calculations. The $\mathcal{A}_{k(CTDP)}$ parameters have the largest difference of $5.6 \text{ km} \cdot \text{mol}^{-1}$ for the QCISD/aug–cc–pVTZ of the CF bending estimate that is only a bit larger than the $4.9 \text{ km} \cdot \text{mol}^{-1}$ difference cited above. The largest difference between these levels occurs for the CF charge contribution estimate, $49.9 \text{ km} \cdot \text{mol}^{-1}$ that is 17.6% larger than the QCISD/aug–cc–pVTZ value.

In spite of these numerical differences, the interpretation of the electronic structure changes occurring for these vibrations is the same for all three quantum levels. These results are a strong statement of the robustness of the QTAIM/CCTDP model. The three different theory levels used are of similar quality, although the QCISD/aug–cc–pVTZ level is significantly better when compared to MP2/6–311++G(3p,3d). When it comes to the electronic correlation treatment, it is pretty clear that second order Møller Plesset perturbation theory is conceptually very different from quadratic configuration interaction with single and double excitations. The basis sets used are also rather different, even though they are both triple zeta.

The 6–311G++(3p,3d) basis set is smaller than cc–pVTZ. The Pople’s set has 308 primitive functions while the Dunning’s set has 449 primitives for CCl_4 . One might say that, even though the 6–311G++(3p,3d) set is smaller, it is more thorough than cc–pVTZ (without the augmentation), as it has both diffuse and polarization functions, which is not the case for cc–pVTZ. The aug–cc–pVTZ basis set, however, is a very large basis set that has s, p, d, and f functions included to add diffuse character to the wave function. Regardless of all the differences mentioned above, and even though there are some minor differences in the magnitude of specific contributions (charge transfer or

dipolar polarization), the overall analysis of electronic density changes during vibrations remains unchanged.

3.4 Concluding Remarks

Changes in molecular electronic density as the molecule vibrates can be described as movements of the static equilibrium atomic charges and changes in the atomic electronic densities that are represented by intramolecular charge transfer and atomic dipolar polarization effects. The inclusion of atomic dipoles along with atomic charges obtained from QTAIM allows a characterization of the natures of the electronic density changes occurring for different kinds of molecular vibrations. The CH stretchings and bendings have dominant charge transfer-dipolar polarization contributions, the CF and CO stretches have dominant charge contributions and the CF and CCl bends have charge and charge transfer-dipolar polarization contribution sums that are mostly canceled by the CCT and CDP interaction contributions. This successful classification has not been achieved previously using models with only static atomic charge and charge transfer parameters.

Moreover, the charge transfer-counterpolarization effect occurs in the majority of vibrations reported in this thesis. The most recurring instances in which the counterpolarization effect does not take place is for the out-of-plane bending modes, where symmetry imposes a zero charge transfer constraint. For these molecules, the inclusion of atomic dipole moments is mandatory to properly reproduce the infrared intensity. In fact, the polarization of the atomic basins is the main factor behind the rehybridization moment, a key component used to explain the huge intensity difference between the out-of-plane normal mode of benzene and hexafluorobenzene. this topic is explored in the next chapter.

This chapter contains excerpts from texts previously published by the author. The following materials were reprinted with permission:

Duarte, L. J., Richter, W. E., Silva, A. F., Bruns, R. E. *Quantum theory of atoms in molecules charge-charge transfer-dipolar polarization classification of infrared intensities*. The Journal of Physical Chemistry A, 121(42), 8115-8123, 2017, American Chemical Society.

Silva, A. F., **Duarte, L. J.**, Bruns, R.E., *Probing the robustness of the charge-charge transfer-dipolar polarization model and infrared intensities*. Journal of Molecular Modeling 24(7), 1-7, 2018, Springer.

Chapter 4

Out-of-Plane vibrations

The previous chapter mentioned that charge-transfer is always null for an out-of-plane normal mode. Considering this fact, earlier studies explained the high intensity of benzene CH out-of-plane bending by introducing the “rehybridization” moment.

Taking the benzene molecule for example: if the molecule rests over the xy Cartesian plane (see Figure 4.1) then, during the molecular vibration, the hydrogen atom is displaced in the z direction and the sp^2 carbon atom is forced to adopt a sp^3 geometry. This means that s character is injected into the p_z orbital, allowing the π electrons to concentrate in the opposite direction of the distorted molecular plane. The molecular dipole moment derivative will reflect this concentration of electrons and, therefore, the normal mode will be intense in the IR spectrum.

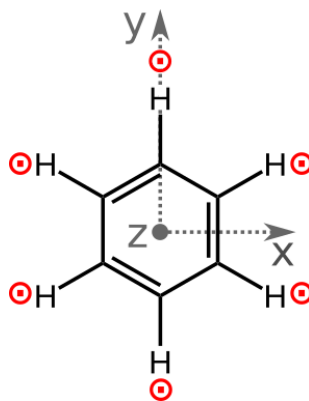


Figure 4.1: Positioning system for planar molecules and normal coordinates for out-of-plane bending vibrations. \odot indicates out-of-plane displacements in the positive direction of z axis.

The problem with this explanation is that it relies on the interpretation of orbitals. Since atomic and molecular orbitals are not observable, they are mathematical functions that do not exist in the tangible world. The electron density, however, is a quantum observable and a real physical object. If the rehybridization moment determines the intensity of the out-of-plane bending, then this effect can also be interpreted in terms of the electron density.

Here, an in-depth analysis on this topic is made. We start by investigating the CH bending of benzene, substituted benzene and other aromatic molecules.

4.1 The Charge Transfer Equals Zero

Dinur and Hagler[91, 92] have presented a first-principles proof that intramolecular charge transfer does not occur for out-of-plane vibrations of planar molecules. In fact, there are two factors that make this statement to be always true. The first one is a geometric constraint that ensures that the sum of the charge-transfer terms is zero, regardless of the derivative values and/or the molecular positioning in the reference frame. The second one is an electronic effect that arises from the system’s chemistry.

Dinur’s proof is as follows: if the molecular plane coincides with the Cartesian xy plane, then the p_z component of the dipole moment derivative with respect to the out-of-plane normal coordinate, Q_{oop} , becomes:

$$\frac{\partial p_z}{\partial Q_{oop}} = \sum_{A=1}^N q_A \frac{\partial z_A}{\partial Q_{oop}} + \sum_{A=1}^N \left(z_A \frac{\partial q_A}{\partial Q_{oop}} + \frac{\partial m_{A,z}}{\partial Q_{oop}} \right) \quad (4.1)$$

Since the system is closed, the charges must be conserved and are, therefore, subject to the constraint:

$$\sum_{A=1}^N \frac{\partial q_A}{\partial Q_{oop}} = 0 \quad (4.2)$$

solving equation 4.2 for atom $A = 1$, one obtains:

$$\sum_{A=1}^N z_A \frac{\partial q_A}{\partial Q_{oop}} = \sum_{A=2}^N (z_A - z_1) \frac{\partial q_A}{\partial Q_{oop}} \quad (4.3)$$

As the molecule is planar and rests over the Cartesian xy plane, the term $z_A - z_1$ in equation 4.3 is zero for every atom A . Consequently, the charge-transfer term in equation 4.1 is zero.

The second factor that makes the charge-transfer term null is related to the fact that any infinitesimal change in the atomic charge is the same for negative and positive angular displacements. At the equilibrium position, the atomic charge is either a maximum or a minimum point, implying that every charge derivative with respect to out-of-plane displacement equals zero. This is shown in Figure 4.2. The points in the graph were obtained through single point calculations starting from the equilibrium structure of benzene. The hydrogen atoms were displaced along the z positive and negative directions. Hydrogen AIM charges were obtained using the AIMAll software[102].

A symmetry argument can also be utilized to clarify this point. The hydrogen atom, when displaced in the positive direction ($+\partial\alpha$) has its atomic charge increased ($+\partial q$). Because of the symmetry, the exact same increase must occur when the hydrogen is displaced in the negative direction ($-\partial\alpha$), as shown in Figure 4.3. The overall charge change during the atom’s movement in the positive direction is $\frac{+\partial q}{+\partial\alpha}$ while the overall change in the negative direction is $\frac{+\partial q}{-\partial\alpha}$. During the molecular vibration, these contributions cancel each other, resulting in the null charge transfer contribution.

A similar analysis can be made on the atomic polarizations. Given the same reference system, changes in the hydrogen atomic dipole moment are of the same magnitude if the atom is displaced in the positive or negative direction. However, the atomic

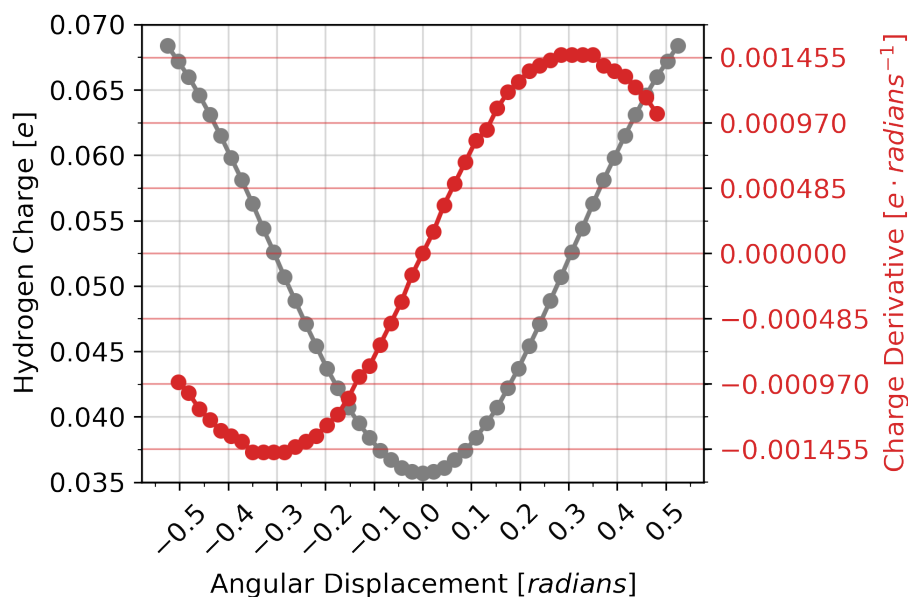


Figure 4.2: Atomic charge and its derivatives with respect to displacements perpendicular to the molecular plane. The grey line correspond to the hydrogen charge during benzene out-of-plane normal mode. The red line correspond to the charge derivative. Notice that at the equilibrium geometry, the charge derivative is zero.

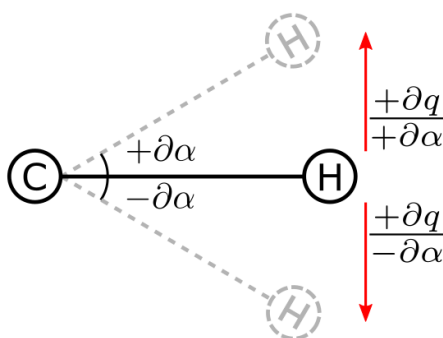


Figure 4.3: Schematic representation of a CH Bond in a planar molecule during an out-of-plane angular bending vibrational movement. Note that the infinitesimal changes in the charge q are the same for both negative and positive angular movements, α . By symmetry, as pointed out by the red arrows, the overall change in charge during this vibration is null, resulting in a charge transfer derivative equal to zero.

dipole moment is not a scalar, but a vector, giving those changes opposite signs. At equilibrium, the atomic dipole is always an inflection point with respect to out-of-plane displacements, as shown in Figure 4.4.

The consequence of the existence of the inflection point is that the atomic dipole derivative is a maximum (or minimum, depending of the phase of vibration) at the equilibrium. While the charge-transfer term does not contributes to the IR intensity of the out-of-plane bendings, the dipolar-polarization term is the highest possible. The proper description of atomic dipoles is, therefore, mandatory in order to correctly calculate the IR spectra of planar molecules.

Although these considerations are made within the harmonic model, it is important to notice that the planar geometry of the molecule causes the nullity of the charge transfer term even when corrections for anharmonicity are included.

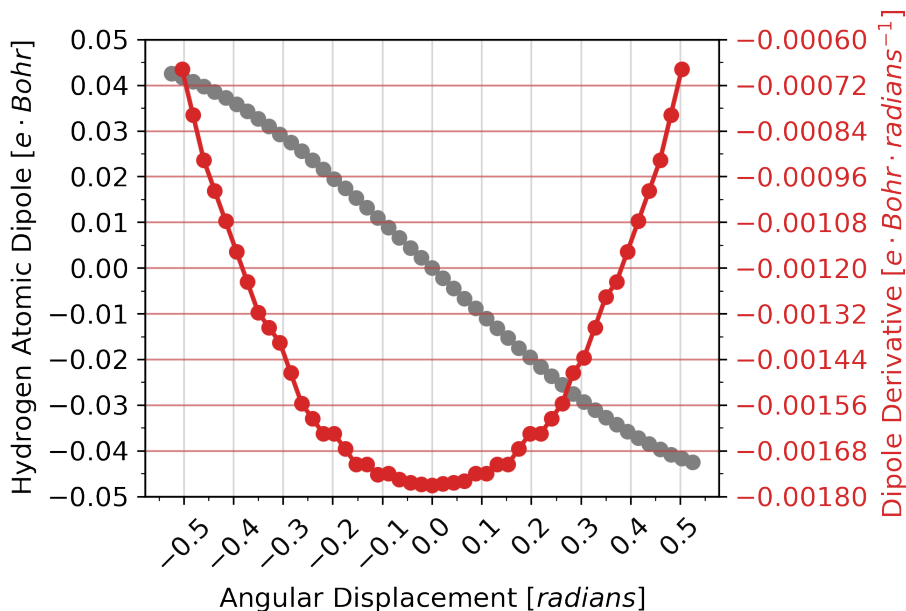


Figure 4.4: Atomic dipole and its derivative with respect to displacements perpendicular to the molecular plane. The grey line corresponds to the hydrogen z component of the atomic dipole moment during benzene out-of-plane normal mode. The red line correspond to the atomic dipole derivative.

4.2 CH Out-of-Plane Bending Intensities of Benzene Molecules

Due to the mass of hydrogen, the normal coordinate of the CH out-of-plane dipole moment derivatives in the substituted benzenes can be approximated by movements of only the hydrogen atoms in the direction perpendicular to the benzene plane as their displacements are much larger than those of the carbon and substituent atoms. This modifies equation 4.1 that can be approximated by summing over only the hydrogen atoms in the substituted benzenes, that is:

$$\frac{\partial p_z}{\partial Q_{oop}} = \sum_{A=1}^{N_H} \left[q_A \frac{\partial z_A}{\partial Q_{oop}} + \sum_{B=1}^N \left(z_B \frac{\partial q_B}{\partial z_A} \frac{\partial z_A}{\partial Q_{oop}} + \frac{\partial m_{B,z}}{\partial z_A} \frac{\partial z_A}{\partial Q_{oop}} \right) \right] \quad (4.4)$$

where N_H is the number of hydrogen atoms that moves in the out-of-plane normal coordinates.

However, as demonstrated in the previous section, the out-of-plane bending

vibrations have no charge transfers, so we can write:

$$\frac{\partial p_z}{\partial Q_{oop}} = \sum_{A=1}^{N_H} \left(q_A \frac{\partial z_A}{\partial Q_{oop}} + \sum_{B=1}^N \frac{\partial m_{B,z}}{\partial z_A} \frac{\partial z_A}{\partial Q_{oop}} \right) \quad (4.5)$$

The first term in this equation gives the contributions of the static hydrogen charge displacements whereas the second gives the contributions from atomic dipole changes on the displaced hydrogens and other atoms. The summation over all atoms, N , inside the parenthesis is necessary as movements of the hydrogen atoms can provoke polarizations on the other atoms.

Taking the square of this derivative and multiplying by $\frac{N_A\pi}{3c^2}$ gives the intensity contribution for the displacements of the hydrogen atoms in the out-of-plane normal coordinate:

$$\begin{aligned} \mathcal{A}_{oop} &= \frac{N_A\pi}{3c^2} \left(\frac{\partial p_z}{\partial Q_{oop}} \right)^2 = \frac{N_A\pi}{3c^2} \sum_{A=1}^{N_H} \sum_{B=1}^{N_H} q_A q_B \frac{\partial z_A}{\partial Q_{oop}} \frac{\partial z_B}{\partial Q_{oop}} + \\ &2 \frac{N_A\pi}{3c^2} \sum_{A=1}^{N_H} q_A \frac{\partial z_A}{\partial Q_{oop}} \sum_{B=1}^{N_H} \sum_{C=1}^N \frac{\partial m_{C,z}}{\partial z_B} \frac{\partial z_B}{\partial Q_{oop}} + \frac{N_A\pi}{3c^2} \sum_{A=1}^{N_H} \sum_{B=1}^N \frac{\partial m_{B,z}}{\partial z_A} \frac{\partial z_A}{\partial Q_{oop}} \sum_{C=1}^{N_H} \sum_{D=1}^N \frac{\partial m_{D,z}}{\partial z_C} \frac{\partial z_C}{\partial Q_{oop}} \end{aligned} \quad (4.6)$$

In order to simplify equation 4.6, we introduce the symbols \mathcal{A}_{C^2} , \mathcal{A}_{2CDP} and \mathcal{A}_{DP^2} to represent the squared charge contribution, the charge and dipolar polarization interaction and the squared dipolar polarization contribution. Equation 4.6 becomes:

$$\mathcal{A}_{oop} = \mathcal{A}_{C^2} + \mathcal{A}_{2CDP} + \mathcal{A}_{DP^2} \quad (4.7)$$

4.2.1 Ab Initio Calculations

The B3LYP/6-311++(d,p) level of theory was used as well as the geometry of a set of substituted benzenes with the GAUSSIAN09 program[25] that also provides the Hessian matrices and the \mathbf{L} matrices that contains the Cartesian coordinates derivatives with respect to the normal coordinates¹. The IR intensities were analytically calculated by GAUSSIAN09 and numerically calculated from the atomic charges and dipoles by the PLACZEK[103] program. From the equilibrium geometry, PLACZEK generates $6N$ distorted geometries with each atom being displaced 0.01\AA in the positive and negative directions for each Cartesian coordinate. Each one of these distorted geometries had their electron densities integrated by the AIMALL program[102] within the atoms in molecules criteria to obtain the charges and dipoles for each atom. Once these values were obtained, the polar tensor elements were calculated by simple numerical differentiation. This procedure can also be reproduced using the Theovib python library in appendix E.

¹See Appendix C.

4.2.2 Calculated and Experimental Intensities

The intensity values determined from the spectra in the PNNL library are given in Figure 4.5 along with values calculated at the B3LYP/6-311++(d,p) level. The theoretical values are plotted against the experimental ones, showing that the B3LYP values tend to overestimate the experimental ones with an RMSE of $8.7 \text{ km} \cdot \text{mol}^{-1}$. This accuracy seems reasonable as the intensities range from close to zero to $105.1 \text{ km} \cdot \text{mol}^{-1}$. The B3LYP benzene out-of-plane CH bending intensity of $122.1 \text{ km} \cdot \text{mol}^{-1}$ is about 20% higher than the PNNL experimental value of $105.1 \text{ km} \cdot \text{mol}^{-1}$. This out-of-plane intensity has been measured using low resolution instruments and pressure broadening techniques by two research groups[96, 104] presenting values of $88.2 \text{ km} \cdot \text{mol}^{-1}$ and $84.6 \text{ km} \cdot \text{mol}^{-1}$. Higher level ab initio QCISD/cc-pVTZ calculations provide an out-of-plane CH intensity for benzene of $106.2 \text{ km} \cdot \text{mol}^{-1}$ in almost exact agreement with the value from the PNNL spectral library, $105.1 \text{ km} \cdot \text{mol}^{-1}$. Table 4.1 contains the charge and dipolar polarization

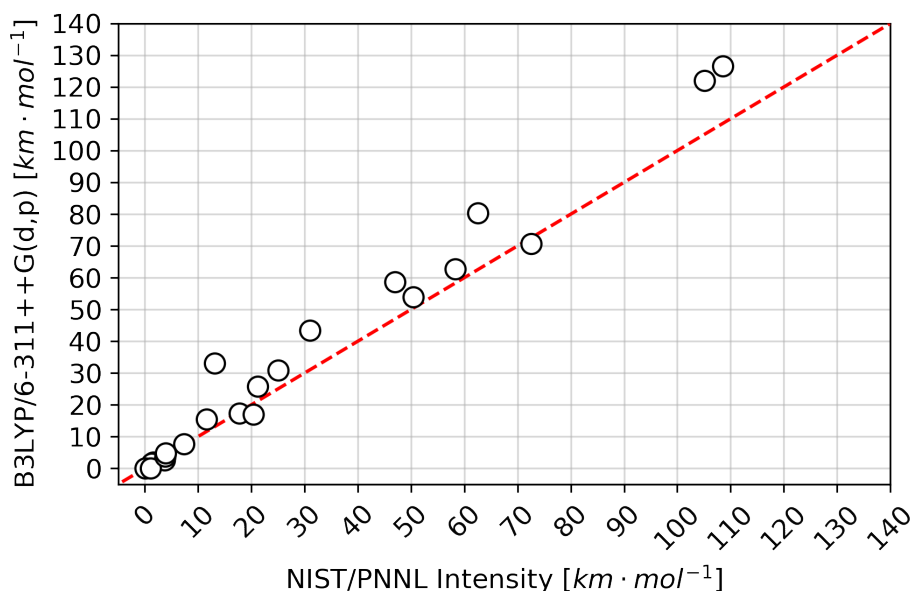


Figure 4.5: Experimental NIST/PNNL intensities versus calculated B3LYP/6-311++G(d,p) intensities (both in $\text{km} \cdot \text{mol}^{-1}$).

contributions to the fundamental intensities. The QTAIM/CCTDP total intensity is a sum of the charge, \mathcal{A}_{C^2} , dipolar polarization \mathcal{A}_{DP^2} , and charge-polarization interaction terms, \mathcal{A}_{2CDP} , as specified by equation 4.7. These values are given in the first columns of Table 4.1 with their sum in the fifth column. As can be seen there, the agreement with the B3LYP/6-311++(d,p) values is excellent with a RMSE of only $2.1 \text{ km} \cdot \text{mol}^{-1}$, confirming the validity of the assumption that the dynamic hydrogen intensity contributions are sufficient for estimating the total intensities.

The dipolar polarization contributions are much larger than the charge contributions for most of these out-of-plane CH bends. In fact, the polarization contribution and its interaction with the charge explains almost all of the total intensities. The agreement is excellent with a small $4.6 \text{ km} \cdot \text{mol}^{-1}$ RMSE. The largest deviation occurs for the 755 cm^{-1} band of fluorobenzene for which the polarization terms sum to $67.0 \text{ km} \cdot \text{mol}^{-1}$ and the total calculated intensity is $81.2 \text{ km} \cdot \text{mol}^{-1}$. This is expected as the very electronegative fluorine atom tends to drain electrons from its next-neighbour hydrogen atoms

resulting in the largest charge contribution in Table 4.1, $14.1 \text{ km} \cdot \text{mol}^{-1}$.

Figure 4.6 shows a comparison involving the individual charge, polarization, and their interaction contributions to the calculated intensities. The charge contributions are much smaller than the dipolar polarization contributions. The charge–polarization interactions are only large owing to their larger dipolar polarization factors. Even the largest charge contribution in Table 4.1 for the “q” mode of fluorobenzene vibration is about half the size of its polarization contribution. This is one of the few substituted benzene vibrations for which this interaction term is greater than the dipolar polarization one.

Table 4.1: CCTDP contributions and their sums for the CH out-of-Plane bending intensities (in $\text{km} \cdot \text{mol}^{-1}$) and estimates made with simpler models

| Molecule | Mode | CCTDP Model | | | | | Simple Model | | |
|---------------------|------|---------------------|----------------------|----------------------|---|---------------------|--------------|---------------|---------------------|
| | | \mathcal{A}_{C^2} | \mathcal{A}_{DP^2} | \mathcal{A}_{2CDP} | $\mathcal{A}_{DP^2} + \mathcal{A}_{2CDP}$ | \mathcal{A}_{oop} | Equation 4.9 | Equation 4.10 | Carbon contribution |
| 1,2-Dichlorobenzene | a | 5.68 | 36.48 | 28.80 | 65.29 | 71.02 | 72.96 | 71.67 | 78.29 |
| | b | 0.70 | 0.34 | 0.92 | 1.26 | 2.01 | 2.05 | 3.05 | 3.33 |
| | c | 3.00 | 5.88 | 8.32 | 14.20 | 17.30 | 26.10 | 30.67 | 33.50 |
| 1,3-Dichlorobenzene | d | 3.70 | 22.21 | 18.20 | 40.37 | 44.06 | 40.67 | 41.10 | 44.90 |
| | e | 2.96 | 4.76 | 7.41 | 12.17 | 15.13 | 14.04 | 18.16 | 19.84 |
| | f | 0.05 | 0.02 | 0.03 | 0.05 | 0.17 | 0.03 | 0.32 | 0.35 |
| 1,4-Dichlorobenzene | g | 7.80 | 23.78 | 27.10 | 50.86 | 59.00 | 60.77 | 63.63 | 69.51 |
| | h | 0.86 | 23.31 | 8.94 | 32.25 | 33.11 | 37.32 | 35.79 | 39.10 |
| Benzaldehyde | i | 6.32 | 25.54 | 25.40 | 50.91 | 57.25 | 57.84 | 54.63 | 59.68 |
| | j | 6.56 | 1.55 | -6.31 | -4.76 | 1.84 | 2.04 | 2.32 | 2.53 |
| Benzene | k | 1.86 | 100.90 | 27.40 | 128.34 | 130.22 | 129.45 | 128.85 | 140.75 |
| | l | 1.75 | 14.20 | 10.00 | 24.20 | 25.95 | 31.18 | 32.96 | 36.00 |
| Chlorobenzene | m | 2.87 | 38.72 | 21.00 | 59.72 | 62.73 | 61.57 | 58.18 | 63.55 |
| | n | 0.68 | 0.88 | 1.42 | 2.30 | 3.19 | 2.60 | 3.95 | 4.31 |
| | o | 0.05 | 0.05 | 0.06 | 0.11 | 0.18 | 0.04 | 0.03 | 0.03 |
| Fluorobenzene | p | 0.18 | 21.73 | -4.07 | 17.66 | 17.84 | 20.63 | 26.28 | 28.71 |
| | q | 14.14 | 27.54 | 39.4 | 66.97 | 81.20 | 64.88 | 65.79 | 71.87 |
| | r | 4.75 | 0.68 | 3.51 | 4.19 | 9.04 | 3.59 | 8.18 | 8.94 |
| Nitrobenzene | s | 0.01 | 0.13 | -0.04 | 0.09 | 0.14 | 0.02 | 0.22 | 0.24 |
| | t | 0.24 | 28.41 | 5.07 | 33.48 | 33.87 | 49.12 | 44.72 | 48.85 |
| | u | 3.41 | 0.07 | 0.81 | 0.88 | 4.38 | 4.15 | 7.38 | 8.06 |
| Naphthalene | v | 2.06 | 99.32 | 28.70 | 127.98 | 130.26 | 118.53 | 110.07 | 120.24 |
| | w | 0.08 | 3.63 | 0.98 | 4.61 | 4.71 | 5.18 | 4.07 | 4.45 |

4.2.3 L-Matrix Element Dependence

Figure 4.7 shows the directions of the displacements of all the ring hydrogens in all the 23 out-of-plane vibrations. Note that, in comparison with Figure 4.6, the vibrations where all hydrogen atoms are vibrating in phase and moving in the same direction usually have larger dipolar polarization contributions. If the hydrogens all move above the benzene ring, the individual dipolar polarizations of the electronic densities will sum constructively, resulting in a larger dipole moment change. On the other hand, if the hydrogens move in opposite directions, the atomic dipolar polarizations will cancel each

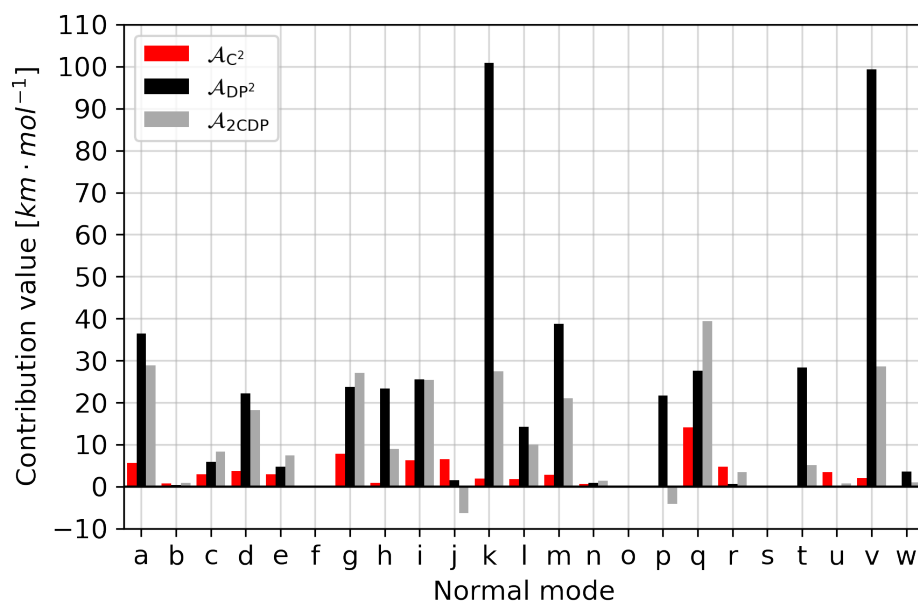


Figure 4.6: Static charge \mathcal{A}_{C^2} , dipolar polarization \mathcal{A}_{DP^2} , and interaction \mathcal{A}_{2CDP} contributions for all vibrational modes. Note the predominance of the dipolar polarization terms.

other, resulting in a small intensity. This is especially evidenced by the “a” and “b” vibrations of 1,2-chlorobenzene. Mode “a” has all the hydrogens moving in the same direction so the dipolar polarization vectors sum constructively, but mode “b” has two hydrogens moving above the ring while two hydrogens are moving below it, so their contributions to the dipole moment change will cancel, resulting in a much smaller polarization contribution and intensity.

By far, the largest polarization values occur for benzene and naphthalene. The benzene vibration, of course, has all six CH bonds bending in the same direction, resulting in a $128 \text{ km} \cdot \text{mol}^{-1}$ intensity contribution. Naphthalene has two out-of-plane CH bending vibrations. The one with eight CH bendings in the same direction has a polarization value about the same as that of benzene. Its other vibration has four CH bonds bending in a direction opposite to the other four. Its total polarization contribution is only $3.6 \text{ km} \cdot \text{mol}^{-1}$. All the vibrations having appreciable polarization contributions between 20 and $40 \text{ km} \cdot \text{mol}^{-1}$ have CH bendings predominantly in the same direction whereas those with contributions less than $5 \text{ km} \cdot \text{mol}^{-1}$ have CH bendings in opposite directions.

It appears that the out-of-plane CH bending dipole moment derivatives increase with the net sum of the hydrogen atom displacements. This is indeed true, as can be seen in Figure 4.8 where the square roots of the intensities calculated at the B3LYP/6-311++G(d,p) level are plotted against the sum of the hydrogen atom displacements perpendicular to the benzene plane. The correlation coefficient between these values is 0.979 and the regression line has a slope of $4.7 \text{ km}^{\frac{1}{2}} \cdot \text{mol}^{-\frac{1}{2}} \cdot \text{amu}^{\frac{1}{2}}$ and an intercept that passes through the origin. As a test of this relation, the B3LYP intensities of the out-of-plane vibrational modes of seven different molecules with N-fused benzene rings ($N = 3, 4, 5$), represented in Figure 4.9, have been included in the graph of Figure 4.8. For this test set, the net sums of the perpendicular hydrogen displacements were able to predict the intensities with a root-mean-square error of only $1.22 \text{ km}^{\frac{1}{2}} \cdot \text{mol}^{-\frac{1}{2}} \cdot \text{amu}^{\frac{1}{2}}$.

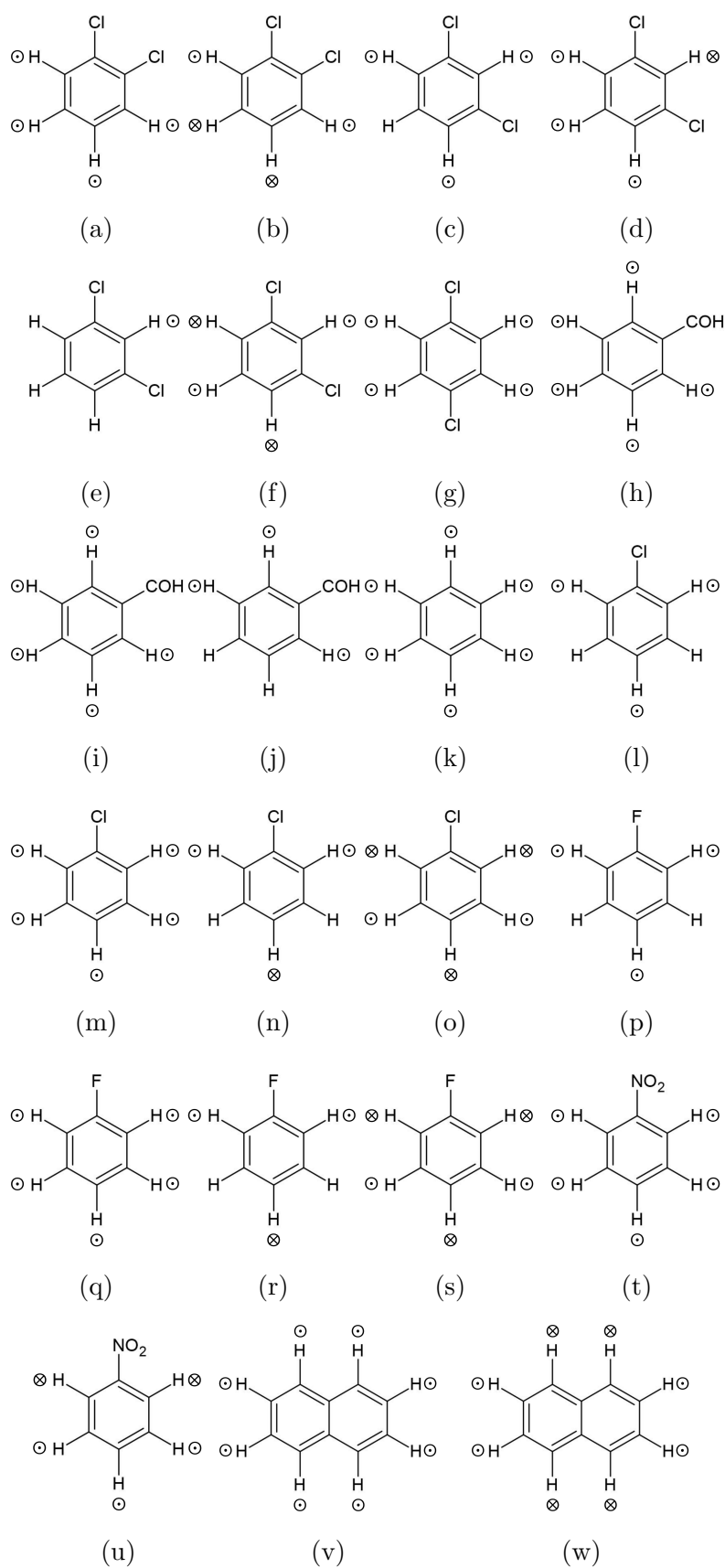


Figure 4.7: Schematic representation of the 23 out-of-plane vibrations investigated in this section. \odot and \otimes indicates, respectively, out-of-plane displacements in the positive and negative direction of z axis.

This excellent linear fit suggests that the electronic factors causing the CH out-of-plane intensities for the substituted benzenes are very similar.

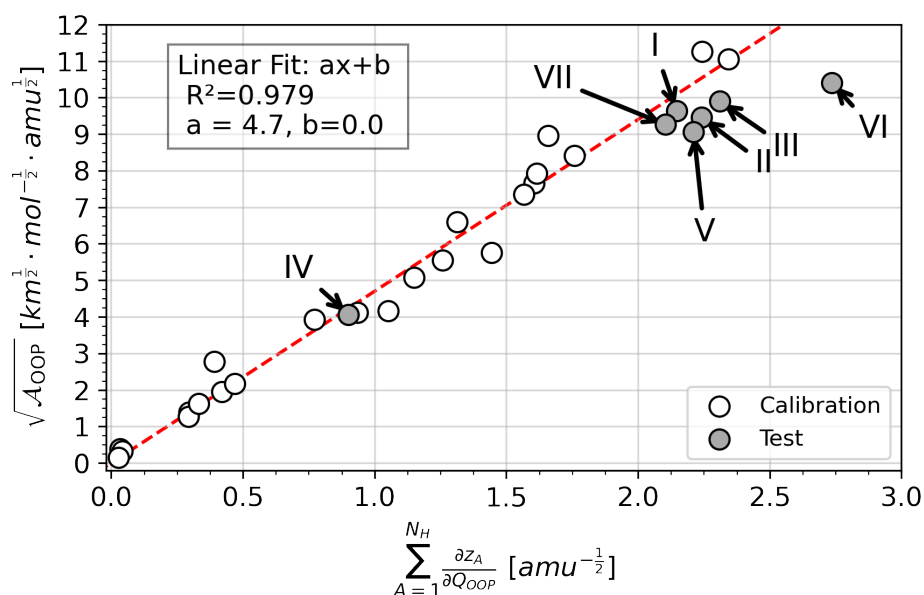


Figure 4.8: Linear dependence of square root of experimental intensities and the sum of the hydrogen out-of-plane displacements. The linear regression is expressed in the form $y = ax + b$. The white dots are the 23 vibrational modes in Figures 4.7 2. The grey dots are the test set listed in Figure 4.9.

4.2.4 A Simple Model

Examination of the values of the individual terms in equation 4.5 shows that the CCTDP model can be further simplified. Dipole moment changes owing to polarizations of the substituent atoms are small for the out-of-plane CH bends and can be neglected. For this reason, the electron density changes for the out-of-plane CH bends can be simply described by displacements of the hydrogen static charges and the atomic dipole changes on the hydrogen and carbon atoms. As such equation 4.5 takes the form:

$$\frac{\partial p_z}{\partial Q_{oop}} = \sum_{A=1}^{N_H} \left(q_A + \sum_{B=1}^{N_H} \frac{\partial m_{B,z}}{\partial z_A} + \sum_{C=1}^{N_C} \frac{\partial m_{C,z}}{\partial z_A} \right) \frac{\partial z_A}{\partial Q_{oop}} \quad (4.8)$$

where N_C and N_H are the total number of these carbon and hydrogen atoms. Notice that A and B are dummy variables for hydrogen labels and C is the dummy variable for carbon atom labels. The derivatives of the atomic dipoles in this equation are of two types, polarizations of the carbon and hydrogen atoms involved in the CH bend and those polarizations owing to the other atoms in the aromatic ring. The latter are calculated to be very small and provide negligible contributions to the infrared intensities, except for the polarization terms of the two nearest neighbour carbon atoms directly bonded to the displaced CH bond $\left(\frac{\partial m_{nbr_{A,z}}}{\partial z_A} \right)$. So, equation 4.8 can be simplified even more.

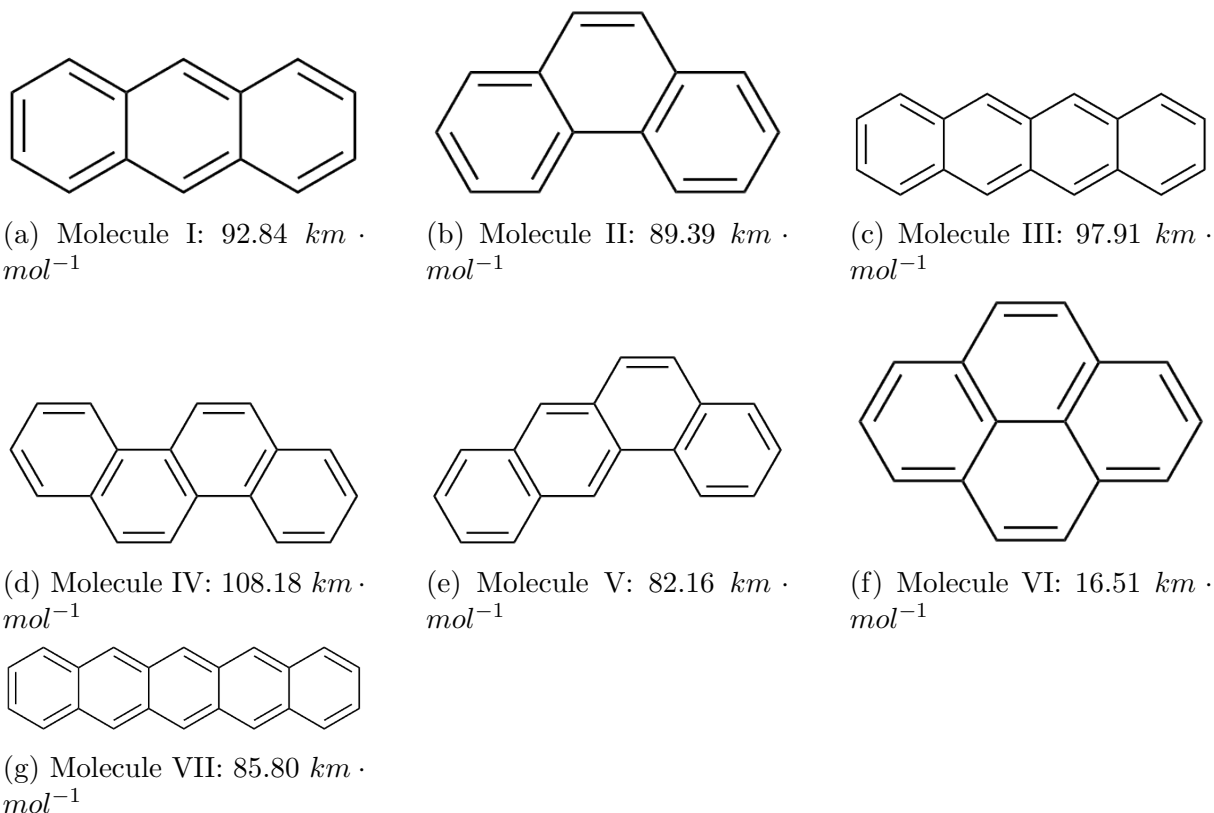


Figure 4.9: N-Fused benzene ring molecules ($N = 3, 4, 5$) and intensities used as test set

$$\frac{\partial p_z}{\partial Q_{oop}} = \sum_{A=1}^{N_H} \left(q_A + \frac{\partial m_{A,z}}{\partial z_A} + \frac{\partial m_{C_{A,z}}}{\partial z_A} + \frac{\partial m_{nbr_{A,z}}}{\partial z_A} \right) \frac{\partial z_A}{\partial Q_{oop}} \quad (4.9)$$

with $\frac{\partial m_{C_{A,z}}}{\partial z_A}$ being the polarization of the carbon atom bonded to the displaced hydrogen.

The terms in parenthesis are contributions to elements of the atomic polar tensor of the substituted benzenes. These quantities are presented in Table 4.2 for hydrogen and the ring carbon atoms bonded to hydrogen and their neighbouring carbon atoms. The hydrogen atom charges are very similar with an average of $0.036 \pm 0.018 e$. The atomic polarization derivatives for carbon have an average of $0.214 e$ with a 7% standard deviation, $0.016 e$. The hydrogen atomic dipole moment derivatives are also almost constant, $-0.043 \pm 0.002 e$. The same can be said about the neighbouring carbon atom derivatives, which is $-0.052 \pm 0.007 e$.

These standard deviations for the electronic parameters are all less than $0.02 e$, indicating they are transferable among the substituted benzenes. As such, the model can use average values moving the electronic factors out from the sum in equation 4.9:

$$\frac{\partial p_z}{\partial Q_{oop}} = \left(\overline{q_A} + \frac{\overline{\partial m_{A,z}}}{\partial z_A} + \frac{\overline{\partial m_{C_{A,z}}}}{\partial z_A} + \frac{\overline{\partial m_{nbr_{A,z}}}}{\partial z_A} \right) \sum_{A=1}^{N_H} \frac{\partial z_A}{\partial Q_{oop}} \quad (4.10)$$

These average values can be used to estimate all the intensities of the 23 out-of-plane vibrations. The intensities of the CH out-of-plane bending modes of the substituted benzenes can be expressed by the sum of only four transferable electronic parameters,

Table 4.2: Equilibrium charge of hydrogen atoms and atomic polarization dipole moment derivatives (in units of e) with respect to hydrogen atom displacements.

| Molecule | q_A | $\frac{\partial m_{A,z}}{\partial z_A}$ | $\frac{\partial m_{C_{A,z}}}{\partial z_A}$ | $\frac{\partial m_{nbr_{A,z}}}{\partial z_A}$ |
|---------------------|-------|---|---|---|
| 1,2-Dichlorobenzene | 0.051 | -0.043 | 0.200 | -0.046 |
| | 0.033 | -0.043 | 0.214 | -0.061 |
| | 0.033 | -0.043 | 0.225 | -0.061 |
| | 0.051 | -0.043 | 0.199 | -0.047 |
| 1,3-Dichlorobenzene | 0.051 | -0.045 | 0.203 | -0.045 |
| | 0.038 | -0.041 | 0.210 | -0.060 |
| | 0.051 | -0.045 | 0.210 | -0.049 |
| | 0.070 | -0.045 | 0.183 | -0.033 |
| 1,4-Dichlorobenzene | 0.054 | -0.043 | 0.194 | -0.047 |
| | 0.054 | -0.043 | 0.199 | -0.049 |
| | 0.054 | -0.043 | 0.194 | -0.047 |
| | 0.054 | -0.043 | 0.199 | -0.049 |
| Benzaldehyde | 0.028 | -0.042 | 0.219 | -0.053 |
| | 0.026 | -0.043 | 0.226 | -0.049 |
| | 0.063 | -0.048 | 0.185 | -0.052 |
| | 0.029 | -0.042 | 0.218 | -0.056 |
| Benzene | 0.029 | -0.041 | 0.218 | -0.057 |
| | 0.017 | -0.042 | 0.226 | -0.053 |
| | 0.017 | -0.042 | 0.237 | -0.053 |
| | 0.017 | -0.042 | 0.235 | -0.053 |
| | 0.017 | -0.042 | 0.226 | -0.053 |
| Chlorobenzene | 0.017 | -0.042 | 0.237 | -0.053 |
| | 0.045 | -0.044 | 0.207 | -0.044 |
| | 0.028 | -0.042 | 0.219 | -0.057 |
| | 0.028 | -0.042 | 0.213 | -0.057 |
| Fluorobenzene | 0.045 | -0.044 | 0.208 | -0.044 |
| | 0.025 | -0.043 | 0.226 | -0.055 |
| | 0.049 | -0.046 | 0.216 | -0.038 |
| | 0.028 | -0.042 | 0.218 | -0.056 |
| Nitrobenzene | 0.028 | -0.042 | 0.213 | -0.056 |
| | 0.049 | -0.046 | 0.221 | -0.038 |
| | 0.023 | -0.044 | 0.231 | -0.054 |
| | 0.038 | -0.042 | 0.202 | -0.057 |
| Naphtalene | 0.087 | -0.052 | 0.174 | -0.040 |
| | 0.087 | -0.051 | 0.174 | -0.040 |
| | 0.038 | -0.042 | 0.209 | -0.058 |
| | 0.036 | -0.042 | 0.209 | -0.059 |
| | 0.017 | -0.042 | 0.229 | -0.054 |
| | 0.019 | -0.043 | 0.229 | -0.055 |
| | 0.017 | -0.042 | 0.225 | -0.056 |
| | 0.017 | -0.042 | 0.228 | -0.054 |
| Average | 0.036 | -0.043 | 0.214 | -0.052 |
| Std. Dev. | 0.018 | 0.002 | 0.016 | 0.007 |

the displaced equilibrium hydrogen charge, and the carbon and hydrogen atomic dipole derivatives of the bent CH bonds and their nearest neighbour carbon dipole derivatives, multiplied by the sum of the amplitudes of the perpendicular displacements of the hydrogen atoms out of the benzene ring plane for the normal coordinate.

The results of equation 4.9 are given in the third last column of Table 4.1 and those assuming transferability, equation 4.10, in the second last column. The results using the individual electronic parameters have an rms difference $6.0 \text{ km} \cdot \text{mol}^{-1}$ when compared with the B3LYP/6-311++(d,p) intensities. On assuming transferability this difference is only $1.1 \text{ km} \cdot \text{mol}^{-1}$ higher, $7.1 \text{ km} \cdot \text{mol}^{-1}$, an increase much less than the expected experimental error.

Accurate intensity estimates can also be made using only the electronic parameters of the carbon atoms as the hydrogen charge displacement ($0.036 e$) and its dipolar polarization ($-0.43 e$) almost cancel each other. These values are given in the last column of Table 4.1. As can be seen there, the estimated intensities using only the carbon atom parameters are all 9.2% higher than those calculated with all the parameters of equation 4.10.

4.2.5 The Origins of the Rehybridization Moment

The rehybridization moment during the out-of-plane vibration consists of changes that occur in the electron density of the CH bond when the sp^2 carbon is forced into a nonplanar configuration, which tends toward sp^3 geometry as the hydrogen atom moves out of the molecular plane. Steele and Wheatley[98] defined the rehybridization moment as the difference between the dipole moment derivative of the out-of-plane vibration (a_{2u}) and the in-plane vibration (e_{1u}), and they obtained a value of $0.3 \text{ D} \cdot \text{radian}^{-1}$. This value agrees with the results of Spedding and Whiffen[96]. They found a CH dipole moment of $0.61 \text{ D} \cdot \text{radian}^{-1}$ for the a_{2u} mode and $0.3 \text{ D} \cdot \text{radian}^{-1}$ for the e_{1u} modes.

From our proposed model, the dipole moment derivative for the a_{2u} mode can be obtained using the terms in parenthesis of equation 4.10, as show in Figure 4.10. Considering a displacement of 15° for the CH bond out of the plane of the aromatic ring, taking the projection along z , multiplying by and finally dividing by the displaced angle, we obtain a value of $0.80 \text{ D} \cdot \text{radian}^{-1}$, which is slightly higher than the value of $0.69 \text{ D} \cdot \text{radian}^{-1}$ found by Cole and Michell[104], which was obtained from an average of 51 aromatic compounds.

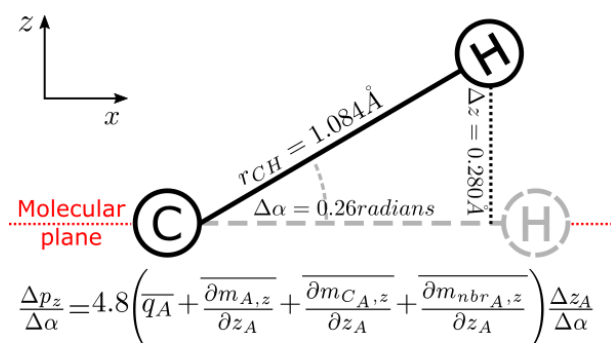


Figure 4.10: The dipole moment of the CH bond for the out-of-plane vibration can be obtained from the angular coefficient of Equation 4.10. Here, a displacement of 15° in the z -axis direction was used to estimate the out-of-plane normal coordinate. Converting the values from electron \cdot Angstrom ($e \cdot \text{\AA}$) to Debyes (D), a value of $0.80 D \cdot \text{radians}^{-1}$ was obtained for the bond moment of the CH bond, which is in agreement with literature values mentioned in the text.

Note that the simple model provides a detailed physical interpretation of the rehybridization moment. When the hydrogen of the CH bond moves in the positive direction along the z -axis, the point charges of the CH hydrogen and carbon atoms give rise to a dipole moment, whose magnitude is equal to the first term of the electronic parameter coefficient of the model described by equation 4.10. This dipole moment is almost completely canceled by the hydrogen dipolar polarization, the second term in the model. This phenomenon is accompanied by the appearance of a large atomic dipole moment that emerges as the sp^2 orbital tends toward the nonplanar sp^3 geometry. The magnitude of this dipole moment corresponds to the third term inside the parenthesis of equation 4.10. Once the carbon atom of the displaced CH bond is polarized, it induces polarizations on the neighbouring carbon atoms in the opposite direction (last term inside the brackets of equation 4.10). The total rehybridization moment is then described as the resultant of these four effects. This interpretation is summarized in Figure 4.11.

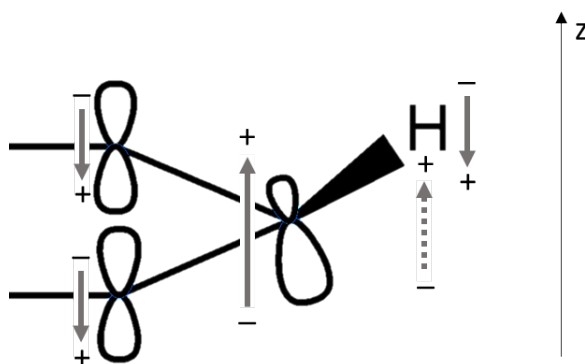


Figure 4.11: Components of the rehybridization moment (not to scale): The dashed arrow indicates the point charge contribution and the solid arrows indicate the atomic dipole moment contributions

4.2.6 Benzene and Hexafluorobenzene

The intensity of the out-of-plane CH bending in benzene is $130 \text{ km} \cdot \text{mol}^{-1}$, whereas the intensity for the CF bending in hexafluorobenzene is below $5 \text{ km} \cdot \text{mol}^{-1}$. In Chapter 3, the difference between the CH and CF out-of-plane bending was associated with the large negative atomic charge of fluorine. Considering the components of the rehybridization moment, displacements of the fluorine atoms in the positive z direction results in a charge contribution pointing in the negative direction, in contrast to the positive contribution in benzene, annihilating the polarization contribution from the carbon atoms.

4.2.7 Notes on Anharmonicity

In this chapter, it was shown that within the harmonic approximation the charge-transfer contribution for out-of-plane bending of planar molecules is always equal to zero due to symmetry constraints, i.e. any infinitesimal change in atomic charges during the vibration will be the same for both the positive and negative phases of the normal coordinate, making the dipole moment derivative equal to zero at the equilibrium. However, when anharmonicity is to be considered, one needs to include the second derivative of the molecular dipole moment with respect to the normal coordinate. Although the first derivative of charge is equal to zero, that is not necessarily true for the second derivative.

Starting with equation 4.1, the second derivative of the molecular dipole moment is:

$$\frac{\partial^2 p_z}{\partial Q_{oop}^2} = \sum_{A=1}^N \frac{\partial q_A}{\partial Q_{oop}} \frac{\partial z_A}{\partial Q_{oop}} + \sum_{A=1}^N q_A \frac{\partial^2 z_A}{\partial Q_{oop}^2} + \sum_{A=1}^N \frac{\partial z_A}{\partial Q_{oop}} \frac{\partial q_A}{\partial Q_{oop}} + \sum_{A=1}^N z_A \frac{\partial^2 q_A}{\partial Q_{oop}^2} + \sum_{A=1}^N \frac{\partial^2 m_{A,z}}{\partial Q_{oop}^2} \quad (4.11)$$

As the charge derivative is equal zero, equation 4.11 is simplified to:

$$\frac{\partial^2 p_z}{\partial Q_{oop}^2} = \sum_{A=1}^N q_A \frac{\partial^2 z_A}{\partial Q_{oop}^2} + \sum_{A=1}^N z_A \frac{\partial^2 q_A}{\partial Q_{oop}^2} + \sum_{A=1}^N \frac{\partial^2 m_{A,z}}{\partial Q_{oop}^2} \quad (4.12)$$

since the system is closed, no charge can leave the system, so the sum of the atomic charge second derivatives becomes:

$$\sum_{A=1}^N \frac{\partial^2 q_A}{\partial Q_{oop}^2} = 0 \quad (4.13)$$

solving equation 4.13 for atom $A = 1$ and substituting in equation 4.14:

$$\frac{\partial^2 p_z}{\partial Q_{oop}^2} = \sum_{A=1}^N q_A \frac{\partial^2 z_A}{\partial Q_{oop}^2} + \sum_{A=2}^N (z_A - z_1) \frac{\partial^2 q_A}{\partial Q_{oop}^2} + \sum_{A=1}^N \frac{\partial^2 m_{A,z}}{\partial Q_{oop}^2} \quad (4.14)$$

For a planar molecule, $z_A - z_1$ is always zero. Therefore, the anharmonic charge-transfer

term is also zero, that is:

$$\frac{\partial^2 p_z}{\partial Q_{oop}^2} = \sum_{A=1}^N q_A \frac{\partial^2 z_A}{\partial Q_{oop}^2} + \sum_{A=1}^N \frac{\partial^2 m_{A,z}}{\partial Q_{oop}^2} \quad (4.15)$$

The same derivation applies for higher order derivatives.

4.3 IR Intensities of Fundamental Bands for Out-of-Plane bending in Ethylene and Dichloro and Difluoroethylenes

Intensities calculated at the M06-2X/aug-cc-pVTZ level for out-of-plane bendings in ethylene, dichloroethylene, difluoroethylene and their deuterated analogues are given in Table 4.3 along with the experimental intensity. Ethylene, with small equilibrium atomic charges of 0.016 and -0.031 e for the hydrogen and carbon atoms has the largest experimental intensity, 82.1 $\text{km} \cdot \text{mol}^{-1}$ [64, 65]. In contrast, *cis*- $\text{C}_2\text{H}_2\text{F}_2$ with larger atomic charges, 0.611 and -0.691 e for carbon and fluorine, has less than half the ethylene intensity, 29.6 $\text{km} \cdot \text{mol}^{-1}$. The CH and CD bending intensities of 1,1-difluoroethylene [105] have values of 60.3 and 28.9 $\text{km} \cdot \text{mol}^{-1}$ and are much larger than those of the corresponding CF bendings, 0.3 and 5.9 $\text{km} \cdot \text{mol}^{-1}$. Similar behaviour is found for the out-of-plane bendings of *trans*- $\text{C}_2\text{H}_2\text{F}_2$ and $\text{C}_2\text{D}_2\text{F}_2$, for which the CH and CD intensities are two to four times larger than the values for the CF bendings [106]. The changes in the electron density occurring for the CH and CF bendings are similar to the ones occurring for the out-of-plane bending in benzenes.

The data in Table 4.3 can be classified into three groups, the CH and CD bendings, the CF and CCl bendings and mixed bending modes. The C_2H_4 and high frequency modes of 1,1- and *trans*- $\text{C}_2\text{H}_2\text{F}_2$ and *trans*- $\text{C}_2\text{H}_2\text{Cl}_2$ have experimental intensities ranging from 48.0 to 82.1 $\text{km} \cdot \text{mol}^{-1}$. Experimental CD bending intensities of C_2D_4 , 1,1- and *trans*- $\text{C}_2\text{D}_2\text{F}_2$ range between 27.8 and 44.8 $\text{km} \cdot \text{mol}^{-1}$. These smaller values are expected as the amplitudes of the CD bendings are smaller than those for CH. The range of intensities for the CD vibrations is almost half of the one for CH owing to the larger mass of the deuterium atom. The CF bendings of 1,1- and *trans*- $\text{C}_2\text{H}_2\text{F}_2$ and their deuterated analogues have much smaller experimental intensities ranging from 0.3 to 12.7 $\text{km} \cdot \text{mol}^{-1}$. These values are close to the theoretical value of 4.5 $\text{km} \cdot \text{mol}^{-1}$ calculated for C_2F_4 . The CCl bend of *trans*- $\text{C}_2\text{H}_2\text{Cl}_2$ also has a weak experimental intensity of 0.1 $\text{km} \cdot \text{mol}^{-1}$. Although the experimental intensity has not been measured for the CCl bending vibration of 1,1- $\text{C}_2\text{H}_2\text{Cl}_2$ it does have a small theoretical value of 5.6 $\text{km} \cdot \text{mol}^{-1}$.

The differences between the high CH and CD out-of-plane bending intensities relative to the very low CF and CCl intensities can be understood by examining the theoretical charge and polarization contributions to their dipole moment derivatives. The CH bending intensities are characterized by a small average charge and large dipolar polarizations contributions having the same sign, reinforcing one another and resulting in larger intensity values. On the other hand, the CF bending vibrations have charge

Table 4.3: Total charge and dipolar polarization contributions to the dipole moment derivative and IR intensities $\text{km} \cdot \text{mol}^{-1}$ of out-of-plane bending vibrations of ethylene, tetrafluoroethylene and difluoro- and dichloroethylenes as well their isotopologues. Frequencies (cm^{-1}) and experimental intensities (\mathcal{A}_{exp}) are also reported.

| Molecule | Mode | Freq. | \mathcal{A}_{exp} | \mathcal{A}_{C^2} | $\mathcal{A}_{\text{DP}^2}$ | $\mathcal{A}_{2\text{CDP}}$ | \mathcal{A}_{oop} |
|--|-------|-------|----------------------------|----------------------------|-----------------------------|-----------------------------|----------------------------|
| C_2H_4 | CH | 1002 | 82.1 | 1.1 | 79.1 | 18.9 | 99.0 |
| C_2D_4 | CD | 758 | 44.8 | 0.7 | 45.5 | 10.9 | 57.1 |
| C_2F_4 | CF | 428 | | 396.5 | 316.5 | -708.6 | 4.4 |
| cis- $\text{C}_2\text{H}_2\text{F}_2$ | Mixed | 818 | 29.6 | 2.1 | 68.4 | -23.8 | 46.7 |
| cis- $\text{C}_2\text{D}_2\text{F}_2$ | Mixed | 640 | 17.6 | 14.7 | 70.5 | -64.5 | 20.7 |
| 1,1- $\text{C}_2\text{H}_2\text{F}_2$ | CH | 855 | 60.3 | 10.9 | 27.8 | 34.9 | 73.6 |
| | CF | 648 | 0.3 | 84.8 | 85.4 | -170.1 | 0.1 |
| 1,1- $\text{C}_2\text{D}_2\text{F}_2$ | CD | 716 | 28.9 | 44.6 | 0.6 | -10.4 | 34.8 |
| | CF | 599 | 5.9 | 53.8 | 106.7 | -151.6 | 8.9 |
| trans- $\text{C}_2\text{H}_2\text{F}_2$ | CH | 953 | 56.7 | 2.0 | 49.3 | 19.7 | 71.0 |
| | CF | 343 | 12.7 | 122.8 | 80.2 | -198.5 | 4.5 |
| trans- $\text{C}_2\text{D}_2\text{F}_2$ | CD | 705 | 27.8 | 1.2 | 47.6 | -15.1 | 33.7 |
| | CF | 333 | 12.6 | 116 | 71.5 | -182.2 | 5.3 |
| cis- $\text{C}_2\text{H}_2\text{Cl}_2$ | Mixed | 736 | 35.2 | 7.2 | 20.8 | 24.5 | 52.5 |
| | CH | 928 | | 2.9 | 26.8 | 17.8 | 47.5 |
| 1,1- $\text{C}_2\text{H}_2\text{Cl}_2$ | CCl | 472 | | 0.4 | 3.3 | 2.3 | 6.0 |
| trans- $\text{C}_2\text{H}_2\text{Cl}_2$ | CH | 969 | 48.0 | 13.3 | 14.0 | 27.4 | 54.7 |
| | CCl | 201 | 0.1 | 8.8 | 6.1 | -14.6 | 0.3 |

and dipolar polarization values of opposite signs. These contributions almost completely cancel each other resulting in very small net dipole moment derivatives and IR intensities.

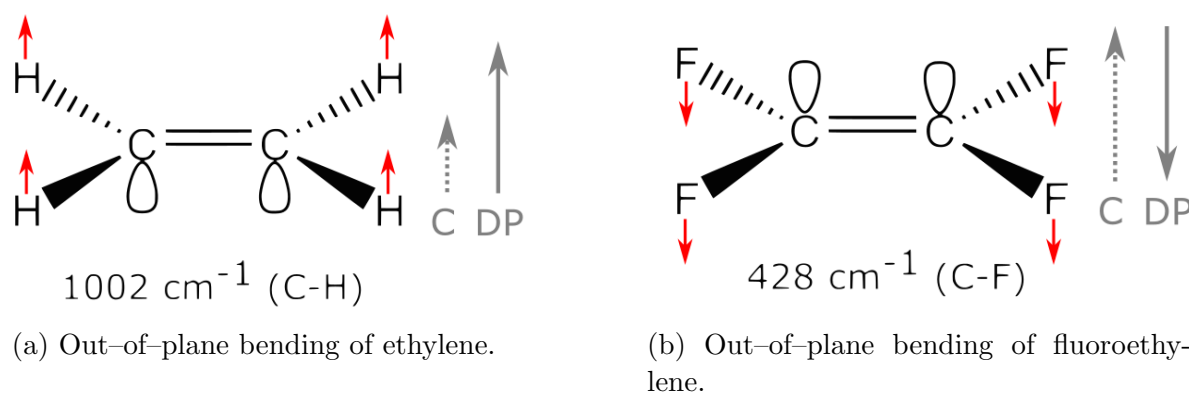


Figure 4.12: Relative displacements of the hydrogen and fluorine atoms with their accompanying carbon atom polarizations for normal coordinates of out-of-plane bendings of ethylene and fluoroethylene. Red arrows indicate the displacement of atoms. Grey arrows indicate the direction of the charge and dipolar polarization contributions.

The polarizations of carbon atom's electron densities of C_2F_4 are of about the same size as those in ethylene although they have negative signs. The positive phase of the normal coordinate has fluorine atom displacements in the negative z direction as shown in Figure 4.12 with polarizations of the carbon electronic densities in the opposite direction. The carbon charge and polarization contributions largely cancel one another and together account for an estimated intensity of $14.7 \text{ km} \cdot \text{mol}^{-1}$. The fluorine atomic charges and polarizations reinforce those on the carbon atoms resulting in a $4.5 \text{ km} \cdot \text{mol}^{-1}$

intensity estimate.

Dipolar Polarization of the carbon atom electron densities in the opposite direction to the displacements of the hydrogen and fluorine atoms of $\text{cis-C}_2\text{H}_2\text{F}_2$ and its deuterated analogue provide the dominant contributions (0.129 and $0.121 e \cdot \text{amu}^{-\frac{1}{2}}$) to their dipole moment derivatives. These are twice the size of all the charge contributions that are between -0.06 and $+0.05 e \cdot \text{amu}^{-\frac{1}{2}}$ for $\text{cis-C}_2\text{H}_2\text{F}_2$ and -0.07 and $+0.03 e \cdot \text{amu}^{-\frac{1}{2}}$ for $\text{cis-C}_2\text{D}_2\text{F}_2$. Even though the fluorine equilibrium charges ($-0.691 e$) are much larger than the hydrogen ones ($+0.080 e$) their contributions to the dipole moment derivatives are smaller owing to their much larger masses resulting in their relatively small vibration amplitudes. The electron density changes for the $\text{cis-C}_2\text{H}_2\text{Cl}_2$ bend are similar to those of $\text{cis-C}_2\text{H}_2\text{F}_2$ except for the smaller chlorine charges and higher atomic masses resulting in a negligible dipole moment derivative contribution of $-0.002 e \cdot \text{amu}^{-\frac{1}{2}}$.

$1,1\text{-C}_2\text{H}_2\text{F}_2$ has two distinct out-of-plane bendings characterized as CH and CF vibrations. The CH bend has larger carbon atom polarizations than any of the charge contributions. By far the larger polarization occurs for the carbon atom of the methylene group, $0.425 e \cdot \text{amu}^{-\frac{1}{2}}$. Its polarization is in the opposite direction to the displaced hydrogen atoms. Dipolar polarization ($-0.141 e \cdot \text{amu}^{-\frac{1}{2}}$) occurs for the other carbon atom bonded to the relatively stationary fluorine atoms. Even this polarization is more than twice as large as any of the charge contributions and the small polarization of the hydrogen and fluorine atoms. In fact, the carbon atoms polarization alone result in an intensity value of $79.0 \text{ km} \cdot \text{mol}^{-1}$, only $5 \text{ km} \cdot \text{mol}^{-1}$ higher than the theoretical values. Dipolar polarization of the carbon atoms also occurs for the CF bending vibration. The electron density of the CF_2 group carbon is polarized in the opposite direction to the displaced neighbouring fluorine atoms ($-0.266 e \cdot \text{amu}^{-\frac{1}{2}}$). For this vibration the large positive charge on the carbon bonded to the electronegative fluorine atoms makes a substantial contribution, $+0.261 e \cdot \text{amu}^{-\frac{1}{2}}$, canceling almost all this carbon polarization consistent with the very small experimental intensity of $0.3 \text{ km} \cdot \text{mol}^{-1}$. Similar dipole moment derivative contributions explain the small theoretical estimate, $6.0 \text{ km} \cdot \text{mol}^{-1}$, of the out-of-plane CCl bend of $1,1\text{-C}_2\text{H}_2\text{Cl}_2$.

The trans isomer has distinct out-of-plane bending vibrations with the CH bend having an intensity more than four times that of the CF bend. The CH bend has a polarization contribution ($0.225 e \cdot \text{amu}^{-\frac{1}{2}}$) about five times larger than the charge one ($0.045 e \cdot \text{amu}^{-\frac{1}{2}}$). In contrast both charge and polarization contributions are large and have opposite signs ($+0.355$ and $-0.287 e \cdot \text{amu}^{-\frac{1}{2}}$) accounting for the small intensity of the CF bend. A similar situation occurs for $\text{trans-C}_2\text{D}_2\text{F}_2$ bendings with negligible charge and large polarization contributions for the CD bend and large-opposite sign contributions for the CF bend.

4.4 The Unavoidable Failure of Point Charges

Considering only point charges, the molecular dipole moment will be given only by the sum of the atomic charges multiplied by the position of the atom. Instead of using equation 1.15, the following applies:

$$\vec{p} = \sum_{A=1}^N q_{\Omega_A} \vec{r}_{\Omega_A} \quad (4.16)$$

this means that the dipole moment derivatives for the out-of-plane bendings will be reduced to only the equilibrium atomic charges, while the models based on charges and dipoles will describe this total derivative as a combination of equilibrium charges and changes in the atomic polarizations. The σ component of the dipole moment derivative with respect to the out-of-plane normal coordinate is:

$$\frac{\partial p_\sigma}{\partial Q_{oop}} = \begin{cases} \sum_{A=1}^N q_A \frac{\partial \sigma_A}{\partial Q_{oop}} & \text{atomic charges only} \\ \sum_{A=1}^N q_A \frac{\partial \sigma_A}{\partial Q_{oop}} + \sum_{A=1}^N \frac{\partial m_{A,\sigma}}{\partial Q_{oop}} & \text{charges and dipoles} \end{cases} \quad (4.17)$$

In order to compare the outcome from these two approaches for intensities of out-of-plane vibrations, the complete IR intensity analyses for ethylene, cis-difluoroethylene, benzene and F₂CO were carried out. Moreover, two linear molecules (CO₂ and HCN) were also included since their angular bendings are also subject to the zero charge transfer constraint. QTAIM[4], Hirshfeld [107], DDEC6 [106], CM5[108], ADCH[109], VDD[110], NPA[111] and CHELPG[112] models were investigated, as multiple representatives for each case of equation 4.17.

QTAIM, Hirshfeld and DDEC6 models will automatically reproduce the dipole moment if both charges and dipoles are employed. ADCH also satisfies the static dipole, but employing only atomic charges, whereas CM5 aims to reproduce the experimental molecular dipole moment, which may not have the same value determined from the wavefunction. Conversely, VDD and NPA charges do not reproduce the molecular dipole moment from the wavefunction. CHELPG parameters were computed under three different situations: point charges, without constraint to reproduce the dipole moment from the wavefunction (labeled CHELPG-q); point charges, but constrained to reproduce the dipole moment (CHELPG-qcd); and atomic charges and atomic dipoles, again constraining the entire set to reproduce the dipole moment (CHELPG-qmcd).

It is important to stress that the inclusion of atomic polarizations does not make the atomic charges and dipoles from QTAIM, Hirshfeld, DDEC6 and CHELPG-qmcd conceptually equivalent. They belong to a common group but their electron density changes can be completely different and even incompatible with one another, depending on the relative magnitudes of their charges and dipoles. The same can be said about the different models with only point charges.

The charges and dipoles from these models were used to calculate the electron density changes accompanying vibrations, in order to determine their infrared intensities. Table 4.4 shows the wavenumbers and intensities for some of the IR active vibrations of ethylene, cis-difluoroethene, benzene, F₂CO and HCN. Only vibrations with intensities larger than 10.00 km · mol⁻¹ were considered so inherent numerical errors will be small compared to the total intensities.

The table was divided and colored in a way to facilitate the interpretation of the results. The second and third columns contains frequency and intensities obtained directly from Gaussian09[25]. Columns 4–7 show the results for the four charge models that employ both atomic charges and atomic dipoles, whereas columns 8–12 show the results from the models employing only atomic charges. The intensities from Gaussian are used as reference. Grey cells show the values that deviate from the reference by at least 8 km · mol⁻¹ from the target values.

It is evident that models including atomic dipoles perform much better. Except for a few results from CHELPG-qmcd, all results approach the target values within

numerical accuracy. Notice that the ways in which these models are defined may be completely different (starting from reference atomic densities and then iterating them for DDEC6 and Hirshfeld, from ESP fit for CHELPG-qmcd and from the topology of the molecular density for QTAIM), but nearly all of them are equally capable of accurately reproducing all these intensities.

A totally different situation is found for the results from the point charge models. CHELPG-q, VDD and NPA charges disagree with the target intensities for almost all vibrations. Only three intensities from CHELPG-q, two from VDD and one from NPA match those from the wavefunctions. This was expected since the IR intensity depends on the derivative of the molecular dipole moment, and if the chosen model cannot reproduce even the static equilibrium dipole moment predicting its derivatives will be even more unlikely. One might expect CM5 charges to perform better than CHELPG-q and VDD, since CM5 charges were developed to reproduce the experimental dipole moment, but this is not the case. Parametrization for the experimental dipole moment prevents these charges from capturing the real modifications in the wavefunctions of the distorted geometries.

Point charge models that reproduce the dipole moment of the wavefunction, CHELPG-qcd and ADCH are capable of accurately calculating the intensities of all vibrations for each molecule but one, specifically the out-of-plane modes (which are in bold face in table 4.4).

The static charges from the equilibrium geometry completely determine the charge contribution in equation 4.17. Since the distortions lead to rearrangements in the electron density, the charges must vary, and the new charges calculated for the distorted geometries are also constrained to agree with the non-equilibrium dipole moments; the difference between these charges and equilibrium ones determines the charge transfer term. Therefore, for in-plane vibrations, combination of charge and charge transfer contributions satisfactorily reproduce the correct dipole moment derivative and thus the correct IR intensity. However, since for out-of-plane vibrations the charge transfer term vanishes, the intensities will be erroneously predicted because the equilibrium charges cannot describe changes in the electron density distribution as the atoms move in the normal coordinate.

The reason why all charge and dipole models can accurately reproduce the IR intensity is evident. Even though the charge transfer term vanishes, there is still an additional degree of freedom available in the form of the dipolar polarization term, which ensures the correct calculation of the dipole moments of distorted geometries and hence the intensities. In other words, explicit consideration of atomic polarizations is necessary for quantitative assessment of IR intensities of out-of-plane vibrations. A general conclusion is that reproducing the dipole moment is a necessary, but not sufficient condition for accurate and meaningful prediction of dipole moment derivatives and IR intensities. The inclusion of atomic dipoles is mandatory for accurate intensity estimates as well as for any study focused on the electron density changes accompanying molecular distortions, including (but not restricted to) vibrations.

Table 4.4: IR wavenumbers (cm^{-1}) and intensities (in $km \cdot mol^{-1}$) from Gaussian and from various charge models. Values in grey presents an error greater than $8 km \cdot mol^{-1}$.

| Molecule | Frequency | Gaussian | QTAIM | Hirshfeld | DDEC6 | CHELPG - qmcd | CHELPG- qcd | CHELPG- q | ADCH | VDD | CM5 | NPA |
|--|---------------|--------------|--------------|--------------|--------------|------------------|----------------|--------------|--------------|-------------|-------------|--------------|
| Ethylene | 3251.4 | 12.6 | 13.9 | 13.8 | 13.8 | 14.8 | 13.8 | 21.3 | 13.8 | 14.7 | 0.1 | 262.1 |
| | 3148.4 | 8.5 | 10.0 | 10.0 | 10.0 | 10.6 | 10.0 | 12.4 | 10.0 | 24.8 | 2.1 | 110.6 |
| | 1476.3 | 10.8 | 10.3 | 10.3 | 10.3 | 9.3 | 10.3 | 4.8 | 10.5 | 0.5 | 0.2 | 38.7 |
| cis-C ₂ H ₂ F ₂ | 1002.1 | 98.1 | 99.2 | 98.0 | 97.6 | 98.1 | 74.3 | 73.9 | 70.4 | 4.3 | 38.1 | 158.2 |
| | 1802.6 | 66.3 | 66.1 | 65.6 | 65.7 | 67.9 | 65.6 | 70.5 | 65.7 | 141.0 | 27.0 | 0.0 |
| | 1413.7 | 35.6 | 36.0 | 37.2 | 37.2 | 41.8 | 37.0 | 28.2 | 36.7 | 37.5 | 28.5 | 0.4 |
| | 1297.1 | 42.4 | 43.4 | 42.7 | 42.7 | 38.6 | 42.8 | 34.6 | 42.2 | 1.0 | 25.2 | 86.8 |
| | 1170.3 | 121.2 | 119.4 | 119.9 | 119.9 | 115.6 | 120.0 | 121.6 | 119.9 | 68.6 | 95.9 | 136.9 |
| | 1054.9 | 65.0 | 64.1 | 64.6 | 64.7 | 65.0 | 64.6 | 75.2 | 64.8 | 148.2 | 30.7 | 45.7 |
| Benzene | 817.9 | 47.2 | 47.0 | 47.5 | 47.5 | 45.9 | 21.9 | 21.2 | 32.1 | 4.5 | 19.1 | 28.5 |
| | 785.2 | 31.7 | 32.1 | 31.9 | 32.0 | 30.8 | 31.9 | 37.5 | 31.9 | 15.9 | 18.1 | 16.5 |
| | 3199.9 | 20.1 | 22.3 | 22.3 | 22.2 | 25.2 | 22.2 | 29.0 | 22.6 | 24.6 | 0.2 | 382.9 |
| | 3198.4 | 19.1 | 21.1 | 22.2 | 22.2 | 18.3 | 22.6 | 27.2 | 22.4 | 901.1 | 0.1 | 380.3 |
| | 699.0 | 112.7 | 115.0 | 112.2 | 112.2 | 107.4 | 40.8 | 46.0 | 101.7 | 11.1 | 59.7 | 271.1 |
| F ₂ CO | 2020.2 | 510.7 | 511.0 | 511.1 | 510.6 | 511.1 | 511.1 | 533.7 | 510.0 | 365.9 | 267.3 | 629.1 |
| | 1301.1 | 429.3 | 430.0 | 429.4 | 429.4 | 429.3 | 429.4 | 451.2 | 428.8 | 330.5 | 279.8 | 542.5 |
| | 1010.9 | 59.9 | 59.9 | 60.0 | 60.0 | 59.9 | 59.9 | 59.7 | 59.9 | 55.5 | 41.9 | 62.7 |
| CO ₂ | 798.0 | 42.0 | 42.2 | 42.0 | 41.9 | 41.8 | 83.2 | 83.8 | 18.9 | 15.1 | 19.6 | 134.9 |
| | 2433.5 | 803.2 | 803.1 | 802.6 | 801.8 | 803.0 | 802.7 | 859.2 | 800.8 | 561.7 | 391.3 | 1109.5 |
| HCN | 694.2 | 36.9 | 37.0 | 37.0 | 36.9 | 36.4 | 69.1 | 70.3 | 17.5 | 17.1 | 20.4 | 118.8 |
| | 3466.3 | 70.7 | 72.6 | 72.4 | 72.7 | 69.0 | 73.2 | 63.9 | 72.4 | 255.5 | 79.0 | 432.2 |
| | 785.4 | 34.1 | 33.9 | 34.1 | 34.0 | 30.9 | 16.7 | 14.9 | 52.8 | 12.6 | 15.6 | 25.8 |

4.5 The Rehybridization Moment in Boron Trihalides

Although the existence of the rehybridization dipole moment has been discussed so far in terms of the carbon atom, the same approach can be taken for any planar molecule. In this section, the out-of-plane bendings of boron trihalides (and borane) will be investigated. Figure 4.13 presents the atom positioning and numbering scheme utilized here. As the molecular plane of all molecules is the xy plane, the only elements of the \mathbf{L} matrix that are not null are those in the z direction. Expanding these terms equation 4.1 then becomes

$$\begin{aligned} \frac{\partial p_z}{\partial Q_{oop}} = & q_B \frac{\partial z_B}{\partial Q_{oop}} + \frac{\partial m_{B,z}}{\partial z_B} \frac{\partial z_B}{\partial Q_{oop}} + \frac{\partial m_{X_1,z}}{\partial z_B} \frac{\partial z_B}{\partial Q_{oop}} + \\ & \frac{\partial m_{X_2,z}}{\partial z_B} \frac{\partial z_B}{\partial Q_{oop}} + \frac{\partial m_{X_3,z}}{\partial z_B} \frac{\partial z_B}{\partial Q_{oop}} + \dots + q_{X_3} \frac{\partial z_{X_3}}{\partial Q_{oop}} + \\ & \frac{\partial m_{B,z}}{\partial z_{X_3}} \frac{\partial z_{X_3}}{\partial Q_{oop}} + \frac{\partial m_{X_2,z}}{\partial z_{X_3}} \frac{\partial z_{X_3}}{\partial Q_{oop}} + \frac{\partial m_{X_3,z}}{\partial z_{X_3}} \frac{\partial z_{X_3}}{\partial Q_{oop}} + \frac{\partial m_{X_3,z}}{\partial z_{X_3}} \frac{\partial z_{X_3}}{\partial Q_{oop}} \end{aligned} \quad (4.18)$$

notice that the subscripts correspond to the atomic symbols as showed in Figure 4.13.

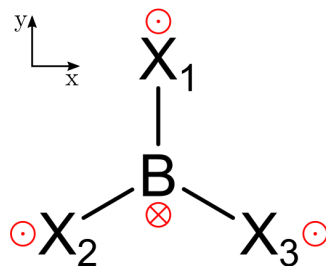


Figure 4.13: Out-of-plane normal coordinates of boron trihalides and borane. $X = \text{F, Cl, Br or H}$.

To simplify the analysis and reduce the number of terms, the \mathbf{L} matrix elements are transformed by considering only the relative displacements of atoms with respect to the position of the boron atom. In doing so, the boron equilibrium charge contributions become equal to zero and its original displacement values are redistributed into those of the X_i atoms. The relative displacement terms, $\frac{\partial z'_B}{\partial Q_{oop}}$ and $\frac{\partial z'_{X_i}}{\partial Q_{oop}}$, are defined as:

$$\frac{\partial z'_B}{\partial Q_{oop}} = 0 \text{ and } \frac{\partial z'_{X_i}}{\partial Q_{oop}} = \frac{\partial z_{X_i}}{\partial Q_{oop}} - \frac{\partial z_B}{\partial Q_{oop}} \text{ for } i = 1, 2, 3 \quad (4.19)$$

The dipole moment derivative can, then, be approximated by

$$\begin{aligned} \frac{\partial p_z}{\partial Q_{oop}} \approx & \sum_{i=1}^3 \frac{\partial m_{B,z}}{\partial z_{X_i}} \frac{\partial z'_{X_i}}{\partial Q_{oop}} + q_{X_1} \frac{\partial z'_{X_1}}{\partial Q_{oop}} + \sum_{i=1}^3 \frac{\partial m_{X_1,z}}{\partial z_{X_i}} \frac{\partial z'_{X_i}}{\partial Q_{oop}} + \\ & q_{X_2} \frac{\partial z'_{X_2}}{\partial Q_{oop}} + \sum_{i=1}^3 \frac{\partial m_{X_2,z}}{\partial z_{X_i}} \frac{\partial z'_{X_i}}{\partial Q_{oop}} + q_{X_3} \frac{\partial z'_{X_3}}{\partial Q_{oop}} + \sum_{i=1}^3 \frac{\partial m_{X_3,z}}{\partial z_{X_i}} \frac{\partial z'_{X_i}}{\partial Q_{oop}} \end{aligned} \quad (4.20)$$

The first term on the right-hand side of equation 4.20 corresponds to the polarization derivative of the sp^2 central atom, B, that is forced to assume a sp^3 -like geometry for out-of-plane displacements of the terminal atoms.

Table 4.5 presents the intensities determined by the quantum chemical parameters of equation 4.18 and the approximate intensities from equation 4.20. This transformation is exact, although the \mathbf{L} matrix elements are calculated within a molecular-fixed coordinate system and the use of relative displacements is equivalent to using a space-fixed system with the boron atom always at its origin, which does not suffice the Eckart conditions. The RMSE for the approximate intensities is very small, $0.64 \text{ km} \cdot \text{mol}^{-1}$ (or 0.18% of the average intensity). The BF_3 intensities calculated at the QCISD/aug-cc-pVTZ level

Table 4.5: CCTDP (\mathcal{A}_{oop}), approximate and decision tree transferred intensities (in $\text{km} \cdot \text{mol}^{-1}$) of boron halides and borane.

| Molecule | Freq. | \mathcal{A}_{oop} | Equation 4.20 | Decision tree model |
|-------------------------|---------|----------------------------|---------------|---------------------|
| BH_3 | 1162.43 | 81.76 | 81.77 | 81.77 |
| BF_3 | 697.52 | 106.05 | 105.05 | 104.89 |
| BCl_3 | 460.11 | 6.26 | 5.75 | 6.03 |
| BBr_3 | 393.64 | 0.75 | 0.91 | 0.91 |
| BH_2F | 1097.60 | 74.80 | 77.85 | 76.49 |
| BHF_2 | 944.07 | 74.04 | 75.09 | 77.06 |
| BH_2Cl | 1014.37 | 28.54 | 27.35 | 26.85 |
| BHCl_2 | 800.87 | 12.63 | 12.32 | 13.53 |
| BH_2Br | 990.40 | 21.11 | 19.96 | 19.43 |
| BHBr_2 | 752.30 | 6.98 | 6.93 | 8.02 |
| BF_2Cl | 607.40 | 51.74 | 48.26 | 53.20 |
| BFCl_2 | 530.46 | 21.96 | 23.31 | 21.44 |
| BF_2Br | 576.64 | 41.07 | 37.34 | 35.00 |
| BFBr_2 | 478.60 | 10.39 | 10.02 | 11.90 |
| BCl_2Br | 437.50 | 3.64 | 2.67 | 2.45 |
| BClBr_2 | 415.23 | 1.69 | 2.16 | 0.00 |
| | | RMSE | 0.64 | 2.10 |

are in excellent agreement with experimental results. An out-of-plane experimental intensity value[113] of $108.8 \text{ km} \cdot \text{mol}^{-1}$ measured from the gas phase high-resolution spectra of the NIST/PNNL library is very close to the theoretical estimate of $106.1 \text{ km} \cdot \text{mol}^{-1}$. The experimental in-plane stretching[113] and bending[114] intensities of 871.3 and $27.1 \text{ km} \cdot \text{mol}^{-1}$ are in very good agreement with the QCISD/aug-cc-pVTZ values, 888.7 and $27.3 \text{ km} \cdot \text{mol}^{-1}$. As such, it appears that this theoretical level adequately describes the electron density changes owing to the BF_3 vibrations. The BCl_3 and BBr_3 experimental intensity data are limited but their stretching intensities of 700.8 and $555.6 \text{ km} \cdot \text{mol}^{-1}$ are in good agreement with the QCISD/aug-cc-pVTZ results of 703.76 and $570.56 \text{ km} \cdot \text{mol}^{-1}$.

Table 4.6 shows the charge, dipolar polarization, and their interaction contributions for each molecule and the average sums of the atomic contributions. These values are given in the last column of Table 4.6 and their sums for all the atomic contributions of each molecule result in the intensity values given in the second column of Table 4.5. One can notice that the interaction terms between the charge and the dipolar polarization contributions are always negative. This means these contributions have opposite signs, i.e. they correspond to dipole moment changes with different polarities. An individual displacement of an equilibrium atomic charge perpendicular to the molecular plane results in a net polarization of its corresponding atomic dipole in the opposite direction. The

charge and dipolar polarization sums are of about the same size as the negative charge and polarization interactions. This results in the small total atomic contribution values in the last columns of Table 4.6.

Figure 4.14 contains a bar graph of the atomic contributions for each molecular vibration. Just as found for the individual atoms, the charge and polarization sums are large and positive. These are almost completely cancelled by their negative interaction terms. Even though each of these contributions can be as large as $1000 \text{ km} \cdot \text{mol}^{-1}$, their sums are at least an order of magnitude smaller. Their total intensity values in Table 4.5 range from 0.8 to $106.1 \text{ km} \cdot \text{mol}^{-1}$.

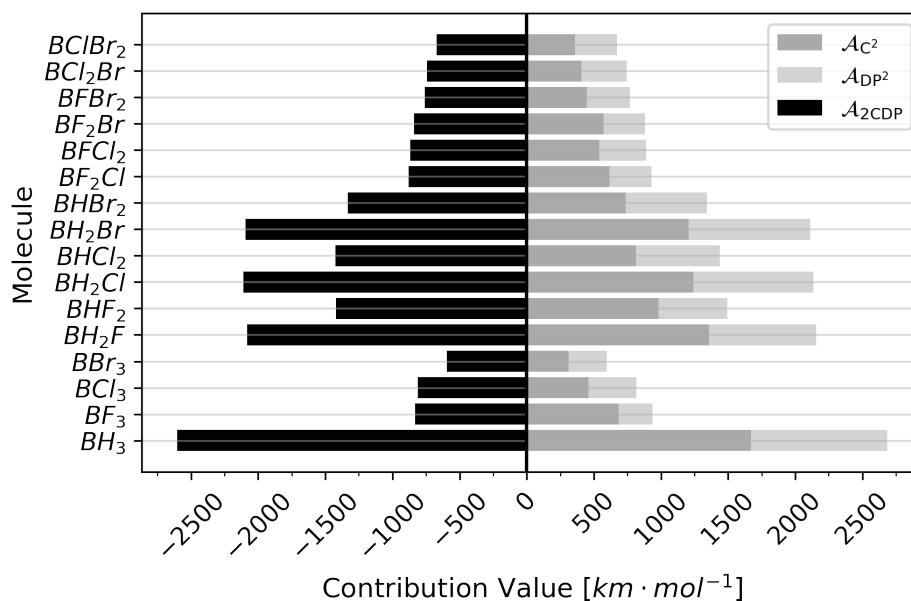


Figure 4.14: Stacked bar chart for charge, polarization, and their interaction contributions to the total intensities obtained at the QCISD/aug-cc-pVTZ level. As the charge and dipolar polarization contributions have opposite signs, the interaction term almost cancels completely the infrared intensity.

These induced atomic dipole moments from the atomic displacements are diagrammed in Figure 4.15 for the out-of-plane vibrations of BH_3 and BF_3 .

Table 4.6: Atomic contributions to the out-of-plane intensity of boron halides. The CCTDP model intensity contributions are reported for each atom in each molecule, as well as their averages and standard deviations.

| Molecule | \mathcal{A}_{C^2} | \mathcal{A}_{DP^2} | \mathcal{A}_{2CDP} | Atomic contribution | Molecule | \mathcal{A}_{C^2} | \mathcal{A}_{DP^2} | \mathcal{A}_{2CDP} | Atomic contribution |
|---------------------|---------------------|----------------------|----------------------|---------------------|---------------------|---------------------|----------------------|----------------------|---------------------|
| Hydrogen | | | | | | | | | |
| BH ₃ | 437.14 | 265.18 | -680.94 | 21.38 | BHBr ₂ | 3.63 | 2.90 | -6.49 | 0.05 |
| BH ₂ F | 468.17 | 278.19 | -721.75 | 24.52 | BH ₂ Br | 3.28 | 2.27 | -5.47 | 0.09 |
| BHF ₂ | 484.64 | 268.05 | -720.93 | 31.76 | BFBr ₂ | 4.85 | 3.60 | -8.35 | 0.09 |
| BH ₂ Cl | 448.44 | 326.12 | -764.84 | 9.69 | BF ₂ Br | 4.90 | 2.88 | -7.52 | 0.27 |
| BHCl ₂ | 464.56 | 363.21 | -821.50 | 6.21 | BClBr ₂ | 4.78 | 4.08 | -8.84 | 0.03 |
| BH ₂ Br | 443.93 | 337.05 | -773.57 | 7.32 | BCl ₂ Br | 4.93 | 4.00 | -8.87 | 0.05 |
| BHBr ₂ | 451.22 | 370.20 | -817.31 | 4.00 | BBr ₃ | 4.63 | 4.19 | -8.80 | 0.01 |
| average | 452.74 | 306.64 | -743.57 | | average | 4.46 | 3.57 | -7.97 | |
| std. dev. | 15.25 | 40.61 | 49.98 | | std. dev. | 0.59 | 0.67 | 1.19 | |
| Fluorine | | | | | | | | | |
| BH ₂ F | 29.06 | 13.98 | -40.35 | 2.72 | BH ₃ | 360.18 | 218.49 | -561.06 | 17.57 |
| BHF ₂ | 26.21 | 13.90 | -38.22 | 1.93 | BF ₃ | 575.13 | 211.82 | -698.07 | 88.66 |
| BF ₃ | 37.02 | 13.64 | -44.94 | 5.70 | BCl ₃ | 415.73 | 324.36 | -734.43 | 5.64 |
| BF ₂ Cl | 38.57 | 18.88 | -53.98 | 3.47 | BBr ₃ | 298.48 | 270.02 | -567.79 | 0.71 |
| BFCl ₂ | 39.91 | 23.99 | -61.92 | 2.01 | BH ₂ F | 396.32 | 226.00 | -598.61 | 23.70 |
| BF ₂ Br | 38.29 | 19.89 | -55.19 | 2.98 | BHF ₂ | 437.31 | 219.73 | -620.14 | 36.98 |
| BFBr ₂ | 38.73 | 26.66 | -64.28 | 1.12 | BH ₂ Cl | 336.78 | 236.56 | -564.55 | 8.80 |
| average | 35.65 | 17.58 | -49.85 | | BHCl ₂ | 327.99 | 245.43 | -567.48 | 5.96 |
| std. dev. | 4.67 | 4.51 | 8.71 | | BH ₂ Br | 314.14 | 231.93 | -539.86 | 6.21 |
| Chlorine | | | | | | | | | |
| BHCl ₂ | 10.33 | 7.60 | -17.72 | 0.21 | BHBr ₂ | 279.61 | 226.63 | -503.45 | 2.77 |
| BH ₂ Cl | 9.17 | 6.02 | -14.88 | 0.33 | BF ₂ Cl | 526.67 | 266.56 | -749.38 | 43.75 |
| BF ₂ Cl | 14.26 | 9.41 | -23.17 | 0.50 | BFCl ₂ | 473.72 | 303.10 | -757.84 | 18.92 |
| BFCl ₂ | 13.81 | 7.53 | -20.41 | 0.94 | BF ₂ Br | 492.17 | 265.13 | -722.44 | 34.75 |
| BCl ₃ | 14.54 | 11.34 | -25.69 | 0.20 | BFBr ₂ | 398.72 | 287.47 | -677.09 | 9.06 |
| BCl ₂ Br | 14.25 | 11.75 | -25.88 | 0.12 | BCl ₂ Br | 376.46 | 308.93 | -682.04 | 3.33 |
| BClBr ₂ | 13.94 | 12.32 | -26.21 | 0.05 | BClBr ₂ | 337.43 | 292.76 | -628.60 | 1.58 |
| average | 13.19 | 9.78 | -22.68 | | average | 396.68 | 258.43 | -635.80 | |
| std. dev. | 1.99 | 2.15 | 4.00 | | std. dev. | 85.45 | 36.37 | 82.10 | |

As the positively charged boron atom is displaced above the molecular plane resulting in a positive dipole contribution, the polarization of its electron density occurs in the same direction, providing a negative contribution. Movements of the terminal atoms also result in opposite signs for the charge and dipolar polarization contributions also represented by similar length arrows pointed in opposite directions. This charge counter-polarization phenomenon has already been observed in the CH vibrations of hydrocarbons. The heavier the atom, the smaller the charge and dipolar polarization contributions for

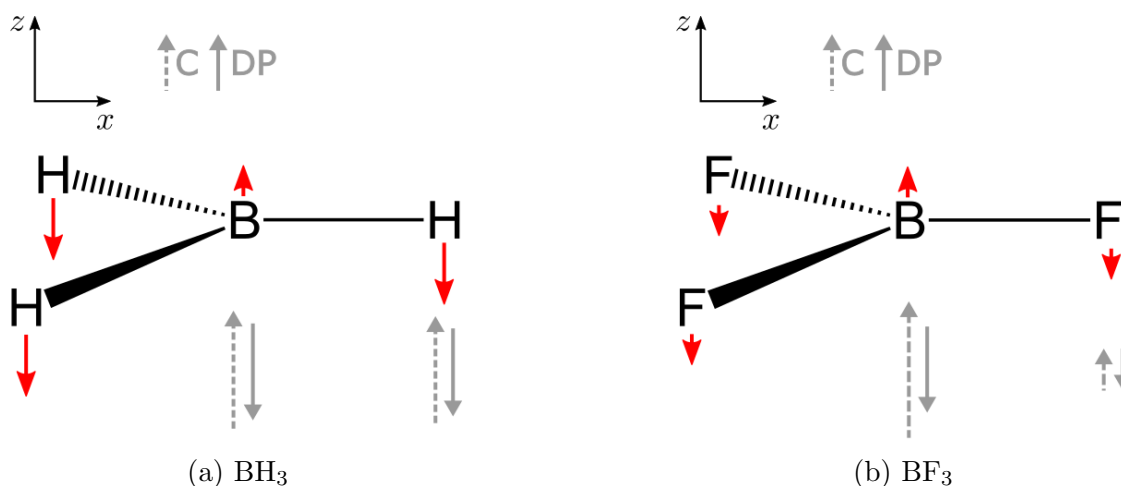


Figure 4.15: Schematic representation of dipole moment derivatives vectors for the out-of-plane normal modes of BH_3 and BF_3 . The red arrows correspond to the normal coordinate displacements.

the terminal atoms. From Table 4.6, the average for the $\mathcal{A}_{\text{DP}^2}$ contributions are $306.64 \text{ km} \cdot \text{mol}^{-1}$ for hydrogen, $17.58 \text{ km} \cdot \text{mol}^{-1}$ for fluorine, $9.78 \text{ km} \cdot \text{mol}^{-1}$ for chlorine, and $3.57 \text{ km} \cdot \text{mol}^{-1}$ for bromine. The average values for the charge contributions are 452.74 , 35.65 , 13.19 , and $4.46 \text{ km} \cdot \text{mol}^{-1}$, respectively. Besides electronic effects, these values are also caused by the mechanical influences of atomic mass in the determination of normal coordinate. The lighter the atom, the greater its displacement within the vibrational movement. As a consequence, the polarization it provokes on the central and other terminal atoms is greater than for the displacement of the heavier atoms.

Relative Displacements and Rehybridization Moments

Equation 4.20 contains five less terms than equation 4.18, making it more convenient for machine-learning applications and can be rewritten in a simpler way as:

$$\frac{\partial p_z}{\partial Q_{oop}} \approx \sum_{i=1}^3 R(X_i) \frac{\partial \alpha_{X_i}}{\partial Q_{oop}} \quad (4.21)$$

where $R(X_i)$ is the rehybridization moment (in $D \cdot \text{radians}^{-1}$) of atom i defined by

$$R(X_i) = 4.8 \left(q_{x_i} + \frac{\partial m_{B,z}}{\partial z'_{x_i}} + \sum_{j=1}^3 \frac{\partial m_{x_j,z}}{\partial z'_{x_i}} \right) \frac{\partial z'_{x_i}}{\partial \alpha_{x_i}} \quad (4.22)$$

and $\frac{\partial \alpha_{x_i}}{\partial Q_{oop}}$ is the angular relative displacement of atom i , that is:

$$\frac{\partial \alpha_{x_i}}{\partial Q_{oop}} = \frac{\partial z'_{x_i}}{\partial Q_{oop}} \frac{\partial \alpha_{x_i}}{\partial z'_{x_i}} \quad (4.23)$$

Note that the boron equilibrium charge term is not included as it is fixed in the molecular plane within the approximation leading to these equations.

The average rehybridization moment for the H, F, Cl, and Br atom are -0.26 ± 0.08 , -0.69 ± 0.10 , -0.33 ± 0.12 , -0.23 ± 0.11 $D \cdot \text{radians}^{-1}$ respectively. As these standard deviations are much larger than those calculated for the substituted benzene parameters, poor intensity predictions are obtained showing that the boron parameters are not transferable for the boron molecules.

The reason behind such a poorly transferability is the wide range of electronegativities of X atoms. The molecules studied here present more diversified chemical environments than exist in the benzenes, for example, requiring a more sophisticated model that can transfer CCTDP parameters from atoms in similar chemical environments. In order to improve the transferability, it is necessary to define a set of criteria to specify the similarity of fragments and select those most appropriate for transference. A simple Machine-Learning Decision-Tree algorithm, discussed in the next section, can be the basis of a similarity transference procedure to predict CCTDP parameters that result in more accurate intensity values.

4.5.1 Transferability of AIM Parameters

In order to implement the transference procedure, a simple decision-tree algorithm was applied to the electronic parameters of equation 4.20. Four molecules, BHFC1, BHFB1, BHClBr, and BFC1Br, were added to our data set to optimize the model parameters. The data set was split into a training set of only eight molecules, where $X_1 = X_2 = X_3$ or $X_1 \neq X_2 \neq X_3$, and a test set of 12, where $X_1 = X_2 \neq X_3$ or $X_1 \neq X_2 = X_3$.

Because of the nature of our system and the limited number of molecules, we are not able to produce a validation set to optimize the hyper-parameters of our model. The amount of data is limited even for performing an n -fold cross-validation procedure without compromising the error estimate. Considering that we are dealing with all possible combinations of the $BX_1X_2X_3$ molecules, *i.e.*, it is not possible to add new molecules to our data or to produce another test set, we decided to combine the test and validation sets. We are aware that this methodology could introduce bias into the hyper-parameter determinations.

The predicted properties correspond to the dipole moment derivative and point charge terms of equation 4.20. For each term, a decision tree has been constructed using only training set CCTDP parameter values. The algorithm was trained to find the best set of decision trees that reduce the mean absolute error (MAE) of each derivative in the training set and reduce the RMSE of all the intensities. In this way, it is not necessary to determine CCTDP models for the test set models but only calculate their intensities directly with a quantum chemical program. This saves considerable computer time as QTAIM atomic charges and dipoles need not be calculated. The features were organized so that X_1 corresponds to the lighter atom and X_3 corresponds to the heavier one. This

causes each tree to be different from the others that predict the same type of electronic term.

Compared with the test set CCTDP values determined from the *ab initio* wave functions, small RMSE values, between 0.0101 and 0.0565 e , were obtained for charges and derivatives with absolute magnitudes ranging from 0.0380 to 0.8600 e . A more critical analysis of these errors can be made examining the graphs in Figures 4.16 and 4.17 for which decision-tree CCTDP parameters are plotted against those obtained at the QCISD/aug-cc-pVTZ quantum level.

Figure 4.16 contains the halogen atomic charge values. Almost all the transference values have points close to the perfect agreement line except for three. The outlier on the far left side corresponds to BH_2F , for which the fluorine charge was assigned a value expected for hydrogen. The two other outliers correspond to BH_2Cl and $BClBr_2$, where Cl charges were estimated by values similar to those for H and Br. Such outliers were generated because the composition of our training set does not allow the model to learn all the different chemical environments that exist in the test set. The presence of outliers could be reduced if it were possible to increase the size and diversity of the training set. The percentage RMSE for the test set charge estimates range from 0.42 to 2.35%. Figure 4.17 contains the CCTDP parameters estimated for derivatives of the

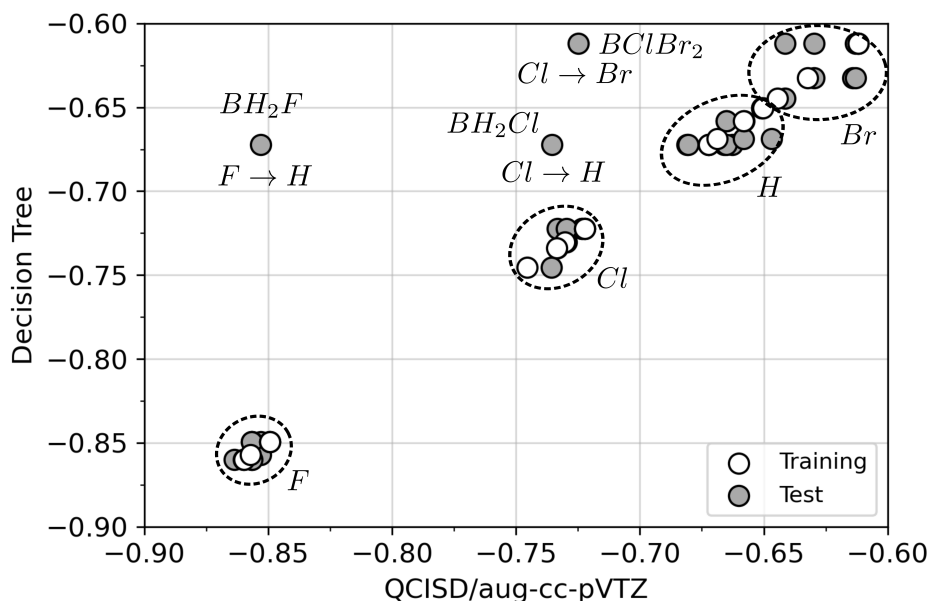


Figure 4.16: Graph of estimated atomic charges obtained from the optimized decision trees against QTAIM charges calculated at the QCISD/aug-cc-pVTZ level (in e).

atomic dipoles with respect to atomic displacement. The polarization points in the upper right hand quadrant correspond to polarizations occurring for the electron densities of the displaced atoms. Overall agreement is good with RMSE between 1 and 1.5%. These derivative values ranging from 0.25 to 0.45 e are significantly higher than the derivatives for polarizations of neighbouring atoms to the displaced atom. Although the points of the training set values of these derivatives ranging from 0.05 to 0.15 e are on the perfect agreement line, the estimated test set derivatives appear to be randomly scattered about it.

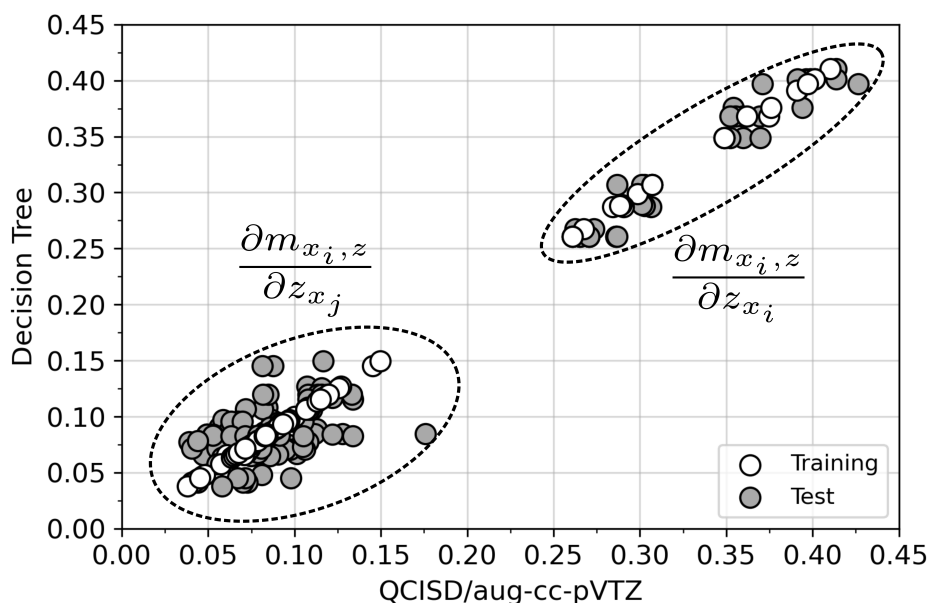


Figure 4.17: Graph of estimated atomic dipole derivatives obtained from the optimized decision trees against QAIM derivatives calculated at the QCISD/aug-cc-pVTZ level (in e).

4.5.2 Interpreting the rehybridization moment

Boron and the halogen atoms have large electronegativity differences. This is reflected in the boron atomic charge values that range from 1.84 to 2.55 e in the trisubstituted borons. The inclusion of atomic dipoles to account for polarization effects counteracts the change in dipole moment owing to the perpendicular displacement of the atomic charges. The atomic contributions to the intensities in Table 4.6 are useful for diagnosing changes in molecular dipole moments of the boron trihalides at the atomic level. The square roots of these charge and polarization contributions multiplied by the appropriate unit conversion factor yields the charge and polarization dipole moment derivatives for the normal coordinate displacement of each atom in the molecule.

The boron atoms are displaced in the positive direction, as depicted in Figure 4.15, for all vibrational movements of positive charge in the positive direction results in positive induced dipoles. On vibration, the boron sp^2 orbital tends toward an sp^3 orbital resulting in polarization of electron density in the positive direction and a negative induced moment. The opposite derivative signs for the terminal atoms arises from electron density polarizations in the opposite direction to that of the displaced atoms.

The hydrogen and boron charge derivatives of borane have similar absolute magnitudes, 0.670 and 0.607 $e \cdot \text{amu}^{-\frac{1}{2}}$. This is due to the much larger perpendicular displacement of the hydrogen atoms. The hydrogen and boron DP derivatives also have similar sizes and opposite signs to the charge derivatives, -0.522 and -0.473 $e \cdot \text{amu}^{-\frac{1}{2}}$. Each of these polarization values are about 80% of their charge values. The sum of the charge and polarization derivatives are +0.148 and +0.134 $e \cdot \text{amu}^{-\frac{1}{2}}$. The squares of these values results in the hydrogen and boron atom contributions to the borane molecular intensity, 21.3 and 17.5 $\text{km} \cdot \text{mol}^{-1}$. The sum of these atomic contributions for the atoms in BH_3 , 21.3 + 17.5 = 81.4 $\text{km} \cdot \text{mol}^{-1}$, in agreement with the CCTDP quantum value in Table 4.5.

The boron charge derivative of $+0.767 e \cdot \text{amu}^{-\frac{1}{2}}$ for BF_3 has a magnitude about four times larger than the fluorine one, $+0.195 e \cdot \text{amu}^{-\frac{1}{2}}$. The polarization derivatives -0.466 and $-0.118 e \cdot \text{amu}^{-\frac{1}{2}}$ cancel the charge derivatives to a large extent. The sums of these derivatives yield $+0.301$ and $+0.077 e \cdot \text{amu}^{-\frac{1}{2}}$. The boron and fluorine dynamic contributions to the BF_3 molecular intensity are 88.3 and $5.8 \text{ km} \cdot \text{mol}^{-1}$, respectively. The hydrogen charge derivatives have the largest average owing to the large displacements of the hydrogen atoms in the normal coordinates. The average values for the halogens decrease as their atomic weights increase, resulting in smaller normal coordinate displacements. The polarization derivatives are negatively correlated with the charge derivatives and have magnitudes that are about 70–90% smaller.

4.6 Concluding Remarks

Due to the lack of charge transfer, the out-of-plane intensities are sensitive probes for the importance of atomic dipole moments. Using a set of substituted benzene, it was possible to demonstrate that the rehybridization moment, an old factor used explain the infrared intensity of benzene and hexafluorobenzene, is mostly determined by atomic dipole moments that arise from the uneven distribution of the electron density inside each atomic basin as the atoms move within a vibrational movement.

Population analysis schemes that neglect the atomic dipole moments cannot reproduce the intensity of out-of-plane normal modes. When dealing with other normal modes, even if the atomic polarizations are ignored, the charge transfer term acts as a correction factor for the derivative of the molecular dipole moment, ensuring that the total intensity is calculated correctly. However, when the CT term is absent and the population analysis scheme does not consider the polarization of the atoms, the intensity is calculated using only with the equilibrium charge. Since intensity is a dynamic property, it cannot be expected that a property calculated at the equilibrium geometry will be sufficient for its calculation. Thus, out-of-plane normal modes constitute an experimental evidence in favor of including atomic dipole moments when we want a dynamic description of electron density and can be used as an evaluation tool for the quality of charge models.

This chapter contains excerpts from texts previously published by the author. The following materials were reprinted with permission:

Duarte, L. J., Bruns, R. E. *Atomic Polarizations, Not Charges, Determine CH Out-of-Plane Bending Intensities of Benzene Molecules*. The Journal of Physical Chemistry A, 122(51), 9833-9841, 2018, American Chemical Society.

Richter, W. E., **Duarte, L. J.**, Bruns, R. E. *Atomic charge and atomic dipole modeling of gas-phase infrared intensities of fundamental bands for out-of-plane CH and CF bending vibrations*. Spectrochimica Acta Part A: Molecular and Biomolecular Spectroscopy, 251, 119393, 2021, Elsevier.

Richter, W. E., **Duarte, L. J.**, Bruns, R. E. *Unavoidable failure of point charge descriptions of electronic density changes for out-of-plane distortions*. Spectrochimica Acta Part A: Molecular and Biomolecular Spectroscopy, 271, 120891, 2022, Elsevier.

Duarte, L. J., Bruns, R. E. *QTAIM Atomic Charge and Polarization Parameters and Their Machine-Learning Transference among Boron-Halide Molecules*. The Journal of Physical Chemistry A, 124(17), 3407-3416, 2020, American Chemical Society.

Chapter 5

Infrared Intensification and Hydrogen Bond Stabilization

IR spectroscopy has long been considered one of the most successful techniques for studying hydrogen bonding[115]. The most notable spectral changes occur for the AH stretching band, although other bands are also perturbed. The position of this band often decreases by up to several hundred wavenumbers, but by far, the most striking change occurs for the band intensity that can increase by a factor of 10 or even more. The symmetric OH stretching intensity in the gas-phase water molecule[87] is only $3.0 \pm 0.4 \text{ km} \cdot \text{mol}^{-1}$, but in the water dimer, its intensity increases to $144 \text{ km} \cdot \text{mol}^{-1}$ (estimated error of 20%) [116]. This spectral change provides a very sensitive probe of H-bonding in the water dimer. Although strong hydrogen bonds show a red frequency shift, blue shifts occur for weaker ones, and these are accompanied by intensity decreases[117].

Iogansen[118] has published a review of about 150 papers reporting correlations between experimental values of the formation enthalpies and the square root of the intensifications of the H-bond stretching mode for 138 donor-acceptor pairs in CCl_4 , CH_2Cl_2 , C_6H_6 , and C_2Cl_4 solvents, HOD in liquid water at 11 different temperatures, and equimolar mixtures of chloroform with 15 different bases.

Hydrogen bond stretching intensification has been investigated in the past[71, 119], but a definitive chemically meaningful explanation for both the intensity enhancement and its relation with the enthalpy of formation has yet to be given. These intensities provide information on changes in electronic structures of the complexes and donor molecules as their acidic protons are displaced. In fact, the dominant change in the molecular geometry on H-bond formation is an elongation of the donor AH bond in the complex. For this reason, the AH stretching intensities can be expected to shed light on the electronic changes that are related to the stability of the H-bonds. One might expect that these same changes occur as the AH donor bond lengthens on complex formation. This is not the only instance in which IR-related properties were shown to be ingrained in fundamental experimentally measured chemical information or indeed chemical reactivity.

Electronic structure changes for molecular vibrations are successfully described using the QTAIM, including some hydrogen bonding systems[120]. Within this formalism, a charge, charge transfer, and dipolar polarization model has been used to accurately reproduce the theoretical infrared intensities of most molecules for which experimental

atomic polar tensors have been determined[80]. Indeed, QTAIM studies have already been carried out for some H-bonding complexes where electronic structure changes are interpreted using equilibrium atomic charge displacement, interatomic charge transfer, and dipolar polarization as the proton is displaced from its equilibrium position[87]. QTAIM also permits the partitioning of the total intensity into atomic contributions, which are very convenient to access information about the A–H···D–B model system, composed of the most relevant atoms of H-bond formation. With QTAIM, the importance of each atom in hydrogen bond intensification can be assessed. As these intensifications are correlated with the formation energies, the atomic intensity contributions could provide useful information as to the electronic structure changes that are important to understand the origins of H-bond stabilization.

QTAIM models are reported with the aim of explaining IR hydrogen bond stretching intensification and its relation to hydrogen bond stability in terms of charge, charge transfer, and dipolar polarization atomic parameters. Taking computer demand and theoretical interest into consideration, the model systems used here involve small donors, HF and HCl, with nine different small bases, HF, HCl, NH₃, H₂O, HCN, acetonitrile, acetaldehyde, formaldehyde, and formic acid electron donor molecules. Although the experimental evidence of the proportionality between the enthalpy of formation and A–H stretching band intensification was observed in condensed phases for other more complex systems, one can expect that this behaviour also exists for the simpler isolated gas-phase complexes as well.

5.1 The CCTDP Model for Infrared Intensification

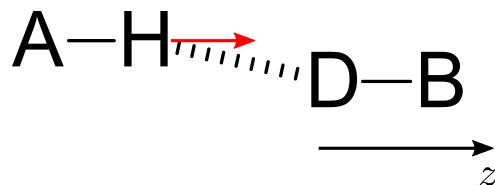


Figure 5.1: Schematic representation of the hydrogen bond complex. “A” represents all atoms in the acid molecule, while B represents all atoms in the base molecule. H is the hydrogen atom and D is the electron pair donor atom of the Lewis base. The AH bond is aligned with the Cartesian z axis. Red arrow represents the AH stretch normal coordinate.

The hydrogen-bond complexes are represented in Figure 5.1. The square root of the hydrogen bond intensification, as defined by Iogansen[118], is:

$$\Delta\mathcal{A}^{\frac{1}{2}} = \mathcal{A}_{\text{Complex}}^{\frac{1}{2}} - \mathcal{A}_{\text{Acid}}^{\frac{1}{2}} \quad (5.1)$$

introducing equation 3.10, yields:

$$\Delta\mathcal{A}^{\frac{1}{2}} = \sqrt{\frac{N_A\pi}{3c^2}} \sum_{\sigma=1}^3 \left[\left(\frac{\partial p_{\sigma}}{\partial Q} \right)_{\text{Complex}} - \left(\frac{\partial p_{\sigma}}{\partial Q} \right)_{\text{Acid}} \right] = \sqrt{\frac{N_A\pi}{3c^2}} \sum_{\sigma=1}^3 \Delta \frac{\partial p_{\sigma}}{\partial Q} \quad (5.2)$$

As the AH bond is aligned with the Cartesian z , it is possible to consider only p_z contributions to the IR intensity. Considering the AH normal mode, the IR intensification becomes:

$$\Delta\mathcal{A}^{\frac{1}{2}} = \sqrt{\frac{N_A\pi}{3c^2}} \Delta \frac{\partial p_z}{\partial Q_{AH}} = \sqrt{\frac{N_A\pi}{3c^2}} \left[\Delta \left(\frac{\partial p_z}{\partial Q_{AH}} \right)_{(C)} + \Delta \left(\frac{\partial p_z}{\partial Q_{AH}} \right)_{(CT)} + \Delta \left(\frac{\partial p_z}{\partial Q_{AH}} \right)_{(DP)} \right] \quad (5.3)$$

The calculations show that about 90% of the total intensity is accounted by only the hydrogen displacement of the vibration. The hydrogen atom intensity contribution permits a simple interpretation of the intensity behaviour in terms of intra-acid, and intermolecular charge transfer and acid and base polarizations. The hydrogen contribution along the z -axis can be expressed as:

$$\frac{\partial p_z}{\partial Q_{AH}} \approx \left(\frac{\partial p_z}{\partial Q_{AH}} \right)^{(H)} \approx q_H + \sum_{C=1}^N \left(z_C \frac{\partial q_C}{\partial z_H} + \frac{\partial m_{C,z}}{\partial z_H} \right) \quad (5.4)$$

The individual values obtained by this equation for the three CCTDP contributions are investigated for their relations with the changes in enthalpy and the total hydrogen bond intensifications. This further simplifies the analysis to only the equilibrium atomic charge of hydrogen, q_H , and the changes in atomic charges weighted by their z component equilibrium coordinates and changes in the atomic dipole moments of all the atoms. The QTAIM theory provides all these parameter values necessary for numerical evaluation. This permits an electron density description of specific charge transfer and dipolar polarization changes as the hydrogen bonded atom is displaced from its equilibrium position.

Considering only the AH proton donor molecule, the electron donor atom of the base, D , and its nearest neighbour, B , and for complexes with the donor aligned along the z -axis, equation 5.4 becomes:

$$\frac{\partial p_z}{\partial Q_{AH}} = q_H + z_A \frac{\partial q_A}{\partial z_H} + z_H \frac{\partial q_H}{\partial z_H} + z_D \frac{\partial q_D}{\partial z_H} + z_B \frac{\partial q_B}{\partial z_H} + \frac{\partial m_{A,z}}{\partial z_H} + \frac{\partial m_{H,z}}{\partial z_H} + \frac{\partial m_{D,z}}{\partial z_H} + \frac{\partial m_{B,z}}{\partial z_H} \quad (5.5)$$

From the charge conservation law:

$$\frac{\partial q_H}{\partial z_H} = - \frac{\partial q_A}{\partial z_H} - \frac{\partial q_B}{\partial z_H} - \frac{\partial q_D}{\partial z_H} - \dots \quad (5.6)$$

substituting into equation 5.5 and considering only contributions from the A, H, D and

B atoms, results:

$$\frac{\partial p_z}{\partial Q_{AH}} \approx q_H + (z_A - z_H) \frac{\partial q_A}{\partial z_H} + (z_D - z_H) \frac{\partial q_D}{\partial z_H} (z_B - z_H) \frac{\partial q_B}{\partial z_H} + \frac{\partial m_{A,z}}{\partial z_H} + \frac{\partial m_{H,z}}{\partial z_H} + \frac{\partial m_{D,z}}{\partial z_H} + \frac{\partial m_{B,z}}{\partial z_H} \quad (5.7)$$

notice that $(z_A - z_H)$ is the projection along the z axis of the distance between atom A and H. Equation 5.7 can be written in a compact form:

$$\frac{\partial p_z}{\partial Q_{AH}} \approx q_H + \left(\frac{\partial p_z}{\partial Q_{AH}} \right)_{(CT)}^{\text{intra-acid}} + \left(\frac{\partial p_z}{\partial Q_{AH}} \right)_{(CT)}^{\text{intermolecular}} + \left(\frac{\partial p_z}{\partial Q_{AH}} \right)_{(DP)}^{\text{acid}} + \left(\frac{\partial p_z}{\partial Q_{AH}} \right)_{(DP)}^{\text{base}} \quad (5.8)$$

where the acid terms contains only atoms of the acid, the base term contains only atoms of the base and the inter-molecular term contains one atom from the Lewis acid and one atom from the Lewis base. The first term, q_H , is just the equilibrium charge on the hydrogen atom. The intra-acid charge transfer term is given by the change in the atomic charge of the A atom owing to the displacement of the hydrogen atom multiplied by the AH bond distance. The intermolecular charge transfer term contains the change in the atomic charges of the D and B atoms relative to the displacement of the H atom multiplied by their respective distances from it. Finally, the dipolar polarization contribution of the acid and the base terms contain derivatives of the atomic dipoles of the acid and base molecules, respectively.

5.1.1 Calculations and hydrogen bond enthalpies

The structures were optimized using the GAUSSIAN09[25] at the second-order Møller–Plesset Perturbation Theory electron correlation (MP2) level[121]. Augmented correlation-consistent polarized triple-zeta (aug-cc-pVTZ) basis sets were used as they are able to provide a precise treatment of long-range interactions[122]. The counterpoise method was applied for complex optimizations to correct formation enthalpy values for basis set superposition error (BSSE) [123, 124].

The formation enthalpy of the hydrogen-bond complexes were obtained including the thermal energy correction, that is:

$$\begin{aligned} \Delta H_f^\circ(298K) &= H_{Complex}^\circ(298K) - H_{Acid}^\circ(298K) - H_{Base}^\circ(298K) \\ &= E_{Complex}^{\text{electronic}} + H_{Complex}^{\circ \text{ corrections}} - E_{Acid}^{\text{electronic}} - H_{Acid}^{\circ \text{ corrections}} - E_{Base}^{\text{electronic}} + H_{Base}^{\circ \text{ corrections}} \end{aligned} \quad (5.9)$$

$H^{\circ \text{ corrections}}$ includes the translation, vibrational, rotational and zero-point energy corrections.

Table 5.1 contains the formation enthalpy values, the AH stretching intensification values, $\Delta \mathcal{A}^{\frac{1}{2}}$, and the hydrogen atom contributions, $\Delta \mathcal{A}_{\text{H}}^{\frac{1}{2}}$, to the intensification for

Table 5.1: Hydrogen-bond formation enthalpy, $-\Delta H_f^\circ(298K)$, (in $\text{kJ} \cdot \text{mol}^{-1}$), differences in square roots of the complex and monomer intensities of the AH stretching mode, $\Delta \mathcal{A}_{\text{H}}^{\frac{1}{2}}$, and the corresponding dynamic hydrogen atom differences, $\Delta \mathcal{A}_{\text{H}}^{\frac{1}{2}}$, (in $\text{km}^{\frac{1}{2}} \cdot \text{mol}^{-\frac{1}{2}}$).

| Acid | Base | $-\Delta H_f^\circ(298K)$ | $\Delta \mathcal{A}_{\text{H}}^{\frac{1}{2}}$ | $\Delta \mathcal{A}_{\text{H}}^{\frac{1}{2}}$ |
|------|------------------|---------------------------|---|---|
| HF | HF | 17.71 | 10.58 | 9.54 |
| HF | NH ₃ | 51.37 | 27.87 | 26.95 |
| HF | H ₂ O | 33.56 | 18.50 | 17.27 |
| HF | HCN | 30.76 | 18.84 | 18.32 |
| HF | Acetonitrile | 37.18 | 25.36 | 23.91 |
| HF | Acetaldehyde | 37.52 | 23.15 | 22.50 |
| HF | Formaldehyde | 33.19 | 19.31 | 18.76 |
| HF | Formic Acid | 31.94 | 15.38 | 16.52 |
| HCl | HCl | 8.48 | 8.96 | 8.75 |
| HCl | NH ₃ | 35.71 | 36.30 | 35.72 |
| HCl | H ₂ O | 21.92 | 16.95 | 16.61 |
| HCl | HCN | 20.42 | 17.35 | 17.07 |
| HCl | Acetonitrile | 25.35 | 22.54 | 22.25 |
| HCl | Acetaldehyde | 27.21 | 24.97 | 24.95 |
| HCl | Formaldehyde | 23.48 | 20.29 | 19.99 |
| HCl | Formic Acid | 21.90 | 18.63 | 18.40 |

two group of complexes, one with HF and one with HCl being the Lewis acid. The intensifications are obtained by analyzing distortions of all atoms as specified by the normal coordinate, whereas the hydrogen contributions are determined by considering only the hydrogen atom displacement in this normal mode. Note that the hydrogen intensification contributions are about the same as the total intensity values, having an RMSD of only $0.7 \text{ km}^{\frac{1}{2}} \cdot \text{mol}^{-\frac{1}{2}}$. As such, the analysis of the correlation between $-\Delta H_f$ and $\Delta \mathcal{A}_{\text{H}}^{\frac{1}{2}}$ can be carried out by simply displacing the hydrogen atom according to the H-bond stretching normal coordinate rather than having to include the displacements of all the other atoms. This is shown in Figure 5.2, which contains a plot of the enthalpy of formation against differences in the square roots of the complex and monomer intensities, owing to only the movement of the hydrogen atom participating in the H-bond.

The linear correlations, indicated as the black and grey dotted lines, suggest that the enthalpies of formation of the HF and HCl complexes are correlated. Therefore, the relative stabilization within each series of complexes seems to only be dependent on the electronic structure changes of the bases on complex formation. This excellent agreement has never been reported before, as it was not included in Iogansen's work, and it points to the conclusion that the infrared intensity enhancements of the HCl and HF complexes have a common source.

The square of the dipole moment derivative, as shown in equation 3.10, is a sum of six terms that contains the square of the charge, charge transfer and dipolar polarization contributions and their interactions. All these terms for both the HF and HCl complexes are presented in Table 5.2 along with the total intensities in the last column. The contributions to the total intensity are defined as:

$$\mathcal{A}_{(C)}^2 = \frac{N_A \pi}{3c^2} \sum_{\sigma=1}^3 \left(\frac{\partial p_{\sigma}}{\partial Q_{AH}} \right)_{(C)}^2 \quad (5.10)$$

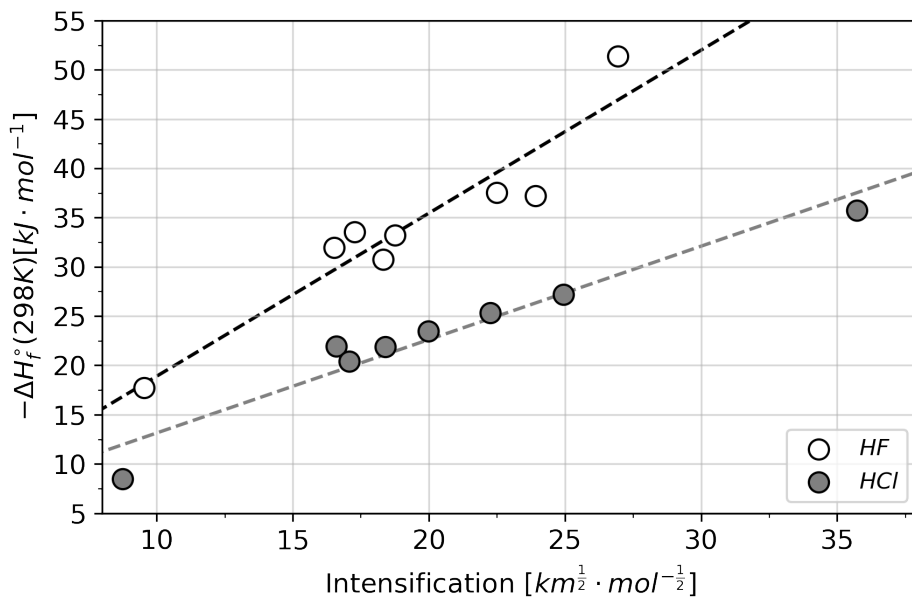


Figure 5.2: Negatives of hydrogen bond formation enthalpies plotted against the differences of the square roots of complex and monomer intensification of the hydrogen contributions for the AH stretching vibrations.

$$\mathcal{A}_{(CT)^2} = \frac{N_A \pi}{3c^2} \sum_{\sigma=1}^3 \left(\frac{\partial p_{\sigma}}{\partial Q_{AH}} \right)_{(CT)}^2 \quad (5.11)$$

$$\mathcal{A}_{(DP)^2} = \frac{N_A \pi}{3c^2} \sum_{\sigma=1}^3 \left(\frac{\partial p_{\sigma}}{\partial Q_{AH}} \right)_{(DP)}^2 \quad (5.12)$$

$$\mathcal{A}_{(2CCT)} = \frac{2N_A \pi}{3c^2} \sum_{\sigma=1}^3 \left(\frac{\partial p_{\sigma}}{\partial Q_{AH}} \right)_{(C)} \left(\frac{\partial p_{\sigma}}{\partial Q_{AH}} \right)_{(CT)} \quad (5.13)$$

$$\mathcal{A}_{(2CDP)} = \frac{2N_A \pi}{3c^2} \sum_{\sigma=1}^3 \left(\frac{\partial p_{\sigma}}{\partial Q_{AH}} \right)_{(C)} \left(\frac{\partial p_{\sigma}}{\partial Q_{AH}} \right)_{(DP)} \quad (5.14)$$

$$\mathcal{A}_{(2CTDP)} = \frac{2N_A \pi}{3c^2} \sum_{\sigma=1}^3 \left(\frac{\partial p_{\sigma}}{\partial Q_{AH}} \right)_{(CT)} \left(\frac{\partial p_{\sigma}}{\partial Q_{AH}} \right)_{(DP)} \quad (5.15)$$

The HF complex intensities are 4 to 13 times larger than the monomer intensity of $108.7 \text{ km} \cdot \text{mol}^{-1}$. For HCl, the complex intensifications are even larger with values ranging from 5 to 40 times larger than the monomer value of $47.1 \text{ km} \cdot \text{mol}^{-1}$. These estimates are expected to be reasonably accurate as QCISD/cc-pVTZ quantum calculations predict an increase from $4 \text{ km} \cdot \text{mol}^{-1}$ for the monomer to $163 \text{ km} \cdot \text{mol}^{-1}$ in the water dimer[87], whereas the experimental values are 3 and $144 \text{ km} \cdot \text{mol}^{-1}$ ($\pm 20\%$), respectively[116].

It can be seen from the values in Table 5.2 that charge transfer is the largest source of H-bond enhancement for the HCl complexes as their $\mathcal{A}_{(CT)^2}$, $\mathcal{A}_{(2CCT)}$, and $\mathcal{A}_{(2CTDP)}$ RMSD are much larger than the values of the other contributions. The val-

ues of the dipole moment derivative contributions, in Table 5.3, confirm this conclusion, as the charge transfer derivative RMSD of $0.524 e \cdot \text{amu}^{\frac{1}{2}}$ between the HCl complexes and the HCl monomer is five times larger than those for charge and dipolar polarization. Their dipole moment derivative values are all positive for charge transfer and all negative for polarization. This behavior is only exhibited by the H₂O and acetonitrile complexes for the less polarizable HF acid complexes. Also, the charge transfer direction in most of the complexes is opposite to the one in the monomer. Owing to these sign differences, the $\mathcal{A}_{(\text{CT})^2}$ contributions are relatively small, and the RMSD between complexes and HF monomer is only $51.2 \text{ km} \cdot \text{mol}^{-1}$. The $\mathcal{A}_{(\text{CT})^2}$ contributions are largest for all HF complexes and monomer owing to the large electronegativity difference between fluorine and hydrogen. However, the $\mathcal{A}_{(\text{C})^2}$ RMSD is only $106.8 \text{ km} \cdot \text{mol}^{-1}$, also indicating small variations between the complexes and HF monomer.

Charge transfer is also the most important source of the large intensity values for the HF complexes. The largest dipole moment derivative RMSD occurs for the charge transfer term, $0.493 e \cdot \text{amu}^{\frac{1}{2}}$, that is three times larger than the difference for polarization and five times the one for charge. The large variation in the charge transfer derivatives owing to sign changes is amplified by the large and relatively constant charge derivatives resulting in the large $\mathcal{A}_{(2\text{CCT})}$ RMSD, $556.1 \text{ km} \cdot \text{mol}^{-1}$, in Table 5.2. A similar behavior produces the $323.4 \text{ km} \cdot \text{mol}^{-1}$ RMSD for the $\mathcal{A}_{(2\text{CDP})}$ contribution, the second largest source of intensity enhancement.

Table 5.2: AH stretching CCTDP intensity contributions for the HF and HCl proton donors and monomers ($\text{km} \cdot \text{mol}^{-1}$).

| Acid | Base | $\mathcal{A}_{(\text{C})^2}$ | $\mathcal{A}_{(\text{CT})^2}$ | $\mathcal{A}_{(\text{DP})^2}$ | $\mathcal{A}_{(2\text{CCT})}$ | $\mathcal{A}_{(2\text{CDP})}$ | $\mathcal{A}_{(2\text{CTDP})}$ | \mathcal{A} |
|------|------------------|------------------------------|-------------------------------|-------------------------------|-------------------------------|-------------------------------|--------------------------------|---------------|
| HF | HF | 659.6 | 18.7 | 0.2 | -220.9 | -6.2 | 1.4 | 452.8 |
| HF | NH ₃ | 634.0 | 50.0 | 40.0 | 356.2 | 318.3 | 89.4 | 1487.9 |
| HF | H ₂ O | 815.8 | 2.7 | 5.2 | -93.4 | 129.8 | -7.4 | 852.6 |
| HF | HCN | 604.6 | 29.2 | 0.2 | 265.6 | -21.3 | -4.7 | 873.6 |
| HF | Acetonitrile | 673.8 | 218.4 | 21.8 | 767.1 | -242.5 | -138.1 | 1300.5 |
| HF | Acetaldehyde | 600.9 | 153.5 | 12.7 | 196.6 | 170.8 | 11.3 | 1145.7 |
| HF | Formaldehyde | 600.2 | 96.1 | 10.4 | 33.0 | 157.8 | 3.2 | 900.6 |
| HF | Formic Acid | 342.6 | 139.7 | 1.0 | 206.0 | 8.8 | -17.8 | 680.7 |
| HF | – | 519.8 | 85.8 | 9.7 | -422.3 | -141.9 | 57.6 | 108.7 |
| RMSD | | 106.8 | 51.2 | 15.9 | 556.1 | 323.2 | 48.2 | 964.8 |
| HCl | HCl | 95.3 | 281.3 | 114.8 | 326.7 | -209.2 | -358.1 | 250.9 |
| HCl | NH ₃ | 191.6 | 1331.4 | 51.2 | 1010.1 | -198.0 | -521.9 | 1864.3 |
| HCl | H ₂ O | 157.0 | 503.6 | 124.1 | 562.3 | -279.1 | -499.9 | 567.9 |
| HCl | HCN | 133.5 | 669.0 | 174.0 | 597.7 | -304.8 | -682.3 | 587.1 |
| HCl | Acetonitrile | 144.3 | 967.6 | 187.7 | 747.3 | -329.1 | -852.4 | 865.4 |
| HCl | Acetaldehyde | 145.8 | 879.9 | 91.3 | 657.6 | -230.6 | -529.4 | 1014.6 |
| HCl | Formaldehyde | 138.9 | 608.3 | 91.6 | 548.9 | -224.2 | -425.1 | 738.5 |
| HCl | Formic Acid | 134.3 | 621.5 | 118.1 | 561.2 | -251.5 | -533.0 | 650.6 |
| HCl | – | 83.2 | 118.7 | 172.8 | 198.7 | -239.8 | -286.5 | 47.1 |
| RMSD | | 64.5 | 683.8 | 68.0 | 465.3 | 46.0 | 300.4 | 891.2 |

Table 5.3 contains the charge, charge transfer, and dipolar polarization values of the hydrogen contributions to the dipole moment derivatives for the HF and HCl complexes.

The charge contributions for the HF complexes are about twice those for the HCl ones. This occurs because fluorine is much more electronegative than chlorine. Charge transfer and dipolar polarizations are larger for the HCl complexes than

Table 5.3: Charge–charge transfer–dipolar polarization hydrogen contributions to the dipole moment derivatives ($e \cdot amu^{-1/2}$) for HF and HCl hydrogen bond complexes.

| Acid | Base | $\left(\frac{\partial p_\sigma}{\partial Q_{AH}}\right)_{(C)}$ | $\left(\frac{\partial p_\sigma}{\partial Q_{AH}}\right)_{(CT)}$ | $\left(\frac{\partial p_\sigma}{\partial Q_{AH}}\right)_{(DP)}$ |
|---------|------------------|--|---|---|
| HF | HF | 0.768 | -0.125 | 0.001 |
| HF | NH ₃ | 0.758 | 0.284 | 0.209 |
| HF | H ₂ O | 0.777 | 0.060 | 0.070 |
| HF | HCN | 0.768 | 0.209 | -0.035 |
| HF | Acetonitrile | 0.809 | 0.495 | -0.149 |
| HF | Acetaldehyde | 0.768 | 0.151 | 0.103 |
| HF | Formaldehyde | 0.767 | 0.034 | 0.106 |
| HF | Formic Acid | 0.769 | 0.140 | 0.038 |
| HF | – | 0.753 | 0.306 | -0.103 |
| Average | | 0.771 | 0.105 | 0.027 |
| RMSD | | 0.025 | 0.493 | 0.182 |
| HCl | HCl | 0.315 | 0.536 | -0.349 |
| HCl | NH ₃ | 0.414 | 1.199 | -0.225 |
| HCl | H ₂ O | 0.373 | 0.734 | -0.348 |
| HCl | HCN | 0.361 | 0.829 | -0.416 |
| HCl | Acetonitrile | 0.376 | 1.010 | -0.444 |
| HCl | Acetaldehyde | 0.386 | 0.902 | -0.299 |
| HCl | Formaldehyde | 0.374 | 0.758 | -0.300 |
| HCl | Formic Acid | 0.366 | 0.802 | -0.363 |
| HCl | – | 0.298 | 0.355 | -0.429 |
| Average | | 0.362 | 0.792 | -0.354 |
| RMSD | | 0.075 | 0.524 | 0.108 |

for the HF complexes. Higher dipolar polarization contributions are expected for the HCl complexes as chlorine is much more polarizable than fluorine. The small RMSD and large average value for the fluorine charges of the HF complexes, in Table 5.3, show that even though the equilibrium charge contributions are large, they are relatively constant, having important intensity effects on both the monomer and the complexes but not much on the hydrogen bond intensifications. In the HCl complexes, the values of the chlorine charges are also similar to the one in the monomer. As a result, the charge contribution to intensification is smaller than that owing to charge transfer.

Figure 5.3 shows graphs of the hydrogen bond formation enthalpies against the variation of the sum of the charge transfer and dipolar polarization derivatives induced by the displacement of only the hydrogen atom of these complexes. As can be seen for both the HF and HCl complexes, the changes in the charge transfer and dipolar polarization sums vary linearly with the formation enthalpies. It is noteworthy that the dominant charge transfer derivative changes alone do not correlate as strongly as the charge transfer and dipolar polarization sum. All the HCl complexes are calculated to have important charge transfer and counterpolarization cancellations of dipole moment derivatives, whereas the dipolar polarization contributions are small for the HF complexes and have the same direction as the charge transfer except for the HCN and CH₃CN bases that contain triple bonds as neighbours to the acidic hydrogens.

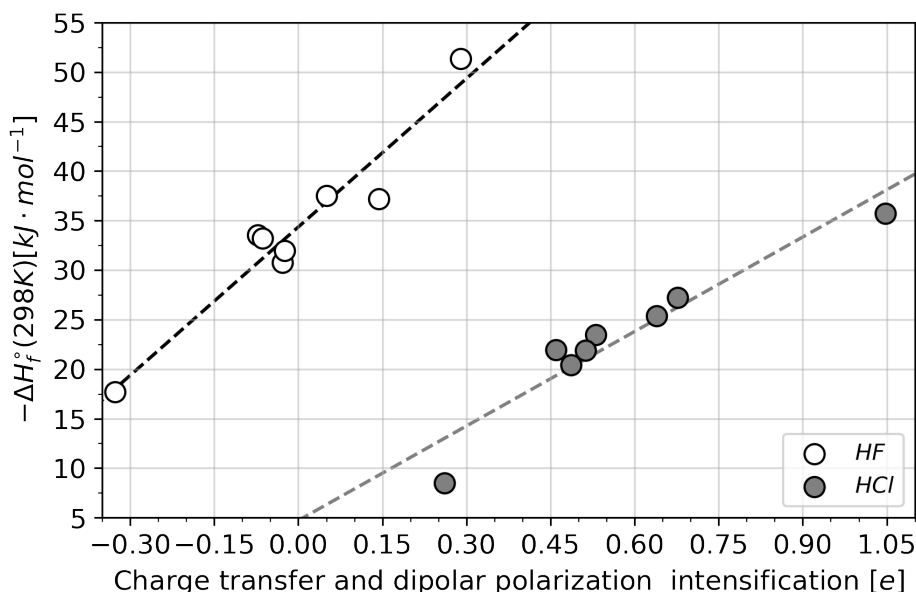


Figure 5.3: Theoretical formation enthalpy values graphed against complex–monomer differences in the sum of the charge transfer and dipolar polarization hydrogen contributions to the dipole moment derivatives.

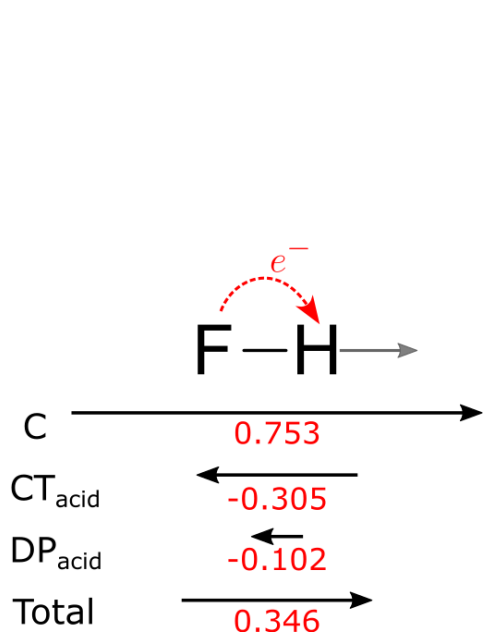
5.2 Charge Transfer and Dipolar Polarization Mechanism for Hydrogen Bonding Intensity Enhancement

Equations 5.7 and 5.8 simplify the analysis of the electronic factors contributing to infrared intensity enhancements which correlate with hydrogen bond stability. These equations contain terms describing contributions to the change in dipole moment along the z axis for a displacement of the H atom. The results for the individual terms in equation 5.7, including the terms for the nearest neighbour atom, B, are presented in Table 5.4 for both the H-bonded complexes and the HF and HCl monomers. The individual hydrogen contributions to the AH stretching normal coordinates can be obtained multiplying the values in this table by their appropriate \mathbf{L} matrix elements.

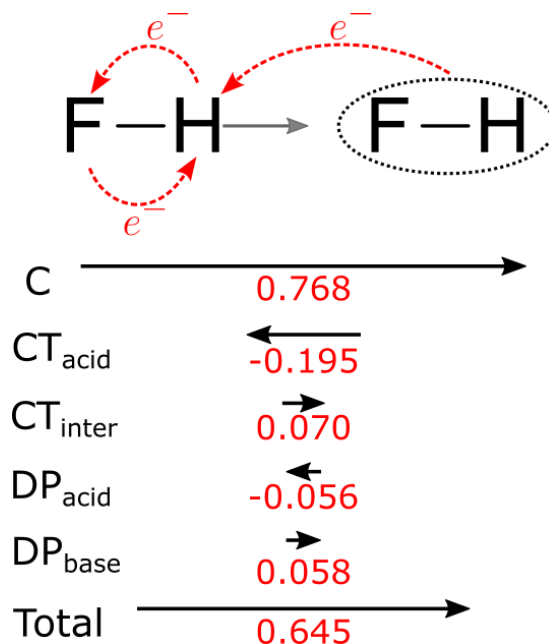
Dynamic effects occurring in both the monomer and complex contribute to the intensity enhancements and can be conveniently analysed with the aid of equation 5.8. Taking the HF monomer and dimer as archetypes, we notice that the equilibrium charge of the hydrogen atom in HF is very positive, resulting in a large positive charge contribution, $0.753 e$ (Figure 5.4). Counteracting this effect, a negative intramolecular electron transfer occurs for this vibration, that is, the hydrogen atom becomes less positive (gains electronic charge) when the HF bond stretches contributing $-0.305 e$ to the dipole moment derivative. This causes a partial cancellation between charge and charge transfer effects in the HF monomer (Figure 5.4a). The dipolar polarization contribution of $-0.102 e$ is smaller and also of opposite sign to the charge, resulting in a total dipole moment derivative of $0.346 e$.

The formation of the $(\text{HF})_2$ complex leads to the donation of electrons from

the donor to the acceptor moiety. This donation contributes more electron density to the fluorine atom rather than the hydrogen atom as quantified in Figure 5.4. When the HF bond stretches, intramolecular electron transfer is smaller in the complex than in the free acid molecule, $-0.195 e$. Also, intermolecular electron transfer occurs from the electron donor molecule to the acid, $+0.070 e$, owing to the HF bond length increase. The acid and base dipolar polarizations essentially cancel one another, resulting in a total dipole moment derivative of $0.645 e$. The total effect is that, after complexation, the charge contribution does not change significantly, but the net charge transfer decreases by almost a third of the value found for the monomer, producing a total dipole moment derivative almost twice as large in the complex (Figure 5.4b). The net polarization is almost zero for the complex reinforcing the intensification.



(a) CCTDP contributions to the dipole moment derivative of HF. The grey vector represents the normal coordinate. Dotted arrows show the flux of electrons.



(b) CCTDP contributions to the dipole moment derivative of the HF dimer. The black vectors correspond to the terms of equation 5.8. The grey vector represents the normal coordinate. Dotted arrows show the flux of electrons.

Figure 5.4: Charge, charge transfer and dipolar polarization contributions (in units of e) for the HF monomer and dimer that explain the intensity enhancement of the hydrogen stretch on complexation. Vectors point to the positive end.

It seems reasonable to assume that the intermolecular charge transfers are proportional to the capacities of the Lewis bases to donate electrons to the acids and that they would correlate with chemically relevant quantities such as basicities and heats of reaction. That is indeed confirmed by the respective order of $-\Delta H_f$ for $\text{HF} \cdot \text{HF}$; $\text{H}_2\text{O} \cdot \text{HF}$; $\text{NH}_3 \cdot \text{HF}$ (17.71 , 33.56 , and $51.37 \text{ kJ} \cdot \text{mol}^{-1}$) and the total electron transfer for the dynamic hydrogen contributions to the dipole moment derivatives (-0.1250 , 0.0600 , and $0.2844 e$). Figure 5.5 illustrates a charge transfer–dipolar polarization mechanism for the HF complexes. The equilibrium hydrogen charge contributions are almost constant. Although the intramolecular charge transfer shows relatively small variations

for the three complexes, the intermolecular charge transfer increases with base strength, from 0.070, 0.202, to 0.424 e . These results are consistent with the simple additive model summing the constant effective charge of the AH bond and the effective charge for the HD bond that increases with increasing H-bond intensification[120]. Indeed, Rozenberg provides evidence of linear correlations between both the H-bonding intensifications and stabilization energies with the QTAIM electron density at the HD bond critical point.

Table 5.4: Individual charge, charge transfer and dipolar polarization contributions (in e) to the dipole moment derivative of AH stretching.

| Acid | Base | q_H | $(z_A - z_H) \frac{\partial q_A}{\partial z_H}$ | $(z_D - z_H) \frac{\partial q_D}{\partial z_H}$ | $(z_B - z_H) \frac{\partial q_B}{\partial z_H}$ | $\frac{\partial m_{A,z}}{\partial z_H}$ | $\frac{\partial m_{D,z}}{\partial z_H}$ | $\frac{\partial m_{H,z}}{\partial z_H}$ | $\frac{\partial m_{B,z}}{\partial z_H}$ |
|------|------------------|-------|---|---|---|---|---|---|---|
| HF | HF | 0.768 | -0.195 | 0.006 | 0.065 | -0.066 | 0.055 | 0.010 | 0.002 |
| HF | NH ₃ | 0.758 | -0.139 | -0.009 | 0.433 | 0.112 | 0.026 | 0.035 | 0.036 |
| HF | H ₂ O | 0.775 | -0.142 | -0.058 | 0.261 | -0.026 | 0.049 | 0.025 | 0.022 |
| HF | HCN | 0.768 | -0.159 | -0.079 | 0.448 | -0.023 | -0.009 | 0.016 | -0.019 |
| HF | Acetonitrile | 0.809 | -0.149 | -0.037 | 0.681 | -0.084 | 0.010 | 0.027 | -0.102 |
| HF | Acetaldehyde | 0.768 | -0.143 | -0.042 | 0.335 | 0.028 | 0.077 | 0.027 | -0.029 |
| HF | Formaldehyde | 0.767 | -0.152 | -0.035 | 0.220 | 0.011 | 0.069 | 0.022 | 0.004 |
| HF | Formic Acid | 0.769 | -0.152 | -0.048 | 0.341 | -0.016 | 0.065 | 0.008 | -0.019 |
| HF | - | 0.753 | -0.306 | - | - | -0.058 | - | -0.043 | - |
| HCl | HCl | 0.315 | 0.439 | 0.043 | 0.055 | -0.508 | 0.049 | 0.112 | -0.001 |
| HCl | NH ₃ | 0.414 | 0.720 | 0.027 | 0.452 | -0.413 | 0.010 | 0.144 | 0.034 |
| HCl | H ₂ O | 0.373 | 0.572 | -0.042 | 0.204 | -0.523 | 0.024 | 0.136 | 0.016 |
| HCl | HCN | 0.361 | 0.549 | -0.056 | 0.337 | -0.516 | -0.015 | 0.129 | -0.014 |
| HCl | Acetonitrile | 0.376 | 0.587 | -0.065 | 0.487 | -0.507 | -0.022 | 0.131 | -0.047 |
| HCl | Acetaldehyde | 0.386 | 0.634 | -0.002 | 0.271 | -0.476 | 0.057 | 0.137 | -0.018 |
| HCl | Formaldehyde | 0.374 | 0.597 | -0.003 | 0.164 | -0.490 | 0.048 | 0.134 | 0.008 |
| HCl | Formic Acid | 0.366 | 0.563 | -0.022 | 0.262 | -0.507 | 0.036 | 0.132 | -0.024 |
| HCl | - | 0.298 | 0.355 | - | - | -0.514 | - | 0.084 | - |

The net dipolar polarization contributions in Figure 5.5 also vary significantly as base strength increases, 0.002, 0.071, and 0.209 e , reinforcing the charge transfer changes. The dipolar polarization values of the bases are almost constant, 0.058, 0.071, and 0.062 e , even though they form a very diverse group of molecules. On the other hand, the HF acid polarization ranges from -0.056 e for the dimer to +0.147 e for the ammonia complex. The sums of the intermolecular charge transfer and acid dipolar polarizations for the HF, H₂O, and NH₃ complexes with HF are 0.014, 0.202, and 0.571 e and are highly correlated with the formation enthalpy values. The sums of the intermolecular charge transfer and acid polarizations for the eight HF complexes have a 0.92 correlation coefficient with the intensifications and 0.95 for the enthalpy values.

The intermolecular charge transfer–acid dipolar polarization mechanism shown in Figure 5.5 is also valid for the HCl complexes. As chlorine is much more polarizable than fluorine, the polarization contributions to the dipole moment derivatives are much larger. The sums of the intermolecular charge transfer and acid polarizations have a 0.94 correlation with the intensifications and 0.97 with the stabilization enthalpies. It should be mentioned that the charge transfer derivative becomes more negative as the hydrogen bond stabilization decreases. This behaviour was also found in the literature [117]. In addition, the inclusion of atomic polarization in the CCTDP model reinforces the electron transfer trend. Although no blue shift hydrogen bonds are included in this chapter, there is no reason to suspect that the CCTDP model will not provide a unified explanation of the decreased intensities as well.

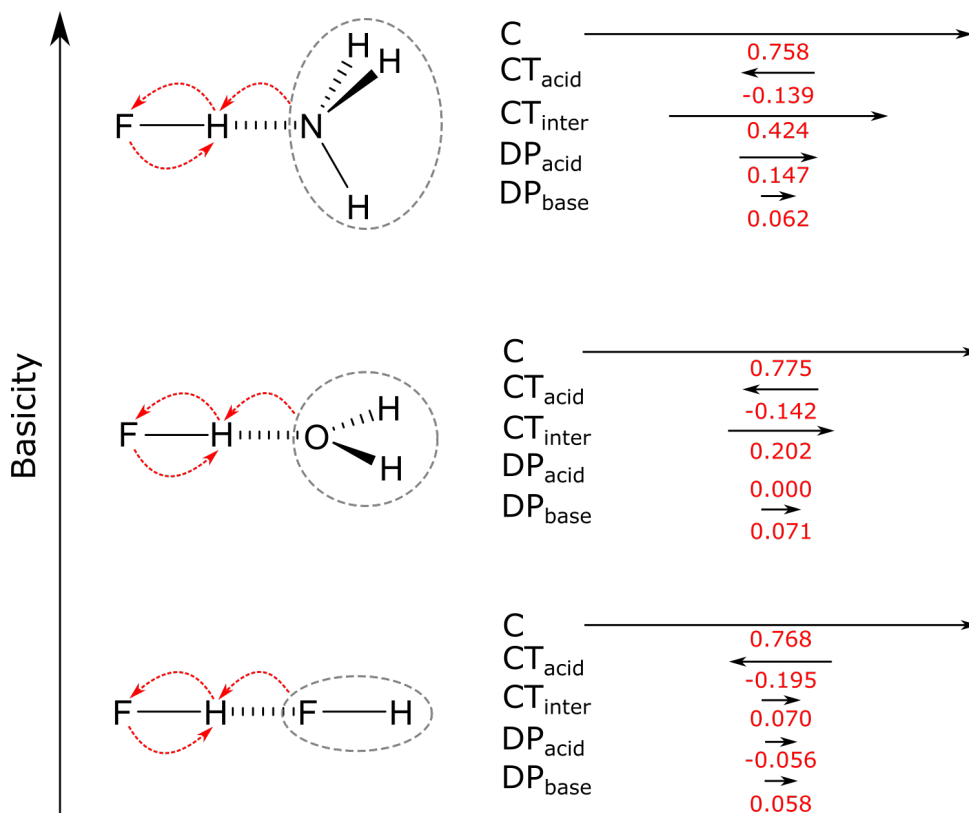


Figure 5.5: Charge, charge transfer, and dipolar polarization contributions to the dipole moment derivatives of the HF complexes with HF, H₂O, and NH₃ bases. Note that the intermolecular charge transfer and net polarizations increases with the base strengths in the HF + H₂O + NH₃ series. The directions of arrows to the right point to positive poles of the dipole moment. On the left, dotted red arrows for intermolecular and acid (intramolecular) charge transfer and full for acid (intra-molecular) charge transfer.

5.3 Complex Formation

The electronic charge transferred from the Lewis base to the acid is an important source of hydrogen bond stabilization[125]. Because this charge transfer depends on the capacity of the Lewis base to donate electrons to the acid, the enthalpy of formation of the resulting complex is expected to be proportional to the base strength. Table 5.5 contains values of the electronic charge transferred from the base to the acid for the HF and HCl complexes. This is the net charge on the acid. It is clear that stronger bases transfer more electronic charge to both HF and HCl.

The top graph of Figure 5.6 contains a graph of the negative enthalpy of formation against the charge transferred from base to acid. With the exception of the HF and HCl dimers, there appears to be linear relationships between these quantities. In any case, the results provide a very strong argument that electron donation plays a key role in complex stabilization.

However, electron transfer, alone, could not account for the linearity between the formation enthalpy and the hydrogen bond intensification. Only its sum with the dipolar polarization reproduces this linearity. As such, one might expect that the change in atomic polarizations on complex formation would also provide important contributions to the stabilization. The HF and HCl atomic polarizations (z-component sums of atomic

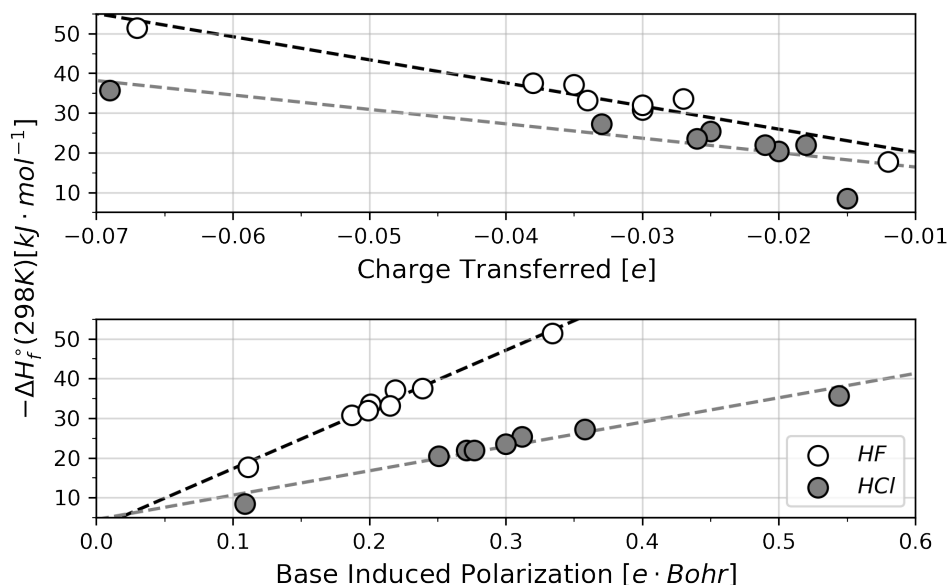


Figure 5.6: Plots of the hydrogen bond enthalpy of formations versus the charge transferred (top) and the sum of the hydrogen and halogen atomic dipole moments along the z axis (bottom).

dipoles) have been included in Table 5.5.

The bottom graph Figure 5.6 shows the hydrogen bond formation enthalpies as a function of the atomic polarizations of the HF and HCl acids on complex formation. The atomic polarization values are a sum of the z -components of the atomic dipoles of the hydrogen and halogen atoms. The linear relationships are indeed impressive with correlation coefficients of 0.98 and 0.95 for HF and HCl, respectively. One can expect polarization changes occurring in the AH bond to be very important for energy changes on H-bond formation. The polarization changes occurring for the base are not as systematic as those of the acids.

5.4 Concluding Remarks

According with the CCTDP model, the stabilization of the hydrogen bond and the infrared band intensification of the H-bond result from charge transfer and dipolar polarization contributions, once again emphasizing the importance of including atomic dipoles to properly describe the molecular dipole moment and its derivative. Although the charges have important contributions for both the complexes and the monomer intensities, they make small contributions to intensity enhancements for bases with the same electron acceptor. It is very important to draw attention to the fact that one of the simplest reaction mechanisms, an acid-base reaction, cannot be properly represented without polarization obtained through atomic dipoles.

Electronic structure changes for the acid-base reactions are strongly correlated with changes occurring for their AH stretching vibrations. This seems reasonable considering that the change in the AH bond length on H-bond formation is expected to be comparable to the A-H vibrational amplitudes. This provides a theoretical basis for the experimental observations of the strong correlations between hydrogen bond enthalpies of

Table 5.5: Charge transferred from the base to the acid (e) and base-induced polarization ($e \cdot Bohr$) in the acid for the HF and HCl complexes. The “-” sign indicates that the charge is transferred to the acid.

| Acid | Base | Electron transfer | Acid polarization |
|------|------------------|-------------------|-------------------|
| HF | HF | -0.012 | 0.111 |
| HF | NH ₃ | -0.067 | 0.334 |
| HF | H ₂ O | -0.027 | 0.201 |
| HF | HCN | -0.030 | 0.187 |
| HF | Acetonitrile | -0.035 | 0.219 |
| HF | Acetaldehyde | -0.038 | 0.239 |
| HF | Formaldehyde | -0.034 | 0.215 |
| HF | Formic Acid | -0.030 | 0.199 |
| HCl | HCl | -0.015 | 0.109 |
| HCl | NH ₃ | -0.069 | 0.544 |
| HCl | H ₂ O | -0.018 | 0.271 |
| HCl | HCN | -0.020 | 0.251 |
| HCl | Acetonitrile | -0.025 | 0.312 |
| HCl | Acetaldehyde | -0.033 | 0.358 |
| HCl | Formaldehyde | -0.026 | 0.300 |
| HCl | Formic Acid | -0.021 | 0.277 |

formation and infrared proton stretching intensification.

This chapter contains excerpts from texts previously published by the author. The following material were reprinted with permission:

Duarte, L. J., Silva, A. F., Richter, W. E., Bruns, R. E. *Infrared intensification and hydrogen bond stabilization: Beyond point charges*. The Journal of Physical Chemistry A, 123(30), 6482-6490, 2019, American Chemical Society.

Chapter 6

Infrared Intensities of Imaginary Frequencies

The mechanism of gas phase S_N2 reactions is well-known and taught in every introductory organic chemistry course. Proposed for the first time in 1934 by Hughes and Ingold[126], understanding of this mechanism has been refined by quantum mechanics since the first computational methods were available. When occurring on sp^3 carbons, the mechanism consists of a nucleophile (Nu) that approaches the electrophile center forming a stable complex leading to the formation of a pentacoordinate transition state (TS). One of the atoms initially bonded to the electrophile, namely the leaving group (LG), is displaced and the reaction produces another stable complex formed by the reaction product and the non-bonded LG. The reaction potential energy surface and energy profile of a S_N2 reaction can depend on the natures of the nucleophile, leaving group, as well as the central electrophilic atom, substituents and reaction medium [127, 128]. In Figure 6.1 we present a typical energy profile for the nine $NuCX_3LG^-$ system treated here with Nu, LG = H, F, Cl and X = H, F systems, although other systems can have different forms. On the far left

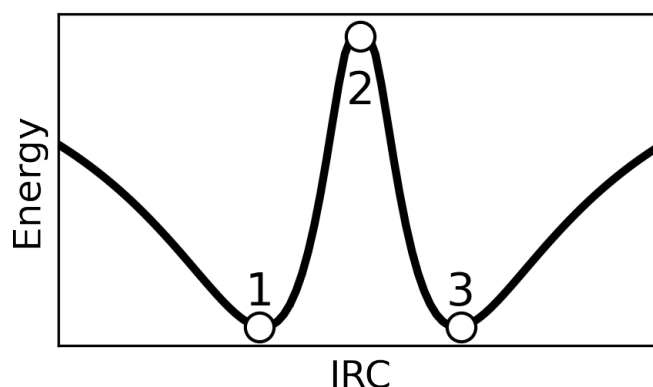


Figure 6.1: Reaction path for a generic S_N2 reaction. In 1: ion-dipole complex (ϵ_R); 2: transition state (ϵ_{TS}); 3: ion-dipole complex (ϵ_P).

side of Figure 6.1, the nucleophile and the reactant molecule are at an infinite distance

from each other and the system's energy is equal to the sum of reactants individual energies. Following the reaction, represented by the bold curve, the reactants approach forming a stable complex[129], also called ion-dipole complex[127], with complexation energy equal to $E_{\text{cp},\text{R}}$. From this point, the system must overcome a potential barrier to reach the TS saddle point. The energy needed for this step is called activation energy, $E_{\text{atv},\text{R}}$. The TS corresponds to a local maximum in the direction of the intrinsic reaction coordinate (IRC)[130, 131] and tends towards a minimum in either direction. On the right, at the minimum, the complex between the products and the LG appears, stabilized by an amount of energy equal to $E_{\text{cp},\text{P}}$. On the far right, the product and the leaving group are infinitely separated. For some reactions, however, the complexation energies are too small and/or highly dependent on solvation effects [132]. The spectator atoms also change the energy profile of the reactions. For example, one can find an ion-dipole complex in the reaction path of $\text{Cl}^- + \text{CH}_3\text{Cl} \rightarrow \text{ClCH}_3 + \text{Cl}^-$, but the substitution of the spectator H by F atoms will make the complex disappear[128]. Also, substituting the central carbon atom by another, such as Si, will change the reaction PES completely[128]. In order to simplify the analysis, all calculations presented in this chapter are carried out in the gas phase and the central atom is always carbon.

A Quantum Chemical Topology/Interacting Quantum Atoms (QCT/IQA) analysis performed by Alkorta[133] demonstrated that the forces driving the S_N2 reactions arise from intratomic energies of Nu and LG and exchange-correlation energy between C and Nu and between C and LG. Since the intratomic energy contribution accounts for both steric effects and charge transfers[134] the ergodography of S_N2 is determined almost entirely by changes in the electron density of Nu, C and LG.

In a series of four papers[135–138] considering a linear collision $\text{A} + \text{BC} \rightarrow \text{AB} + \text{C}$, Marcus has suggested that the reacting system can be described by large amplitude vibrations along the reaction path. In the first two papers of that series, Marcus has developed a quantum and classical formulation to study the above mentioned collision, which later led to the introduction of the Natural Collision Coordinates. Miller[139] extended the formulation of the reaction path Hamiltonian to deal with polyatomic molecules. For a N atom system, there are six zero frequency modes corresponding to translations and rotations and $3N - 7$ non-zero real frequencies, corresponding to normal modes that are perpendicular to the reaction path. Since the TS is a first-order saddle point on the Potential Energy Surface (PES) it has a normal mode with imaginary frequency, corresponding to the steepest descent path leading from TS to the products (or reactants). The connection between molecular vibrations and chemical reactions has already been explored by Cremer and Kraka in an insightful review[140].

In this chapter, we propose the investigation of the S_N2 mechanism by decomposing the TS imaginary frequency infrared intensity into its charge, charge-transfer and dipolar polarization contributions of the CCTDP model. The infrared intensities are intimately related to the changes in the molecular electron density. By means of CCTDP analysis the dipole moment derivative is divided into atomic contributions, evidencing the dynamic electronic behavior along the Intrinsic Reaction Path (IRC), as defined by Fukui[130, 131].

As IRC calculations are performed from the TS, there is only one single negative eigenvalue λ whose eigenvector unveils the path to the product or reactant equilibrium point. In a well detailed work[141], Quapp showed that the determination of the reaction path is independent of the coordinate system in a way that it can be solved in terms of $3N - 6$ normal coordinates Q , corresponding to molecular vibrations. To find the normal

modes of vibration, and thus the starting point of the IRC, one can simply diagonalise the mass-weighted Hessian matrix. The negative eigenvalue corresponds to the frequency of the imaginary normal mode of vibration, coinciding with the IRC.

6.1 The Intrinsic Reaction Coordinate

Following the formulation proposed by Fukui [130], the IRC is a line dependent on a length parameter l that connects the PES critical points ϵ_P , ϵ_{TS} and ϵ_R , where ϵ_P and ϵ_R are minimum points corresponding to the products and reactants at equilibrium geometries and ϵ_{TS} is the maximum point corresponding to the geometry of the transition state. If the potential energy, $V(\vec{X})$, is defined in terms of N nuclear positions, $\vec{X} = \{x_1, x_2, \dots, x_{3N}\}$ and within the adiabatic approximation, then, at the critical points:

$$\left. \frac{dV(\vec{X})}{d\vec{X}} \right|_{\epsilon_R} = \left. \frac{dV(\vec{X})}{d\vec{X}} \right|_{\epsilon_{TS}} = \left. \frac{dV(\vec{X})}{d\vec{X}} \right|_{\epsilon_P} = 0 \quad (6.1)$$

Since the IRC is, by definition, the path of steepest descent, to find $\vec{x}_i(l)$ it is necessary to solve the gradient problem [141]:

$$\frac{d\vec{x}_i(l)}{dl} = -\frac{\partial V(\vec{X})}{\partial \vec{x}_i} \vec{x}_i(l) \quad (6.2)$$

Because of the conditions imposed by equation 6.1, the solution of 6.2 needs to be defined in terms of ϵ_R , ϵ_{TS} and ϵ_P and be orthogonal to the tangential plane of any equipotential energy surface of $V(\vec{X})$. The derivative on the LHS of equation 6.2 implies that the displacement vector direction is coincident with the direction of force, therefore, determining the steepest path. At an equilibrium point, the force $\frac{\partial V(\vec{X})}{\partial \vec{x}_i}$ is null and at a point very near to equilibrium, $\epsilon + \Delta \vec{x}$:

$$\frac{\partial V(\vec{X})}{\partial \vec{x}_i} \approx \sum_{j=1}^{3N} \left. \frac{\partial^2 V(\vec{X})}{\partial \vec{x}_i \partial \vec{x}_j} \right|_{\vec{X}=\epsilon} \Delta \vec{x}_j \quad (6.3)$$

Substituting equation 6.3 into equation 6.2 results in the following:

$$\begin{aligned} \frac{\sum_{j=1}^{3N} \left(\left. \frac{\partial^2 V(\vec{X})}{\partial \vec{x}_1 \partial \vec{x}_j} \right|_{\epsilon + \Delta \vec{x}_j} \Delta \vec{x}_j \right)}{\Delta \vec{x}_1} &= \frac{\sum_{j=1}^{3N} \left(\left. \frac{\partial^2 V(\vec{X})}{\partial \vec{x}_2 \partial \vec{x}_j} \right|_{\epsilon + \Delta \vec{x}_j} \Delta \vec{x}_j \right)}{\Delta \vec{x}_2} = \dots \\ &= \frac{\sum_{j=1}^{3N} \left(\left. \frac{\partial^2 V(\vec{X})}{\partial \vec{x}_{3N} \partial \vec{x}_j} \right|_{\epsilon + \Delta \vec{x}_j} \Delta \vec{x}_j \right)}{\Delta \vec{x}_{3N}} = \text{constant} = \lambda \quad (6.4) \end{aligned}$$

where the second derivatives inside the summations are the elements, h_{ij} , of the Hessian

matrix, \mathbf{H} , which leads to the eigenvalue problem:

$$\det(\mathbf{H} - \lambda\mathbf{I}) = 0 \quad (6.5)$$

Solutions of equation 6.5 are also the solutions of the vibrational problem.

6.2 Translational Invariability of the Dipole Moment Derivative for Charged Systems

The calculated molecular dipole moment for a charged molecule will be dependent on its position in the Cartesian coordinate system. The dipole moment derivative, however, is under the charge conservation law, as discussed in Chapter 4.

Considering the negatively charged TS, as shown in Figure 6.2 and taking the carbon atom of $\text{Nu}^- \text{CX}_3 \text{LG}$ as reference, we can write:

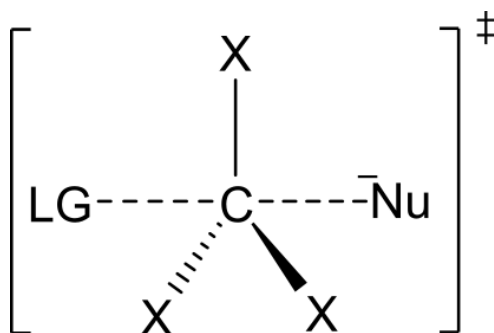


Figure 6.2: Structure of the transition states. Nu is the nucleophile and LG is the leaving group. X represents the spectator H, F or Cl.

$$\frac{\partial q_C}{\partial \sigma_A} = -\frac{\partial q_{\text{Nu}}}{\partial \sigma_A} - \frac{\partial q_{X(1)}}{\partial \sigma_A} - \frac{\partial q_{X(2)}}{\partial \sigma_A} - \frac{\partial q_{X(3)}}{\partial \sigma_A} - \frac{\partial q_{\text{LG}}}{\partial \sigma_A} \quad (6.6)$$

The $\frac{\partial q_C}{\partial \sigma_A}$ is the carbon charge derivative with respect to the displacement of atom A in the σ coordinate. Substituting it in equation 3.2, results in:

$$\frac{\partial p_\sigma}{\partial \sigma_A} = \sum_{B=1}^N q_j \frac{\partial \sigma}{\partial \sigma_A} + \sum_{B=1}^N (\sigma_B - \sigma_C) \frac{\partial q_j}{\sigma_A} + \sum_{B=1}^N \frac{\partial m_{j,\sigma}}{\sigma_A} \quad (6.7)$$

The second term on the RHS becomes dependent only on difference in Cartesian coordinates rather than the positioning vector. The other terms are not dependent of any positioning vector, consequently all these individual contributions are invariant to translations. Any atom can be chosen as reference for this analysis. Here the carbon atom was chosen as the differences in Cartesian coordinates correspond to chemical bond lengths. In this way the dipole moment derivative is a sum of atomic and chemical bond contributions.

6.3 Imaginary Normal Mode

The transition states of 9 S_N2 reactions, as schematized in Figure 6.2, were obtained and optimized at the QCISD/aug-cc-pVTZ level of theory. The infrared frequencies were analytically calculated by Gaussian [25] making sure only one imaginary frequency is present. The CCTDP parameters were obtained following the procedure described in appendix E.

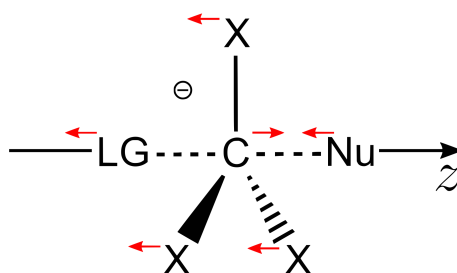


Figure 6.3: Positioning system and normal coordinate displacements (red arrows) utilized in all transition states. Nu = H, F, Cl, LG = H, F, Cl and X = H or F.

The transition states were positioned in such way that the reaction coordinate is aligned with the z -Cartesian axis and the carbon atom of the electrophilic part is at the origin. Since the TS is the same for the direct and reverse reactions, the definition of Nu and LG is arbitrary. In fact, following the IRC formulation there is no univocal definition of reagents and products. Here, we adopt the definition that the nucleophile is to the right of the origin. When adopting this positioning system, all charge transfer terms, as defined by equation 6.7, will be relative to the carbon atom. The molecular dipole moment derivative with respect to the normal coordinate, Q , becomes:

$$\frac{\partial p}{\partial Q} = \sum_{\sigma=1}^3 \sum_{A=1}^N \left[q_A \frac{\partial \sigma_A}{\partial Q} + (\sigma_A - \sigma_C) \frac{\partial q_A}{\partial Q} + \frac{\partial m_{A,\sigma}}{\partial Q} \right] \quad (6.8)$$

The CT term for each atom A is weighted by the bond distance between this atom and carbon and, therefore, can be interpreted as a bond property, in contrast to the atomic terms C and DP. The positions of the Nu and C are also important. For the normal coordinate phase (the derivatives were evaluated in the direction of breaking the Nu-C bond, and as the nucleophile is always on the right side of the origin, its charge derivative, $\frac{\partial q_A}{\partial Q_k}$ is positive, if the CT contribution is positive. The opposite occurs for the LG terms.

Red arrows in Figure 6.3 depict the normal coordinate distortion, i.e. atomic displacements, of the imaginary frequency. When following it, one will reach a minimum point on the potential energy surface which corresponds to the products (or reactants) of the reaction. This is the idea behind the IRC procedure.

Although recent methods, such as the unified reaction valley approach, demonstrated that changes in the electron density do not occur necessarily at the transition states, but at curvature peaks along the reaction path, as demonstrated by Kraka and Nanayakkara[142], abrupt changes in the electron density, such as bond breaking or bond formation, occur at, or nearly at; the curvature maxima rather than at the TS. We,

however, focus the analysis presented in this chapter solely at the imaginary frequency of the TS, as it is the starting point for defining the IRC and will capture the tendency of change in the electron density at that point.

6.4 CCTDP analysis of CH₄, CH₃F and CH₃Cl

Before proceeding to the investigation of the transition states, it is convenient to investigate some of the products/reagents. The objective is to understand the predominant electronic changes occurring when the bonds between CH, CF and CCl are broken. As such, the CCTDP analysis was performed over the \mathbf{a}_1 normal modes of CH₃D, CH₃F and CH₃Cl, which correspond to CD, CF and CCl bond stretching. The CCTDP contributions are shown in Table 6.1 and intensity contributions in the z direction are given as \mathcal{A}_z .

Table 6.1: CCTDP parameters for CH₄(or CH₃D), CH₃F and CH₃Cl.

| Mol. | Atom | \mathcal{A}_{C^2} | \mathcal{A}_{CT^2} | \mathcal{A}_{DP^2} | \mathcal{A}_{2CCT} | \mathcal{A}_{2CDP} | \mathcal{A}_{2CTDP} | \mathcal{A}_z |
|--------------------|------|---------------------|----------------------|----------------------|----------------------|----------------------|-----------------------|-----------------|
| CH ₃ D | C | 0.0 | 10.6 | 14.2 | 0.0 | 0.1 | -24.6 | 0.2 |
| | H | 0.0 | -2.9 | -4.6 | 0.0 | 0.0 | 7.3 | -0.2 |
| | H | 0.0 | -2.9 | -4.6 | 0.0 | 0.0 | 7.3 | -0.2 |
| | H | 0.0 | -2.9 | -4.6 | 0.0 | 0.0 | 7.3 | -0.2 |
| | D | 0.0 | 91.6 | 149.2 | -0.1 | 0.2 | -233.8 | 7.0 |
| CH ₃ F | C | 31.0 | 21.2 | 49.7 | -51.7 | 79.3 | -65.0 | 64.6 |
| | H | 0.9 | -0.9 | -2.7 | 0.5 | -1.5 | 3.1 | -0.6 |
| | H | 0.9 | -0.8 | -2.6 | 0.4 | -1.4 | 2.9 | -0.6 |
| | H | 0.9 | -0.7 | -2.5 | 0.4 | -1.3 | 2.8 | -0.5 |
| | F | 25.8 | 13.9 | 29.9 | -37.9 | 55.5 | -40.8 | 46.4 |
| CH ₃ Cl | C | 2.3 | 15.9 | 0.9 | 14.6 | -3.1 | -7.6 | 23.1 |
| | H | 0.6 | -2.1 | 0.0 | -0.7 | -0.2 | 0.7 | -1.7 |
| | H | 0.6 | -1.9 | 0.1 | -0.5 | -0.3 | 0.5 | -1.6 |
| | H | 0.6 | -2.2 | -0.1 | -0.7 | -0.2 | 0.8 | -1.8 |
| | Cl | 2.0 | 2.4 | 0.1 | 4.5 | -1.1 | -1.1 | 6.8 |

Owing to its tetrahedral geometry, the \mathbf{a}_1 symmetry normal mode of methane is inactive. However, the symmetry is broken by substituting one of the hydrogen atoms by deuterium. CH₃D belongs to the same point group as methylfluoride and methylchloride, therefore, the \mathbf{a}_1 stretch of CH₃D is active as the amplitude of the vibration of the C–D bond is larger than those for the C–H bonds in this normal mode.

Aligning the stretching bonds with the z axis, the contributions from the x and y directions are negligible. The total intensity is determined completely by changes in the electron density that are in proper alignment with the z direction. This is not surprising considering that the normal coordinate displacements for this vibrational motion are parallel to the z -axis, with the exception of small x and y components of the angular bending of CH bonds.

Atomic contribution decomposition reveals that the intensity of this normal mode is determined almost only by contributions from the central C and terminal D, F and Cl atoms. The contributions from the remaining atoms are small approaching 15% of the intensity for CH₃Cl, 1.5% for CH₃F and 8% for CH₃D.

The sign of the CTDP term, which corresponds to the interaction between CT and DP, is negative for all the three molecules, meaning that CT and DP vectors

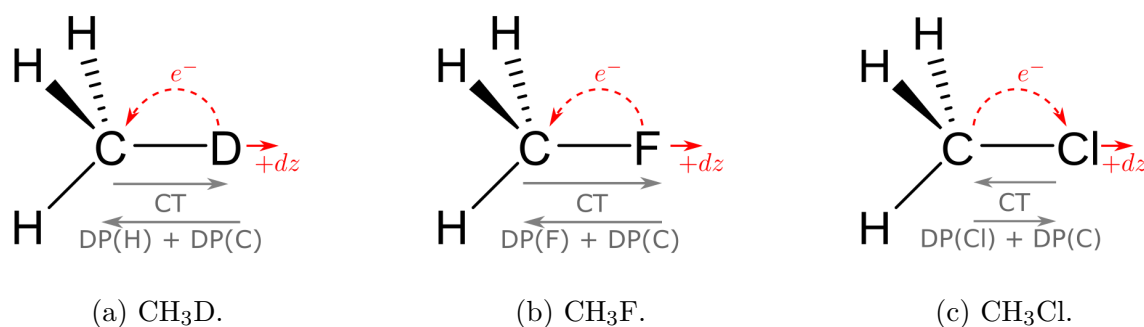


Figure 6.4: Structure of the z component of the atomic polar tensor of D, F and Cl atoms aligned with the Cartesian z direction.

are of opposite sense. Physically it can be interpreted as a counterpolarization effect. As the atoms are displaced from their equilibrium positions, electron density starts to concentrate in the domain of one atom and diminishes in others. In order to better accommodate these electronic changes, the electronic densities around the nuclei need to relax. As consequence, DP contributions counterbalance those owing to the charge transfer.

Charge contributions correspond to the equilibrium geometry atomic charges weighted by their normal coordinate displacements. The AIM charges in deuterated methane are small and plays no important role in the infrared intensity. However, $56.79 \text{ km} \cdot \text{mol}^{-1}$ of methyl fluoride intensity arises from the F and C atomic charge contributions. The magnitudes of atomic charges and their interactions with CT and DP accounts to nearly half of the bond stretching intensity.

The molecular dipole moment derivative can also be evaluated in terms of equation 6.8. With the carbon atom utilized as reference, the Cartesian components of CT terms become bond properties. For each system, the CD, CF or CCl bond along the Cartesian z axis is stretched and the changes in the dipole moment are components of the zz term of the atomic polar tensor of H, F or Cl.

All dipolar polarization contributions in methane arise from deformations of the carbon atom electron density. This is expected since hydrogen atoms are small and their electron densities are not easily deformed. This polarization contribution is counterbalanced by the charge transfer of the C–H bond. The grey arrows in figure 6.4 represent the z contribution of the charge transfer vector and of the dipolar polarization. The curved dotted arrow shows the tendency of electron transfer with small displacements of H. With this displacement, electrons tends to flow to carbon, triggering its counterpolarization.

The same CT mechanism is observed for CH₃F, with the exception that F contributes, albeit modestly, to the total DP term. However, methyl chloride acts in a different way. As Cl is displaced, the tendency of the electron density is to concentrate on the chlorine and polarize in the opposite direction. The major contribution to the total DP term comes from the changes in the polarizable electron density.

6.5 CCTDP Partitioning of Transition States

CCTDP contributions for the TS imaginary normal mode are presented in Table 6.2. The data was obtained with equation 6.8. Contributions from all X atoms

are grouped and displayed as 3X. Even when summed together, contributions from X are always small when compared to contributions from other atoms. This implies that their low contribution to the infrared intensities is intrinsic and not a consequence of cancellation between its individual terms. The electron density changes occurring during the vibration emerge mostly from terms belonging to Nu and LG. For these atoms, terms that are dependent on charge transfer are always higher in magnitude. This is equivalent to stating that the molecular dipole moment derivative is mostly determined by the transference of electrons between atomic basins, while reorganization of electronic densities inside each basin, expressed by dipolar polarization terms, are less prominent.

Almost all of the transition states have positive CTDP interaction terms in Table 6.2. This indicates that the charge transfer-counterpolarization effect, which attenuates intensities in the stable molecules, is not operative in transition states, resulting in much larger intensities than those found for the reactants and products. Only $\text{Cl}^- \text{CF}_3\text{F}$ and $\text{Cl}^- \text{CF}_3\text{H}$ transition states exhibit counterpolarization. However they do have larger intensities owing to the dominance of the charge and charge transfer terms as well as their interactions. The large carbon atomic charge contributions for these transition states as well as for $\text{F}^- \text{CF}_3\text{H}$, as can be seen in Table 6.3, is due to the presence of the highly electronegative fluorine substituents compared with hydrogen in all the other transition states.

Adopting the referential system of equation 6.8 the CT term is expressed as a property of C–X, C–Nu and C–LG bonds. The term $CT(\text{Nu} \rightarrow \text{C})$ and $CT(\text{C} \rightarrow \text{LG})$ are interpreted as charge transfer between Nu and C and between C and LG respectively. Since the contributions from X are negligible, it is convenient to analyse the contributions of the principal atoms, i.e. Nu, C and LG, that are aligned with the z axis. The results are also presented in atomic units in Table 6.3

Charge transfer terms for Nu and LG with carbon always have the same sign, as the nucleophile is expected to lose electrons while an increase in electronic charge occurs in the leaving group. To understand those terms, we return to equation 6.8 and the positive phase of the normal coordinate.

The positioning system adopted in Figure 6.3 ensures that, the quantity $(r_{\text{Nu}} - r_{\text{C}})$ is positive while $(r_{\text{LG}} - r_{\text{C}})$ is negative, implying that $\frac{\partial q_{\text{Nu}}}{\partial Q_k} > 0$ and $\frac{\partial q_{\text{LG}}}{\partial Q_k} < 0$. This suggests that, in the positive phase of the Q_k normal mode, Nu is losing electrons and LG is gaining electrons. The transition state is unique for both directions, from reactants to products and from products to reagents, and the CCTDP contributions are invariant with the phase. The electron density derivatives are always evaluated when the nucleophile is displaced in the positive direction of the IRC in Figure 6.1 That is, the derivative corresponds to the breaking of Nu–C bond. The TS is the same for both direct or reverse reaction and the same is valid for its infrared intensities. Proper definition of the phase that derivatives are being evaluated is necessary in order to preserve the physical interpretation of the system. Derivative values are available in the electronic supporting information material.

Taking into consideration the phase in the direction of products formation, one has: $\frac{\partial q_{\text{Nu}}}{\partial Q_k} > 0$ and $\frac{\partial q_{\text{LG}}}{\partial Q_k} < 0$. In other words, the charge transfer terms correspond nearly exclusively to the electron movement from the nucleophile to the leaving group, passing through C, which is consistent with the well-known S_N2 mechanism, represented in Figure 6.5.

Considering the average of the dipole moment derivatives for the nine transition states, the transference of electrons from Nu to LG accounts for $\frac{2}{3}$ of the total

Table 6.2: CCTDP contributions to the intensities (in $km \cdot mol^{-1}$) of the imaginary normal mode.

| TS | Atom | \mathcal{A}_{C^2} | \mathcal{A}_{CT^2} | \mathcal{A}_{DP^2} | \mathcal{A}_{2CCT} | \mathcal{A}_{2CDP} | \mathcal{A}_{2CTDP} |
|--------------|-------|---------------------|----------------------|----------------------|----------------------|----------------------|-----------------------|
| H^-CH_3H | C | -3.5 | 1310.1 | 271.5 | 297.5 | 139.3 | 1193.0 |
| | Nu | 169.4 | 1979.5 | 365.9 | 1182.8 | 511.9 | 1702.8 |
| | 3X | -12.6 | 404.6 | 119.5 | 43.7 | 40.8 | 449.0 |
| | LG | 169.4 | 1994.0 | 361.8 | 1186.2 | 509.7 | 1700.1 |
| | Total | 322.8 | 5688.2 | 1118.7 | 2710.2 | 1201.8 | 5044.8 |
| F^-CH_3F | C | 22.5 | 254.5 | 78.4 | 155.3 | 86.1 | 282.4 |
| | Nu | 12.7 | 29.1 | 10.6 | 45.0 | 26.1 | 35.2 |
| | 3X | -2.5 | 14.3 | 2.0 | -1.2 | -2.4 | 11.4 |
| | LG | 12.7 | 29.1 | 10.5 | 45.0 | 26.0 | 35.0 |
| | Total | 45.5 | 326.9 | 101.4 | 244.0 | 135.8 | 364.0 |
| Cl^-CH_3Cl | C | 3.9 | 967.0 | 19.0 | 135.4 | 19.1 | 270.7 |
| | Nu | 3.5 | 65.0 | 0.7 | 41.2 | 5.3 | 14.2 |
| | 3X | 0.0 | 1.0 | 0.1 | -0.3 | 1.5 | 0.5 |
| | LG | 3.5 | 65.0 | 0.8 | 41.2 | 5.3 | 14.5 |
| | Total | 10.8 | 1097.9 | 20.5 | 217.5 | 31.2 | 299.8 |
| F^-CH_3H | C | 23.0 | 840.0 | 111.3 | 345.9 | 136.4 | 616.2 |
| | Nu | -3.2 | 44.3 | 5.2 | 4.9 | 1.9 | 29.2 |
| | 3X | 17.9 | 239.2 | 37.0 | 132.9 | 55.7 | 193.2 |
| | LG | 167.5 | 781.4 | 42.0 | 766.7 | 206.4 | 381.3 |
| | Total | 205.2 | 1904.8 | 195.5 | 1250.4 | 400.4 | 1220.0 |
| F^-CF_3H | C | 443.9 | 634.0 | 5.5 | 1067.2 | 99.5 | 117.4 |
| | Nu | 16.1 | 43.2 | -1.0 | 53.9 | -3.7 | -3.2 |
| | 3X | 46.0 | 91.4 | 1.0 | 130.0 | 12.0 | 16.7 |
| | LG | 280.4 | 626.2 | 8.1 | 843.6 | 98.5 | 143.9 |
| | Total | 786.4 | 1394.8 | 13.6 | 2094.6 | 206.3 | 274.7 |
| Cl^-CH_3F | C | 8.8 | 536.4 | 20.3 | 147.9 | 28.8 | 208.4 |
| | Nu | -0.1 | 2.7 | -0.1 | 0.0 | -0.2 | 0.0 |
| | 3X | 4.1 | 47.7 | 0.3 | 30.8 | 4.5 | 10.7 |
| | LG | 10.2 | 54.4 | 3.4 | 64.3 | 13.8 | 28.2 |
| | Total | 23.0 | 641.2 | 23.8 | 243.0 | 46.8 | 247.2 |
| Cl^-CF_3F | C | 509.9 | 973.3 | 102.9 | 1409.3 | -459.6 | -633.9 |
| | Nu | 0.3 | -2.3 | 0.1 | -1.3 | -0.3 | 0.4 |
| | 3X | 19.5 | 38.9 | 1.5 | 55.2 | -11.9 | -17.0 |
| | LG | 54.8 | 56.2 | -3.8 | 115.5 | -13.5 | -4.8 |
| | Total | 584.5 | 1066.0 | 100.8 | 1578.7 | -485.2 | -655.3 |
| Cl^-CH_3H | C | 8.9 | 1338.3 | 34.7 | 403.6 | 76.2 | 438.3 |
| | Nu | -1.7 | 26.0 | 0.4 | 1.3 | 0.0 | 6.3 |
| | 3X | 10.4 | 245.5 | 4.9 | 105.5 | 15.1 | 69.3 |
| | LG | 181.7 | 978.5 | 6.4 | 926.2 | 100.9 | 178.9 |
| | Total | 199.3 | 2588.3 | 46.4 | 1436.5 | 192.3 | 692.8 |
| Cl^-CF_3H | C | 709.0 | 2352.4 | 45.2 | 2595.7 | -362.5 | -653.3 |
| | Nu | 24.4 | 84.8 | 1.4 | 91.7 | -11.1 | -21.0 |
| | 3X | 64.2 | 207.0 | 2.0 | 231.5 | -23.8 | -43.1 |
| | LG | 379.2 | 554.5 | 6.1 | 961.5 | -109.6 | -118.5 |
| | Total | 1176.9 | 3198.7 | 54.7 | 3880.4 | -507.0 | -835.8 |

intensity. Not only are the normal coordinates of the imaginary mode related to the IRC, but the electronic changes that occur during the reaction seem to be described by the CCTDP partitioning of infrared intensities. For symmetric transition states, H^-CH_3H , F^-CH_3F and Cl^-CH_3Cl the CT contributions are the same for Nu-C and LG-C, which is consistent with the fact that, for these reactions, the initial and final points are the

Table 6.3: Atomic contributions and bond contributions (in $e.amu^{1/2}$) for the imaginary normal mode of transition states.

| TS | Atomic Contributions | | | Bond Contribution | |
|--------------|----------------------|--|---|-------------------|---|
| | Atom | $\left(\frac{\partial p}{\partial Q}\right)_{(C)}$ | $\left(\frac{\partial p}{\partial Q}\right)_{(DP)}$ | Bond | $\left(\frac{\partial p}{\partial Q}\right)_{(CT)}$ |
| H^-CH_3H | C | -0.006 | 0.056 | - | - |
| | Nu | 0.302 | 0.418 | Nu-C | 1.113 |
| | LG | 0.302 | 0.416 | LG-C | 1.130 |
| | Sum | 0.598 | 0.891 | Sum | 2.243 |
| F^-CH_3F | C | 0.107 | 0.182 | - | - |
| | Nu | 0.060 | 0.065 | Nu-C | 0.277 |
| | LG | 0.060 | 0.065 | LG-C | 0.277 |
| | Sum | 0.228 | 0.312 | Sum | 0.554 |
| Cl^-CH_3Cl | C | 0.038 | 0.037 | - | - |
| | Nu | 0.034 | 0.033 | Nu-C | 0.530 |
| | LG | 0.034 | 0.033 | LG-C | 0.530 |
| | Sum | 0.105 | 0.104 | Sum | 1.060 |
| F^-CH_3H | C | 0.051 | 0.095 | - | - |
| | Nu | 0.054 | 0.136 | Nu-C | 0.377 |
| | LG | 0.374 | 0.120 | LG-C | 0.933 |
| | Sum | 0.480 | 0.352 | Sum | 1.310 |
| F^-CF_3H | C | 0.507 | -0.235 | - | - |
| | Nu | 0.016 | 0.160 | Nu-C | 0.122 |
| | LG | 0.321 | 0.234 | LG-C | 0.971 |
| | Sum | 0.843 | 0.159 | Sum | 1.093 |
| Cl^-CH_3F | C | 0.059 | 0.091 | - | - |
| | Nu | 0.029 | 0.005 | Nu-C | 0.515 |
| | LG | 0.068 | 0.043 | LG-C | 0.287 |
| | Sum | 0.156 | 0.138 | Sum | 0.802 |
| Cl^-CF_3F | C | 0.675 | -0.218 | - | - |
| | Nu | 0.025 | 0.031 | Nu-C | 0.732 |
| | LG | 0.073 | 0.083 | LG-C | 0.330 |
| | Sum | 0.773 | -0.104 | Sum | 1.062 |
| Cl^-CH_3H | C | 0.020 | 0.021 | - | - |
| | Nu | 0.031 | 0.101 | Nu-C | 0.691 |
| | LG | 0.412 | 0.053 | LG-C | 0.905 |
| | Sum | 0.464 | 0.175 | Sum | 1.597 |
| Cl^-CF_3H | C | 0.662 | -0.348 | - | - |
| | Nu | 0.014 | 0.101 | Nu-C | 0.748 |
| | LG | 0.354 | 0.163 | LG-C | 0.927 |
| | Sum | 1.030 | -0.083 | Sum | 1.676 |

same.

Figure 6.6 shows a bar plot of the CCTDP contributions to the dipole moment derivative. One can see that CT is always the largest contribution, followed by charge, except for the H^-CH_3H system where polarization is substantially larger than the charge. The substitution of $X = H$ by $X = F$ increases the charge term since the introduction of an electronegative substituent increases the magnitude of the carbon atomic charge. Dipolar polarization terms are comparable to charge contribution or even smaller. It follows the opposite trend: whereas the charge on carbon becomes more positive and, as consequence, its polarization decreases, the DP contribution is attenuated. This is expected since electronegative atoms concentrate the electron density nearer to the nuclei which prevents it from deforming.

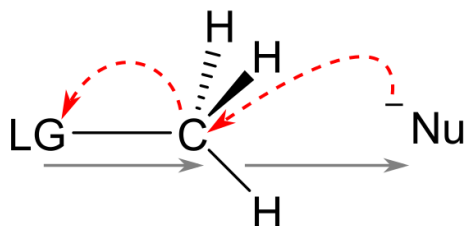


Figure 6.5: SN2 mechanism represented by red curved arrows. Grey arrows correspond to the weighted charge transfer vectors that points to the positive end. (Polarity convention $- \rightarrow +$).

Earlier work by Matta and co-workers[143] investigating atomic charges and dipoles along the reaction coordinate for $\text{CH}_4 + \cdot\text{X} \rightarrow \text{CH}_3\cdot + \text{HF}$, $\text{X} = \text{F}, \text{Cl}$ also finds greater contribution from CT for all the systems investigated, specially with $\text{X} = \text{F}$, whereas dipolar polarization terms increase when the more polarizable Cl atom is introduced.

When compared to the isolated reagent, transition states express greater intensity and greater CCTDP contributions, as clearly illustrated in Figure 6.6. While the CT term is enhanced by the charge transference from Nu^- to LG, the charge contributions are enhanced by the distribution of the nucleophile's negative charge. Dipolar polarization for TS and reagents are of comparable magnitude, except for $\text{H}^- \text{CH}_3\text{H}$, for which the introduction of an extra electron causes a significant increase in the system's polarizability and, in combination with the larger displacements of hydrogen owing to its lower mass, magnifies the DP contribution.

Contributions from the substituent X atoms and normal coordinate displacements of Nu, C and LG along the x and y axes can be neglected. The second column contains intensity values corresponding to dipole moment changes occurring only along the z -axis. The z direction was chosen since it is aligned with the reaction coordinate represented in Figure 6.3. These values are very close to the total intensities. Contributions from only the z direction, as show in column 2, sum to almost all the total intensities meaning that the change in the molecular dipole moment has the same direction as the reaction path, i.e. the changes in the electron density occur along the normal coordinates that define the IRC.

Figure 6.7 summarizes the data of Table 6.4. The ordinate contains the intensities calculated analytically by GAUSSIAN with the abscissa representing the intensities calculated numerically, including only contributions in the z direction. The slope, obtained by a linear regression, of the black dots (all atoms) for the nine TS is equal to 1.03 with a correlation coefficient of 0.9994. For the white dots, corresponding to the Nu, C and LG atoms, the slope is 1.07 and the correlation coefficient is 0.9975. The data also show that the contributions of the X atoms are small and can be neglected. Contributions that are not aligned with the reaction coordinate are also negligible. The data show that changes in electronic densities occur in the same direction of the reaction coordinate and atoms that are not directly involved in the reaction mechanism are mere spectators and influence the reaction by secondary effects, such as increasing or decreasing the carbon

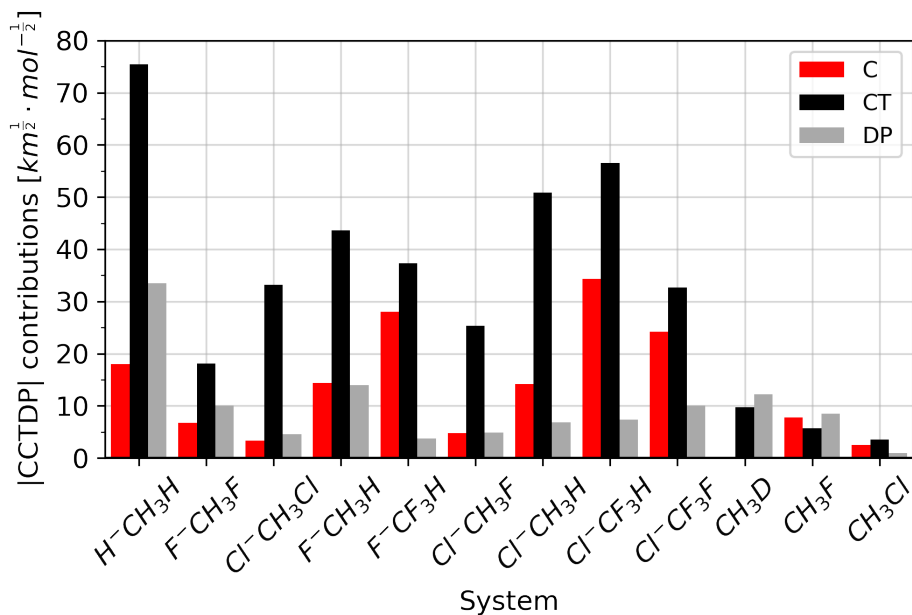


Figure 6.6: Charge, charge transfer and dipolar polarization contributions for the molecular dipole moment derivative [$e \cdot amu^{-1/2}$].

Table 6.4: IR intensities (in $km \cdot mol^{-1}$) of the imaginary normal modes.

| TS | \mathcal{A}^i | \mathcal{A}_z^{ii} | $\mathcal{A}_{Nu,C,LG}^{iii}$ | $\mathcal{A}_{Nu,C,LG;z}^{iv}$ |
|------------------------------------|-----------------|----------------------|-------------------------------|--------------------------------|
| H ⁻ CH ₃ H | 16086.6 | 15653.6 | 15041.6 | 15069.1 |
| F ⁻ CH ₃ F | 1217.7 | 1199.4 | 1196.1 | 1239.1 |
| Cl ⁻ CH ₃ Cl | 1676.2 | 1672.0 | 1675.1 | 1572.0 |
| F ⁻ CH ₃ H | 5176.3 | 5015.5 | 4911.3 | 4904.9 |
| F ⁻ CF ₃ H | 4770.4 | 4380.4 | 4455.1 | 4384.2 |
| Cl ⁻ CH ₃ F | 1225.1 | 1212.3 | 1217.5 | 1179.5 |
| Cl ⁻ CF ₃ F | 2189.5 | 2219.5 | 2198.0 | 2922.1 |
| Cl ⁻ CH ₃ H | 5155.6 | 5090.1 | 6448.9 | 4996.8 |
| Cl ⁻ CF ₃ H | 6967.8 | 6430.3 | 5066.7 | 7017.7 |

ⁱ Total intensity. ⁱⁱ Only z -axis contributions. ⁱⁱⁱ Only contributions from Nu, C and LG. ^{iv} Only z -axis contributions from Nu, C and LG.

charge.

6.6 Charges Along the Reaction Coordinate

Figure 6.8 displays the changes in atomic charge along the reaction coordinate for the nine NuCX₃LG⁻. Since the aim of this work is not to analyse the thermodynamics of the reactions, but changes in the electronic densities of the reacting systems, the reaction paths were restricted to a region near the TS. Because there is no analytical second derivative method at the QCISD level¹, the IRCs were determined at the MP2 level. However, for each point, the electronic properties and energies were calculated at the QCISD/aug-cc-pVTZ level.

For each point along the reaction coordinate, QTAIM atomic charges and

¹See GAUSSIAN09 user's reference manual

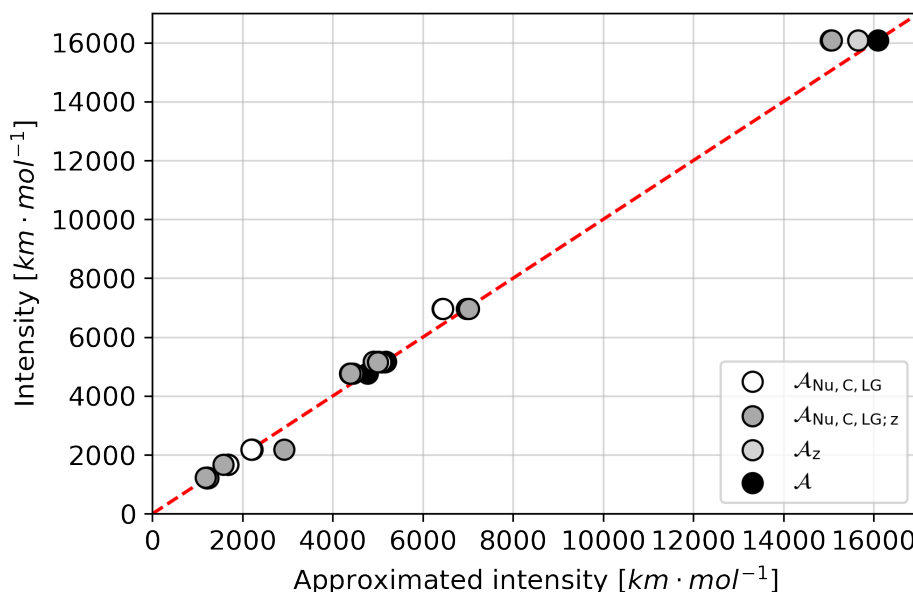


Figure 6.7: Comparison between the intensities calculated with all atomic terms in all three Cartesian directions and the intensities calculated using only atomic contributions in z direction (light grey dots), using only contributions from the Nu, C and LG in z directions (dark grey dots) and using only contributions from the Nu, C and LG in all directions (white dots).

dipoles were obtained. In the first three cases, i.e. $\text{H}^- \text{CH}_3\text{H}$, $\text{F}^- \text{CH}_3\text{F}$ and $\text{Cl}^- \text{CH}_3\text{Cl}$, due to the system's symmetry, the Nu and LG charges are mirrored. Every fraction of electron density lost by the Nu is captured by the leaving group. Throughout the entire process, the carbon charge remains nearly constant. If the IRC symmetry is broken, the charge of the spectator atoms remains relatively constant, but the carbon charge will change. The difference between black and red curves is related to the carbon charge variation, i.e. the solid grey curve. This means that some of the nucleophile charge will end up on the electrophilic center.

Although the charges of the spectator atoms do not change along the energy profile for the systems studied here, Santos Jr. et al.[128] found that QTAIM descriptors, such the Laplacian at the bond critical point, of the CX bond changes with the nature of X.

Comparing the tendency displayed in the plots of Figure 6.8 with the data in Table 6.3 one can notice that the charge transfer terms are also influenced by the symmetry of the path. In fact, it is expected, regarding mechanical effects, that the difference between the charge transfer term of equation 6.8, $CT(\text{Nu} \rightarrow \text{C})$ and $CT(\text{C} \rightarrow \text{LG})$, is related to the change in carbon's atomic charge.

Considering that these charge transfers reflect the tendency of the variation of the C atomic charge throughout the entire reaction, we define the quantity $\Delta q_C = q_C^{+\infty} - q_C^{-\infty}$ that corresponds to the difference between the carbon charge in the product and in the reactant. From figure 6.9 one can see that Δq_C correlates linearly with the $CT(\text{C} \rightarrow \text{LG}) - CT(\text{Nu} \rightarrow \text{C})$ difference, with a correlation coefficient of $R^2 = 0.953$ and slope equal to 1.13 ± 0.09 .

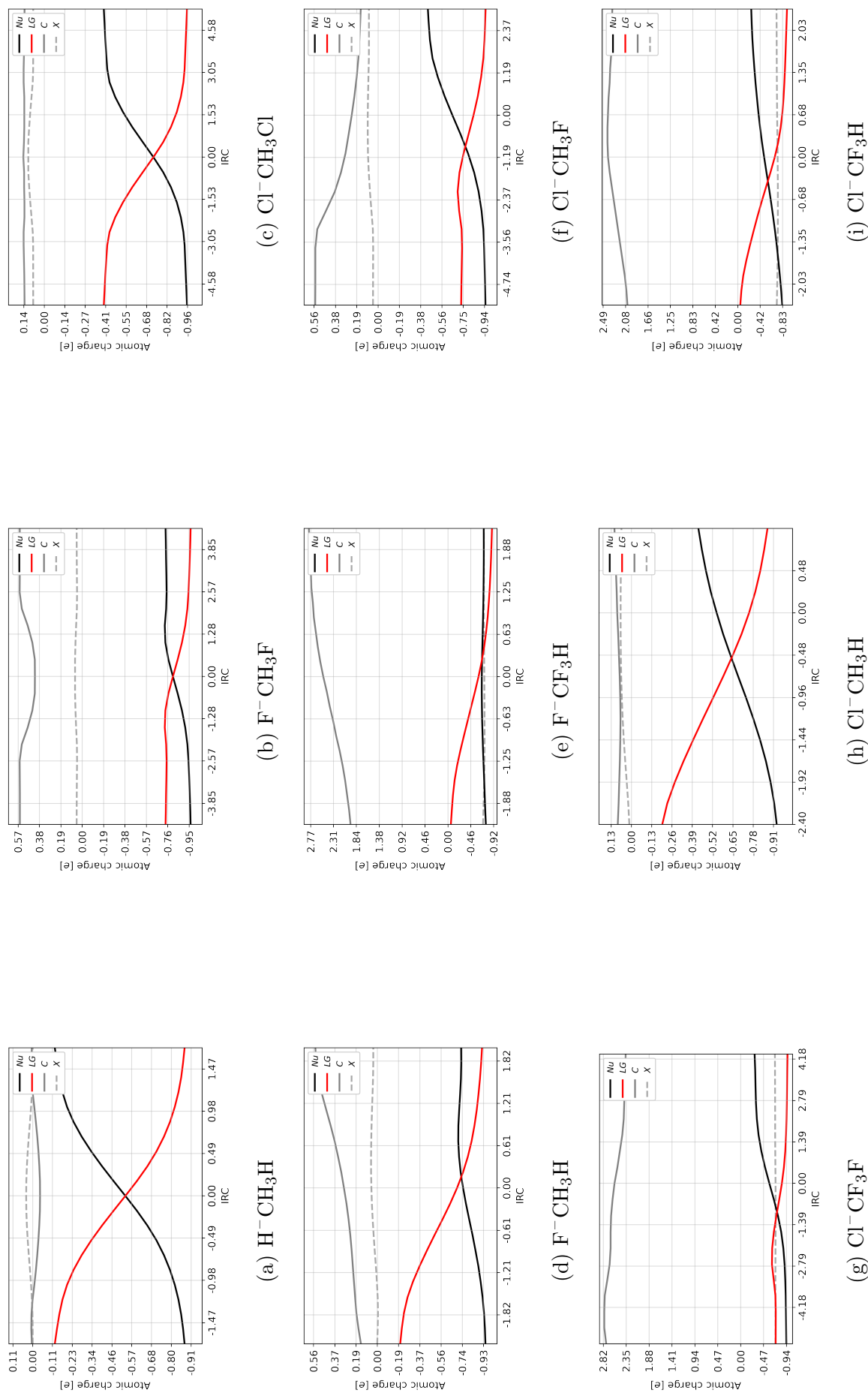


Figure 6.8: Atomic AIM charges [e] along the IRC path of nine transition states. In black: Nu; red: LG; light grey: X and ; dark grey: C.

The last contribution to be analyzed is the dipolar polarization. In the TS presented in this work, DP contributions arise mostly from the displacement of the negative charge from the positive side of z axis to the negative side. Atoms other than Nu and LG remains almost non-polarized. Other polarization effects emerge when carbon becomes polarized by the substitution of hydrogen by a halogen atom.

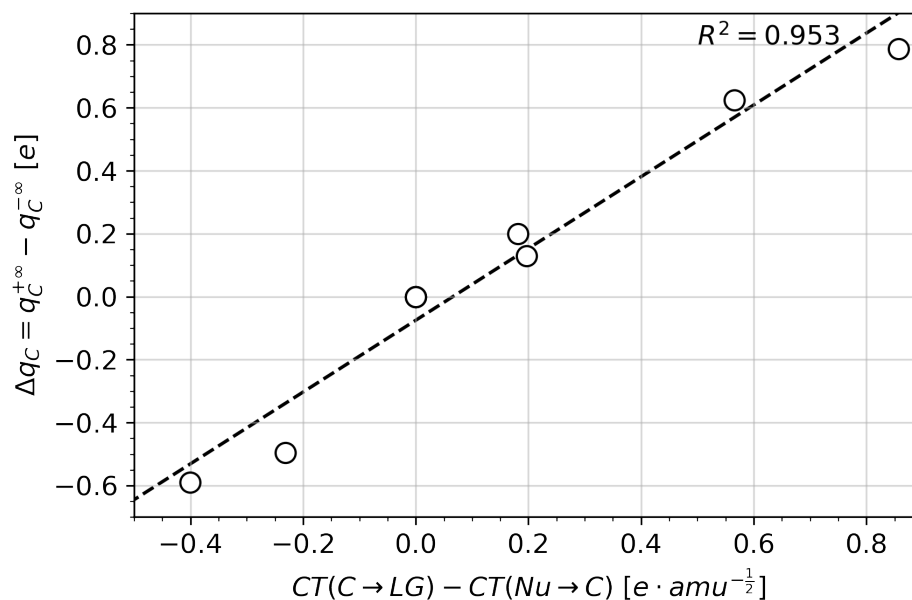


Figure 6.9: Variation of carbon charge after $q_C^{+\infty}$ and before $q_C^{-\infty}$ the reaction against the difference between charge transfer of the nucleophile and leaving group. The regression line is represented by the dotted line in the graph.

6.7 Concluding Remarks

The infrared intensities of the imaginary bands result only from contributions of atoms that participate actively in the reaction, that is Nu, LG, and C. For the systems presented in this chapter, the principal contributions are the charge transfers between the nucleophile and the leaving group through the carbon atom. As the atoms vibrate inside the normal coordinate of imaginary frequency, the changes in the molecular electronic density are consistent with the mechanism of the reaction itself and the direction of the CT vectors corresponds to the movement of electrons as described by the curved arrow representation of the reaction mechanism.

The difference between the charge transfer of the nucleophile and the charge transfer of the leaving group indicates the tendency of carbon to receive charge along the reaction coordinate. Dipolar polarization contributions result from the inversion of the molecular geometry and from the substitution of LG by Nu with different electronegativities. Changes in the molecular geometry following the IRC path are similar to those described by the normal coordinates. Since this is a consequence of the IRC definition, not only is this true for S_N2 reactions but also it can be generalized to any system.

This chapter contains excerpts from texts previously published by the author. The following material was reprinted with permission:

Duarte, L. J., Silva, A. F., Richter, W. E., Bruns, R. E. *Infrared intensification and hydrogen bond stabilization: Beyond point charges*. The Journal of Physical Chemistry A, 123(30), 6482-6490, 2019, American Chemical Society.

Chapter 7

Energetic Origins of Force Constants

The infrared spectrum contains a wealth of information about the molecular structure. Through detailed manipulations, the frequencies can be reduced to bond and angle force constants, whereas the intensities can be used to investigate the molecular dipole moment derivatives. Insights about other molecular properties, such as symmetry and intermolecular interactions can also be obtained.

Until this point, the use of the QTAIM atomic charges and dipoles allowed the decomposition of the infrared intensity through the Charge – Charge Transfer – Dipolar Polarization model, enabling the investigation of the electron density dynamics during a molecular vibration using atomic parameters.

However, not only electronic properties can be determined by QTAIM, but the molecular energy can also be partitioned into atomic contributions following the Interacting Quantum Atoms (IQA) energy decomposition scheme[6]. In this method, the system energy is divided into intra- and interatomic contributions. The intra-atomic contribution, E_{intra}^A , is related to the kinetic and potential energies of electrons inside an atomic basin, while the interatomic contributions V_{cl}^{AB} and V_{xc}^{AB} are, respectively the Coulomb and exchange-correlation potential between atomic basins A and B . These contributions reflect the ionic and covalent properties of chemical bonds and inter-molecular interactions. Within this partitioning scheme, the total system energy is:

$$E_{\text{total}} = \sum_{A=1}^N E_{\text{intra}}^A + \sum_{A=1}^{N-1} \sum_{B>A}^N V_{cl}^{AB} + \sum_{A=1}^{N-1} \sum_{B>A}^N V_{xc}^{AB} \quad (7.1)$$

Since force constants are second derivatives of the energy and the derivative of a sum equals the sum of derivatives, they can also be divided into IQA contributions. This is done by partitioning the Hessian matrix into IQA derivative matrices and performing the usual calculations to determine the vibrational modes.

In this chapter, a new dimension is added to the Hessian matrix in order to account for the different IQA terms. Wilson's **FG** method[144] is modified to be applied to the new 3-dimensional Hessian matrix in order to extract chemical bond information inherent in force constants.

7.1 The 3D Hessian Matrix

The following equations are a generalization of the **FG** method and the conversion from Cartesian to internal coordinates is described in detail in the works of McIntosh[145–149]. Herein, the main equations are presented with the proper modifications that are needed to deal with the new dimension of the Hessian matrix.

Consider the Hessian matrix, with dimensions $3N \times 3N$, where N is the number of atoms in the molecule. Each element h_{ij} is the second derivative of the total energy of the system with respect to Cartesian coordinates $\sigma = x, y, z$ of atoms i and j evaluated at their equilibrium positions, that is:

$$h_{ij} = h_{ji} = \frac{\partial^2 E_{\text{total}}}{\partial \sigma_i \partial \sigma_j} \quad (7.2)$$

The normal modes of vibration and frequencies can be obtained by transforming the Hessian matrix from the σ coordinates into their mass-weighted version, where each coordinate is weighted by its atomic mass. Let \mathbf{M} be the diagonal matrix containing triples of reciprocals of the square root of the atomic masses:

$$\mathbf{M} = \begin{bmatrix} \frac{1}{\sqrt{m_1}} & 0 & 0 & \dots & 0 & 0 & 0 \\ 0 & \frac{1}{\sqrt{m_1}} & 0 & \dots & 0 & 0 & 0 \\ 0 & 0 & \frac{1}{\sqrt{m_1}} & \dots & 0 & 0 & 0 \\ \vdots & \vdots & \vdots & \ddots & \vdots & \vdots & \vdots \\ 0 & 0 & 0 & \dots & \frac{1}{\sqrt{m_N}} & 0 & 0 \\ 0 & 0 & 0 & \dots & 0 & \frac{1}{\sqrt{m_N}} & 0 \\ 0 & 0 & 0 & \dots & 0 & 0 & \frac{1}{\sqrt{m_N}} \end{bmatrix} \quad (7.3)$$

and the mass-weighted Hessian is then obtained by:

$$\mathbf{H}^{\text{mw}} = \mathbf{M}^\dagger \mathbf{H} \mathbf{M} \quad (7.4)$$

To find the frequencies of vibrations, one needs to solve the eigenvalue problem:

$$\mathbf{A}^\dagger \mathbf{H}^{\text{mw}} \mathbf{A} = \mathbf{\Lambda} \quad (7.5)$$

where $\mathbf{\Lambda}$ is the diagonal matrix of eigenvalues λ_i and \mathbf{A} is the matrix that diagonalizes the mass-weighted Hessian and is formed by the juxtaposition of eigenvectors of \mathbf{H}^{mw} . From the $3N$ eigenvalues, only $3N - 6$ (or $3N - 5$ if the molecule is linear) correspond to the vibrational motion, whereas the others correspond to translations and/or rotations. The frequencies of vibration, in cm^{-1} , are given by:

$$\nu_i = \left(\frac{\lambda_i}{4\pi^2 c^2} \right)^{\frac{1}{2}} \quad (7.6)$$

However, since the energy of the system can be decomposed to IQA contri-

bution terms, the same is true for its derivatives. Following the IQA partitioning, one has:

$$\frac{\partial^2 E_{\text{total}}}{\partial \sigma_i \partial \sigma_j} = \sum_{A=1}^N \frac{\partial^2 E_{\text{intra}}^A}{\partial \sigma_i \partial \sigma_j} + \sum_{A=1}^{N-1} \sum_{B>A}^N \frac{\partial^2 V_{cl}^{AB}}{\partial \sigma_i \partial \sigma_j} + \sum_{A=1}^{N-1} \sum_{B>A}^N \frac{\partial^2 V_{xc}^{AB}}{\partial \sigma_i \partial \sigma_j} = \sum_{k=1}^{N^2} \frac{\partial^2 E_k}{\partial \sigma_i \partial \sigma_j} \quad (7.7)$$

where each E_k corresponds to one of the *intra* or *interatomic* IQA contributions. The total number of IQA contributions is N^2 , corresponding to the sum of N intra-atomic contributions, $\frac{N(N-1)}{2}$ Coulomb contributions and $\frac{N(N-1)}{2}$ exchange-correlation contributions. \mathbf{H}^{mw} is, therefore, a sum of matrices of IQA term derivatives, i.e. $\sum \mathbf{H}_{\mathbf{k}}^{\text{IQA,mw}}$. Equation 7.5 is rewritten as:

$$\mathbf{A}^\dagger \left(\sum_{k=1}^{N^2} \mathbf{H}_{\mathbf{k}}^{\text{IQA,mw}} \right) \mathbf{A} = \sum_{k=1}^{N^2} \Lambda_{\mathbf{k}}^{\text{IQA}} \quad (7.8)$$

with $\sum_{k=1}^{N^2} \Lambda_{\mathbf{k}}^{\text{IQA}} = \Lambda$. Since Λ is diagonal, one has:

$$\sum_{k=1}^{N^2} \lambda_{ijk}^{\text{IQA}} = \begin{cases} \lambda_{ij} & \text{if } i = j \\ 0 & \text{if } i \neq j \end{cases} \quad (7.9)$$

Equation 7.9 implies that a diagonal element of $\Lambda_{\mathbf{k}}^{\text{IQA}}$, $\lambda_{i,j=i,k}^{\text{IQA}}$ is the contribution of the IQA component k to the frequency of normal mode ν_i . The idea is visualized in Figure 7.1. This procedure will identify which IQA contributes the most to the frequency value of the normal modes.

With the exception of the most simple cases, the frequency of vibration is not dependent on only one force constant, but on a combination of force constants and their interactions. For this reason, interpreting the IQA decomposition of frequencies can be difficult. However, if one applies the decomposition method to the force constants itself, then chemical information can be easily accessed. This can be done by the use of internal coordinates, which is described in the following section.

7.2 Force Constants in Internal Coordinates

In order to calculate, and decompose the force constants into its IQA components, one needs first to convert the Cartesian Hessian into the the Wilson's \mathbf{F} matrix, that contains the force constants, and their interactions, expressed in internal coordinates. To do this, it is necessary to define the \mathbf{B} matrix, that converts the $3N \times 1$ Cartesian coordinate matrix, \mathbf{X} , into internal coordinates matrix, \mathbf{R} :

$$\mathbf{B}\mathbf{X} = \mathbf{R} \quad (7.10)$$

The process of setting-up the \mathbf{B} matrix is tedious and can be found elsewhere in the literature[145] . Different authors have distinct, although equivalent, definitions

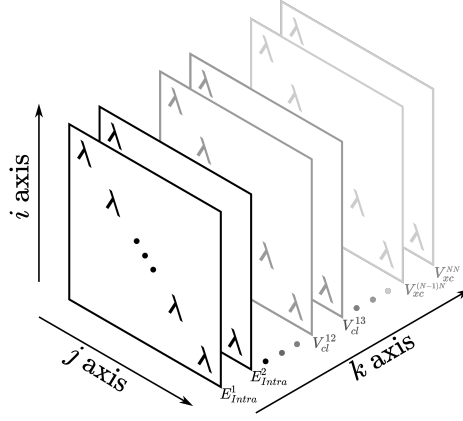


Figure 7.1: Structure of $\Lambda_{\mathbf{k}}^{\text{IQA}}$ matrices. Moving along the k -axis, each λ_{ijk} corresponds to the contribution of energy component k to the eigenvalue of normal mode j . Since their sum equals zero, off-diagonal elements are not represented in the figure. The sum over k results in the eigenvalues matrix Λ .

for the internal coordinates. To avoid any ambiguity the derivation of the \mathbf{B} matrix for ethylene is presented in the appendix as an example. We start by calculating the pseudo-inverse of \mathbf{B} by:

$$\mathbf{B}^{-1} = \mathbf{M}^2 \mathbf{B}^\dagger \mathbf{G}^{-1} \quad (7.11)$$

\mathbf{G} contains the inverse of the kinetic energy terms and its inverse, \mathbf{G}^{-1} , is given by:

$$\mathbf{G}^{-1} = \mathbf{D} \mathbf{\Phi}^{-1} \mathbf{D}^\dagger \quad (7.12)$$

where \mathbf{D} and $\mathbf{\Phi}$ are, respectively, the eigenvectors and the diagonal eigenvalue matrices of \mathbf{G} . Eventual problems with redundant internal coordinates can be solved by the method described by Gussoni and Zerbi[150]. The force constants in internal coordinates are then obtained as follows:

$$\mathbf{F} = \mathbf{B}^{\dagger-1} \mathbf{H} \mathbf{B}^{-1} \quad (7.13)$$

A detailed derivation can be found elsewhere[149]. The decomposition of the force constants into the IQA contributions is done using equation 7.7:

$$\sum_{k=1}^{N^2} \mathbf{F}_{\mathbf{k}}^{\text{IQA}} = \mathbf{B}^{\dagger-1} \left(\sum_{k=1}^{N^2} \mathbf{H}_{\mathbf{k}}^{\text{IQA}} \right) \mathbf{B}^{-1} \quad (7.14)$$

Each $F_{\mathbf{k}}^{\text{IQA}}$ is a matrix containing the contribution of the k^{th} IQA term of \mathbf{F} .

7.3 Calculating the IQA Hessian

Since there is no analytical method to obtain the second derivative of each IQA term, the construction of each $\mathbf{H}_{\mathbf{k}}^{\text{IQA}, \text{mw}}$ has to be done numerically. From the equilibrium structure, new geometries are generated by displacing the atoms in the positive and

negative direction of each Cartesian axis. For each new geometry, the wavefunction is calculated by GAUSSIAN16[151], from which the IQA terms are obtained using AIMAll. The derivatives are calculated by the Theovib python library as described in appendix E.

All molecules had their geometries optimized by GAUSSIAN 16[151] at the B3LYP/aug-cc-pVTZ level of theory. The use of DFT is justified by the number of single point calculations that are needed to obtain the 3D-Hessian matrix. AIM properties such as IQA energies, atomic charges and dipoles were obtained by AIMAll[102] using the default integration grids. The non-equilibrium geometries utilized to obtain the numerical derivatives were generated with Theovib. Theovib also performed the infrared analysis, including the calculations of the \mathbf{B} matrix, infrared intensities and IQA force constants.

7.4 QTAIM IR Spectra

Figure 7.2 contains an illustrative example for water, the red lines are obtained using only AIM parameters, the dotted lines are the spectrum obtained by Gaussian and the gray shadow peaks are the experimental data from the NIST/PNNL library. One will notice that the calculated curves are shifted to the right, as consequence of the level of theory, which produces only an approximate electronic structure, and of the potential energy surface anharmonicity. No scaling factors were applied, since it will equally affect all IQA contributions, thus having no impact on the interpretation of our results.

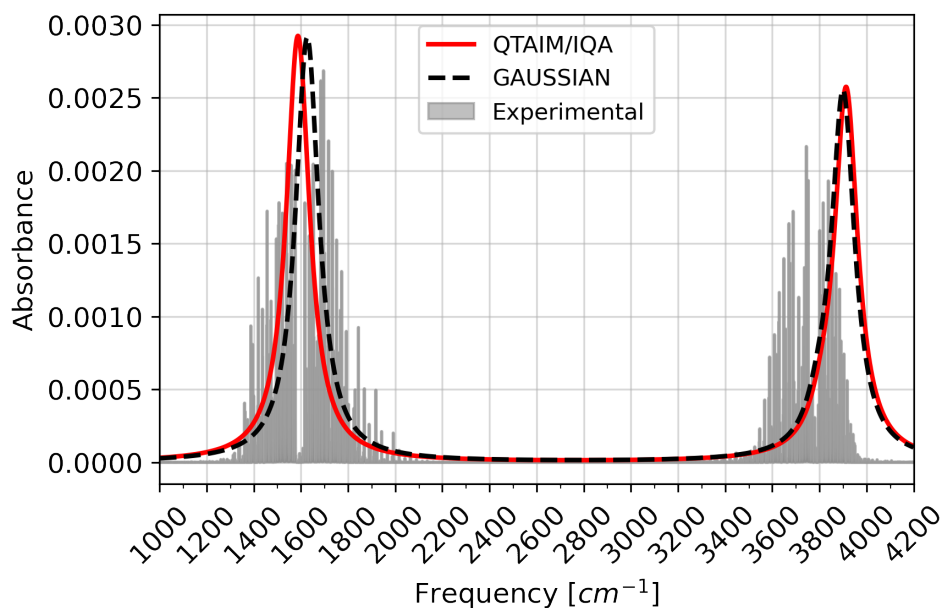


Figure 7.2: Infrared spectra of H_2O obtained by three different methods: Analytically calculated by Gaussian16 (dotted black line), numerically calculated with AIM parameters (red line) and, experimentally obtained from PNNL database. Calculated bands were simulated using a Lorentz distribution.

The differences between the Gaussian and the QTAIM spectra are caused by numerical errors from two distinct sources. First, the recovery error for the IQA parameters, that is measured by the difference between the wavefunction energy and the

sum of all IQA terms¹. Second the numerical error of the IQA/AIM charges and dipole derivatives.

The force constants in internal coordinates, calculated only using IQA derivatives, are also in good agreement with the ones calculated by Gaussian and with the experimental data. Figure 7.3 compares the results obtained with IQA terms and the 3D-Hessian matrix. Our results are in good agreement with the experimental (MAE = $0.60 \text{ mdyne} \cdot \text{\AA}^{-1}$) data.

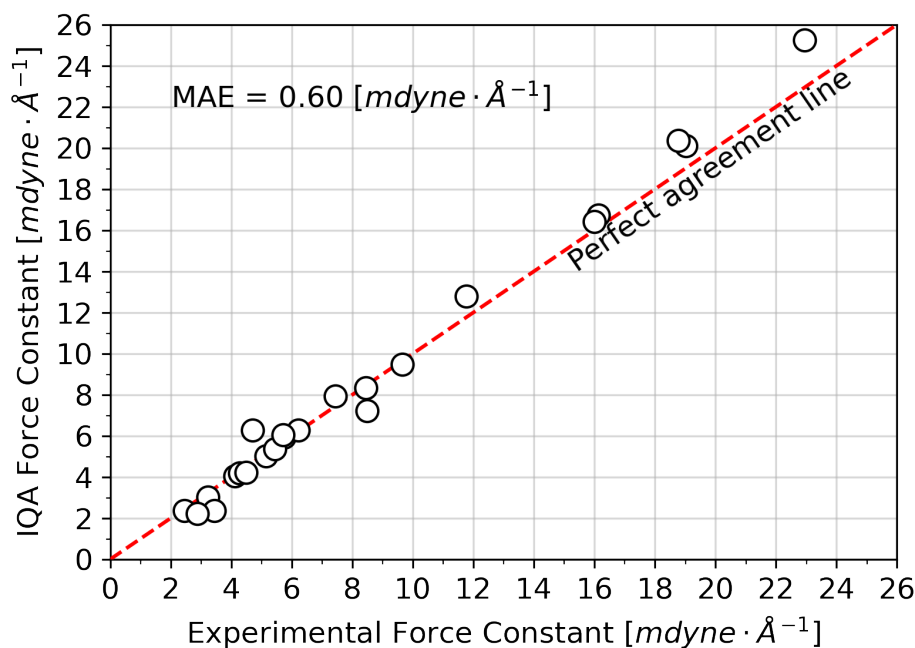


Figure 7.3: Comparison of force constants calculated with the IQA components with experimental results. Experimental results contains only bond stretching force constants in units of $\text{mdyne} \cdot \text{\AA}^{-1}$.

7.5 Force Constants and Bond Dissociation Energies

The term “bond strength”, although not present in IUPAC’s gold[152] or green[153] book, is frequently used as a measure of the bond dissociation energy D_e (or D_o), which is often mistaken as a measure of the bond force constant. Relating D_e to the force constant, however, is only valid when the energy curve can be approximated by a Morse potential [154]. Considering a diatomic molecule whose bond length is equal to R_e , the Morse potential, $E(R) = D_e[1 - \exp^{-\alpha(R-R_e)}]^2$, with the force constant being equal to $k_e = \left. \frac{\partial^2 E(R)}{\partial R^2} \right|_{R=R_{eq}} = 2D_e \cdot \alpha^2$, then the linear relation between D_e and k_e appears as:

$$D_e = \frac{k_e}{2\alpha^2} \quad (7.15)$$

¹The recovery error is given by $E_{\text{total}} \sum_{k=1}^{N^2} E_k^{\text{IQA}}$

Looking at the experimental data (Figure 7.4), taken from the CRC Handbook of Chemistry and Physics[155], one can find that Equation 7.15 generates diagonal lines for different values of α . Points for similar bonds will lay along the same line, e.g. correlation between D_e and force constant values can be found as indicated by the red dotted line for the CH and CC bonds that corresponds to an α value of $6.5 \text{ kJ}^{\frac{1}{2}} \cdot \text{\AA}^{\frac{1}{2}} \cdot \text{mdyne}^{-\frac{1}{2}} \cdot \text{mol}^{-\frac{1}{2}}$.

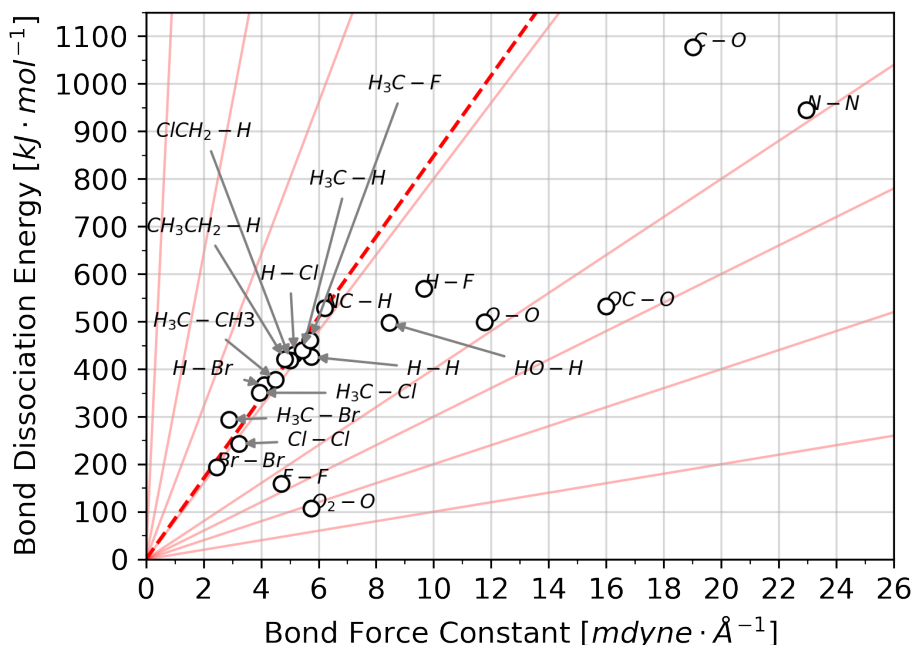
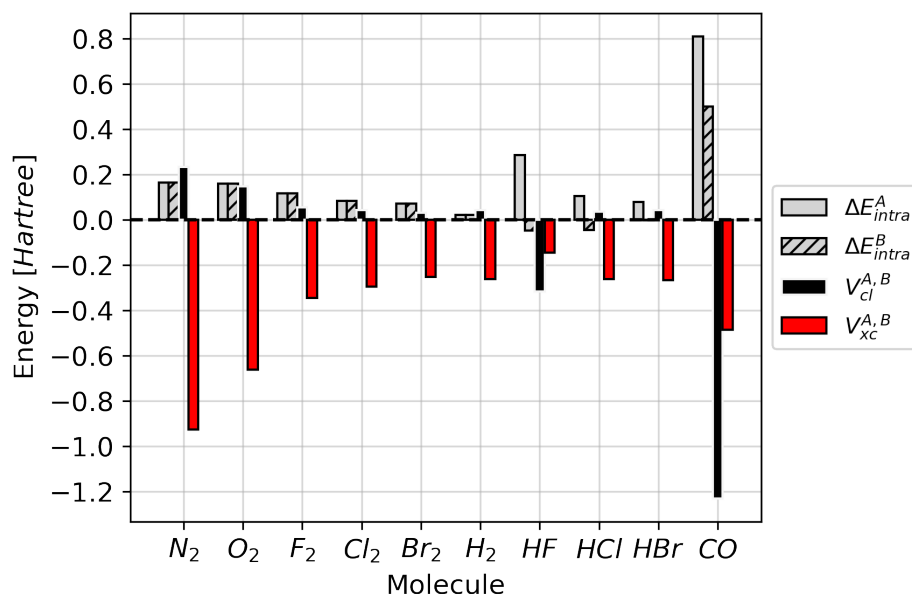


Figure 7.4: Bond dissociation energy D_o , in $\text{kJ} \cdot \text{mol}^{-1}$ versus bond stretching force constant, in $\text{mdyne} \cdot \text{\AA}^{-1}$. Data was taken from the CRC Handbook of Chemistry and Physics. Each red line corresponds to a different value of α .

However, taking D_e directly as a measure of the bond force constant can lead to inconsistencies, e.g. the bond dissociation energy for Cl_2 is greater than for F_2 , although, the force constant of the latter is $4.7 \text{ mdyne} \cdot \text{\AA}^{-1}$ compared to $3.2 \text{ mdyne} \cdot \text{\AA}^{-1}$ for Cl_2 . In fact, bond dissociation energy is a measure of the potential energy well depth, while the force constant is a measure of its curvature and accounts for bond stiffness[156]. The difference between the bond stability and stiffness can be investigated by examining their IQA energetic origins.

On calculating the bond dissociation energy for diatomic molecules, AB, by subtracting the atomic energy of A and B from the sum of the IQA terms of the molecule, i.e. $D_e = E_{\text{intra}}^{A(\text{molecule})} + E_{\text{intra}}^{B(\text{molecule})} + V_{cl}^{A,B} + V_{xc}^{A,B} - E_{\text{intra}}^{A(\text{isolated})} - E_{\text{intra}}^{B(\text{isolated})} = \Delta E_{\text{Intra}}^A + \Delta E_{\text{Intra}}^B + V_{cl}^{A,B} + V_{xc}^{A,B}$, one obtains the plot shown in Figure 7.5a. In Figure 7.5b, the IQA contributions to the force constants are shown. The IQA contributions are listed using their original symbols. However, the reader should keep in mind that the IQA contributions to the force constant were obtained via Equation 7.14 and, therefore, are second derivatives of the IQA terms with respect to the internal coordinates.

Force constants measure the curvature of the potential well and, therefore, they are a descriptor of bond stiffness. A negative value of the IQA contributions to the force constant implies that the contributions makes the bond more “elastic”. At this point, it is important to stress that the IQA contributions that increase the force constant



(a) IQA components of the dissociation energy, in Hartrees.

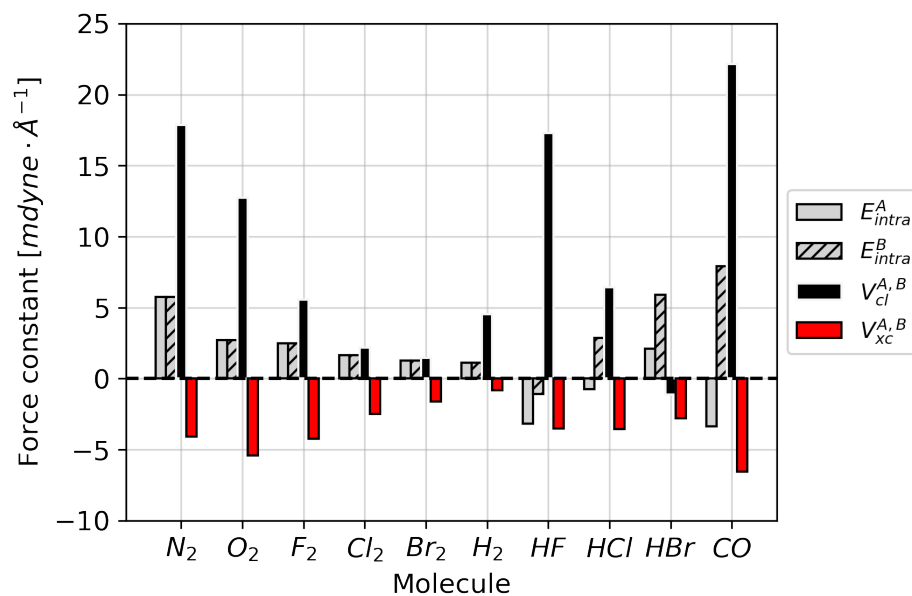
(b) IQA components of force constants in diatomic molecules, in $\text{mdyne} \cdot \text{\AA}^{-1}$.

Figure 7.5: IQA partitioning of dissociation energy and force constants in diatomic molecules. The legends display the original IQA term symbols, however, for force constants the plot shows second derivatives of each term.

may not be the same as contributions that increase the bond stability. The exchange-correlation contribution stabilizes all the bonds of these diatomic molecules but tends to increase their elasticities as can be seen in these figures. Having a larger force constant means that the bond is more difficult to distort, but this does not necessarily imply it is more difficult to break. Bond stability and stiffness can have strikingly different energetic origins.

For all the homonuclear diatomic molecules, the exchange-correlation contri-

bution is the only stabilizing contribution to the bond energy but also the only one making the bonds more elastic. In these molecules the classical Coulomb contributions are positive, tending to increase bond stiffness while also making the bonds a little less stable.

The force constant value of the H–H bond, although its stability results from V_{xc} , is mostly determined by the Coulomb interaction between the hydrogen atoms, receiving only a small and negative contribution from the exchange-correlation potential. Intra-atomic contributions are also important, corresponding to about one third of the total force constant. In the F_2 , Cl_2 and Br_2 molecules, a different trend can be observed: their exchange-correlation force constant contributions are always negative, essentially canceling the Coulomb terms. As a result, their force constants are determined almost completely by the intra-atomic terms, E_{intra} . Since there is no charge transfer occurring during the formation of these bonds, changes in intra-atomic energies arise only from deformations of the electronic densities. The greater stiffness of F–F bond when compared with Cl_2 and Br_2 results from a higher intra-atomic contribution and to a residual Coulomb contribution that is not completely balanced by the exchange-correlation contribution. Coulombic contributions to the dissociation energy, on the other hand, are very small and almost constant, having a negligible bond stabilization effect.

Considering the distance between the nuclei, one can see that the Coulomb contributions to the force constant decrease with increasing bond length, while an increase is observed for the exchange-correlation contribution. Since the Coulomb law states that the electric potential is proportional to the inverse of the distance between charges, taking its second derivative results in a force constant that is proportional to the inverse of the third power of bond distances. The shortening of the bond length as the bond order increases results in a higher contribution from the IQA classical term.

These effects are especially pronounced for diatomic molecules with different bond orders. Increasing the bond order results in an increase of the exchange-correlation stabilization, $-V_{xc}^{N,N} > -V_{xc}^{O,O} > -V_{xc}^{F,F}$, while slightly increasing the repulsive classical potential, $V_{cl}^{N,N} > V_{cl}^{O,O} > V_{cl}^{F,F}$. Although V_{xc}^{AB} is dominant for bond stability, V_{cl}^{AB} accounts for bond stiffness. Considering F–F, O=O and N≡N, the increase in bond order is accompanied by an increase in the force constant, which is caused mostly by the classical IQA V_{cl} term.

For the HF and CO heteronuclear molecules, where there are large electronegativity differences between the bonding atoms, the classical Coulomb contribution becomes negative, stabilizing the bonds. The stabilities of H–F and CO bonds are resultants of both the V_{cl} and V_{xc} contributions. The stabilities of HCl and HBr, in turn, result only from exchange-correlation, as expected for small atomic charges.

HF, HCl and HBr, differing from the single-bonded homonuclear diatomic halogens, have force constants exhibiting a greater dependence on Coulomb and intra-atomic force constant contributions, while the exchange-correlation contributions remain almost constant going from HF to HBr. The Coulomb contribution decreases from HF to HBr, becoming negative for HBr. The intra-atomic contributions, on the other hand, increase. In fact the force constant f_{HBr} is only positive due to the intra-atomic energy second derivatives. Intra-atomic contributions result from a sum of the electron kinetic energy plus their electron-electron repulsion and electron-nucleus attraction[134], calculated inside a single atomic basin. The increase in the kinetic energy for the hydrogen atom can be associated with the increase in its electron density, which is consistent with the electronegativity of the halogen atom. The reduction of f_{HX} in the series is, mostly,

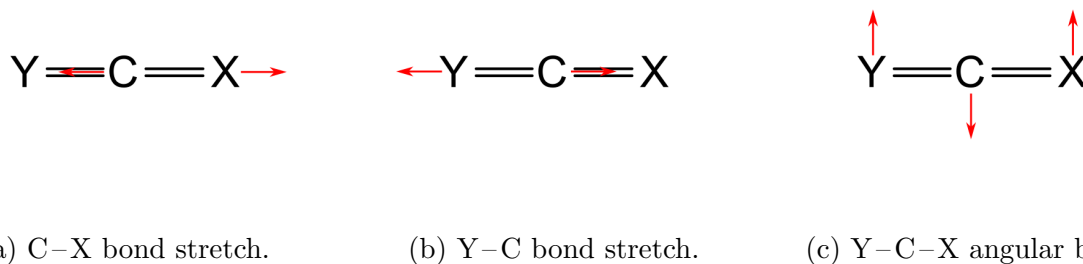


Figure 7.6: Internal coordinates for linear YCX, X, Y = O, S. Red vectors indicate the **B** matrix element.

a consequence of lowering atomic charges while increasing the bond distance.

7.6 Force Constants of CO, CO₂, SCO and CS₂

Figure 7.6 shows the internal coordinates for the stretching of C–X and Y–C bonds and the Y–C–X angular bending.

From the data presented in Table 7.1, one can see that, for the bond stretching force constant, contributions from atoms that are not part of the internal coordinate are small when compared with contributions from the other atoms. Significant force constant contribution profiles are shown in Figure 7.7. The Coulomb term for C–X is always positive when X = O, but negative when X = S, differentiating the C=O from the C=S bond. A similar trend is found for the intra-atomic terms that are positive, i.e. increase the bond stiffness, for C=S, but negative, or very small, for C=O. Exchange-correlation contributions are negligible for CS and slightly negative for CO. The IQA profile for CO is closer to the profile of the CO bond in SCO than in CO₂. The inclusion of an extra oxygen atom enhances the Coulomb contribution, but also decreases the intra-atomic contribution from carbon. These two effects counterbalance each other and the force constant values remain almost unaffected, as can be seen in the last column of Table 7.1.

For angular bending force constants of CO₂ and CS₂ the Coulomb contributions are about the same for both terminal atoms, presenting relatively high and positive magnitudes. The intra-atomic contributions are negative. The exchange contributions are negligible for CO₂, but become positive and small, for CS₂. Even though the intra-atomic and Coulomb force constant contributions are all significantly smaller for the OCS angle than for those in CO₂ and CS₂, all three angular force constants have very similar values.

7.6.1 The C=O Bond in X₂CO Molecules

The magnitude of a bond constant is usually given by an average of that bond in related molecules. However, although this methodology is well established, the decomposition of the force constants into IQA components reveals that the IQA profile of the same bond may vary significantly between molecules, even if their sum doesn't. In Figure 7.8 the IQA profiles of f_{CO} in F₂CO, Cl₂CO, Br₂CO and H₂CO are shown. The profile of C=O bond in F₂CO resembles the one in CO₂, while profiles of the bond in the others

Table 7.1: Second derivatives of IQA contributions to the forces constants of CO₂, SCO, CS₂ and CO in [*mdyne* · Å⁻¹].

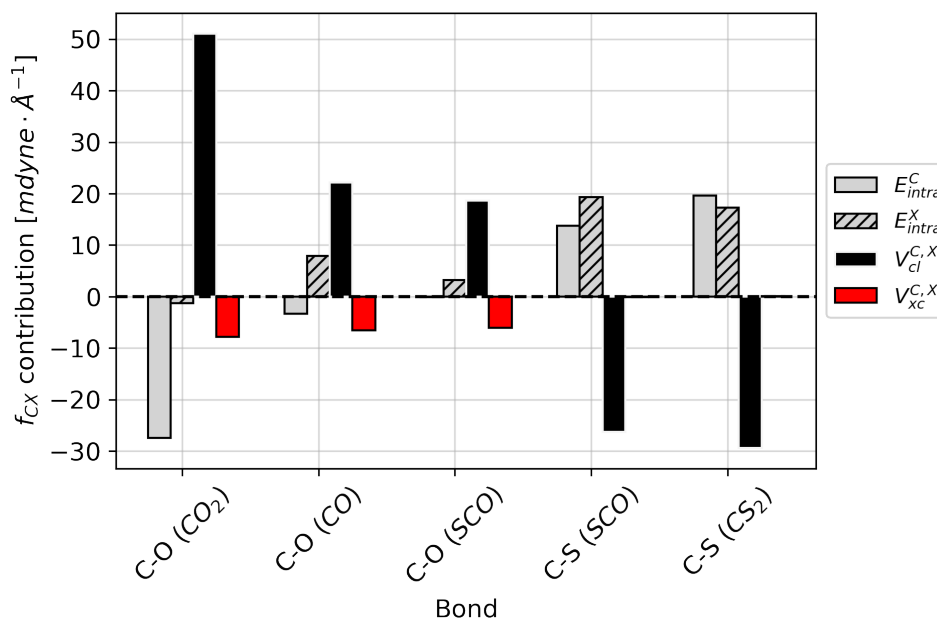
| | | Bond Stretch | | | | | | | | | |
|-----------------|---------------------|---------------|---------------|---------------|----------------|----------------|----------------|----------------|----------------|----------------|----------------------------|
| Molecule | Internal coordinate | E_{intra}^C | E_{intra}^Y | E_{intra}^X | $V_{cl}^{C,Y}$ | $V_{cl}^{C,X}$ | $V_{cl}^{Y,X}$ | $V_{xc}^{C,Y}$ | $V_{xc}^{C,X}$ | $V_{xc}^{Y,X}$ | f_{CX} or f_{CY} |
| CO ₂ | O-C (Y-C) | - | - | - | 51.05 | 13.85 | - | - | 0.30 | 0.05 | 16.44 |
| | | 27.43 | 1.29 | 2.15 | | | 10.09 | 7.85 | | | |
| | C-O (C-X) | - | - | - | 13.85 | 51.05 | - | 0.30 | - | 0.05 | 16.39 |
| | | 27.43 | 2.15 | 1.29 | | | 10.13 | 7.85 | | | |
| SCO | S-C (Y-C) | 13.71 | 19.29 | - | - | 6.46 | - | - | 0.11 | 0.03 | 7.24 |
| | | | | 0.84 | 26.28 | 5.13 | 0.10 | | | | |
| | C-O (C-X) | - | - | 3.17 | - | 18.62 | 6.57 | 0.78 | - | 0.22 | 16.73 |
| | | 0.12 | 1.83 | | 4.62 | | | 6.06 | | | |
| CS ₂ | S-C (Y-C) | 19.65 | 17.26 | - | - | 0.78 | 0.20 | 0.07 | 0.28 | 0.02 | 7.92 |
| | | | | 0.98 | 29.36 | | | | | | |
| | C-S (C-X) | 19.65 | - | 17.26 | 0.78 | - | 0.22 | 0.28 | 0.07 | 0.02 | 7.94 |
| | | | 0.98 | | 29.37 | | | | | | |
| CO | C-O (C-X) | - | - | 7.91 | - | 22.14 | - | - | - | - | 20.11 |
| | | 3.37 | | | | | | 6.57 | | | |

| | | Angle Bend | | | | | | | | | |
|-----------------|---------------------|---------------|---------------|---------------|----------------|----------------|----------------|----------------|----------------|----------------|-----------|
| Molecule | Internal coordinate | E_{intra}^C | E_{intra}^Y | E_{intra}^X | $V_{cl}^{C,Y}$ | $V_{cl}^{C,X}$ | $V_{cl}^{Y,X}$ | $V_{xc}^{C,Y}$ | $V_{xc}^{C,X}$ | $V_{xc}^{Y,X}$ | f_{YCX} |
| CO ₂ | O-C-O (Y-C-X) | - | - | - | 7.96 | 7.96 | - | - | - | - | 0.79 |
| | | 8.07 | 2.15 | 2.15 | | | 2.20 | 0.22 | 0.22 | 0.13 | |
| SCO | S-C-O (Y-C-X) | - | - | - | 0.94 | 5.43 | 1.36 | 0.49 | 0.04 | - | 0.68 |
| | | 3.37 | 1.07 | 3.05 | | | | | | 0.09 | |
| CS ₂ | S-C-S (Y-C-X) | - | - | - | 6.53 | 6.53 | - | 0.72 | 0.73 | - | 0.60 |
| | | 6.44 | 2.82 | 2.82 | | | 1.78 | | | 0.05 | |

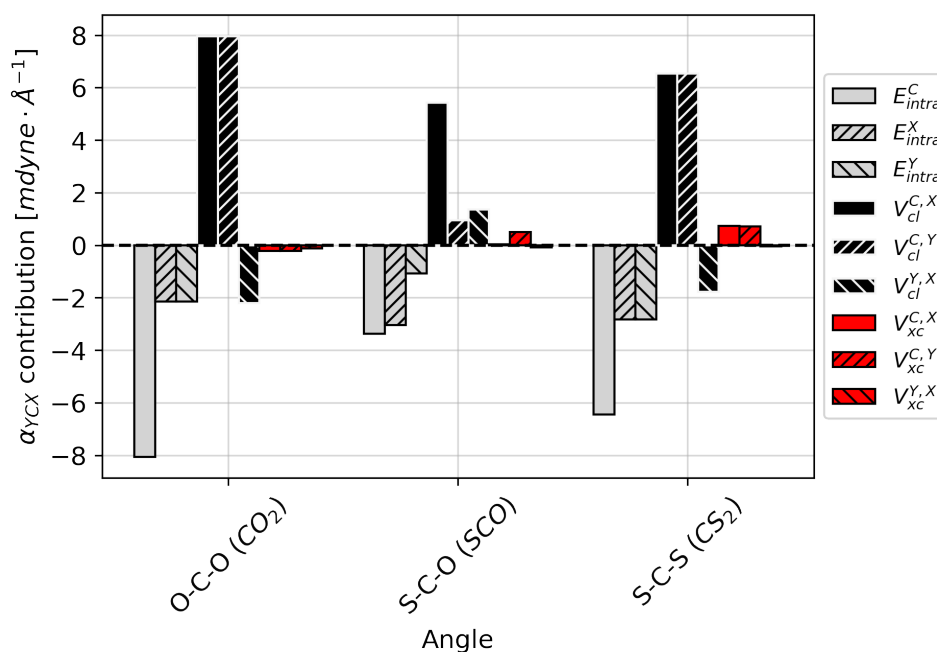
X₂CO molecules are similar with those in SCO and CO. One can notice that the second derivatives of V_{cl}^{CO} increase with the electronegativity of X. However, the Coulomb contribution in F₂CO is partially counterbalanced by the intra-atomic contribution. This effect is not as significant, but positive, for the other three molecules in this series. Exchange-correlation contributions are always negative and about the same for all these carbonyls. As such, the total force constant from the DFT calculations vary slightly, from 13.6 to 15.5 *mdyne* · Å⁻¹.

7.7 Bond order: the C–C Bond in Ethane, Ethylene and Benzene and the O–O, Bond in O₂, O₃ and H₂O₂

It is known that an increase in bond order also increases the force constant. As the data presented in Table 7.2 suggests, this happens due to the increase in the contributions from Coulomb terms for the oxygen bonds and both the Coulomb and intra-atomic terms for the carbon bonds. In molecules with resonance (O₃ and benzene), intra-atomic contributions do not increase force constant, but Coulomb interactions do. Contributions from atoms that do not participate in the bond are small, i.e. about



(a) IQA contributions to C-X bond stretch force constant.



(b) IQA contributions to the Y-C-X angle bent force constant.

Figure 7.7: Contributions from second derivatives of IQA terms to the bond stretch, f_{CX} , and angular bend, f_{YCX} , force constants, where $X, Y \in \{O, S\}$.

1 mdyne $\cdot \text{\AA}^{-1}$ or less, except for molecules that presents resonance: ozone and benzene. Intra-atomic contributions from both atoms in the bond are equivalent, except for O₃, where the symmetry is broken. For the C-C bond series, differences between E_{intra}^{C1} and

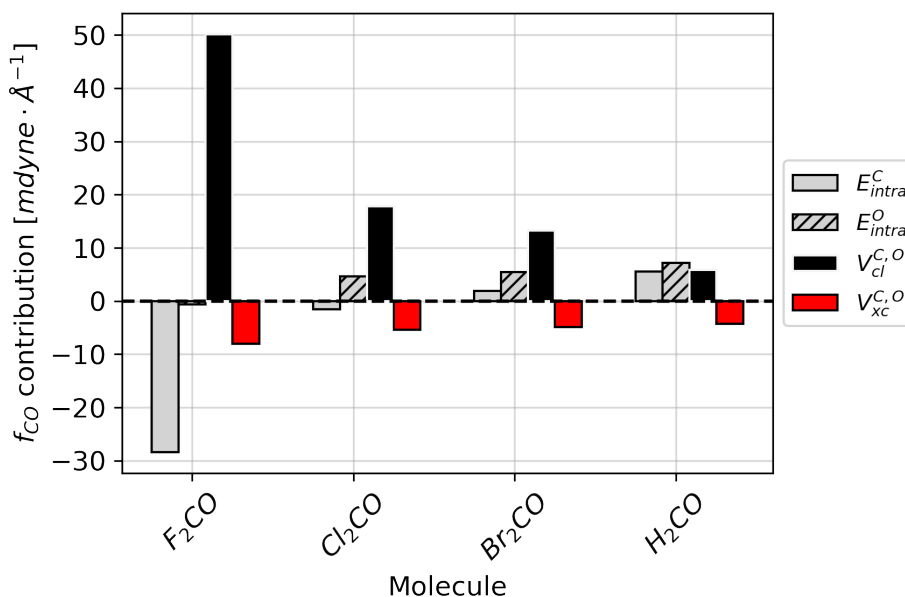


Figure 7.8: Trend in IQA force constant contributions for F₂CO, Cl₂CO, Br₂CO and H₂CO. Only contributions from C and O are presented since others contributions are negligible

Table 7.2: Bond force constant for the series: ethane, ethylene, benzene and O₂, O₃, H₂O₂. Values in mdyne · Å⁻¹.

| Mol. | E_{intra}^{O1} | E_{intra}^{O2} | $V_{cl}^{O1,O2}$ | $V_{xc}^{O1,O2}$ | $\sum^{O1,O2}$ | \sum^{others} | f_{OO} |
|-------------------------------|------------------|------------------|------------------|------------------|----------------|-----------------|----------|
| H ₂ O ₂ | 2.3 | 2.2 | 2.8 | -3.4 | 3.9 | 1.1 | 4.9 |
| O ₃ ⁱ | 2.4 | 1.4 | 11.2 | -5.9 | 9.1 | -1.8 | 7.4 |
| O ₂ | 2.7 | 2.7 | 12.7 | -5.4 | 12.8 | 0.0 | 12.8 |
| Mol. | E_{intra}^{C1} | E_{intra}^{C2} | $V_{cl}^{C1,C2}$ | $V_{xc}^{C1,C2}$ | $\sum^{C1,C2}$ | \sum^{others} | f_{CC} |
| Ethane | 1.5 | 1.3 | 2.5 | -1.8 | 3.5 | 0.8 | 4.2 |
| Benzene | 1.3 | 1.3 | 3.0 | -1.8 | 3.7 | 1.2 | 5.0 |
| Ethylene | 3.0 | 3.0 | 5.1 | -2.2 | 8.9 | 0.7 | 9.6 |

ⁱ O1 and O2 are neighbouring atoms.

E_{intra}^{C2} results from the greater numerical error.

7.8 Concluding Remarks

The force constants arise from the potential energy second derivatives. Since the energy of a molecular system results from a sum of atomic terms, the force constant can also be divided into atomic contributions. In order to calculate these contributions, a modification of the Wilson's **FG** method was made, in which a new dimension is added to the Hessian matrix. The new dimension contains second derivatives of IQA contributions to the total energy of the system. The method is able of reproducing experimental and theoretical data obtained with analytical methods. A python library was written in order to facilitate the implementation of the procedure presented in this chapter. The software is open-source and distributed under the MIT license at github.com/ljduarte/theovib.

Origins of bond stabilization energies and force constants are found to be

very different for ten diatomic molecules. Exchange-correlation contributions result in more stable and elastic bonds, whereas Coulomb interactions are most important for increasing force constants. Increases in bond order in homonuclear diatomic molecules are accompanied by increases in the Coulomb contributions to the force constants, while exchange-correlation and intra-atomic terms remain almost unchanged.

Although the magnitude of a bond force constant is almost constant for the same functional group in different molecules, their contribution profiles can differ. For the case of the X_2CO molecules, the Coulomb contributions correlate with the electronegativity of X. Force constant contributions to the stretching constants in CO are very similar to those for the CO bond in OCS, but quite different from the ones in CO_2 . The origins of resonance effects for the O–O and C–C stretching force constants of ozone and benzene are identified.

The results herein are incipient. The refinement of the methodology can lead to a better understanding of the potential energy surface and can act as an auxiliary tool in designing force fields for molecular mechanics. Currently, the authors are working on the application of this method for hydrogen–bonding systems in order to identify the energetic origins of the hydrogen stretching frequency red–shift.

This chapter contains excerpts from texts previously published by the author. The following material was reprinted with permission:

Duarte, L. J., Bruns, R. E. *Energetic Origins of Force Constants: Adding a New Dimension to the Hessian Matrix via Interacting Quantum Atoms* The Journal of Physical Chemistry A, published online, American Chemical Society.

Appendix A

Dimensions and Units of Infrared Intensities

The acquisition and analysis of IR spectra has been a routine practice in laboratories since the first dispersive spectroscopes become available. Later introduced techniques, such as Nuclear Magnetic Resonance, were much more expensive and insights about molecular structure could be assessed from the vibrational spectra at a lower cost. Those factors, allied with the simpler construction of the apparatus, made spectroscopy present in every chemistry laboratory. The popularization of the technique, however, came at a cost: with the introduction of different equipment, software and methods of analysis, it is not rare to find spectra measured in different units and conversion errors are quite common.

Since experimentalists are frequently more interested in analysing only band frequencies, the dimensional problem of intensities has been neglect and the absorption lines are frequently presented in dimensionless units that lack physical meaning. However, from the theoretical point of view, a solid definition of the dimensions and units¹ of intensities is needed, specially when comparing intensities of different molecules and bands. In order to address this issue, the dimensions and units are defined from first principles for both experimental and theoretical intensities.

A.1 The Beer–Lambert–Bouguer law

The Beer–Lambert–Bouguer law was initially derived from experimental observation. Although the light absorption phenomena was first observed by Bouguer in 1729, its theoretical derivation was presented only in 1952 by Frederick C. Strong [157, 158]. A simplified version of his derivation follows:

Consider a monochromatic beam of light with the initial power P_o , passing through a homogeneous medium of length l , as represented in Figure A.1. If its incidence

¹The terms “dimension” and “unit” should not be confused. The first refers to the physical world quantities that are being measured e.g. “length”, while the second refers to the scale of the measurement e.g. “centimeter”, “yard”, etc. Here, for the sake of simplicity, the unit of centimeter [cm] is used for the dimension of “length”, seconds, [s], represents the dimension of “time” and [g] is the unit of “mass”.

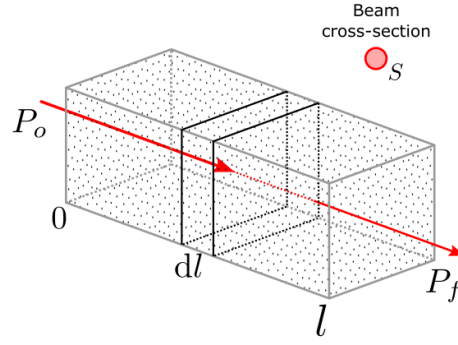


Figure A.1: Consider a beam of light passing through a medium that is uniform in composition. The particles dispersed in the media will absorb part of the radiation, reducing its power.

is perpendicular to the medium and all reflections are neglected, the probability of a photon being absorbed by particles, either atoms or molecules, is proportional to the ratio between the infinitesimal area occupied by the particles, dS_p , and the beam cross section area S .

$$\text{Absorption probability} \propto \frac{dS_p}{S} \quad (\text{A.1})$$

As the beam's power is related to the number of photons, their absorption by the particles in the medium attenuate the beam by a proportional amount, defined as:

$$-\frac{dP}{P} = \frac{dS_p}{S} \quad (\text{A.2})$$

The infinitesimal area occupied by the particles is proportional to its number, n , that is:

$$dS_p = \epsilon(\tilde{\nu})dn \quad (\text{A.3})$$

where n is the number of particles and $\epsilon(\tilde{\nu})$ is a proportion constant that is related with the area occupied by each particle [159]. The number of particles is related to the concentration, γ in the medium. The concentration is given in units² of $[mol][cm]^{-3}$. The number of particles in the infinitesimal length, dl , is given as:

$$dn = \gamma \cdot S \cdot dl \quad (\text{A.4})$$

substituting in equation A.2:

$$\frac{dP}{P} = -\frac{\gamma \cdot \epsilon(\tilde{\nu})Sdl}{S} = \epsilon(\tilde{\nu}) \cdot \gamma \cdot dl \quad (\text{A.5})$$

²All units are displayed inside square brackets, e.g. $[cm]$ refers to "centimeters".

Integrating both sides of equation A.5, results:

$$\int_{P_o}^{P_f} \frac{dP}{P} = - \int_0^l \epsilon(\tilde{\nu}) \cdot \gamma \cdot dl \quad (\text{A.6})$$

$$\ln \left(\frac{P_f}{P_o} \right) = -\epsilon(\tilde{\nu}) \cdot \gamma \cdot l \quad (\text{A.7})$$

which takes the form of the Beer–Lambert–Bouguer law by solving the logarithm.

$$\frac{P_f}{P_o} = e^{-\epsilon(\tilde{\nu}) \cdot \gamma \cdot l} \quad (\text{A.8})$$

The dimensionless quantity on the left hand side of equation A.8 is called “transmittance”³, T . In order to satisfy the principle of dimensional homogeneity, the right hand side must also be dimensionless. This can be verified as follows: the quantity $\epsilon(\tilde{\nu})$ is defined as the area occupied by a certain number of particles, so it has units of $[cm]^2[mol]^{-1}$; Concentration is given in terms of molecules per unit of volume, so it has units of $[mol][cm]^{-3}$ and, l is the length traveled by the beam of light, given also in units of $[cm]$. Putting those definitions together, one has:

$$\frac{[cm]^2 [mol]}{[mol] [cm]^3} [cm] \quad (\text{A.9})$$

which is dimensionless. ϵ_γ is called the “molar absorptivity coefficient” and is dependent on the radiation wavenumber $\tilde{\nu}$.

A.2 Experimental intensities

When a infrared spectrum is acquired, it is represented as a plot of transmittance (or absorbance) versus wavenumber, $\tilde{\nu}$. Wavenumber corresponds to the spatial frequency of radiation that is being absorbed by the sample and is always given in units of $[cm]^{-1}$. The ordinate axis can be either expressed in terms of transmittance, as defined in the previous section, or in terms of decadic or Napierian absorbance. An example is given in figure A.2. The decadic absorbance, Abs_{10} , is defined as:

$$\text{Abs}_{10} = -\log_{10} T = \log_{10} \left(\frac{P_o}{P_f} \right) \quad (\text{A.10})$$

and the Neperian absorbance, Abs_e is:

$$\text{Abs}_e = -\ln T = \ln \left(\frac{P_o}{P_f} \right) = 2.303 \cdot \text{Abs}_{10} \quad (\text{A.11})$$

³It is common to find transmittance expressed as percentage (%). This is done by multiplying $\frac{P_f}{P_o}$ by 100. Note that this form is still dimensionless.

The band intensity, \mathcal{A} , is the integrated absorption coefficient [160], which, by definition,

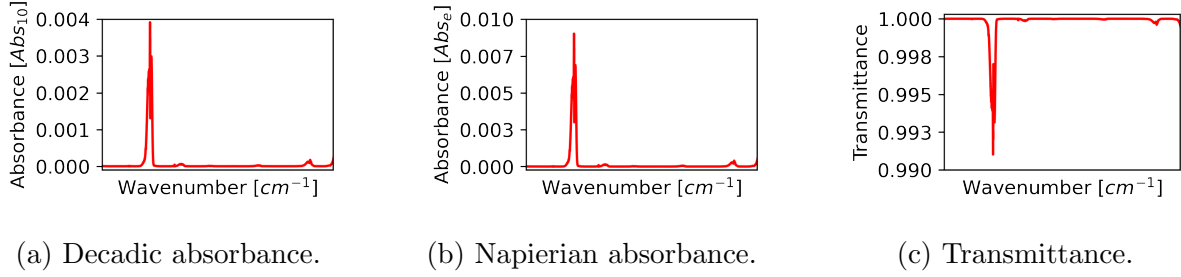


Figure A.2: Infrared spectra of Cl_2CO at 296K . The equivalent concentration \times path length is $4.12 \cdot 10^{-9}[\text{mol}][\text{cm}]^{-2}$. Data obtained from the PNNL library [21].

is:

$$\mathcal{A} = \int \epsilon(\tilde{\nu}) d\tilde{\nu} \quad (\text{A.12})$$

combining the definition of equation A.12 with the Beer Law (equation A.8), gives:

$$\mathcal{A} = \frac{1}{\gamma l} \int \ln \left(\frac{P_o}{P_f(\tilde{\nu})} \right) d\tilde{\nu} = \frac{1}{\gamma l} \int \text{Abs}_e d\tilde{\nu} \quad (\text{A.13})$$

and the units of intensity are:

$$[\mathcal{A}] = \frac{1}{[\text{mol}][\text{cm}]^{-3}[\text{cm}]} [\text{cm}]^{-1} = [\text{cm}][\text{mol}]^{-1} \quad (\text{A.14})$$

Table A.1 contains some conversion constants from $[\text{cm}][\text{mol}]^{-1}$ to other units frequently used in the literature.

Table A.1: Conversion constants for infrared intensity units. Adapted from [160].

| Units | Conversion constant to $[\text{cm}][\text{mol}]^{-1}$ |
|--|---|
| $[\text{mm}][\text{mol}]^{-1}$ | $1.00 \cdot 10^1$ |
| $[\text{m}][\text{mol}]^{-1}$ | $1.00 \cdot 10^{-2}$ |
| $[\text{km}][\text{mol}]^{-1}$ | $1.00 \cdot 10^5$ |
| $[\text{cm}][\text{mmol}]^{-1}$ or [dark] | $1.00 \cdot 10^2$ |
| $[\text{cm}]^{-2}[\text{L}][\text{mol}]^{-1}$ | $1.00 \cdot 10^2$ |
| $[\text{cm}][\text{molecule}]^{-1}$ | $6.02 \cdot 10^{23}$ |
| $[\text{cm}]^{-2}[\text{atm}]^{-1}$ at 300 K | $2.46 \cdot 10^4$ |
| $[\text{cm}]^{-2}[\text{atm}]^{-1}$ at STP ⁱ | $2.24 \cdot 10^4$ |
| $[\text{cm}]^{-1}[\text{km}]^{-1}[\text{atm}]^{-1}$ at STP | $2.24 \cdot 10^2$ |
| $[\text{cm}]^{-1}[\text{km}]^{-1}[\text{atm}]^{-1}$ at STP | $2.24 \cdot 10^{-1}$ |

ⁱ Standard temperature and pressure

Yet, some authors, *e.g.* [99, 161], utilize an alternative definition for equation A.13:

$$\mathcal{A}' = \frac{1}{\gamma l} \int \ln \left(\frac{P_o}{P_f(\tilde{\nu})} \right) d \ln \tilde{\nu} \quad (\text{A.15})$$

intensities obtained with equation A.15 will have different dimensions from those obtained with A.13. The reason for that is the use of the dimensionless quantity $\ln \tilde{\nu}$. An exact conversion between \mathcal{A} and \mathcal{A}' is, therefore, not possible. A good approximation however is $\mathcal{A} \approx \tilde{\nu}_c \cdot \mathcal{A}'$, with $\tilde{\nu}_c$ being the band center wavenumber.

A.3 Calculated Intensities

Recalling the infrared intensity definition of equation 3.5, the dimensional analysis follows:

$$\mathcal{A} = \frac{N_A \pi}{3c^2} \left(\frac{\partial \vec{p}}{\partial Q} \right)^2 \Rightarrow \frac{[mol^{-1}]}{[cm]^2 [s]^{-2}} \left(\frac{\partial \vec{p}}{\partial Q} \right)^2 \quad (\text{A.16})$$

To determine the dimensions of the dipole moment derivative, first one needs to derive the dimensions of the normal coordinate Q and the electric dipole moment, \vec{p} . The dimension of Q is $[cm][g]^{\frac{1}{2}}$, which is proved by comparing the kinetic energy equation:

$$T = \sum_{i,j} \frac{1}{2} m_{ij} \dot{x}_i \dot{x}_j \quad (\text{A.17})$$

with the definition of the normal coordinate.

$$T = \sum_i \frac{1}{2} \dot{Q}_i^2 \quad (\text{A.18})$$

The unit of dipole moment in the CGS unit system ⁴ is Debye [D], which is equivalent to $1.0 \cdot 10^{-18} [cm]^{\frac{5}{2}} [g]^{\frac{1}{2}} [s]^{-1}$. Therefore, neglecting numerical constants:

$$\frac{\partial \vec{p}}{\partial Q_i} \Rightarrow \frac{[cm]^{\frac{5}{2}} [g]^{\frac{1}{2}} [s]^{-1}}{[cm][g]^{\frac{1}{2}}} = [cm]^{3/2} [s]^{-1} \quad (\text{A.19})$$

substituting in equation A.16:

$$[\mathcal{A}] = [mol]^{-1} [cm]^{-2} [s]^2 \left([cm]^{3/2} [s]^{-1} \right)^2 = [cm][mol]^{-1} \quad (\text{A.20})$$

which are the dimensions of infrared intensities.

The same units can be obtained utilizing the International System of units. Starting for the definition of force, one have

$$[N] = [g][cm][s]^{-2} = \frac{[C]^2}{[cm]^{-2}} \quad (\text{A.21})$$

which results as follows.

$$[C]^2 = [g][cm]^3 [s]^{-2} \quad (\text{A.22})$$

⁴Centimeters – Gram – Second

The electric dipole moment units are $[C][cm]$, equivalent to $[g]^{-1/2}[cm]^{5/2}[s]^{-1}$. Therefore, the intensity dimension and unities are:

$$\mathcal{A} = \frac{N_A \pi}{3c^2} \left(\frac{\partial \vec{p}}{\partial Q_i} \right)^2 \Rightarrow [mol]^{-1}[cm]^{-2}[s]^2 \frac{[g][cm]^5[s]^{-2}}{[cm]^2[g]} \Rightarrow [cm][mol]^{-1} \quad (\text{A.23})$$

Appendix B

Absorption of Radiation and Infrared Intensity

Following is the derivation of equation 3.5 from first principles. The treatment presented here is similar to the one presented in the classical book by Pauling and Wilson “Introduction to Quantum Mechanics With Applications to Chemistry” [162]. The notation used in the equations was updated in order to clarify the derivation while maintaining the coherence with symbols used in this thesis.

B.1 Time-Dependent Schrödinger Equation

In order to connect the infrared intensity with the dipole moment derivative, we need to start with the time-dependent Schrödinger equation for an unperturbed system

$$\hat{H}^o \Psi^o = -\frac{h}{2\pi i} \frac{\partial \Psi^o}{\partial t} \quad (\text{B.1})$$

with h being the Planck constant and \hat{H}^o the time-independent Hamiltonian. The solution for the above equation is:

$$\Psi^o = \sum_{l=1}^{\infty} a_l \Psi_l^o \quad (\text{B.2})$$

The coefficients a_l are constants and since the solution in equation B.2 is normalized, we have $\sum_{l=1}^{\infty} a_l^* a_l = 1$ and Ψ_l^o is the wave function for the unperturbed system at the stationary state of energy E_l^o .

If during a certain period of time, the system is perturbed by a time-dependent term \hat{H}' , equation B.1 becomes

$$(\hat{H}^o + \hat{H}') \Psi = -\frac{h}{2\pi i} \frac{\partial \Psi}{\partial t} \quad (\text{B.3})$$

which is solved by:

$$\Psi(\vec{x}, t) = \sum_{l=1}^{\infty} a_l(t) \Psi_l^o(\vec{x}, t) \quad (\text{B.4})$$

with both $a_l(t)$ and $\Psi_l^o(\vec{x}, t)$ being time-dependent. Substituting equation B.4 in equation B.3 and applying the Leibniz product rule¹ we obtain

$$\sum_{l=1}^{\infty} a_l(t) \hat{H}^o \Psi_l^o + \sum_{l=1}^{\infty} a_l(t) \hat{H}' \Psi_l^o = -\frac{h}{2\pi i} \sum_{l=1}^{\infty} \frac{da_l(t)}{dt} \Psi_l^o - \frac{h}{2\pi i} \sum_{l=1}^{\infty} a_l(t) \frac{\partial \Psi_l^o}{\partial t} \quad (\text{B.5})$$

leading to:

$$-\frac{h}{2\pi i} \sum_{l=1}^{\infty} \frac{da_l(t)}{dt} \Psi_l^o = \sum_{l=1}^{\infty} a_l(t) \hat{H}' \Psi_l^o \quad (\text{B.6})$$

The coefficient of the state n can be determined multiplying equation B.6 by the complex-conjugate Ψ_n^{o*} and integrating over the entire space, which results in:

$$\frac{da_n(t)}{dt} = -\frac{2\pi i}{h} \sum_{l=1}^{\infty} a_l(t) \langle \Psi_n^o | \hat{H}' | \Psi_l^o \rangle \quad (\text{B.7})$$

B.2 Einstein Coefficients and Absorption of Radiation

A general discussion of Einstein emission and absorption is given in this section. At the end, the connection between the infrared intensity and the absorption coefficient is presented.

It is known that a system composed by moving electric charged particles will emit and absorb light. Imagine a system that has the stationary states n and m , being state m of lower energy. The frequency of radiation that will be absorbed by the system is:

$$\nu_{m \rightarrow n} = \frac{E_m - E_n}{h} \quad (\text{B.8})$$

When interacting with a photon, the system can absorb its energy and transition to the high energy state n , as represented in Figure B.1.

If there are N_m systems at state m immerse in a radiant energy bath of density $\omega(\nu_{m \rightarrow n})$, the number of systems transitioning from m to n is :

$$N_m B_{m \rightarrow n} \omega(\nu_{m \rightarrow n}) \quad (\text{B.9})$$

with $B_{m \rightarrow n}$ being the Einstein absorption coefficient and the transition probability is given by the term $B_{m \rightarrow n} \omega(\nu_{m \rightarrow n})$. Systems in the upper state n can undergo a transition to the lower energy state m . If N_n is the number of systems initially at state n , then the number

¹Considering functions $f(x)$ and $g(x)$ we have: $\frac{d(f(x) \cdot g(x))}{dx} = g(x) \cdot \frac{df(x)}{dx} + f(x) \cdot \frac{dg(x)}{dx}$

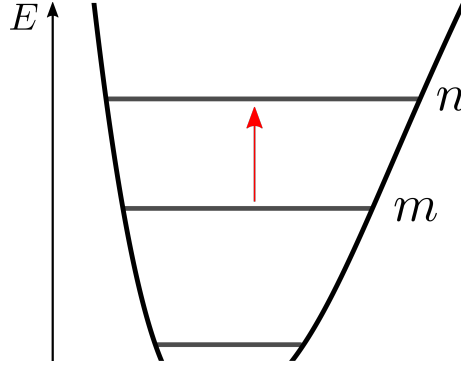


Figure B.1: A system at the stationary state m is promoted to the higher energy state n by absorbing a quantum of frequency $\nu_{m \rightarrow n}$.

of systems transitioning is:

$$N_n (A_{n \rightarrow m} + B_{n \rightarrow m} \omega(\nu_{m \rightarrow n})) \quad (\text{B.10})$$

where $A_{n \rightarrow m}$ is the spontaneous emission coefficient and $B_{n \rightarrow m}$ is the induced emission coefficient. At equilibrium we can write:

$$N_m B_{m \rightarrow n} \omega(\nu_{m \rightarrow n}) = N_n (A_{n \rightarrow m} + B_{n \rightarrow m} \omega(\nu_{m \rightarrow n})) \quad (\text{B.11})$$

which results in:

$$\frac{N_m}{N_n} = \frac{A_{n \rightarrow m} + B_{n \rightarrow m} \omega(\nu_{m \rightarrow n})}{B_{m \rightarrow n} \omega(\nu_{m \rightarrow n})} \quad (\text{B.12})$$

The left-hand side of equation B.12 can be calculated using the Boltzmann distribution, that is

$$e^{\frac{h\nu_{m \rightarrow n}}{k_B T}} = \frac{A_{n \rightarrow m} + B_{n \rightarrow m} \omega(\nu_{m \rightarrow n})}{B_{m \rightarrow n} \omega(\nu_{m \rightarrow n})} \quad (\text{B.13})$$

where k_B is the Boltzmann's constant and T is the temperature. The radiant energy density is, therefore:

$$\omega(\nu_{m \rightarrow n}) = \frac{A_{n \rightarrow m}}{B_{m \rightarrow n} e^{\frac{h\nu_{m \rightarrow n}}{k_B T}} - B_{n \rightarrow m}} \quad (\text{B.14})$$

Comparing equation B.14 with the Planck's radiation law, i.e.

$$\omega(\nu_{m \rightarrow n}) = \frac{8\pi h \nu_{m \rightarrow n}^3}{c^3} \left(e^{\frac{h\nu_{m \rightarrow n}}{k_B T}} - 1 \right)^{-1} \quad (\text{B.15})$$

we found that the absorption coefficient and the induced emission coefficient are equal, $B_{m \rightarrow n} = B_{n \rightarrow m}$, and that $A_{n \rightarrow m} = \frac{8\pi h \nu_{m \rightarrow n}^3}{c^3} B_{m \rightarrow n}$.

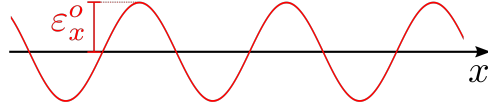


Figure B.2: Amplitude, $\varepsilon_x^o(\nu)$, of a radiation $\varepsilon_x(\nu) = \varepsilon_x^o(\nu) (e^{2\pi i\nu t} + e^{-2\pi i\nu t})$.

B.2.1 The Absorption Coefficient from Classical Electromagnetic Theory

We now go back to equation B.7. Suppose that at the initial time, $t = 0$ we know that the system is at state m , thus the coefficient of Ψ_m^o is equal to one, while the coefficient of all other states equals zero. In this case, the summation vanishes and equation B.7 becomes:

$$\frac{da_n(t)}{dt} = -\frac{2\pi i}{h} \langle \Psi_n^o | \hat{H}' | \Psi_m^o \rangle \quad (\text{B.16})$$

The wavefunction for any state l is dependent of time and of the set of coordinates \vec{x} , i.e:

$$\Psi_l^o = \Psi_l^o(\vec{x}, t) = \psi_l^o(\vec{x}) e^{-\frac{2\pi i}{h} E_l t} \quad (\text{B.17})$$

substituting equation B.17 in equation B.16, gives:

$$\frac{da_n(t)}{dt} = -\frac{2\pi i}{h} e^{\frac{2\pi i t}{h} (E_n^o - E_m^o)} \langle \psi_n^o | \hat{H}' | \psi_m^o \rangle \quad (\text{B.18})$$

Considering a radiation wave of frequency ν propagating in space, the radiation energy density is proportional to the average square of its electric field:

$$\rho(\nu) = \frac{1}{4\pi} \overline{\varepsilon^2(\nu)} \quad (\text{B.19})$$

looking only at the x component of the electric field and the distribution of radiation being isotopic, we have:

$$\rho(\nu) = \frac{6}{4\pi} \varepsilon_x^{o2}(\nu) \quad (\text{B.20})$$

with $\varepsilon_x^{o2}(\nu)$ being the amplitude of the electric field (see Figure B.2). The perturbation energy for a system in a electric field, ε_x , parallel to the x axis is

$$\hat{H}' = \varepsilon_x \hat{p}_x = \varepsilon_x^o(\nu) (e^{2\pi i\nu t} + e^{-2\pi i\nu t}) \hat{p}_x \quad (\text{B.21})$$

with \hat{p}_x being the system's x -axis dipole moment operator. Substituting \hat{H}' in equation B.16:

$$\frac{da_n(t)}{dt} = -\frac{2\pi i}{h} \varepsilon_x^o \left(e^{\frac{2\pi i}{h}(E_n^o - E_m^o + h\nu)t} + e^{\frac{2\pi i}{h}(E_n^o - E_m^o - h\nu)t} \right) \langle \psi_n^o | \hat{p}_x | \psi_m^o \rangle \quad (\text{B.22})$$

The integral $\langle \psi_n^o | \hat{p}_x | \psi_m^o \rangle$ is the transition dipole moment $\vec{p}_{x,m \rightarrow n}$. Solving equation B.22 through integration, we find:

$$a_n(t) = \vec{p}_{x,m \rightarrow n} \varepsilon_x^o \left[\frac{1 - e^{\frac{2\pi i}{h}(E_n^o - E_m^o + h\nu)t}}{E_n^o - E_m^o + h\nu} + \frac{1 - e^{\frac{2\pi i}{h}(E_n^o - E_m^o - h\nu)t}}{E_n^o - E_m^o - h\nu} \right] \quad (\text{B.23})$$

It is clear that the terms inside the square brackets are small except when the frequency ν is closer to $\nu_{m \rightarrow n}$, in this case the second term becomes relevant increasing the absorption probability. The first term, on the other hand, can be neglected. The probability of absorption is:

$$a_n^*(t)a_n(t) = 4\vec{p}_{x,m \rightarrow n}^2 \varepsilon_x^{o2} \frac{\sin^2 \left[\frac{\pi}{h} (E_n^o - E_m^o - h\nu) t \right]}{(E_n^o - E_m^o - h\nu)^2} \quad (\text{B.24})$$

Since the effects of radiations of other frequencies that are not $\nu_{m \rightarrow n}$ are additive, we can account for these other frequencies by integrating equation B.24.

$$a_n^*(t)a_n(t) = 4\vec{p}_{x,m \rightarrow n}^2 \varepsilon_x^{o2} \int_{-\infty}^{\infty} \frac{\sin^2 \left[\frac{\pi}{h} (E_n^o - E_m^o - h\nu) t \right]}{(E_n^o - E_m^o - h\nu)^2} d\nu = \frac{4\pi^2}{h^2} \vec{p}_{x,m \rightarrow n}^2 \varepsilon_x^{o2} t \quad (\text{B.25})$$

If $a_n^*(t)a_n(t)$ is the probability of transition and using the definition of radiation density in equation B.21, then the Einstein absorption coefficient becomes:

$$B_{m \rightarrow n} = \frac{8\pi^3}{3h^2} \omega(\nu_{m \rightarrow n}) \vec{p}_{x,m \rightarrow n}^2 \quad (\text{B.26})$$

B.3 Infrared Intensity of a Normal Mode of Vibration[15]

Since the Einstein coefficient of absorption and induced emission are equal, the net number of systems transitioning from the state m to n is:

$$\frac{8\pi^3}{3h^2} \omega(\nu_{m \rightarrow n}) \vec{p}_{x,m \rightarrow n}^2 (N_m - N_n) \quad (\text{B.27})$$

The change in the power of a beam passing through a absorbing medium² of length dl is:

$$dP = \nu_{m \rightarrow n} \frac{8\pi^3}{3h^2} \omega(\nu_{m \rightarrow n}) \vec{p}_{x,m \rightarrow n}^2 (N_m - N_n) dl \quad (\text{B.28})$$

using $P = c\omega$:

$$-\frac{dP}{P} = \nu_{m \rightarrow n} \frac{8\pi^3}{3ch} \vec{p}_{x,m \rightarrow n}^2 (N_m - N_n) dl \quad (\text{B.29})$$

After integration, we have:

$$\ln \left(\frac{P_o}{P_f} \right) = \nu_{m \rightarrow n} \frac{8\pi^3 l}{3ch} \vec{p}_{x,m \rightarrow n}^2 (N_m - N_n) \quad (\text{B.30})$$

The term $(N_m - N_n)$ can be solved using the Boltzmann distribution, that is:

$$N_m - N_n = \gamma N_A \frac{e^{-\frac{E_m^o}{h_b T}} - e^{-\frac{E_n^o}{h_b T}}}{e^{-\frac{E_m^o}{h_b T}} + e^{-\frac{E_n^o}{h_b T}}} \approx \gamma N_A \quad (\text{B.31})$$

where γ is the concentration. Substituting in equation B.32 gives:

$$\ln \left(\frac{P_o}{P_f} \right) \frac{1}{l} \frac{1}{\gamma} = \nu_{m \rightarrow n} \frac{8N_A \pi^3}{3ch} \vec{p}_{x,m \rightarrow n}^2 \quad (\text{B.32})$$

According to equation A.13, the integration of the left-hand side gives the intensity:

$$\mathcal{A} = \int_{band} \ln \left(\frac{P_o}{P_f} \right) \frac{1}{l} \frac{1}{\gamma} d\nu = \nu_{m \rightarrow n} \frac{8N_A \pi^3}{3ch} \vec{p}_{x,m \rightarrow n}^2 \quad (\text{B.33})$$

In order to solve the transition dipole moment integral, $\vec{p}_{x,m \rightarrow n}$, we rewrite the integral in terms of the normal coordinate Q :

$$\vec{p}_{x,m \rightarrow n} = \langle \psi_n^o | \hat{p}_x | \psi_m^o \rangle = \int \psi_m^{o*}(Q) \hat{p}_x \psi_n^o(Q) dQ \quad (\text{B.34})$$

the operator \hat{p}_x can be expanded in a Taylor series:

$$\hat{p}_x = p_x^o + Q \frac{\partial p_x}{\partial Q} + \dots \quad (\text{B.35})$$

where p_x^o is the x component of the equilibrium dipole moment of the system. Considering only the linear and constant terms:

$$\vec{p}_{x,m \rightarrow n} = p_x^o \int \psi_m^{o*}(Q) \psi_n^o(Q) dQ + \frac{\partial p_x}{\partial Q} \int \psi_m^{o*}(Q) Q \psi_n^o(Q) dQ \quad (\text{B.36})$$

²See equations A.1 – A.6

Due to the orthogonality of the wavefunctions the first term is zero, then:

$$\vec{p}_{x,m \rightarrow n} = \frac{\partial p_x}{\partial Q} \int \psi_m^{o*}(Q) Q \psi_n^o(Q) dQ = \left(\frac{h}{8\pi^2 c \nu_{m \rightarrow n}} \right)^{\frac{1}{2}} \frac{\partial p_x}{\partial Q} \quad (\text{B.37})$$

Generalizing the treatment to the y and z directions and substituting in equation B.33 we have:

$$\mathcal{A} = \frac{N_A \pi}{3c^2} \left(\frac{\partial \vec{p}}{\partial Q} \right)^2 \quad (\text{B.38})$$

Appendix C

Matrix Treatment for the CCTDP Model

Let $(\mathbf{P}_\mathbf{X})^{(\mathbf{A})}$ be the Cartesian APT of atom A for a N atoms molecule. As stated by equation 3.3, each element of $(\mathbf{P}_\mathbf{X})^{(\mathbf{A})}$ is the derivative of a Cartesian component of the molecular electric dipole moment with respect to displacements of atom A in one Cartesian direction. The $(\mathbf{P}_\mathbf{X})^{(\mathbf{A})}$ is, therefore, a 3×3 matrix represented by:

$$\left[\begin{array}{c} (\mathbf{P}_\mathbf{X})^{(\mathbf{A})} \\ \hline \end{array} \right]_{3 \times 3} \quad (\text{C.1})$$

if $(\mathbf{L})^{(\mathbf{A})}$ is the matrix that converts the Cartesian coordinates of atom A into normal coordinates, then:

$$(\mathbf{P}_\mathbf{Q})^{(\mathbf{A})} = \left[\begin{array}{c} (\mathbf{P}_\mathbf{X})^{(\mathbf{A})} \\ \hline \end{array} \right]_{3 \times 3} \left[\begin{array}{c} (\mathbf{L})^{(\mathbf{A})} \\ \hline \end{array} \right]_{3 \times 1} = \left[\begin{array}{c} (\mathbf{P}_\mathbf{Q})^{(\mathbf{A})} \\ \hline \end{array} \right]_{3 \times 1} \quad (\text{C.2})$$

Now, consider a block-diagonalized matrix, $\mathbf{P}_\mathbf{X}$, of dimension $3N \times 3N$ where each diagonal block is an APT and each non-diagonal block is a null matrix, that is:

$$\mathbf{P}_\mathbf{X} = \left[\begin{array}{c|c|c} \mathbf{P}_\mathbf{X}^{(1)} & \mathbf{0}_{3 \times 3} & \mathbf{0}_{3 \times 3} \\ \hline \mathbf{0}_{3 \times 3} & \ddots & \mathbf{0}_{3 \times 3} \\ \hline \mathbf{0}_{3 \times 3} & \mathbf{0}_{3 \times 3} & \mathbf{P}_\mathbf{X}^{(N)} \end{array} \right]_{3N \times 3N} \quad (\text{C.3})$$

The $\mathbf{P}_\mathbf{Q}^{\text{atomic}}$ is a $3N \times 1$ matrix obtained through the matrix multiplication of $\mathbf{P}_\mathbf{X}$ by \mathbf{L} ,

which is matrix formed by juxtaposing vertically the $(\mathbf{L})^{(A)}$ matrices:

$$\mathbf{P}_Q^{\text{atomic}} = \left[\begin{array}{c|c|c} \mathbf{P}_X^{(1)} & \mathbf{0}_{3 \times 3} & \mathbf{0}_{3 \times 3} \\ \hline \mathbf{0}_{3 \times 3} & \ddots & \mathbf{0}_{3 \times 3} \\ \hline \mathbf{0}_{3 \times 3} & \mathbf{0}_{3 \times 3} & \mathbf{P}_X^{(N)} \end{array} \right]_{3N \times 3N} \left[\begin{array}{c} \mathbf{L}^{(1)} \\ \vdots \\ \mathbf{L}^{(N)} \end{array} \right]_{3N \times 1} = \left[\begin{array}{c} \mathbf{P}_Q^{(1)} \\ \vdots \\ \mathbf{P}_Q^{(N)} \end{array} \right]_{3N \times 1} \quad (\text{C.4})$$

Each 3×1 block of $\mathbf{P}_Q^{\text{atomic}}$ corresponds to a atomic contribution to the 3×1 \mathbf{P}_Q matrix, in other words:

$$\mathbf{P}_Q = \sum_{A=1}^N \mathbf{P}_Q^{(A)} \quad (\text{C.5})$$

The IR intensity of the normal mode Q can be obtained by doing:

$$\mathcal{A} = \frac{N_A \pi}{3c^2} \mathbf{P}_Q^T \mathbf{P}_Q \quad (\text{C.6})$$

C.1 Obtaining the CCTDP Contributions

Since the dipole moments derivatives can be decomposed the contributions of the CCTDP model, the same is true for the APT, that is:

$$\mathbf{P}_X^{(A)} = \mathbf{P}_{X(C)}^{(A)} + \mathbf{P}_{X(CT)}^{(A)} + \mathbf{P}_{X(DP)}^{(A)} \quad (\text{C.7})$$

It is possible to show that \mathbf{P}_Q can also be divided into $\mathbf{P}_{Q(C)}$, $\mathbf{P}_{Q(CT)}$ and $\mathbf{P}_{Q(DP)}$. The $(C)^2$, $(CT)^2$, $(DP)^2$, $2(CCT)$, $2(CDP)$, $2(CTDP)$ contributions for the IR intensity are:

$$\mathcal{A}_{(C)^2} = \frac{N_A \pi}{3c^2} \mathbf{P}_{Q(C)}^T \mathbf{P}_{Q(C)} \quad (\text{C.8})$$

$$\mathcal{A}_{(CT)^2} = \frac{N_A \pi}{3c^2} \mathbf{P}_{Q(CT)}^T \mathbf{P}_{Q(CT)} \quad (\text{C.9})$$

$$\mathcal{A}_{(DP)^2} = \frac{N_A \pi}{3c^2} \mathbf{P}_{Q(DP)}^T \mathbf{P}_{Q(DP)} \quad (\text{C.10})$$

$$\mathcal{A}_{2(CCT)} = \frac{N_A \pi}{3c^2} (\mathbf{P}_{Q(C)}^T \mathbf{P}_{Q(CT)} + \mathbf{P}_{Q(CT)}^T \mathbf{P}_{Q(C)}) \quad (\text{C.11})$$

$$\mathcal{A}_{2(CDP)} = \frac{N_A \pi}{3c^2} (\mathbf{P}_{Q(C)}^T \mathbf{P}_{Q(DP)} + \mathbf{P}_{Q(DP)}^T \mathbf{P}_{Q(C)}) \quad (\text{C.12})$$

and

$$\mathcal{A}_{2(CTDP)} = \frac{N_A \pi}{3c^2} (\mathbf{P}_{Q(CT)}^T \mathbf{P}_{Q(DP)} + \mathbf{P}_{Q(DP)}^T \mathbf{P}_{Q(CT)}) \quad (\text{C.13})$$

Appendix D

Definition of Internal Coordinates

In this section, we will use the example of ethylene to show the definition of the internal coordinates used in this work. At the end, the \mathbf{B} matrix elements for this molecule are presented. The equilibrium geometry, in Cartesian coordinates, is given in Table D.1.

Table D.1: Cartesian coordinates (\AA) of ethylene equilibrium structure at the B3LYP/aug-cc-pVTZ level. Atomic symbols are represented along with a numerical label.

| Atom | x | y | z |
|------|--------|--------|-------|
| C1 | -0.662 | 0.000 | 0.000 |
| C2 | 0.662 | 0.000 | 0.000 |
| H3 | -1.232 | -0.921 | 0.000 |
| H4 | 1.232 | -0.921 | 0.000 |
| H5 | 1.232 | 0.921 | 0.000 |
| H6 | -1.232 | 0.921 | 0.000 |

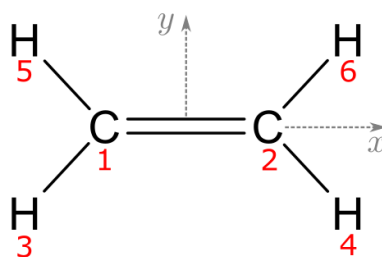


Figure D.1: Cartesian coordinates for ethylene. Atomic symbols are displayed along with a numerical label.

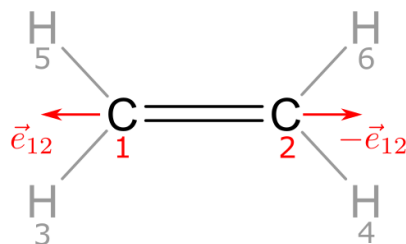


Figure D.2: Bond internal coordinate of the C=C bond in ethylene.

D.1 Bond stretching

The internal bond stretching coordinate is defined in terms of unitary vectors along the bond direction. Taking the C1–C2 bond as an example, the normal vector is obtained by:

$$\vec{e}_{12} = \frac{(x_{C1} - x_{C2})\vec{i} + (y_{C1} - y_{C2})\vec{j} + (z_{C1} - z_{C2})\vec{k}}{\sqrt{(x_{C1} - x_{C2})^2 + (y_{C1} - y_{C2})^2 + (z_{C1} - z_{C2})^2}}$$

\vec{i} , \vec{j} and \vec{k} are unitary vectors pointing towards the x , y and z Cartesian directions.

A representation of this internal coordinate is depicted in Figure below. Notice that the red arrows represent the internal coordinate. The first five rows in Table D.2 contains the bond internal coordinate for ethylene.

D.2 Angular bending

The angular bending vectors are always coplanar with the bonds forming the angle and perpendicular to the bond. Considering the vector \vec{b} that has the same direction of \vec{e}_{12} ,

$$\vec{b} = \|\vec{b}\|\vec{e}_{12} \quad (\text{D.1})$$

and the vector \vec{c} having the same direction of \vec{e}_{13} , that is:

$$\vec{c} = \|\vec{c}\|\vec{e}_{13} \quad (\text{D.2})$$

The angle vector for atom 3 is given by:

$$\vec{e}_{1\alpha} = \vec{b} + \vec{c} \quad (\text{D.3})$$

Since $\vec{e}_{1\alpha}$ is unitary, the, we can write:

$$\cos(\alpha - \pi) = \frac{\|\vec{e}_{3\alpha}\|}{\|\vec{b}\|} \quad (\text{D.4})$$

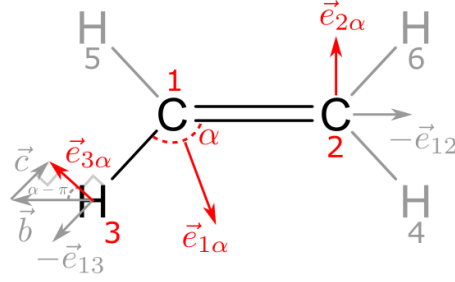


Figure D.3: Angle internal coordinate of the H-C=C bond in ethylene.

which implies:

$$\|\vec{b}\| = \frac{1}{\sin \alpha} \vec{e}_{12} \quad (\text{D.5})$$

The vector \vec{c} is derived following:

$$\tan(\alpha - \pi) = \frac{\|\vec{c}\|}{\|\vec{e}_{3\alpha}\|} \quad (\text{D.6})$$

$$\vec{c} = \frac{1}{\tan \alpha} \vec{e}_{13} \quad (\text{D.7})$$

Finally, the angular bending vector for atom 3 is:

$$\vec{e}_{3\alpha} = \vec{b} + \vec{c} = \frac{1}{\sin \alpha} (\cos \alpha \vec{e}_{13} + \vec{e}_{12}) \quad (\text{D.8})$$

The same derivation applies for the vector $\vec{e}_{2\alpha}$. The vector $\vec{e}_{1\alpha}$ is:

$$\vec{e}_{1\alpha} = -\vec{e}_{2\alpha} - \vec{e}_{3\alpha} \quad (\text{D.9})$$

In order to obtain the force constants in units of $\text{mdynes}\text{\AA}^{-1}$ the vectors are divided by their respective bond lengths.

The derivation of angular bending vector can be easily implemented computational algorithm by the use of cross products. The vectors that describe the angular bending internal coordinate lies in the plane formed by the bonds and are perpendicular to the bond unitary vectors. The normal vector, \vec{n} , to the plane formed by the bonds is given by:

$$\vec{n} = \vec{e}_{13} \times \vec{e}_{12} \quad (\text{D.10})$$

Using the normal vector, the angle bending vectors are obtained as:

$$\vec{e}_{2\alpha} = \frac{\vec{e}_{12} \times \vec{n}}{r_{12}} \quad \text{and} \quad \vec{e}_{3\alpha} = \frac{\vec{e}_{13} \times \vec{n}}{r_{13}} \quad (\text{D.11})$$

where r_{12} and r_{13} are the bond lengths. The \mathbf{B} matrix row 6 to row 11 correspond to the

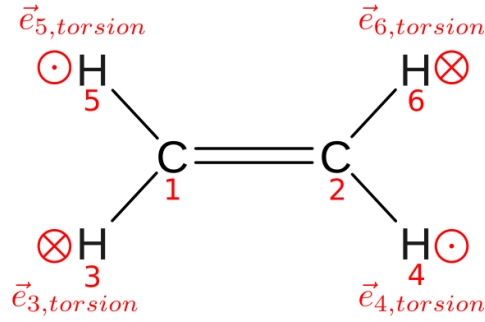


Figure D.4: Torsion internal coordinate in ethylene.

angular bending internal coordinates.

D.3 Dihedral torsion

The vectors of this internal coordinate are represented by into-the-plane, \odot , and out-of-plane vectors, \otimes [163]. Considering the plane formed by bonds $H3 - C1$ and $C1 - C2$, the normal vector to the plane is:

$$\vec{n} = \vec{e}_{13} \times \vec{e}_{12} \quad (\text{D.12})$$

The torsion vector for atom $H3$ has the same direction as \vec{n} . The vector must be divided by the number of atoms bonded to $C1$, and by the bond length.

$$\vec{e}_{3,torsion} = \frac{\vec{n}}{2r_{13}} \quad (\text{D.13})$$

and the torsion vector of $H6$ is:

$$\vec{e}_{6,torsion} = \frac{\vec{e}_{26} \times \vec{e}_{12}}{2r_{26}} \quad (\text{D.14})$$

The same applies for atoms 4 and 5. Finally, the vectors $\vec{e}_{1,torsion}$ and $\vec{e}_{2,torsion}$ are:

$$\vec{e}_{1,torsion} = \sum_{i=3,6} (r_{12} - r_{1i}) (\vec{e}_{i1} \cdot \vec{e}_{12}) \frac{\vec{e}_{i,torsion}}{r_{12}} - \sum_{j=4,5} (\vec{e}_{12} \cdot \vec{e}_{j2}) r_{2j} \frac{\vec{e}_{j,torsion}}{r_{12}} \quad (\text{D.15})$$

$$\vec{e}_{2,torsion} = \sum_{i=4,5} (r_{12} - r_{2i}) (\vec{e}_{i2} \cdot \vec{e}_{21}) \frac{\vec{e}_{i,torsion}}{r_{12}} - \sum_{j=3,6} (\vec{e}_{12} \cdot \vec{e}_{j1}) r_{1j} \frac{\vec{e}_{j,torsion}}{r_{12}} \quad (\text{D.16})$$

This internal coordinate is represented in row 14 of the \mathbf{B} matrix in Table D.2.

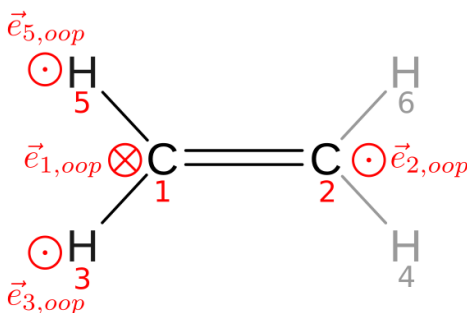


Figure D.5: Ethylene out-of-plane internal coordinate.

D.4 Out-of-plane bending

Consider four atoms in the same plane, i.e. $H5$, $H3$, $C1$ and $C2$. The normal to the plane is:

$$\vec{n} = \frac{\vec{e}_{15} \times \vec{e}_{12}}{\|\vec{e}_{15} \times \vec{e}_{12}\|} \quad (\text{D.17})$$

The vectors that represent this internal coordinate are:

$$\vec{e}_{2,oop} = \frac{\vec{n}}{r_{12}} \quad (\text{D.18})$$

$$\vec{e}_{3,oop} = \frac{\vec{n}}{r_{13}} \frac{\|\vec{e}_{12} \times \vec{e}_{15}\|}{\|\vec{e}_{15} \times \vec{e}_{13}\|} \quad (\text{D.19})$$

$$\vec{e}_{5,oop} = \frac{\vec{n}}{r_{15}} \frac{\|\vec{e}_{12} \times \vec{e}_{13}\|}{\|\vec{e}_{15} \times \vec{e}_{13}\|} \quad (\text{D.20})$$

$$\vec{e}_{1,oop} = -\vec{e}_{2,oop} - \vec{e}_{3,oop} - \vec{e}_{5,oop} \quad (\text{D.21})$$

Table D.2: **B** matrix of ethylene.

| | | | | | | | | | | | | | | | |
|-------|-------|------|-------|-------|-------|-------|-------|-------|-------|-------|-------|-------|-------|------|-------|
| -1.00 | 0.00 | 0.00 | 1.00 | 0.00 | 0.00 | 0.00 | 0.00 | 0.00 | 0.00 | 0.00 | 0.00 | 0.00 | 0.00 | 0.00 | 0.00 |
| 0.53 | -0.85 | 0.00 | 0.00 | 0.00 | 0.00 | 0.00 | 0.00 | 0.00 | 0.00 | 0.00 | 0.00 | 0.00 | 0.00 | 0.00 | -0.53 |
| 0.53 | 0.85 | 0.00 | 0.00 | 0.00 | 0.00 | -0.53 | -0.85 | 0.00 | 0.00 | 0.00 | 0.00 | 0.00 | 0.00 | 0.00 | 0.00 |
| 0.00 | 0.00 | 0.00 | -0.53 | -0.85 | 0.00 | 0.00 | 0.00 | 0.00 | 0.00 | 0.00 | 0.00 | 0.53 | 0.85 | 0.00 | 0.00 |
| 0.00 | 0.00 | 0.00 | -0.53 | 0.85 | 0.00 | 0.00 | 0.00 | 0.00 | 0.53 | -0.85 | 0.00 | 0.00 | 0.00 | 0.00 | 0.00 |
| -1.57 | 0.00 | 0.00 | 0.00 | 0.00 | 0.00 | 0.79 | -0.49 | 0.00 | 0.00 | 0.00 | 0.00 | 0.00 | 0.00 | 0.00 | 0.79 |
| 0.00 | 0.00 | 0.00 | 1.57 | 0.00 | 0.00 | 0.00 | 0.00 | 0.00 | -0.79 | -0.49 | 0.00 | -0.79 | 0.49 | 0.00 | 0.00 |
| 0.79 | 1.24 | 0.00 | 0.00 | -0.75 | 0.00 | 0.00 | 0.00 | 0.00 | 0.00 | 0.00 | 0.00 | 0.00 | 0.00 | 0.00 | -0.79 |
| 0.79 | -1.24 | 0.00 | 0.00 | 0.75 | 0.00 | -0.79 | 0.49 | 0.00 | 0.00 | 0.00 | 0.00 | 0.00 | 0.00 | 0.00 | 0.00 |
| 0.00 | 0.75 | 0.00 | -0.79 | -1.24 | 0.00 | 0.00 | 0.00 | 0.00 | 0.79 | 0.49 | 0.00 | 0.00 | 0.00 | 0.00 | 0.00 |
| 0.00 | -0.75 | 0.00 | -0.79 | 1.24 | 0.00 | 0.00 | 0.00 | 0.00 | 0.00 | 0.00 | 0.00 | 0.79 | -0.49 | 0.00 | 0.00 |
| 0.00 | 0.00 | 0.00 | 0.00 | 0.00 | 0.00 | 0.00 | 0.00 | 0.54 | 0.00 | 0.00 | -0.54 | 0.00 | 0.00 | 0.54 | 0.00 |
| 0.00 | 0.00 | 2.51 | 0.00 | 0.00 | -0.75 | 0.00 | 0.00 | -0.88 | 0.00 | 0.00 | 0.00 | 0.00 | 0.00 | 0.00 | 0.00 |
| 0.00 | 0.00 | 0.75 | 0.00 | 0.00 | -2.51 | 0.00 | 0.00 | 0.00 | 0.00 | 0.00 | 0.88 | 0.00 | 0.00 | 0.88 | 0.00 |

Appendix E

The Theovib library

The *Theovib* library (Theory of Vibrations) is a python package released under the MIT license. The earlier version contains functions to solve the vibrational problem starting from the Hessian matrix or from a 3D-Hessian construct from *Interacting Quantum Atoms* energy decomposition scheme. Infrared intensities are obtained from atomic charges and dipoles obtained by AIMAll. Source-code available at: github.com/ljduarte/theovib.

E.1 Installation

The library can be installed via command line:

```
1 $ pip install theovib
```



Figure E.1: Theovib python library.

E.2 Usage

Following is a guide on how to perform the CCTDP and the IQA force constant analysis with the `theovib` library. Gaussian and AIMAll are used to perform the single point calculations and to obtain the QTAIM/IQA parameters. Start by importing the `theovib` modules:

```
1 from theovib import *
```

In this guide, the water molecule is used as an example, the optimized geometry is given in Table E.1. The equilibrium geometry is used to create an instance of the “Molecule”

Table E.1: Cartesian coordinates of water equilibrium structure (Å) at the B3LYP/aug-cc-pVTZ level. Atomic symbols are represented along with a numerical label.

| Atom | x | y | z |
|------|----------|-----------|-----------|
| O(1) | 0.000000 | 0.000000 | 0.004316 |
| H(2) | 0.000000 | -0.763369 | -0.580667 |
| H(3) | 0.000000 | 0.763369 | -0.580667 |

class, that is:

```
1 water = Molecule(
2     atoms=['O', 'H', 'H'],
3     positions=[np.array([0.000000, 0.000000, 0.004316]),
4                 np.array([0.000000, -0.763369, -0.580667]),
5                 np.array([0.000000, 0.763369, -0.580667])],
6     charge_mult='0 1')
```

notice that the molecular charge and multiplicity is passed as a string to the `charge_mult` attribute.

From the equilibrium structure, new geometries are generated by displacing the atoms in the positive and negative directions of each Cartesian axis. For each new geometry, the wavefunction is calculated by GAUSSIAN, from which the IQA terms are obtained using AIMAll.

The non-equilibrium geometry needed to compute the numerical Hessian matrix are generated with the class method `Molecule.gen_geometries`. The first argument is the directory where the geometries are stored and the second argument is the level of theory:

```
1 water.gen_geometries('inputs_folder', 'b3lyp aug-cc-pvtz')
```

This command generates $18N^2$ Gaussian inputs for a N atoms molecule. $18N^2 - 2N$ are utilized to compute the Hessian non-diagonal elements, and $2N$ are utilized to compute the diagonal elements. The derivatives are calculated following:

$$\frac{\partial^2 E_k}{\partial \sigma_i \partial \sigma_j} \approx \begin{cases} \frac{E_k^{+,0} - 2E_k^{0,0} + E_k^{-,0}}{\Delta \sigma^2} & \text{if } \sigma_i = \sigma_j \\ \frac{E_k^{+,+} - E_k^{+,-} - E_k^{-,+} + E_k^{-,-}}{4\Delta \sigma^2} & \text{if } \sigma_i \neq \sigma_j \end{cases} \quad (\text{E.1})$$

where the superscripts $+$, $-$ and 0 indicate the displacement in the positive and negative directions or no displacement for coordinates σ_i and σ_j . The geometries are generated according to the scheme in Figure E.2.

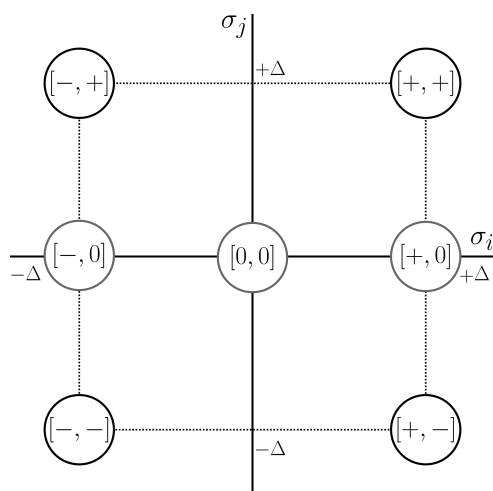


Figure E.2: Displacements needed to compute the numerical second derivatives of IQA energies. Grey circles represent the displacements needed to compute the derivatives where $\sigma_i = \sigma_j$. The central point is the equilibrium geometry.

At this point, it is important to emphasize that the size of the displacement $\Delta\sigma$ must be set considering two conflicting effects: using lower values results in an increase in the numerical error, but bigger displacements will increase the error due to anharmonicity. The dependency of the errors on both, frequency and intensity was examined for a small set of molecules and the results are presented in Figure E.3. Considering the compromise between these two factors, the value of $\Delta\sigma = 0.05\text{\AA}$ is used as default used.

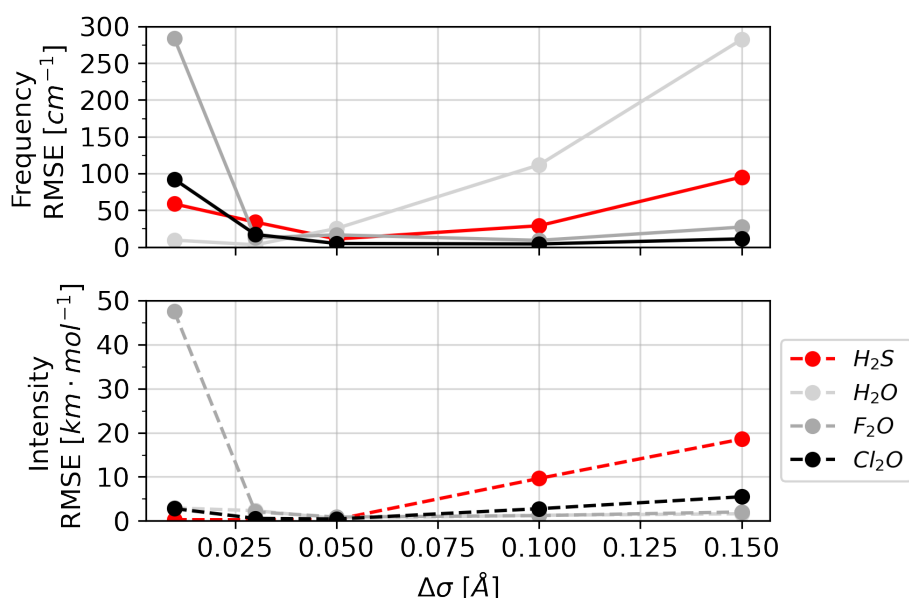


Figure E.3: Dependency of model's accuracy on the parameter $\Delta\sigma$. Top: RMSE for infrared frequencies. Bottom: RMSE for infrared frequency. Small values of $\Delta\sigma$ increase the numerical error, while bigger values increase the error due to the anharmonicity.

The inputs generated by theovib are named $X_Y_Z.com$, where X and Y are numbers from 0 to $3N - 1$ corresponding to the displaced coordinate, that is: 0 is the x coordinate of atom 1 and $3N - 1$ is the z coordinate of atom N . Z is a label that

indicates the displacement direction. If $X = Y$, then $Z = A$ corresponds to the point $[+, 0]$ in Figure E.2 and $Z = B$ corresponds to the point $[-, 0]$. If $X \neq Y$, then $Z = A$ corresponds to the point $[+, +]$, $Z = B$ to the point $[+, -]$, $Z = C$ to the point $[-, +]$ and, $Z = D$ to the point $[-, -]$.

An example of a theovib generated Gaussian input is given bellow. Notice that this input will generate an wavefunction file that will be integrated by AIMAll, obtaining the atomic charges, dipoles and IQA components.

```

1 %mem = 8GB
2 %nproc = 8
3 #b3lyp aug-cc-pvtz density=current nosym output=wfn
4
5 0_0
6
7 0 1
8 O    0.050000    0.000000    0.004316
9 H    0.000000   -0.763369   -0.580667
10 H   0.000000    0.763369   -0.580667
11
12 00_A.wfn

```

Once the AIMAll jobs are completed, the directory structure will be similar to the one depicted in Figure E.4. Intratomic IQA components and atomic charges and dipoles are found in the **.int* files inside the **_atomicfiles* directory.

The **B** matrix can be defined using the theovib module *internal*. In the water molecule example, we need to define three internal coordinates:

1. Bond between atoms 1 and 2;
2. Bond between atoms 1 and 3;
3. Angle defined by atoms 2–1–3.

Using the *Molecule* class, the b matrix can be stored inside the attribute *b_matrix*. The internal coordinates are generated using:

```

1 water.b_matrix=[internal.bond(water.positions, 1, 2),
2                  internal.bond(water.positions, 1, 3),
3                  internal.angle(water.positions, 2, 1, 3)]

```

The Hessian matrix are also stored in the object *water*, using:

```

1 water.hessian, water.iqa_hessian, errors= hessian_from_iqa(
2                  water.atoms, 'inputs_folder/', 0.05)

```

notice that the function *hessian_from_iqa()* receives three arguments that are: the list of atoms in the molecule, the value of $\Delta\sigma$ (0.05 by default), and the path to the directory containing the Gaussian and AIMAll outputs. This function outputs the Hessian matrix, the 3D Hessian matrix and a list of recovery errors, defined by the difference between the elements of the Hessian and the corresponding sum of elements in the 3D-Hessian.

```
inputs_folder
├── 0_0_A.com
├── 0_0_A.extout
├── 0_0_A.log
├── 0_0_A.mgp
├── 0_0_A.mgpviz
├── 0_0_A.mgp
├── 0_0_A.sum
├── 0_0_A.sumviz
├── 0_0_A.wfn
├── 0_0_A_atomicfiles
│   ├── o1.inp
│   ├── o1.int
│   ├── h2.inp
│   ├── h2.int
│   ├── h3.inp
│   ├── h3.int
│   ├── o1_h2.inp
│   ├── o1_h2.int
│   ├── o1_h3.inp
│   ├── o1_h3.int
│   ├── h2_h3.inp
│   └── h2_h3.int
└── ...
```

Figure E.4: Directory structure of theovib generated files.

With the Hessian and the **B** matrix, the force constants, and their IQA components, in internal coordinates can be obtained with the `convert_to_internal()` function:

```
1 water.internal_hessian, water.iqa_forces = convert_to_internal(
2     water.atoms, water.b_matrix,
3     water.iqa_hessian)
```

This function returns the Hessian matrix in internal coordinates, stored in `water.internal_hessian` attribute and the IQA partitioning of force constants, stored in `water.iqa_forces`.

Finally, the infrared intensities are obtained with the `normal_modes()` function. This function receives the list of atoms and the IQA Hessian returning the normal coordinates, the frequencies, the IQA partitioning of vibrational frequencies and the individual IQA terms, that is:

```
1 water.normal_coordinates, water.freq, water.iqa_freq, water.iqa_terms =
2     normal_modes(water.atoms,
3                 water.iqa_hessian)
```

The IR intensities are obtained through the CCTDP analysis using the `intensities()` function that receives as arguments the list of atoms, the equilibrium geometry, the normal coordinates, the path to the inputs folder and the value of $\Delta\sigma$. The function returns a list of IR intensities and the charge, charge transfer and dipolar polarization tensors. The calculations are performed as described in appendix C.

```
1 water.int, water.c_tensors, water.ct_tensors, water.dp_tensors =
2     intensities(
3     water.atoms, water.positions, water.normal_coordinates, 'inputs_folder/'
4     , 0.05)
```

The tensor are obtained numerically. For example, the charge derivative of atom A with respect to the displacement in the σ coordinate is:

$$\frac{\partial q_A}{\partial \sigma} = \frac{q_A^{[+,0]} - q_A^{[-,0]}}{2\Delta\sigma}. \quad (\text{E.2})$$

where $q_A^{[+,0]}$ and $q_A^{[-,0]}$ are the charge of atom A in the non-equilibrium geometries, as depicted in Figure E.2. The same applies for the atomic dipole moment tensors.

Bibliography

- (1) Melsen, A. G. M. v., *From Atomos to Atom: The History of the Concept Atom*; Dover phoenix editions; Dover Publications: Mineola, N.Y, 2004.
- (2) Viana, H. E. B.; Porto, P. A. *Science & Education* **2010**, *19*, 75–90.
- (3) Guillemin, V., *The Story of Quantum Mechanics*; Dover Publications: Mineola, N.Y, 2003.
- (4) Bader, R. F. W., *Atoms in molecules.: A Quantum Theory*; Oxford Univesity Press: 1990.
- (5) Popelier, P., *Atoms in Molecules: An Introduction*; Pearson Education, Essex: 2000.
- (6) Blanco, M. A.; Martín Pendás, A.; Francisco, E. *Journal of Chemical Theory and Computation* **2005**, *1*, 1096–1109.
- (7) Mayer, I. *Physical Chemistry Chemical Physics* **2006**, *8*, 4630.
- (8) Popelier, P. L. A.; Kosov, D. S. *The Journal of Chemical Physics* **2001**, *114*, 6539–6547.
- (9) Salvador, P.; Duran, M.; Mayer, I. *The Journal of Chemical Physics* **2001**, *115*, 1153–1157.
- (10) Symons, B. C. B.; Williamson, D. J.; Brooks, C. M.; Wilson, A. L.; Popelier, P. L. A. *ChemistryOpen* **2019**, *8*, 560–570.
- (11) Wilson, A. L.; Popelier, P. L. A. *The Journal of Physical Chemistry A* **2016**, *120*, Publisher: American Chemical Society, 9647–9659.
- (12) Francisco, E.; Casals-Sainz, J. L.; Rocha-Rinza, T.; Martín Pendás, A. *Theoretical Chemistry Accounts* **2016**, *135*, 170.

-
- (13) Rafat, M.; Popelier, P. L. A. In *The Quantum Theory of Atoms in Molecules*, Matta, C. F., Boyd, R. J., Eds.; Wiley-VCH Verlag GmbH & Co. KGaA: Weinheim, Germany, 2007, pp 121–140.
- (14) Davie, S. J.; Di Pasquale, N.; Popelier, P. L. A. *The Journal of Chemical Physics* **2016**, *145*, Publisher: American Institute of Physics, 104104.
- (15) Overend, J. In *Infrared Spectroscopy and Molecular Structure*, Davies, M., Ed.; Elsevier: Amsterdam, 1963.
- (16) Overend, J. In *Vibrational Intensities in Infrared and Raman Spectroscopy*, Person, W. B., Zerbi, G., Eds.; Elsevier: Amsterdam, 1982.
- (17) Wilson, E. B.; Wells, A. J. *The Journal of Chemical Physics* **1946**, *14*, 578–580.
- (18) Penner, S. S.; Weber, D. *The Journal of Chemical Physics* **1951**, *19*, Publisher: American Institute of Physics, 807–816.
- (19) Sharpe, S.; Sams, R.; Johnson, T. In *Applied Imagery Pattern Recognition Workshop, 2002. Proceedings.* 2002, pp 45–48.
- (20) Johnson, T. J.; Sams, R. L.; Sharpe, S. W. In *Chemical and Biological Point Sensors for Homeland Defense*, SPIE: 2004; Vol. 5269, pp 159–167.
- (21) Sharpe, S. W.; Johnson, T. J.; Sams, R. L.; Chu, P. M.; Rhoderick, G. C.; Johnson, P. A. *Applied Spectroscopy* **2004**, *58*, 1452–1461.
- (22) Scarminio, I. S.; De Barros Neto, B.; De Oliveira, A. E.; Haiduke, R. L. A.; Bruns, R. E. *Journal of Molecular Structure: THEOCHEM* **2001**, *539*, Cited By :6, 149–157.
- (23) Neto, B. B.; Bruns, R. E. *The Journal of Physical Chemistry* **1990**, *94*, 1764–1767.
- (24) Guadagnini, P. H.; Oliveira, A. E.; Bruns, R. E.; De Barros Neto, B. *Journal of the American Chemical Society* **1997**, *119*, Cited By :38, 4224–4231.
- (25) Frisch, M. J. et al. Gaussian 09 Revision B.1, 2009.
- (26) Heicklen, J. *Spectrochimica Acta* **1961**, *17*, Cited By :43, 201–205.
- (27) Van Straten, A.; Smit, W. *The Journal of Chemical Physics* **1977**, *67*, 970–982.
- (28) Mizuno, M.; Saeki, S. *Spectrochimica Acta Part A: Molecular Spectroscopy* **1976**, *32*, 1077–1082.

-
- (29) Kondo, S.; Nakanaga, T.; Saëki, S. *The Journal of Chemical Physics* **1980**, *73*, 5409–5418.
- (30) Morcillo, J.; Zamorano, L.; Heredia, J. *Spectrochimica Acta* **1966**, *22*, 1969–1980.
- (31) Kim, K.; King, W. *The Journal of Chemical Physics* **1980**, *73*, 5591–5597.
- (32) Levine, R. A.; Person, W. B. *The Journal of Physical Chemistry* **1977**, *81*, 1118–1119.
- (33) Kondo, S.; Saëki, S. *The Journal of Chemical Physics* **1981**, *74*, 6603–6611.
- (34) Saëki, S.; Tanabe, K. *Spectrochimica Acta Part A: Molecular Spectroscopy* **1969**, *25*, 1325–1348.
- (35) Tanabe, K.; Saëki, S. *Spectrochimica Acta Part A: Molecular Spectroscopy* **1970**, *26*, 1469–1479.
- (36) Kim, K.; King, W. *The Journal of chemical physics* **1984**, *80*, 978–982.
- (37) Bode, J.; Smit, W. *The Journal of Physical Chemistry* **1980**, *84*, 198–202.
- (38) Morcillo, J.; Herranz, J.; Biarge, J. F. *Spectrochimica Acta* **1959**, *15*, 110–121.
- (39) Golden, W. G.; Horner, D. A.; Overend, J. *The Journal of Chemical Physics* **1978**, *68*, 964–969.
- (40) Person, W. B.; Rudys, S. K.; Newton, J. H. *The Journal of Physical Chemistry* **1975**, *79*, 2525–2531.
- (41) Varanasi, P.; Ko, F.-K. *Journal of Quantitative Spectroscopy and Radiative Transfer* **1977**, *17*, 385–388.
- (42) Varanasi, P.; Chudamani, S. *Journal of Quantitative Spectroscopy and Radiative Transfer* **1988**, *39*, 193–195.
- (43) Li, Z.; Varanasi, P. *Journal of Quantitative Spectroscopy and Radiative Transfer* **1994**, *52*, 137–144.
- (44) Nanes, R.; Silvaggio, P. M.; Boese, R. W. *Journal of Quantitative Spectroscopy and Radiative Transfer* **1980**, *23*, 211–220.
- (45) Roehl, C.; Boglu, D.; Brühl, C.; Moortgat, G. *Geophysical research letters* **1995**, *22*, 815–818.
- (46) Schurin, B. *The Journal of Chemical Physics* **1959**, *30*, 1–5.

-
- (47) Golden, W.; Marcott, C.; Overend, J. *The Journal of Chemical Physics* **1978**, *68*, 2081–2084.
- (48) Kim, K. *Journal of Quantitative Spectroscopy and Radiative Transfer* **1987**, *37*, 107–110.
- (49) Schatz, P.; Hornig, D. *The Journal of Chemical Physics* **1953**, *21*, 1516–1530.
- (50) Levin, I. W.; Lewis, T. P. *The Journal of Chemical Physics* **1970**, *52*, 1608–1609.
- (51) Saeki, S.; Mizuno, M.; Kondo, S. *Spectrochimica Acta Part A: Molecular Spectroscopy* **1976**, *32*, 403–413.
- (52) Russell, J. W.; Needham, C.; Overend, J. *The Journal of Chemical Physics* **1966**, *45*, 3383–3398.
- (53) Barrow, G.; McKean, D. *Proceedings of the Royal Society of London. Series A. Mathematical and Physical Sciences* **1952**, *213*, 27–41.
- (54) Kondo, S.; Koga, Y.; Nakanaga, T.; Saëki, S. *Bulletin of the Chemical Society of Japan* **1983**, *56*, 416–421.
- (55) Dickson, A.; Mills, I.; Crawford Jr, B. *The Journal of Chemical Physics* **1957**, *27*, 445–455.
- (56) Elkins, J. W.; Kagann, R. H.; Sams, R. L. *Journal of Molecular Spectroscopy* **1984**, *105*, 480–490.
- (57) Galabov, B.; Yamaguchi, Y.; Remington, R. B.; Schaefer, H. F. *The Journal of Physical Chemistry A* **2002**, *106*, 819–832.
- (58) Silva, A. F.; Richter, W. E.; Bassi, A. B.; Bruns, R. E. *Physical Chemistry Chemical Physics* **2015**, *17*, 30378–30388.
- (59) Siegbahn, K.; Nordling, C.; Johansson, G.; Hedman, J.; Heden, P.; Hamrin, K.; Gelius, U.; Bergmark, T.; Werne, L.; Manne, R.; Baer, Y., *ESCA Applied to Free Molecules*; Noth-Holland Amsterdam: 1969.
- (60) Crawford Jr, B. *The Journal of Chemical Physics* **1952**, *20*, 977–981.
- (61) Kelly, R.; Rollefson, R.; Schurin, B. *The Journal of Chemical Physics* **1951**, *19*, 1595–1599.
- (62) Kim, K.; King, W. *Journal of Molecular Structure* **1979**, *57*, 201–207.

-
- (63) Koops, T.; Smit, W.; Visser, T. *Journal of molecular structure* **1984**, *112*, 285–299.
- (64) Golike, R.; Mills, I.; Person, W.; Crawford Jr, B. *The Journal of Chemical Physics* **1956**, *25*, 1266–1275.
- (65) Nakanaga, T.; Kondo, S.; Saëki, S. *The Journal of Chemical Physics* **1979**, *70*, 2471–2478.
- (66) Bode, J.; Smit, W.; Visser, T.; Verkruijsse, H. *The Journal of Chemical Physics* **1980**, *72*, 6560–6570.
- (67) Kondo, S.; Koga, Y. *The Journal of Chemical Physics* **1978**, *69*, 4022–4031.
- (68) Nyquist, I. M.; Mills, I.; Person, W.; Crawford Jr, B. *The Journal of Chemical Physics* **1957**, *26*, 552–558.
- (69) Koga, Y.; Kondo, S.; Nakanaga, T.; Saëki, S. *The Journal of Chemical Physics* **1979**, *71*, 2404–2411.
- (70) Levin, I. W.; Pearce, R. A. *The Journal of Chemical Physics* **1978**, *69*, 2196–2208.
- (71) Silva, A. F.; Richter, W. E.; Meneses, H. G.; Bruns, R. E. *Physical Chemistry Chemical Physics* **2014**, *16*, 23224–23232.
- (72) Biarge, J.; Morcillo, J.; Herranz, J. *Anales De La Real Sociedad Espanola De Fisica Y Quimica* **1961**, *57A*, 81.
- (73) Person, W. B.; Newton, J. H. *The Journal of Chemical Physics* **1974**, *61*, 1040–1049.
- (74) Cioslowski, J. *Journal of the American Chemical Society* **1989**, *111*, Publisher: American Chemical Society, 8333–8336.
- (75) Galabov, B.; Dudev, T., *Vibrational Intensities*, 1st ed.; During, J. R., Ed.; *Vibrational Spectra and Structure*, Vol. 22; Elsevier: 1996.
- (76) Richter, W. E.; Duarte, L. J.; Silva, A. F.; Bruns, R. E. *Journal of the Brazilian Chemical Society* **2016**, *27*, 979–991.
- (77) Duarte, L. J.; Silva, A. F.; Richter, W. E.; Bruns, R. E. *Spectrochimica Acta Part A: Molecular and Biomolecular Spectroscopy* **2018**, *205*, 269–275.

-
- (78) Richter, W. E.; Duarte, L. J.; Bruns, R. E. *Journal of Chemical Information and Modeling* **2021**, *61*, 3881–3890.
- (79) Dinur, U.; Hagler, A. T. *The Journal of Chemical Physics* **1989**, *91*, Publisher: American Institute of Physics, 2949–2958.
- (80) Haiduke, R. L. A.; Bruns, R. E. *The Journal of Physical Chemistry A* **2005**, *109*, 2680–2688.
- (81) Richter, W. E.; Silva, A. F.; Vidal, L. N.; Bruns, R. E. *Physical Chemistry Chemical Physics* **2016**, *18*, 17575–17585.
- (82) Silva, A. F.; Duarte, L. J.; Bruns, R. E. *The Journal of Physical Chemistry A* **2016**, *120*, 8387–8399.
- (83) Duarte, L. J.; Bruns, R. E. *The Journal of Physical Chemistry A* **2018**, *122*, Publisher: American Chemical Society, 9833–9841.
- (84) Richter, W. E.; Duarte, L. J.; Bruns, R. E. *Spectrochimica Acta. Part A, Molecular and Biomolecular Spectroscopy* **2021**, *251*, 119393.
- (85) Richter, W. E.; Duarte, L. J.; Bruns, R. E. *Spectrochimica Acta Part A: Molecular and Biomolecular Spectroscopy* **2022**, *271*, 120891.
- (86) Duarte, L. J.; Silva, A. F.; Richter, W. E.; Bruns, R. E. *The Journal of Physical Chemistry A* **2019**, *123*, Publisher: American Chemical Society (ACS), 6482–6490.
- (87) Silva, A. F.; Richter, W. E.; Terrabuio, L. A.; Haiduke, R. L. A.; Bruns, R. E. *The Journal of Chemical Physics* **2014**, *140*, Publisher: American Institute of Physics, 084306.
- (88) Silva, A. F.; Richter, W. E.; Bruns, R. E. *Chemical Physics Letters* **2014**, *610-611*, 14–18.
- (89) Silva, A. F.; Richter, W. E.; Meneses, H. G.; Faria, S. H.; Bruns, R. E. *The Journal of Physical Chemistry A* **2012**, *116*, 8238–8249.
- (90) Da Silva Jr, J. V.; Oliveira, A. E.; Hase, Y.; Bruns, R. E. *The Journal of Physical Chemistry A* **2009**, *113*, 7972–7978.
- (91) Dinur, U.; Hagler, A. *The Journal of chemical physics* **1989**, *91*, 2949–2959.
- (92) Dinur, U.; Hagler, A. *The Journal of chemical physics* **1989**, *91*, 2959–2970.

-
- (93) Dinur, U. *Chemical physics letters* **1990**, *166*, 211–216.
- (94) Eggers Jr, D. *The Journal of Chemical Physics* **1955**, *23*, 221–222.
- (95) King, W.; Mast, G. *The Journal of Physical Chemistry* **1976**, *80*, 2521–2525.
- (96) Spedding, H.; Whiffen, D. H. *Proceedings of the Royal Society of London. Series A. Mathematical and Physical Sciences* **1956**, *238*, 245–255.
- (97) Steele, D.; Whiffen, D. *The Journal of Chemical Physics* **1958**, *29*, 1194–1195.
- (98) Steele, D.; Wheatley, W. *Journal of Molecular Spectroscopy* **1969**, *32*, 265–275.
- (99) Hopper, M. J.; Russell, J. W.; Overend, J. *The Journal of Chemical Physics* **1968**, *48*, 3765–3772.
- (100) Nakanaga, T.; Kondo, S.; Saëki, S. *The Journal of Chemical Physics* **1982**, *76*, 3860–3865.
- (101) Richter, W. E. Intensidade características do grupo carbonila: Partições atômicas. QTAIM/CCFDF e QTAIM/CCTDP. Ph. D. Thesis, Universidade de Campinas, 2016.
- (102) Keith, T. A. AIMAll, Overland Park KS, USA, 2019.
- (103) Gomes, T. C.; Silva Jr, J. V. d.; Vidal, L. N.; Vazquez, P. A.; Bruns, R. E. *Quimica Nova* **2008**, *31*, 1750–1754.
- (104) Cole, A.; Michell, A. *Spectrochimica Acta* **1964**, *20*, 739–746.
- (105) Kagel, R.; Powell, D.; Overend, J.; Ramos, M. N.; Bassi, A.; Bruns, R. E. *The Journal of Chemical Physics* **1983**, *78*, 7029–7037.
- (106) Kagel, R.; Powell, D.; Overend, J.; Ramos, M. N.; Bassi, A.; Bruns, R. E. *The Journal of Chemical Physics* **1982**, *77*, 1099–1106.
- (107) Hirshfeld, F. L. *Theoretica chimica acta* **1977**, *44*, 129–138.
- (108) Marenich, A. V.; Jerome, S. V.; Cramer, C. J.; Truhlar, D. G. *Journal of chemical theory and computation* **2012**, *8*, 527–541.
- (109) Lu, T.; Chen, F. *Journal of Theoretical and Computational Chemistry* **2012**, *11*, 163–183.
- (110) Fonseca Guerra, C.; Handgraaf, J.-W.; Baerends, E. J.; Bickelhaupt, F. M. *Journal of computational chemistry* **2004**, *25*, 189–210.

-
- (111) Reed, A. E.; Weinstock, R. B.; Weinhold, F. *The Journal of Chemical Physics* **1985**, *83*, 735–746.
- (112) Breneman, C. M.; Wiberg, K. B. *Journal of Computational Chemistry* **1990**, *11*, 361–373.
- (113) Richter, W. E.; Bruns, R. E. *Spectrochimica Acta Part A: Molecular and Biomolecular Spectroscopy* **2016**, *164*, 123–127.
- (114) McKean, D. *The Journal of Chemical Physics* **1956**, *24*, 1002–1006.
- (115) Pimentel, G. C.; McClellan, A. L.; MacClellan, A. L., *The hydrogen bond*; WH freeman: 1960.
- (116) Kuyanov-Prozument, K.; Choi, M. Y.; Vilesov, A. F. *The Journal of chemical physics* **2010**, *132*, 014304.
- (117) Joseph, J.; Jemmis, E. D. *Journal of the American Chemical Society* **2007**, *129*, 4620–4632.
- (118) Iogansen, A. *Spectrochimica Acta Part A: Molecular and Biomolecular Spectroscopy* **1999**, *55*, 1585–1612.
- (119) Terrabuio, L. A.; Richter, W. E.; Silva, A. F.; Bruns, R. E.; Haiduke, R. L. *Physical Chemistry Chemical Physics* **2014**, *16*, 24920–24928.
- (120) Rozenberg, M. *RSC advances* **2014**, *4*, 26928–26931.
- (121) Møller, C.; Plesset, M. S. *Physical review* **1934**, *46*, 618.
- (122) Dunning Jr, T. H. *The Journal of chemical physics* **1989**, *90*, 1007–1023.
- (123) Boys, S. F.; Bernardi, F. *Molecular Physics* **1970**, *19*, 553–566.
- (124) Simon, S.; Duran, M.; Dannenberg, J. *The Journal of chemical physics* **1996**, *105*, 11024–11031.
- (125) Da Silva, N. A.; Terrabuio, L. A.; Haiduke, R. L. A. *International Journal of Quantum Chemistry* **2017**, *117*, 197–207.
- (126) Hughes, E. D.; Ingold, C. K. *Journal of the Chemical Society* **1935**, 244.
- (127) Hamlin, T. A.; Swart, M.; Bickelhaupt, F. M. *ChemPhysChem* **2018**, *19*, 1245–1245.

-
- (128) Santos-Jr, C. V.; A. F. de Souza, M.; Kraka, E.; Moura Jr, R. T. *Chemical Physics Letters* **2022**, *787*, 139282.
- (129) Su, T.; Wang, H.; Hase, W. L. *The Journal of Physical Chemistry A* **1998**, *102*, 9819–9828.
- (130) Fukui, K. *The Journal of Physical Chemistry* **1970**, *74*, 4161–4163.
- (131) Fukui, K. *Accounts of Chemical Research* **1981**, *14*, 363–368.
- (132) Chandrasekhar, J.; Smith, S. F.; Jorgensen, W. L. *Journal of the American Chemical Society* **1984**, *106*, 3049–3050.
- (133) Alkorta, I.; Thacker, J. C. R.; Popelier, P. L. A. *Journal of Computational Chemistry* **2018**, *39*, 546–556.
- (134) Gallegos, M.; Costales, A.; Pendás, Á. M. *ChemPhysChem* **2021**, *22*, 775–787.
- (135) Marcus, R. A. *The Journal of Chemical Physics* **1966**, *45*, 4493–4499.
- (136) Marcus, R. A. *The Journal of Chemical Physics* **1966**, *45*, 4500–4504.
- (137) Marcus, R. A. *The Journal of Chemical Physics* **1968**, *49*, 2610–2616.
- (138) Marcus, R. A. *The Journal of Chemical Physics* **1968**, *49*, 2617–2631.
- (139) Miller, W. H.; Handy, N. C.; Adams, J. E. *The Journal of Chemical Physics* **1980**, *72*, 99–112.
- (140) Cremer, D.; Kraka, E. *Current Organic Chemistry* **2010**, *14*, 1524–1560.
- (141) Quapp, W.; Heidrich, D. *Theoretica Chimica Acta* **1984**, *66*, 245–260.
- (142) Nanayakkara, S.; Kraka, E. *Physical Chemistry Chemical Physics* **2019**, *21*, 15007–15018.
- (143) Matta, C. F.; Sowlati-Hashjin, S.; Bandrauk, A. D. *The Journal of Physical Chemistry A* **2013**, *117*, 7468–7483.
- (144) Wilson, E.; Decius, J.; Cross, P., *Molecular Vibrations: The Theory of Infrared and Raman Vibrational Spectra*; Dover Books on Chemistry Series; Dover Publications: 1980.
- (145) McIntosh, D. F.; Michaelian, K. H.; Peterson, M. R. *Canadian Journal of Chemistry* **1978**, *56*, 1289–1295.

-
- (146) D. F. McIntosh; K. H. Michelian *Canadian Journal of Spectroscopy* **1979**, *24*, 1–10.
- (147) D. F. McIntosh; K. H. Michelian *Canadian Journal of Spectroscopy* **1979**, *24*, 35–40.
- (148) D. F. McIntosh; K. H. Michelian *Canadian Journal of Spectroscopy* **1979**, *24*, 65–74.
- (149) McIntosh, D. F. *Theoretical Chemistry Accounts* **2010**, *125*, 177–184.
- (150) Gussoni, M.; Zerbi, G. *Journal of Molecular Spectroscopy* **1968**, *26*, 485–488.
- (151) Frisch, M. J. et al. Gaussian 16 Revision C.01, 2016.
- (152) *The IUPAC Compendium of Chemical Terminology: The Gold Book*, 4th ed.; Gold, V., Ed.; International Union of Pure and Applied Chemistry (IUPAC): Research Triangle Park, NC, 2019.
- (153) Renner, T., *Quantities, Units and Symbols in Physical Chemistry*; Cohen, E. R., Cvitas, T., Frey, J. G., Holström, B., Kuchitsu, K., Marquardt, R., Mills, I., Pavese, F., Quack, M., Stohner, J., Strauss, H. L., Takami, M., Thor, A. J., Eds.; The Royal Society of Chemistry: 2007, P001–232.
- (154) Kaupp, M.; Danovich, D.; Shaik, S. *Coordination Chemistry Reviews* **2017**, *344*, 355–362.
- (155) *CRC handbook of chemistry and physics*, 98th ed.; Rumble, J., Ed.; CRC Press llc Boca Raton, FL: 2017.
- (156) Brandhorst, K.; Grunenberg, J. *Chemical Society Reviews* **2008**, *37*, 1558.
- (157) Strong, F. C. *Analytical Chemistry* **1952**, *24*, 338–342.
- (158) Strong, F. C. *Analytical Chemistry* **1952**, *24*, 2013–2013.
- (159) Braslavsky, S. E. *Pure and Applied Chemistry* **2007**, *79*, 293–465.
- (160) Smith, M. A. H.; Rinsland, C. P.; Fridovich, B.; Rao, K. N. In *Molecular Spectroscopy: Modern Research*; Elsevier: 1985, pp 111–248.
- (161) Hopper, M. J.; Russell, J. W.; Overend, J. *Spectrochimica Acta Part A: Molecular Spectroscopy* **1972**, *28*, 1215–1224.

- (162) Pauling, L.; Wilson, E. B., *Introduction to quantum mechanics with applications to chemistry*; Courier Corporation: 2012.
- (163) Hilderbrandt, R. L. *Journal of Molecular Spectroscopy* **1972**, *44*, 599–601.